Results of the ESO Internal ALMA Development Study "New methods for ALMA beam shaping and the assessment of angular scale sensitivity"

D. Petry[1], M. Díaz Trigo[1], R. Kneissl[2,3], I. Toledo[3], S. Facchini[1], T. Takagi[4]

November 30, 2021

[1] European Southern Observatory, Karl-Schwarzschild-Str. 2, 85748 Garching, Germany
[2] European Southern Observatory, Alonso de Cordova 3107, Santiago, Chile
[3] Joint ALMA Observatory, Alonso de Cordova 3107, Santiago, Chile
[4] Japan Space Forum, 3-2-1 Kandasurugadai, Chiyoda-ku, Tokyo 101-0062, Japan

Contents

1 Summary

This document describes the work and results of the ESO ALMA Internal Development Study "New methods for ALMA beam shaping and the assessment of angular scale sensitivity", performed between January 2020 and November 2021[1]. The main results of this study are the following:

1.1 The Baseline Length Distribution as a tool in scheduling and quality assurance

In order to assess the sensitivity of an observation at all angular scales, we introduce the *Baseline Length Distribution* (BLD) in 1D (ignores baseline orientation) and 2D. The *observed BLD* of an MOUS is the histogram of the baseline lengths (BLs) for a representative channel in the representative spectral window and for a representative target *after flagging*. Each entry is weighted by its integration time and the relative imaging weight (weight divided by average weight for all baselines). So the unit of the histogram content is "visibility seconds" or "visibility hours" (see, e.g., Fig. 3.1). The concept can be extended to also take into account the absolute T_{sys} information rather than just the relative one which is contained in the relative weights[2].

For this report, we have primarily studied the 1D BLD because it permits more clear visualisation (overplotting of different BLDs). Furthermore, for the introduction of an angular-scale-dependent sensitivity assessment, the easy-to-handle 1D plots seem more practical at least as a first iteration. However, we note that the ideal procedure will use 2D BLDs and we propose to extend our assessment tool to full 2D treatment in a follow-up study. Our tools are already prepared for that.

An *expected BLD* can be derived from the science goal parameters: angular resolution (AR), largest angular scale (LAS), exposure time for the representative target (see, e.g., Fig. 3.2). Comparison of the observed and expected BLDs yields information about the BL range(s) where the MOUS lacks sensitivity and where it is overexposed. To quantify the differences, we introduce the *Filling Fraction* (FF) as the ratio of observed and expected visibility seconds in an individual

---

[1] An in-depth review was carried out based on the final draft of this report between August and October 2021. We would like to thank the reviewers Maitee Beltran, John Carpenter, Harold Francke, Neil Phillips, Eric Villlard, and the coordinator Carlos de Breuck for their thorough work.

[2] Already the relative weights are important for more accurately determining the BLD of an observation. In compact configurations with many antennas the effect may average out, but in extended configurations and frequencies where water dominates the opacity there can be large scale variation over the array that can systematically affect the BLD by reducing the weight of long baselines (as more remote stations are at lower altitude on the W and S branches). The absolute T_{sys} information then permits to assess the absolute sensitivity achieved in each BLD bin.

BL bin (see section 3.4 and example plots in, e.g., section 5.3). If the expectation is zero, the FF is defined to be unity.

A quality assessment can then be performed by defining conditions on the FFs. If the conditions are not fulfilled for a given MOUS, one can derive the array configuration in which additional SB executions, if any, should be scheduled. For multi-EB MOUSs, this procedure can already be applied during scheduling when an MOUS cannot be completed in one consecutive set of executions.

In a final implementation, the FFs can also take into account the absolute T_{sys}, instead of only the relative one, and thus become "execution fractions" for each BL bin. This could replace the present overall execution fraction used in scheduling and QA.

1.2 Impact of BLD defects on the imaging results

By studying simulated 12-m array observations of a complex test image with emission at a large range of angular scales, we find that the results of the standard imaging process with CASA tclean are only weakly deteriorated by deviations of the BLD from the ideal *as long as a significant sensitivity to all relevant angular scales is maintained.*

In other words, the deconvolution process is apparently able to repair shortcomings of the BLD (which translate into shortcomings of the point spread function, PSF) quite well unless the angular scale in question is not sampled at all or drowned in noise because the sensitivity at that scale is too low. This is of course also true for defects of the azimuthal BLD. We therefore recommend that in the next step, the BLD assessment is extended to full 2D as mentioned above.

Although we were not able to demonstrate this clearly on an example case (due to the limited time and resources available for this study), we have to assume from other studies that the deconvolution is more accurate if the PSF is better behaved, i.e. more Gaussian. This is a consequence of general linear algebra: If the condition number of the Hessian matrix in a linear least squares formulation of the deconvolution problem is poor, then the reconstruction is harder, and a greedy algorithm (i.e. one which makes the locally optimal choice) will not perform as well (see e.g. Rau et al. 2009). We therefore recommend that tighter conditions are imposed on the BLD shape for MOUSs with science goals which require the best possible image fidelity, e.g., morphological studies of extended objects.

For studies of point sources and detection experiments, the shape of the BLD should also be assessed (BLD/PSF shape is also relevant here, e.g., in the presence of bright off-axis sources) but with more relaxed limits.

1.3 Recommended method to compute the expected BLD

The ideal shape of the BLD can be derived from conditions on the shape of the PSF of the interferometer. These conditions concern (a) the FWHM of a Gaussian fit to the PSF (corresponding to the achieved AR or smallest resolved angular scale), (b) the LAS/MRS (Largest Angular Scale, Maximum Recoverable Scale), and (c) the requirement of a general Gaussian shape of the PSF with minimal negative bowls. We have studied two methods to compute a BLD from the AR and LAS and find that our "analytical" method is the preferred one (see section 3.2.1) since it agrees largely with the present design of the ALMA configurations (which in turn have been optimised for PSF shape). The "analytical" method computes the 2D BLD as a Gaussian with an inner taper and then derives the 1D BLD.

Our second method (named "filled dish", FD, section 3.2.2) fills a 2D aperture of a diameter corresponding to the AR with randomly placed antenna positions imposing a minimum distance between all antennas corresponding to the MRS. The difference in BLD shape w.r.t. our first ("analytical") method consists mainly in a stronger emphasis on longer baselines with a cutoff at the BL which corresponds to the AR. Furthermore, the FD method permits to extrapolate in a simple way to zero BL and may thus be helpful in judging the BLDs of combined 12M+7M+TP datasets when pseudo-visibilities are introduced for the TP data. Filled dish array configurations have been studied in the past (e.g. Woody 2001b) and found to perform well, but in this study we did not have time to explore this in any depth. Also, it is only feasible to produce pseudo-filled-dish configurations with ALMA in the most compact configurations. To summarize: the main reasons why we prefer the "analytical" method over the FD method are that (a) a pure FD BLD cuts off abruptly at a certain maximum BL which leads to larger sidelobes than in the analytical case, and (b) the ALMA configurations are more similar to the analytical expectations and we are trying to make recommendations which are feasible and have a political chance of being adopted. However, in future work we may use the FD method to better determine the inner taper of the analytical expectation.

1.4 Properties of the BLDs of the Cycle 6 and 7 12M MOUSs

1.4.1 Underexposure at intermediate baseline lengths

From our study of nearly 500 Cycle 6 and 7 12M MOUSs, we find that the ALMA 12-m Array observations show in general enough sensitivity at large and small angular scales but fall short of the ideal requirements for scales in between. This is true regardless of the exposure time, the target elevation, and the number of antennas used. Simulations show that this feature is already present in the nominal C43 configurations, although there are significant differences among the configurations, with the compact ones being closer to an ideal[3] interferometer and the extended configurations deviating more significantly from it.

1.4.2 Overexposure at the shortest baselines and implications for TM2

The Cycle 6/7 way of scheduling and the configurations used, resulted in an overexposure of most MOUSs at the shortest baselines. This implies that there is a significant number of cases in which a TM2 (compact-configuration) observation has been added to a TM1 (extended-configuration) observation to match a large requested LAS, even though the TM2 observation adds visibilities only where there were already enough. In such cases the TM2 observations are superfluous since they do not contribute to a better coverage of angular scales. In order to clarify the indications we have found, we recommend to perform a systematic study (as a function of configuration, on-source time, and source elevation) of how the TM2 SB creation procedure could be replaced by the BLD-based scheduling.

---

[3] “ideal” here refers to our “analytical” method of computing the BLD

1.4.3 General overexposure

In general, the sensitivity reached is often significantly better than requested so that methods to improve the BLD shape during offline analysis could be applied. We have produced prototype code to demonstrate the adjustment of the BLD by re-weighting but were not able to study this in depth due to lack of time. First results look promising and our prototype re-weighting code is included in the software products of this study.

1.4.4 Short observations

In the analysed sample of almost 500 Cycle 6/7 MOUSs (see chapter 6), we find that for Set 1, 71% of all MOUSs consist of one execution. The on-source time is less than 5 minutes for 7% of the sample and less than 15 minutes for 45% of the sample. Only 21% of all MOUSs have on-source times longer than 1 hour. Therefore, any future simulation intended to replicate common conditions of ALMA observations should be performed with relatively short on-source times.

1.4.5 Observations with no explicit LAS request

Essentially all observations will profit from BLD assessment. In the analysed sample, for Set 1, only 10% of all MOUSs have no explicit request on LAS (that is, LAS=0). This fraction is too small to obtain a significant overall gain by not evaluating the BLD match. And evaluating the BLD match for such observations will further help understanding operational constraints. However, for such MOUSs, the criterion for the minimum FF in each BLD bin could in principle be relaxed.

1.5 Recommended QA2 criterion

We recommend to define the FFs in *ten equidistant BL bins*[4] *between the minimum possible BL and the maximum expected BL* for the given MOUS. Achievement of the AR is then enforced by requiring an FF of 1.0 in the highest BL bin (bin 10, possibly also 9). The achievement of the overall sensitivity is enforced by requiring the average FF over all ten bins to be $\geq$0.9. Achievement of the LAS and good sensitivity at all intermediate angular scales is enforced by requiring every individual bin 1 - 9 to have a significant FF, e.g. 0.6 (based on the fact that we found in our imaging sub-study in chapter 4 that BLD defects of 40% can be made up for by the off-line deconvolution with CASA tclean). The best value of this limit for scheduling and QA purposes will have to be determined taking into account operational constraints and potential future modifications of the ALMA configurations. For the LAS criterion (or L05) the Gaussian

---

[4] We experimented with various binning schemes going up to ca. 100 bins. The bottom line of these efforts was the following: Subdividing the range of interest into 10 equidistant bins means to improve the angular scale resolution in which the sensitivity is being investigated individually now (in the present Cycle 7/8 QA2 procedure) by an order of magnitude. Reducing it by two orders of magnitude would have been too much for statistical reasons: there would have been too many bins with very low or zero content (we only have ca. 1000 different baselines). And reducing it by less than an order of magnitude makes the method too insensitive to relevant details of the BLD. One could envisage a method which adapts the bin width to the total number of integrations but we wanted to keep the plots uniform from MOUS to MOUS such that QA2 analysts would have a constant reference frame in which to judge the BLD.

signal images from chapter 4 can be used to relate the FF to the current ALMA criterion of 10% flux recovery at LAS (see sect. 3.2.1).
As mentioned above, complete integration of the FF criteria in QA2 would be achieved if the absolute T_{sys} (not only the relative one) is taken into account and the FF becomes equivalent to an execution fraction resolved in BL/angular-scale.

1.6 Implications for scheduling

As mentioned in section 1.4.2, we generally recommend that the use of TM2 observations is re-evaluated. It may be possible to achieve a large LAS and a better overall combined BLD shape in a better way.
E.g., when an MOUS cannot be completed in one session, we recommend to inspect the so-far achieved BLD as part of scheduling in order to determine which array setup is best to complete the MOUS and achieve a near-ideal BLD. This "best next config" for the given MOUS can then be used to replace the originally planned configuration in the scheduler. We have developed an algorithm to automatically choose the best next configuration (`projSelect`, see below).

1.7 Software prototypes developed by this study

We have developed a number of software prototypes for generating BLDs, operating on them, and assessing their properties. They are available in the JAO CVS repository at the location given in brackets. Chapter 5 and Appendix B give more information.

mshistotools: (`AIV/science/ArrayConfiguration/beamWG/mshistotools.py`) a comprehensive Python module for generating observed and expected 1D and 2D BLDs from given sets of MeasurementSets or Science Goal parameters, plotting them, and perform operations like adding, subtracting, scaling. The expected BLDs are computed using the "analytical" method, see above. Uses matplotlib.

filldish: (`AIV/science/ArrayConfiguration/beamWG/filldish.py`) a Python module for generating expected BLDs from Science Goal parameters using the FD method (see above). Uses mshistotools.

assess_ms: (`AIV/science/ArrayConfiguration/beamWG/assess_ms.py`) a Python application for judging the quality of the BLD of a given set of MeasurementSets (MSs, e.g., the calibrated MSs belonging to a given MOUS or those belonging to multiple MOUSs from the same GOUS) by comparing the BLD with an expectation which is computed based on Science Goal parameters. Output is a set of standardised diagnostic plots and the QA2 PASS/FAIL decision. Uses mshistotools and filldish.

thinms: (`AIV/science/ArrayConfiguration/beamWG/thinms.py`) methods to shape the Baseline Length Distribution of a given MS using either flagging or weighting.

projSelect: (`AIV/science/ArrayConfiguration/beamWG/example_case_projSelect_v1.py`) Prototype tool to demonstrate a scheduling algorithm to select the best next array configuration for the execution of a given SB based on the science goal parameters and the BLD of the already existing executions. Uses mshistotools.

1.8 Future work

With this study we have demonstrated that taking into account the BLD is a valuable approach for scheduling and quality assessment of ALMA data, with the following advantages compared to the current procedure:

- Possibility to detect in real-time an array setup that leads to a distorted BLD, and to identify combinations of array configurations/setups, source declination, and HA that result in good/bad BLDs - also for the 7-m array.
- For SBs which need several executions, possibility to optimise the range of HA for each execution to improve the final BLD.
- For GOUS with TM1 and TM2 MOUSs, possibility to significantly reduce the total execution time by removing the TM2 execution.
- More accurate judgement of the observation completion by resolving the Execution Fraction in angular scale.
- Possibility of achieving ideal BLDs during data processing by re-weighting of outliers in the BLD (see below).
- Possibility to determine the need for 7-m observations more accurately.

For an implementation of this technique, there are a few aspects that deserve further in-depth study.

1. (a) Provide a more firm basis for the determination of the BLD quality criteria[5]: Evaluate in a systematic way the BLD matches to analytical expectations for all the nominal configurations and a grid of source declinations and HAs. This can be used not only to set limits to the acceptable deficits but also to improve the observing parameters during scheduling (e.g. avoid certain combinations of declination and HA that lead to deformed BLDs) or even improve the design of some configurations. (b) Revisit the definition of the inner taper, which is a natural Gaussian scale filter representing well the C40, review possible alternatives beyond the filled dish, e.g. sharper edge related to statistics of two-point process, and contrast with the MRS definition.
2. Evaluate the caveats (if any) for the removal of the TM2 MOUS to meet LAS requirements. Demonstrate with imaging results on real data sets that removing TM2 does change the image quality, and simulate a case, where the AR/LAS requirement should really require C-X and C-(X-3).

---

[5] The minimum requested BLD quality (and therefore image quality) could be in principle different for different science intents. However, the science intent of the PI should be first recorded in the OT to enable setting the level of image quality needed to meet the science intents (https://ictjira.alma.cl/browse/SCIREQ-381). We note that even in the case of a “bare” detection experiment, the need of a minimum imaging quality (and therefore of the BLD shape) has been deemed important to avoid imaging artifacts due to a bad PSF that could result in not meeting the QA2 requirements on sensitivity (https://ictjira.alma.cl/browse/SCIREQ-783).

3. Extend the study of the effect of BLD defects on image quality by (a) larger noise and assessing in particular the performance in the image regions with lowest SNR, and (b) finding a way to better quantify the overall image fidelity.

4. Evaluate the effect of re-weighting certain BLs in the BLD (to achieve smoother BLDs) in the quality of the images and derive the parameters that lead to highest image fidelity. Devise a reweighting scheme which uses a smooth function to describe the dependency of weight on BL.

5. Introduce the absolute T_{sys} information in the weights in the BLD (rather than only the relative one which we already use) and derive a new value for measuring the Execution Fraction. Furthermore investigate how the sensitivity loss due to the increase of the phase RMS with BL can be taken into account.

6. For applications in scheduling and QA0, where imaging weights are not yet available, investigate the use of the antenna aperture efficiency in addition to T_{sys} for determining weights in the BLD. Furthermore, enable the assessment tool to read ASDMs directly in order to save the time needed for import.

7. Extend the approach to use the full 2D BLDs.

8. Explore the best way of finding the representative AR of a BLD distribution: iterative process for matching the observed BLD to the expected BLD for several values of AR. Furthermore, take into account that for observations with large fractional bandwidth, the AR and LAS requirements are effectively extended and need to be assessed at the near-lowest frequency (AR) and near-highest frequency (LAS) respectively.

9. Investigate 7-m scheduling in terms of HA and actual 7-m antenna availability since smaller array size and more compact configuration (prone to shadowing) make the potential gain in image quality even larger.

10. Investigate to which extent the OT could already determine the need for 7M and TP observations and whether the OT should request information about image quality (synth. beam shape) requirements from the PI.

In addition, an evaluation of the impact of this approach for all subsystems involved from proposal planning to delivery of data was not in the scope of this project but will necessarily have to be done before implementation.

2 Introduction

The ALMA observatory operates in a service mode which also includes the delivery of fully calibrated data and high-quality imaging products. Before data is cleared for delivery to the PIs, it undergoes a detailed Quality Assurance (QA) process which assesses (after making sure that the calibration meets the quality standards) primarily two parameters: the achieved sensitivity (the "RMS") and the achieved angular resolution (the "beam size").

In the past few years of ALMA operations, we have seen that if observations fail QA, they often do so because they nominally do not achieve the beam and the RMS at the same time within the given margins. The nominally failing datasets represent high-quality data but the system lacks the ability to parametrise in detail what additional observations would have to be carried out to complete the observation and achieve the science goal efficiently. Hence, typically, a relatively wasteful re- observation is necessary which overexposes the target at some of the angular scales. In other words, we now think that the simplified representation of the observational parameters as "RMS and beam" is not good enough to efficiently drive the ALMA observatory. This study wants to take a step forward and move to a more sophisticated approach which is more appropriate for interferometers.

RMS and beam are dependent on each other. For a given observation, it is possible to modify the beam by down-weighting the contribution of certain antenna pairs ("baselines"). This will always also result in an increase of the RMS, i.e. a deterioration of the sensitivity.

The ALMA user presently specifies the desired values of RMS and beam via the Observing Tool (OT) during proposal preparation. By several already well developed methods, a range of acceptable beam sizes is determined and connected to the Scheduling Block (SB) of each planned observation. In the most constrained case, the width of the range is presently +/- 20% of the nominal beam size value. Similarly, for the RMS, the user specifies a desired value for a given bandwidth to which an additional margin depending on the ALMA frequency band is added. The user can also specify a "largest angular scale", LAS, as a third parameter but this is presently not used in scheduling nor in QA. However, the LAS is used by the OT to add a SB in a more compact configuration (so-called TM2) if deemed necessary.

The resulting parameter range in RMS and beam are then what the ALMA scheduler tries to achieve. However, further constraints related to the MOUS (e.g. atmospheric or time constraints driven by astrophysical goals) or to operational issues such as antenna moves and the competition between different observations for a given set of constraints result in SBs not always executed under ideal conditions.

When this happens, it is important that the subsequent data processing and quality assurance do judge the observation precisely without discarding useful data or being too optimistic.

This document summarises the results of the ESO ALMA Internal Development Study "New methods for ALMA beam shaping and the assessment of angular scale sensitivity", performed between January 2020 and July 2021, aimed at investigating new ideas concerning the set of problems described. An intermediate report was already published in Petry et al. (2020). Results from that report are included here.

Having realised that determining the synthesized beam size essentially only measures the achieved sensitivity for the longest baselines, we explore a more complete approach where we separately measure the achieved sensitivity in all ranges of baseline lengths, i.e. all observed angular scales, and then compare these to an expectation which we derive from the AR and LAS specified in the science goal.

We propose to perform this comparison between observation and expectation not only at the end of the observation procedure in the QA stage but already during the scheduling of multi-EB MOUSs, dynamically choosing the array configuration for the next execution based on the baseline length distribution achieved so far.

For all data processing in this study, we have used the CASA data analysis package (Emonts et al. (2019)), mostly version 6.1.1.

3 Basic concepts

3.1 The Baseline Length Distribution - expected and observed

One of the main concepts we need to introduce in our new approach is the Baseline Length Distribution (BLD). This is a histogram of the projected length (in meters) of the baselines formed by the antennas of the interferometer array. For each integration (visibility) recorded in the interferometric dataset (after discarding invalid data, so-called "flagging"), one entry is made in the BLD bin corresponding to the length of the baseline used for that integration. We distinguish between

unweighted BLD - the histogram entry for one integration is given a weight equal to the integration time.

absolutely weighted BLD - the histogram entry for one integration is given a weight equal to the inverse per-channel noise squared (which is what is recorded in the WEIGHT column of a MeasurementSet). The WEIGHT value is proportional to the integration time, the channel bandwidth and inversely proportional to the system temperature squared.

relatively weighted BLD - here the histogram entry is given a weight equal to the WEIGHT value as above but normalised to the average WEIGHT of all baselines.

In this study, if not stated otherwise, we work with relatively weighted BLDs because this does not require us to include T_{sys} *information in our calculation of the expected BLD. Since the overall sensitivity is assessed via the achieved RMS and the "Execution Fraction" during scheduling, QA0, and QA2, our study is mainly concerned with the BLD shape, not the effect of atmospheric absorption on its absolute normalisation. In an upgrade, it would be relatively straight-forward to include the* T_{sys} *information in the expectation calculation and work with absolutely weighted BLDs. This would merge the "Execution Fraction" and the BLD assessment.*

The y-axis of the BLD histogram has units of "visibility hours" in all three cases. Commonly, the "sensitivity" of an observation is regarded as inversely proportional to the achieved RMS image noise. The sensitivity of an interferometric observation is thus proportional to the square root of the product of observation time and number of baselines used, and the value of the individual histogram column of the BLD is proportional to the square of the sensitivity achieved for that baseline length range.

Each baseline length range corresponds to a range of angular scales in the interferometric image derived from the dataset via the equation $a = \lambda/d$ where a is the angular scale, λ is the observing wavelength, and d is the baseline length. The BLD is thus equivalent to a sensitivity vs. angular scale plot. Histogramming the baseline length rather than the angular scale itself, however, is more convenient in the scheduling context because the BLD of a given array configuration does not depend on the observing frequency. Figure 3.1 shows examples of 1D and 2D BLDs.

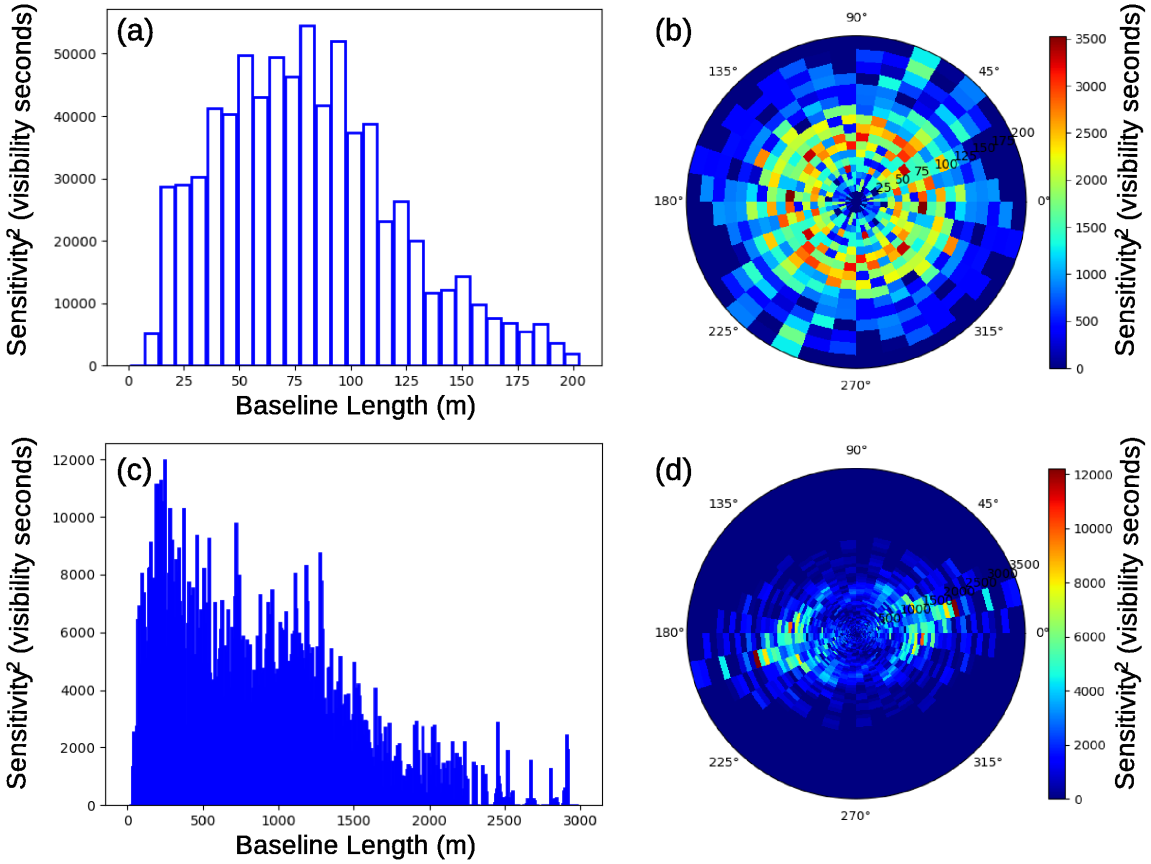

Figure 3.1: Examples of 1D and 2D baseline length distributions (with relative weighting) for (top: (a) and (b)) an ALMA 8 minute observation using 44 antennas in a compact configuration and (bottom: (c) and (d)) a 39 minute exposure using 47 antennas in an extended (hybrid) configuration which is unusually elongated. Histograms (a) and (c) both use 7 m bin width while the 2D histograms (b) and (d) use a variable radial bin width linearly growing with baseline length. See text.

For both forms of representing the sensitivity to different angular scales, there is a problem of low number of counts at the upper end of the histogram (see Fig. 3.1c) and a problem of resolution at the lower end. Also logarithmically increasing the bin width does not result in a flat distribution and is less intuitive to read. Furthermore the inclusion of the important "zero spacings" from single dish observations in the first bin is awkward in a log scale. We have therefore chosen to exclusively work with the BLD representation and remedy the histogramming problems by introducing a special bin width scheme adapted to the ALMA arrays: The first two bins are fixed to 7 m width. Starting with the third bin, the bin width is increasing linearly such that it reaches 700 m at a baseline length of 16000 m. The binning is thus tuned to ALMA observations with BLs up to the present maximum possible and typical numbers of antennas around 43 resulting

in a certain number of total visibilities in the typical shorter observing times of ca. 10 min. This scheme permits to see the distributions in sufficient resolution and with sufficient counts per bin for all ALMA configurations. And it has the additional useful property that the first bin can exclusively be filled by single-dish (TP) observations and the second bin exclusively by ACA observations. Underperformance in these bins can therefore be used as an indicator that TP and/or ACA data is missing. However, in this study we used this non-equidistant binning only for display. QA is done with a different, more coarse, equidistant binning (see 3.3).
A 2D version of the BLD is essentially the familiar "uv coverage" plot which is commonly used in interferometry. The 2D version has the advantage that it also captures the baseline *orientation* and thus the elongation and orientation of the synthesized beam ellipse (see the example in Fig. 3.1d) while the 1D BLD only captures its average diameter. On the other hand, the 1D BLD permits to better visually compare different BLDs (e.g. observed and expected) since one can simply plot one on top of the other.

3.2 The expected baseline length distribution

In order to decide on the array configuration during scheduling and to judge the quality of the observed BLD, we need to derive an expected shape, the Expected Baseline Length Distribution (EBLD) in order to have a reference. This is done by determining the expectation function for the uv coverage from the science goals and filling a histogram with it.

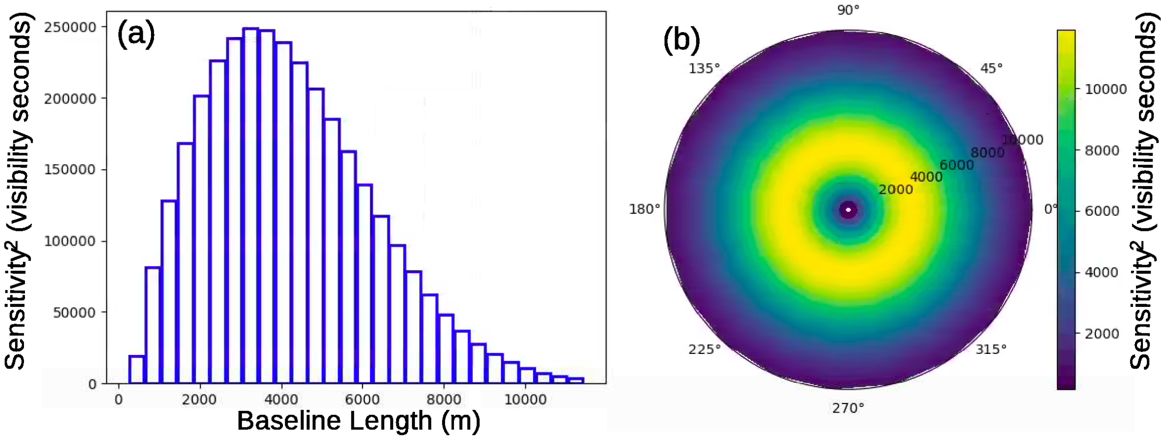

Figure 3.2: Examples of 1D and 2D analytically calculated expected baseline length distributions for a 30 minute observation with 43 antennas in an extended configuration.

Here we explore two approaches:

a) **an analytical approach** which calculates the expected shape from an expected beam shape (derived from the AR) which is Fourier-transformed and then modified by an "inner taper" to account for the LAS requirement.

b) **a simulation approach** which assumes a perfect interferometer with a maximally filled aperture up to the radius of half the maximum BL length, i.e. a disk of the diameter of the maximum BL length (derived from the AR) filled with antennas at a minimum distance (derived from the LAS).

3.2.1 Analytical approach

As described above, the science goals of the PI project w.r.t. image properties are captured by the ALMA Observing Tool (OT) in the proposal submission as the angular resolution (AR) and the largest angular scale (LAS). For an interferometer this translates into the size of the synthesized beam (FWHM) and the maximum recoverable scale (MRS) given the angular modes it is sensitive to, where the latter is defined for ALMA as recovering 10% of the total flux density of a uniform disk of the respective size; the primary beam size, i.e. antenna aperture or mosaic pattern, has to be at least three times larger. As detailed in the ALMA Technical Handbook (ALMA THB, Remijan et al. 2019), the scales for a given *single* configuration are also defined via the 5th and 80th percentile of the BLD. In our approach we effectively generalise this latter definition to a match over the whole BLD and for the case of multi-configuration executions.

In order to formalise the PI imaging request we assume a Gaussian target function for the AR for the following reasons:

1. such aperture is often adopted in optical applications for reasons of imaging quality
2. the functional form is invariant under Fourier transformation
3. it is the form of the "clean" beam adopted in the interferometric image reconstruction algorithm CLEAN, i.e. "dirty" beam = "clean" beam
4. for the aforementioned reasons, the ALMA configurations have been designed with a visibility space density optimization against this functional form for the radial coordinate.

In our present best version of the analytical BLD creation, the expectation function is computed as the Fourier transform of the Gaussian beam with the size given by the AR, and apodized after transformation with an inner uv taper of an inverted Gaussian (1/r) of the transformed LAS size. It is numerically implemented with a regular rectangular map filling the polar visibility density histogram, and directly filling the histogram from the analytical expression considering the pixel sizes,

$$G(\lambda/\mathrm{AR}\times 180/\pi\times 3600, \mathrm{radBin}_j)\times G(1/(\lambda/\mathrm{LAS}\times 180/\pi\times 3600), 1/\mathrm{radBin}_j)\times \mathrm{pixelSize}_{ij}$$

where $G(\mathrm{FWHM}, r) = \exp(-r^2/(2\times(\mathrm{FWHM}\times 0.426)^2))$ and λ is the wavelength.

Figure 3.2 shows an example of a BLD computed with this method. Note that for angular scale range requests less than a factor 18, i.e. LAS < 18×AR we set LAS := 18×AR, aligned with the baseline distributions of the ALMA 12-m configurations.

The effect of the three products in the functional form of the analytic expectation function are illustrated in Figure 3.3 for the properties of selected ALMA configurations.

The expectation function is idealised in terms of the exact radial shape, azimuthal uniformity and overall smoothness. In particular, the designed and actually realised baselines of the antenna array and projection effects during observations inevitably cause deviations, which have to be captured by a metric and evaluated in order to provide guidance for the scheduling task (see Section 9.2). It is an important point (e.g. references 4 and 3) that ample sensitivity can be used to improve imaging with a suitable re-weighting of the uv pixels to better resemble the target function and hence improve resolution match, beam circularity and sidelobe suppression.

AR only (C-10/C-4/C-1):

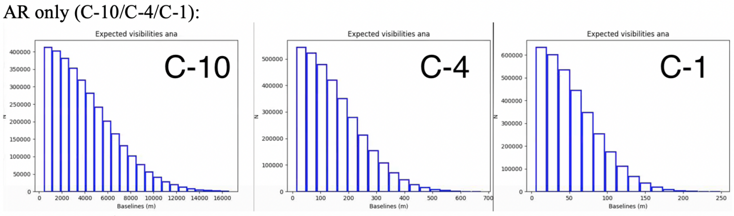

Inner taper only:

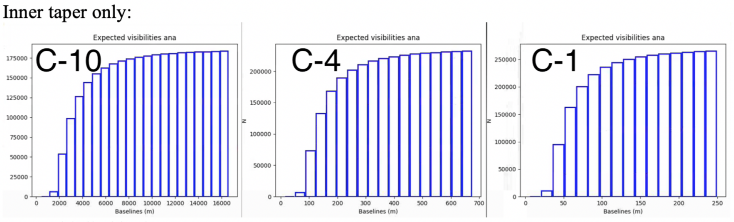

AR multiplied by inner taper:

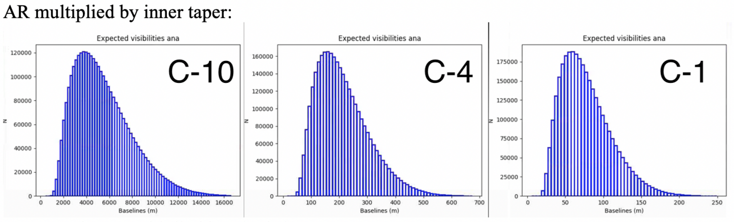

Same as above multiplied by pixel size:

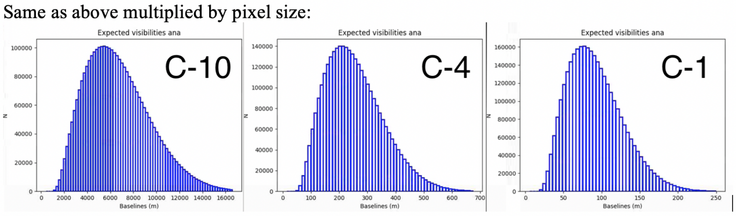

Figure 3.3: Components of the analytical expectation function.

3.2.2 Simulation approach ("Filled Dish")

As an alternative to the analytical approach, we are also exploring the potential benefits of creating the BLD directly by placing antenna positions onto an aperture with uniform spatial density and histogramming their BL lengths. Because we are essentially filling a large dish-shaped aperture with antennas, we call this approach "Filled Dish" (FD).

In order to extract a smooth general shape as in the analytical case, the antennas are placed randomly and the process is repeated a large number of times such that the resulting BLD is an *average* of all possible uniform-density array configurations which obey the constraint that all BL lengths are between a given minimum and maximum.

The minimum BL length is derived from the LAS request, the maximum from the AR. The overall scaling of the BLD is determined by the number of visibilities in the real observation for which the expected BLD is to be derived.

Due to the large-number statistics, the FD approach naturally results in overall bell-curve 1D BLD shapes like those obtained with the analytical approach but without assuming this functional form anywhere. And also the 2D BLD looks similar. See Fig. 3.4 for an example of a BLD derived with the FD approach.

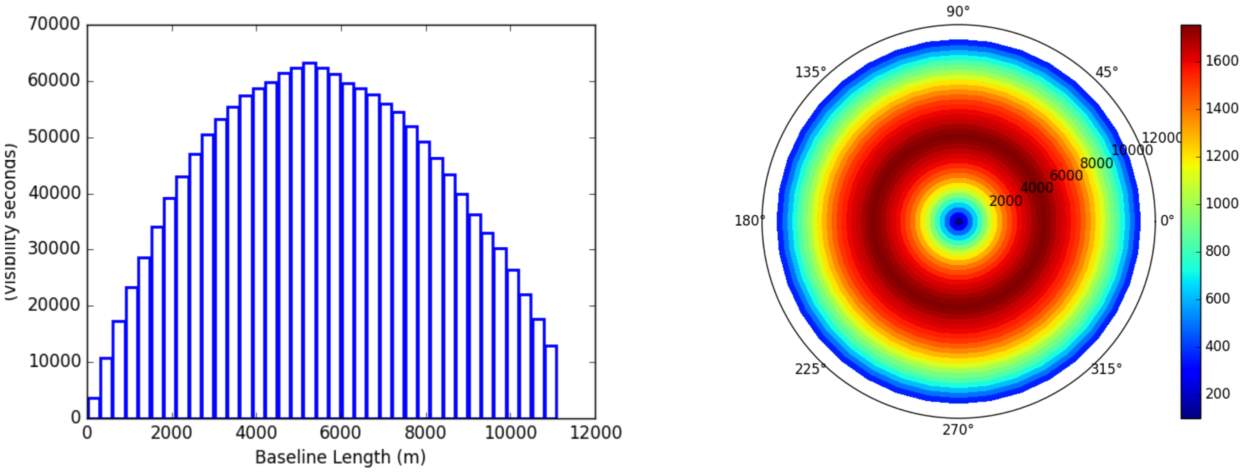

Figure 3.4: Example of a BLD obtained from using the "Filled Dish" (FD) approach with max. BL = 11000 m and min. BL = 36 m, in 1D and 2D.

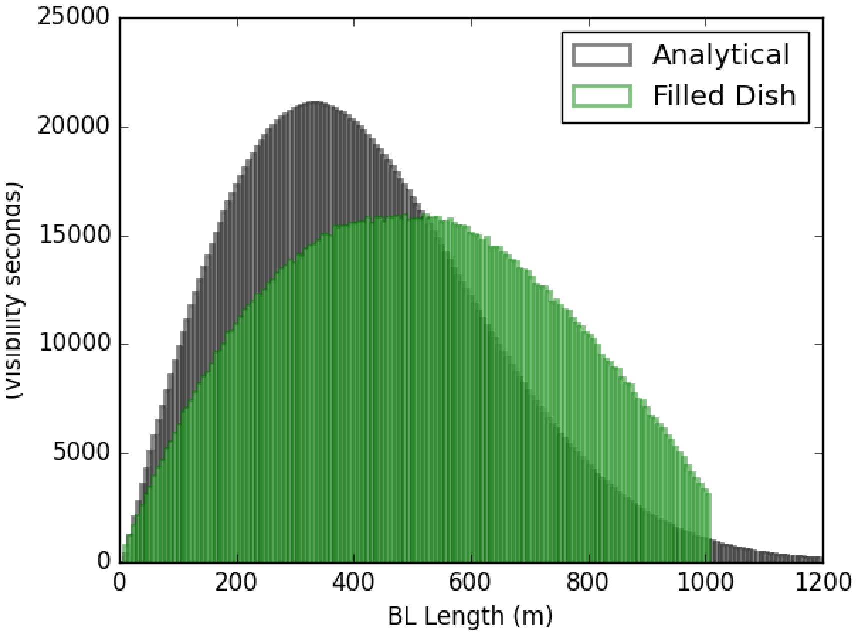

Figure 3.5: Comparison of the expected BLDs obtained for the same parameters (AR=0.62 arcsec, LAS=88 arcsec, observation time = 1800 s, number of antennas = 43) from the "analytical" (black) and the "Filled Dish" (FD) method (green). The AR corresponds to a BL of 1000 m and the LAS to a BL of 7 m. Histogram bin width is 7 m.

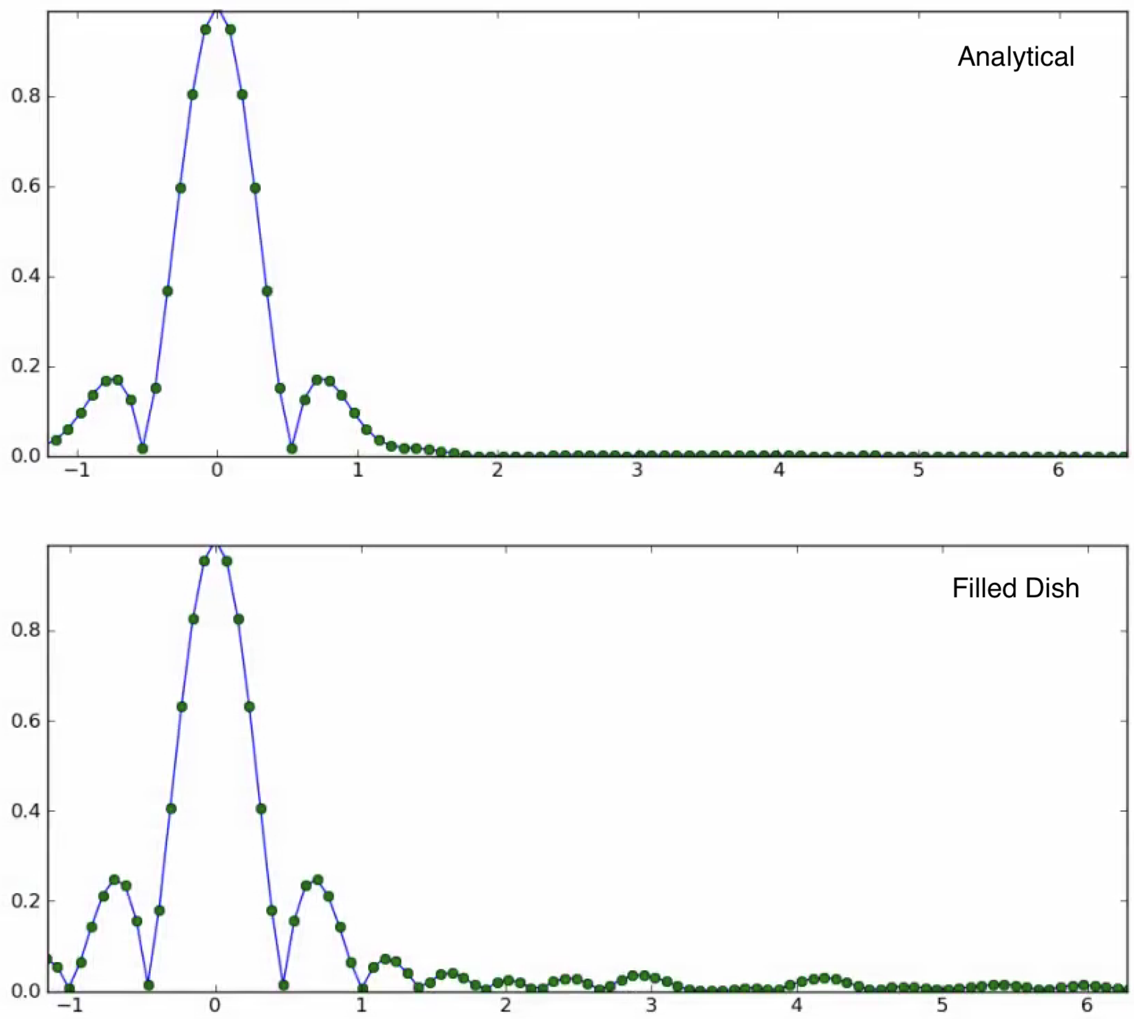

Figure 3.6: Comparison of the cross-sections (absolute value) of PSFs for AR = 0.62 arcsec and LAS = 11.2 arcsec for the two versions of the expectation function. The analytical Gaussian scale filters (top) provide a smooth beam function, while the Filled Dish (bottom) shows the enhanced sidelobes of the Airy function.

However, there is a strong difference in the location of the peak of the BLD, which occurs at larger BLs for the FD method, and in the fact that by construction, the FD BLD cuts off at the BL which corresponds to the specified AR while the analytical approach tapers out beyond it. Figure 3.5 shows a comparison of an analytical BLD and an FD BLD for the same AR and LAS request and total number of visibilities. The FD approach recommends more longer baselines but none beyond the max. BL which corresponds to the AR. At 800 m BL, the FD BLD is a factor 2.4 larger than the analytical BLD. But also at the very shortest baselines of 7 m-14 m, i.e. those which would need to be covered by the ACA, the FD BLD is a factor 2.2 above the analytical BLD. Figure 3.6 shows the comparison of the two PSFs for the same angular parameters and demonstrates the enhanced sidelobes for the Filled Dish.

As the LAS is increased, the BLD of the hypothetical instrument which is constructed in the FD process approaches that of an equivalent optical telescope with similar image fidelity. The FD way of determining the ideal BLD shape naturally arrives at a sensitivity requirement for very short spacings and thus permits to determine how to include single-dish observations. We hope to investigate this aspect more deeply in a follow-up study.

3.3 Comparing the expected, simulated, and observed BLDs

As described above, a comparison of BLDs with their expectation is needed both in the context of scheduling and in quality assurance. To formalise this process, we introduce the "filling fraction" FF which is defined for each BLD bin i as

$$FF_i = o_i/e_i \quad (e_i > 0), FF_i = 1 \quad (e_i = 0)$$

where o_i is the entry in the ith bin of the observed BLD while e_i is the corresponding entry in the expected BLD. A filling fraction of 1 means that the observation has fulfilled the expectation. So for bins where $e_i = 0$, we define the filling fraction to be 1.

We also introduce the total filling fraction $FF_t = \sum o_i / \sum e_i$ and the average filling fraction $FF_a = \sum FF_i/n$ where the sums in the expressions for FF_t and FF_a are computed in the histogram range where $e_i > 0$ and n is the number of bins in that range (which we call *expectation range*).

Using these filling fraction definitions, one can construct metrics for the assessment of observed BLDs. We have tried to devise a simple, universally applicable metric and arrived at a choice which is defined as follows:

1. Determine observed and expected BLDs with ten equidistant bins over the expectation range.

2. Compute FF_i for each of the ten bins.

3. For "pass", require $FF_a \geq 0.9$ and $FF_i > FF_{min}$ for $i = 0, ..., 8$ and $FF_9 \geq 1$, i.e. on average the filling fraction should be at least 90%, at least FF_{min} in each bin, and at least 100% in the uppermost bin which decides on the achievement of the AR.

   FF_{min} is the minimum filling fraction which has to be achieved in all intermediate bins. We find that a value of $FF_{min} = 0.6$ is adequate here if image fidelity is of high importance. Otherwise values down to 0.4 are acceptable. See section 4.5 for the discussion.

We do not claim that this metric is optimal. We do claim that it is a good start and we demonstrate in this study that it can be implemented in a straight-forward way and used in practice. The choice of using the FF rather than, e.g., missing visibility seconds was deemed to be most easily understood by users. It was also easier to compute than, e.g., a χ^2 because our expectation function implementation is still computing intensive. The choice of 10 bins is a compromise between resolution in angular scale, minimising the statistical error on the FF in each bin, and ease of viewing for the users.

3.4 Comparing observations with expectations for a sample of MOUS

In chapter 7 we evaluate the match of the observed BLDs to analytical expectations making use of the FF and the difference between observed and expected visibility hours.

With this purpose we create two types of plots for two independent markers, the filling fraction and the difference of observed and expected visibility hours. The first plot is obtained by calculating the median value of the respective marker for all the MOUS included in a given group and BLD bin. The MOUS belonging to that group are selected based on a given parameter and its value, e.g. the parameter can be "number of executions" and we look at groups of MOUS with number of executions equal to one and more than one. This way, we can evaluate if the number of executions causes any difference in the BLD match. In this plot the uncertainty of each point is simply a median absolute deviation, thus indicating how diverse is the BLD for different MOUS in a given group. The second plot is obtained by calculating the mean value of the respective marker for all the MOUS included in a given group and BLD bin. While the mean value in this second plot should not differ much from the median value in the first plot, the uncertainty in the second plot is significantly different. In this case, to calculate the uncertainty we simply propagate the errors of the uncertainty in each BLD bin for all MOUS (see below) so that the total uncertainty does not tell us about the dispersion of the values but rather on how significant is the deviation from expectations. Typically, the longest BLs have very few visibilities and consequently, a deviation from expectation for such bins is not significant when the uncertainty is considered. Instead, for medium length BLs even a small deviation can be significant.

3.4.1 Filling fraction

To calculate the uncertainty of FF_i, we need to perform an extra step compared to sect. 3.3, namely to compute first the number of visibilities by dividing the Visibility Seconds by the integration time (t_{int}). This step is not needed to calculate the FF_i since the same integration time is used for the observed and expected visibilities, and therefore cancels out. However, this is not the case for the uncertainty estimate.

Therefore, we now estimate the FF per BLD bin as:

$$FF_i = no_i/ne_i \quad (ne_i > 0), FF_i = 1 \quad (ne_i = 0) \tag{3.1}$$

where $no_i = \frac{o_i}{t_{int}}$, $ne_i = \frac{e_i}{t_{int}}$ and t_{int} is the integration time.

Then, we estimate the uncertainty on FF_i as follows:

$$\delta(FF_i) = FF_i * \sqrt{\left(\frac{\delta(no_i)}{no_i}\right)^2 + \left(\frac{\delta(ne_i)}{ne_i}\right)^2} = FF_i * \sqrt{\frac{1}{no_i} + \frac{1}{ne_i}} \tag{3.2}$$

where $\delta(no_i) = \sqrt{no_i}$ and $\delta(ne_i) = \sqrt{ne_i}$.
Finally, for a given bin and a group of N MOUS we estimate the mean and uncertainty for that bin simply by propagating the errors of that bin for all MOUS in the group:

$$Mean(FF_i) = \frac{\sum_{j=1}^{N} FF_{ij}}{N} \tag{3.3}$$

$$\delta(FF_i) = \frac{\sqrt{\sum_{j=1}^{N} \delta(FF_{ij})^2}}{N} \tag{3.4}$$

where $\delta(\mathrm{FF}_{ij}) = \delta(FF_i)$ for MOUS j.

3.4.2 Difference of visibility hours

In addition to the FF, we use in chapter 7 additional diagnostic plots based on the difference of observed and expected visibility hours per BLD bin. This diagnostic gives us information about the absolute difference as opposed to the FF which only refers to ratios.
We take therefore o_i and e_i and calculate their difference:

$$\Delta(oe_i) = o_i - e_i \tag{3.5}$$

and the corresponding uncertainty:

$$\delta(\Delta(oe_i)) = \sqrt{\delta(o_i)^2 + \delta(e_i)^2} = \sqrt{o_i + e_i} \tag{3.6}$$

where $\delta(o_i) = \sqrt{o_i}$ and $\delta(e_i) = \sqrt{e_i}$.
Similarly to the case of the FF, for a given bin and a group of N MOUS we estimate the mean and uncertainty for that bin simply by propagating the errors of that bin for all MOUS in the group.

$$Mean(\Delta(oe_i)) = \frac{\sum_{j=1}^{N} \Delta(oe_{ij})}{N} \tag{3.7}$$

$$\delta(\Delta(oe_i)) = \frac{\sqrt{\sum_{j=1}^{N} \delta(\Delta(oe_{ij}))^2}}{N} \tag{3.8}$$

where $\delta(\Delta(oe_{ij})) = \delta(\Delta(oe_i))$ for MOUS j.

4 Impact of the BLD shape on imaging

The question of how to design the antenna configurations of radio interferometers is not new at all and was especially intensively studied already in the 1980s and 1990s in the phase leading up to the design of ALMA (e.g. Holdaway and Helfer 1999; Woody 2001a,b). These studies already showed that sidelobes in the point spread function (PSF) need to be minimised in order to enable or simplify the deconvolution of images of extended astronomical objects with complex spatial structure. The 2D BLD shape directly translates into the PSF and is thus equivalent.

The ALMA configurations have been optimised in great detail and are mostly fixed due to the unchangeable pad positions and operational constraints. Our "analytical" method of computing the expected BLD (section 3.2.1) approximates the ideal ALMA configurations. In our study, we therefore tried to determine what happens to the image when the BLD of a given MOUS deviates significantly from our "analytical" BLD shape.

To study this systematically for all ALMA configurations, we simulate long Band 3 mosaic observations of a ca. 4 arcmin × 4 arcmin region filled with a test image with emission at a large range of angular scales using the nominal ALMA Cycle 6/7 configurations 1, 3, 5, 7, and 9 as they are defined for the CASA 5.6.1 simulator[1]. We call the native BLD of the obtained MeasurementSets (MSs) the BLD case "I". In the following we also refer to the C6/7 configurations as C43.

Using these five base MSs (case "I"), we create new MSs by modifying the base MSs using a special flagging algorithm to obtain MSs with defined BLDs:

BLD Case A: the ideal BLD according to our "analytical" method

BLD Case B: "analytical" shape but 40% reduced in bins 1 and 2 of the ten equidistant bins of the QA metric (as defined in 3.3) from zero to the max. BL.

BLD Case C: like Case B but 40% reduced in bins 3 and 4 instead of 1 and 2.

BLD Case D: like Case B but 40% reduced in bins 5 and 6 instead of 1 and 2.

BLD Case E: like Case B but 40% reduced in bins 7 and 8 instead of 1 and 2.

BLD Case F: "analytical" shape but 20% reduced in bins 3, 4, 5, 6.

BLD Case G: "analytical" shape but 30% reduced in bins 3, 4, 5, 6.

The "defect" of 1 × 40% reduction or 2 × 20% reduction (i.e. in both cases a total defect size of 40%) corresponds to a sensitivity loss of 23% in the affected angular scales which is roughly the margin which ALMA permits in the QA2 of the achieved image RMS.

---

[1] The configuration definitions for cycles 6 and 7 in CASA are identical.

The resulting MSs for all seven cases A - G have by construction the same number of unflagged visibilities i.e. *the same nominal overall sensitivity.* They only differ in the shape of their BLD, i.e. in the selection of which visibilities are flagged.

To repeat, Case "A" is not the native ALMA configuration but the ideal BLD according to our "analytical" method. The native, unflagged, ALMA configuration in each case is Case "I" which is shown here only for completeness! Since it is not flagged, it has a higher number of unflagged visibilities and therefore *a higher sensitivity than cases A - G*. This has to be taken into account when comparing case "I" with the other cases.

All MSs are then imaged in the same way using CASA multiscale tclean with an identical mask and we extract image parameters, which we can compare to the original input image of the simulation. From this we can derive information about the imaging performance in each case and judge how detrimental the defects are, which we introduced in cases B - G compared to the ideal case A.

4.1 Generating a "test image" as input for simulations

The test of angular scale response requires that the input image for this sub-study contains power at a wide range of angular scales covering the nominal scales accessible to ALMA. Initially, we experimented with random structure images like the one shown in Fig. 4.2, but we soon realised that the results are not educational nor intuitive. To the human eye, a random plot remains a random plot when only relatively subtle changes are made to individual angular scales.

Given the limited time we could dedicate to this question, we then settled on an image which consists of well defined geometric shapes: groups of eight Gaussians in a ring around a ninth Gaussian in the middle (Fig. 4.3). It remotely resembles groups of partially resolved astronomical objects and thus permits to inspect how well such objects can be separated by a given observation and how well their shape and flux can be recovered.

While the pattern already contains power at a range of angular scales, we extend the range further by *repeating it horizontally seven times*, every time doubling in size such that Gaussians with FWHM (and thus angular scales) of between 0.01 arcsec and 10 arcsec occur in the image. Furthermore, we want to study the behaviour at different signal-to-noise ratios (SNRs) and therefore repeat the set of seven patterns three times, every time doubling the total flux. The result can be seen in Fig. 4.4: three rows of seven groups of nine Gaussians each.

The accurate creation of the pattern in a proper FITS file with astronomical coordinate system (as required by the CASA simulator) was implemented using the *gensynthcube* utility[2].

For the three less extended configurations 1, 3, and 5, we choose the pixel size of the simulation input image as 0.05 arcsec and the peak flux of the brightest Gaussian as 0.1 Jy. The image size is 4096 × 4096 pixels.

For the two most extended configurations studied here, 7 and 9, this resolution is not good enough. For these, we shrink the pixel size by a factor 4 to 0.0125 arcsec. The image then has a size of 16384 × 16384 pixels. The peak brightness of the brightest Gaussians in the image is ca. 6.2 mJy/pixel.

---

[2] publicly available from the EU ARC at https://confluence.alma.cl/display/EAPR/gensynthcube

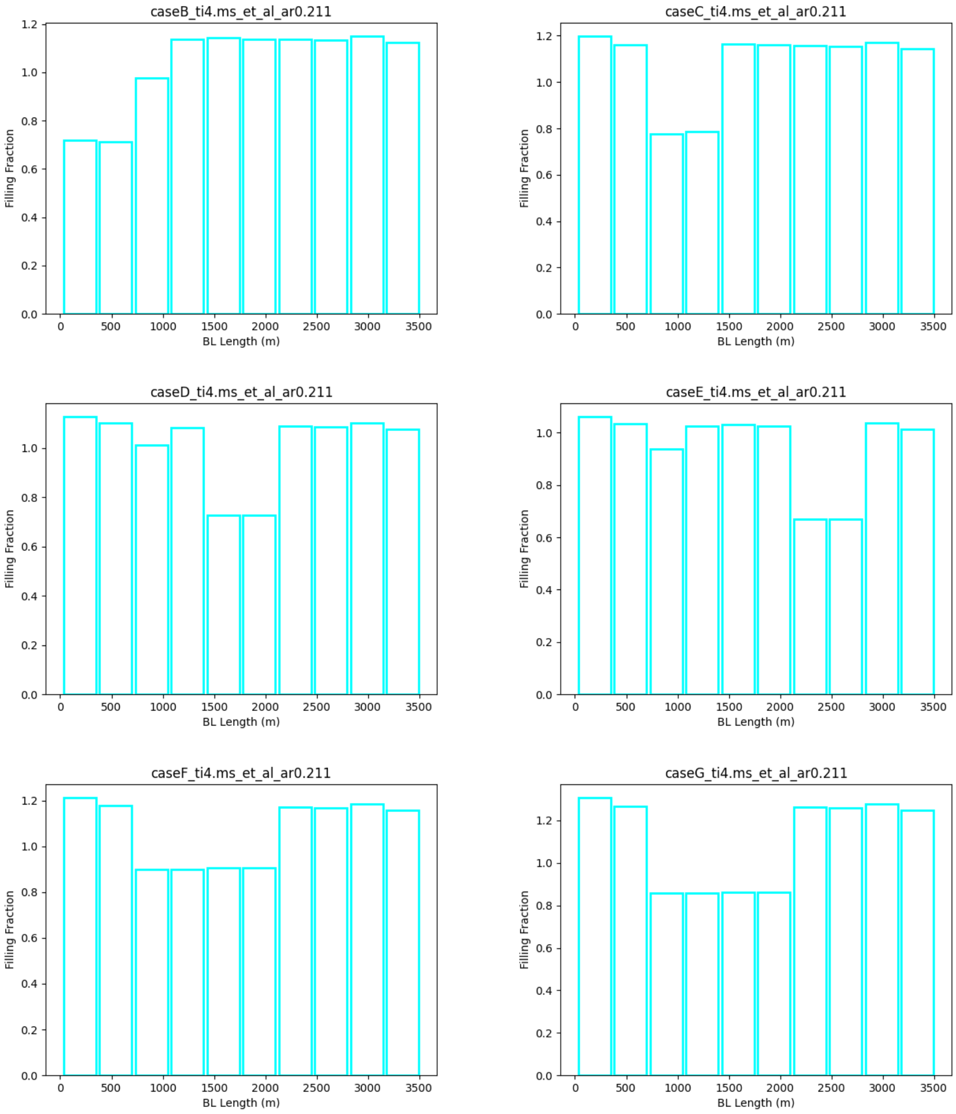

Figure 4.1: The filling fraction plots for the BLD defect cases to be studied (example for the BL range up to 3500 m for config C43-7): From top left to bottom right: case B, C, D, E, F, G. Case "A" (not shown) has a filling fraction of 1.0 for all ten bins. Note that the number of visibilities accepted into the "full" bins was increased in order to keep the total number of visibilities constant in all cases. So the filling fraction is larger than one in the "full" bins. Note also that the method the different datasets are obtained via semi-random flagging is unavoidably not completely accurate due to the non-continuous nature of the set of visibilities. The exact achieved BLD shape in each case also depends on the random seed.

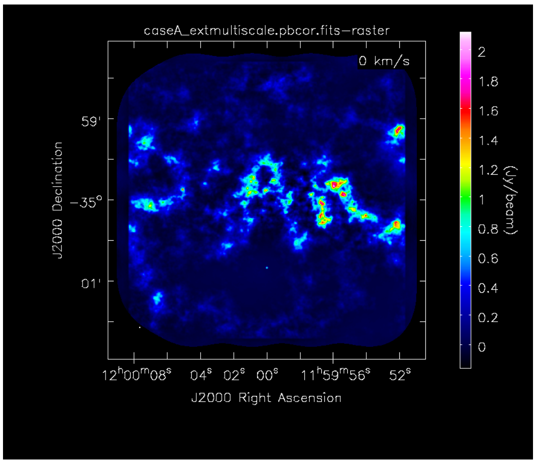

Figure 4.2: A synthetic image in which the power at different angular scales follows a function of the angular scale *which is a power law* over a wide range of scales (power decreases with scale size, original image provided by Peter Teuben, 2020). This image has been studied in detail by the data combination group which formed after the 2019 Leiden workshop on image combination (contact: A. Plunket). The structure shown here has a power spectrum which follows a power law by construction. However, it was found that studying these power spectra in the original and observed images does not give as conclusive indications of the quality of the reconstruction as one would expect.

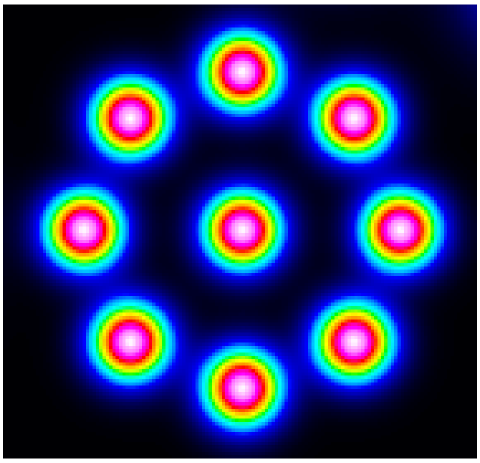

Figure 4.3: The pattern invented in this study for the creation of an input image for simulations. It consists of a ring of eight Gaussians of equal size with a ninth Gaussian in the middle. All of them have the same size and intensity.

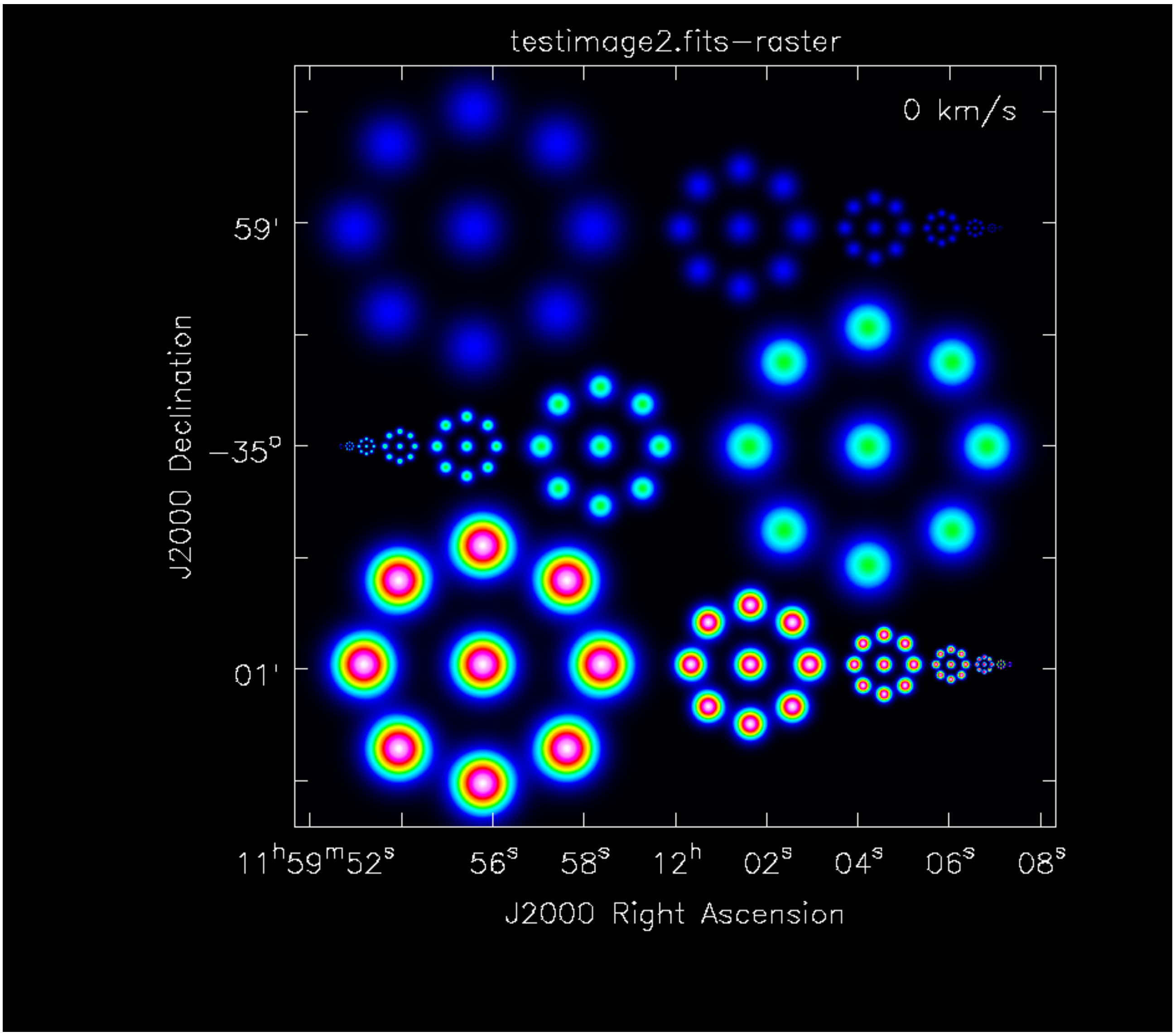

Figure 4.4: The multi-scale, multi-intensity-level input image for the simulations described in this section. There are three rows of seven groups of nine identical Gaussians each. The peak flux of the Gaussians is lowest in the top row of groups, and is doubled in the middle row and then doubled again in the bottom row. The actual input fits file for CASA simobserve was created using the gensynthcube utility developed at the EU ARC. See text.

4.2 Generating simulated ALMA MeasurementSets with given BLDs

4.2.1 Running the CASA simulator

We used as input images the ones described in section 4.1. Hereafter, we call the one with pixel size 0.05 arcsec "normal size" and the one with pixel size 0.0125 arcsec "small size". The antenna configuration for the simulation was chosen from C6-1, C6-3, C6-5, C6-7 and C6-9. The image with small pixel scale was used for the extended configuration, *i.e.* C6-7 and C6-9. The image is square with 4096^2 (16384^2) pixels for normal (small) pixel size, which corresponds to 204.8 arcsec each side. The expected beam size for the adopted configuration ranges from 0.05 arcsec to 3 arcsec at 115 GHz. The peak value of the Gaussian sources given in Jy/pixel is adjusted to have identical total flux in both the normal and small size pixel scale images.
The center coordinate of the image is set as (RA,Dec)= (12h00m00.0s, −35d00m0.0s), and the observing frequency is 115 GHz with 2 GHz bandwidth. For each configuration, we run the `simobserve` task in CASA version 5.6.1 to create simulated measurement sets (MSs).
The mosaic pattern was automatically created based on the algorithm adopted in the ALMA Observing Tool (OT). For the 12-m array, there are 75 fields to cover the simulated image. Matching 7M and TP simulations were also created but the limited time did not permit us to study these and they are not discussed here any further.
For each mosaic field, we set the number of visits, which controls the total on-source time. A visit duration of 10 s was adopted. The adopted number of visits per field is 30 and 60 for the compact (C6-1,3,5) and the extended (C6-7,9) configurations, respectively. These values were chosen to ensure good visibility coverage originally taking into account also the 7M array which was not used in this study.
The simulated observation can be split into multiple days, so that the observing time per night becomes reasonable as in ALMA's nominal operation. A simulated MS is created per observing night. In this simulation, the 12-m observations are done in 2 (4) days for the compact (extended) configurations. For the imaging, the per-night MSs are concatenated to obtain one MS for each configuration.

4.2.2 Creating MSs with modified BLD

From the five simulated 12-m MeasurementSets (MSs) for the five 43-antenna configurations C6-1, 3, 5, 7, and 9, in the following named C43-1, 3, 5, 7, 9, we construct MSs which have BLDs according to the seven cases A - G defined at the beginning of this chapter on page 27. We do this by "thinning", i.e. randomly flagging a certain fraction of baselines in the ten separate, equidistant BL ranges using the following algorithm:

- Create random generator with returns True with a given probability: true_with_prob(prob)
- For a given MS:
    - determine ten-bin boundaries
    - determine ten-bin BLD, expected BLD, and filling fractions
    - loop over MS

  - for each BL determine which bin i it is in
  - if true_with_prob(1 - 1/fillfrac(prob)): flag the baseline (e.g. if fillfrac==3, prob is 0.66: two thirds of the BLs are flagged to get to fillfrac 1)

The whole process results in five sets (one for each studied config 1, 3, 5, 7, 9) of eight MSs (one for each BLD defect case A, B, ..., G, and "I", the simulated MS with the nominal C43 configuration), i.e. 40 MSs.

4.3 Imaging

The 40 MSs obtained in the previous section are sent through a standard multiscale imaging process to deconvolve them and then compare them to the original simulation input image.
To avoid artifacts or differences between the cases from automasking, we use a fixed mask which is computed from the original input image using the CASA immath task requiring the flux to be above 13 mJy/pixel for configs 1, 3, and 5 and above 1 mJy/pixel for configs 7 and 9. The mask is then regridded to the same resolution as the tclean output image (see Fig. 4.5). The pixel sizes chosen for the different configurations are:

Configuration	C43-1	C43-3	C43-5	C43-7	C43-9
tclean pixel size (arcsec)	0.338	0.142	0.063	0.0228	0.0114

We use the standard briggs, robust=0.5, weighting as it is used in ALMA QA2 by default.
We use the multiscale deconvolver as it would be recommended for an image with a wide range of angular scales. We set the "scales" parameter to [0,3,9] in all cases.
We use noninteractive tclean and keep the "niter" and "cycleniter" parameters constant for all MSs belonging to the same base configuration. However, we need to use larger niter values for the more compact configurations as these are sensitive to more extended structures which need more iterations in the deconvolution.

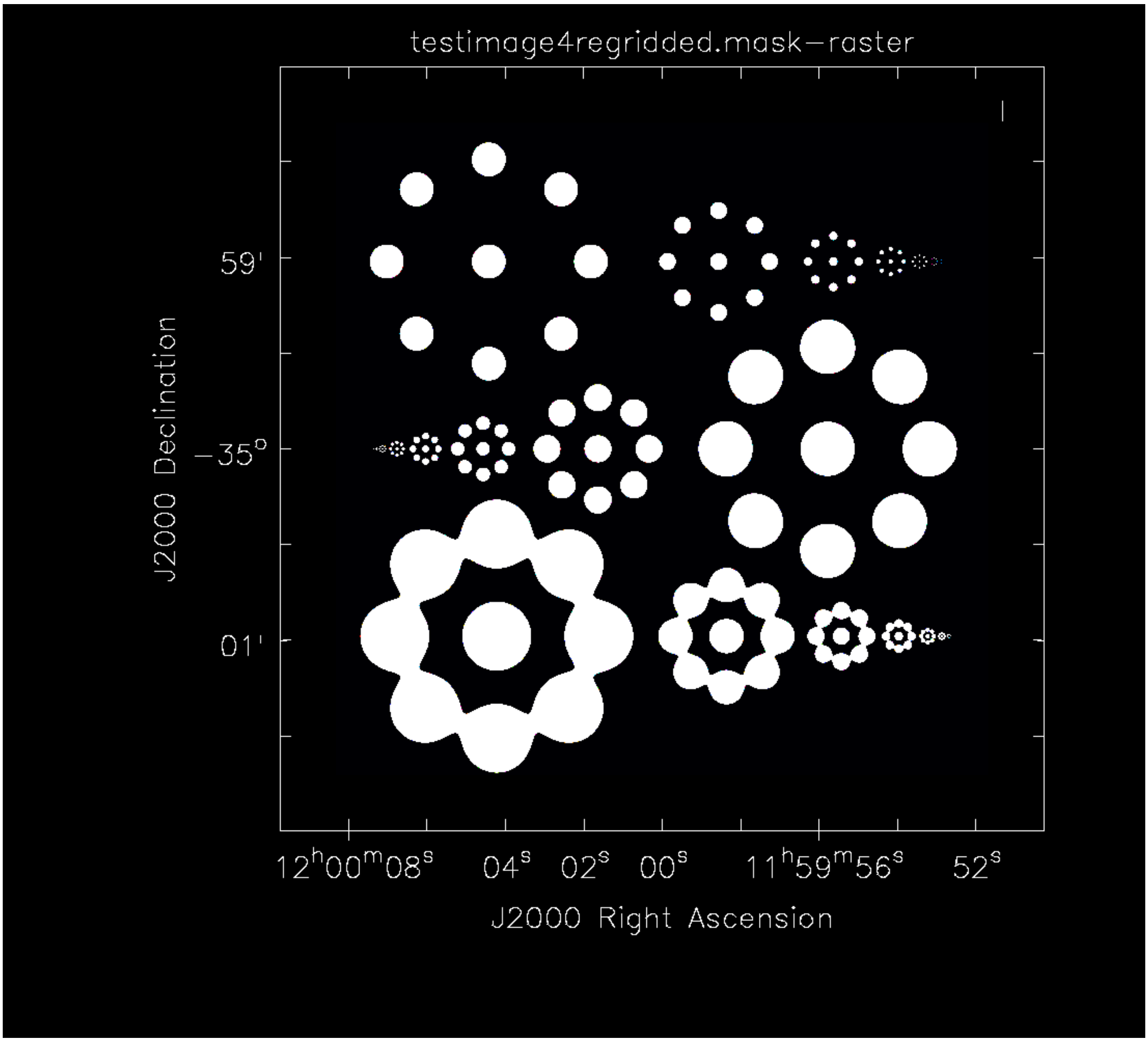

Figure 4.5: The tclean mask used for all imaging. See text. The resolution of this rendering is lower than the actual mask image and so the smallest structures are not fully visible.

The following is the tclean command template:

```
tclean(vis = thevis,
        imagename = casename+'multiscale-noninter',
        field = 'mytarget',
        phasecenter = 'J2000 12:00:00 -35.00.00.0000',
        stokes = 'I',
        spw = '0',
        outframe = 'LSRK',
        specmode = 'mfs',
        nterms = 1,
        imsize = [myimsize, myimsize],
        cell = str(mycell)+'arcsec',
        deconvolver = 'multiscale',
        scales = myscales,
        weighting = 'briggs',
        robust = 0.5,
        mask = 'testimage4regridded.mask',
        gridder = 'mosaic',
        pbcor = True,
        threshold = '0.05Jy',
        interactive=False,
        niter = myniter,
        cycleniter = myniter/6,
        cyclefactor=1.5}
```

The resulting images are shown in full-size (i.e. without zooming in) in Figs. 4.6, 4.7, 4.8, 4.9, 4.11. For the two most extended configurations, as expected, most of the larger-scale structure is completely filtered out. Here only the three or four smallest Gaussians are recovered. Zoomed-in views are shown in Figs. 4.10 and 4.12.

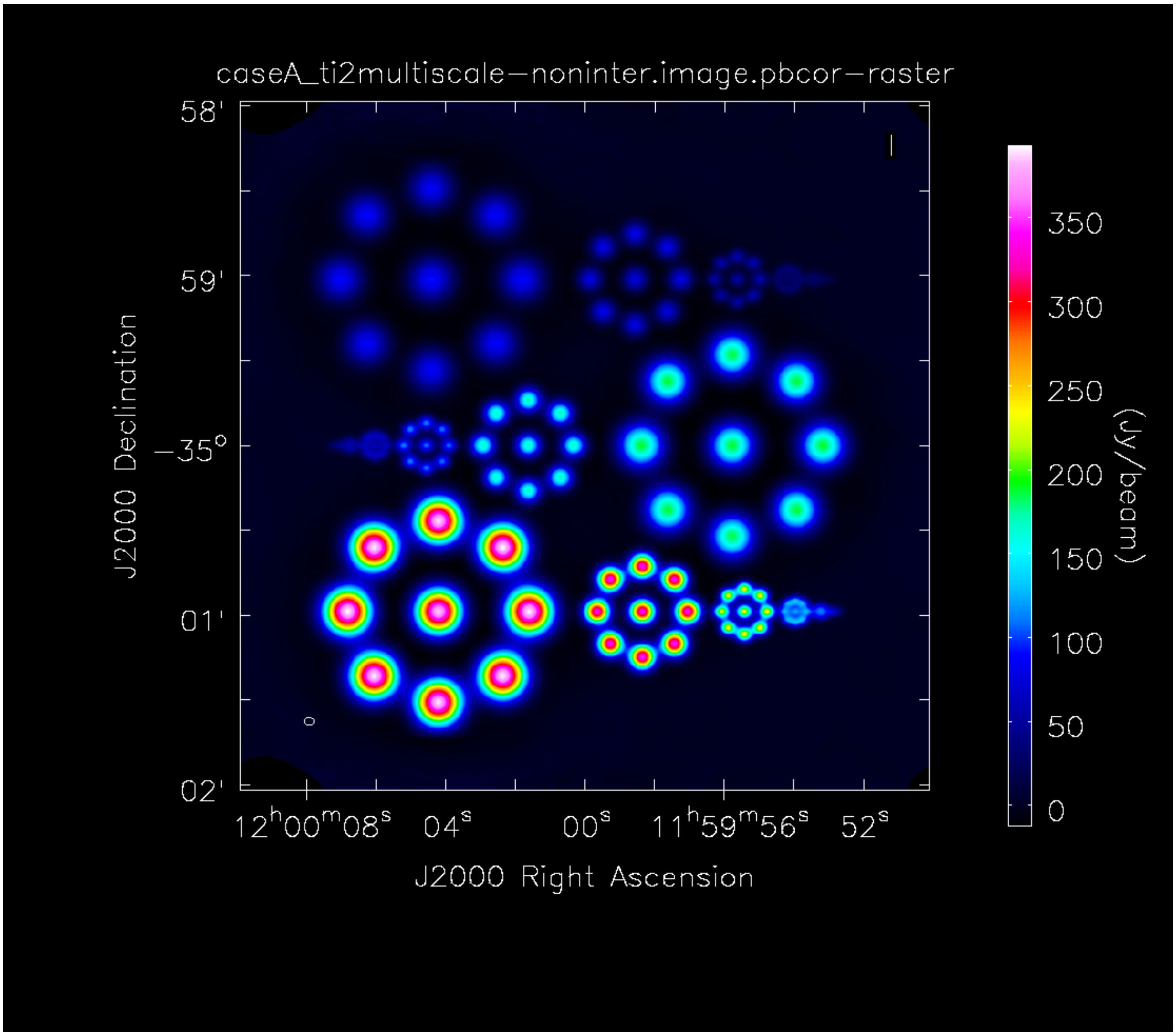

Figure 4.6: The end-result of simulating an observation of testimage 4.4 using configuration C43-1 with the BLD thinned to match the ideal "analytical" shape (case "A"). As one would expect, the largest structures are well recovered, but already in the Gaussian group 3, i.e. the third largest, the structure is beginning to blur. The smallest Gaussians are hardly visible.

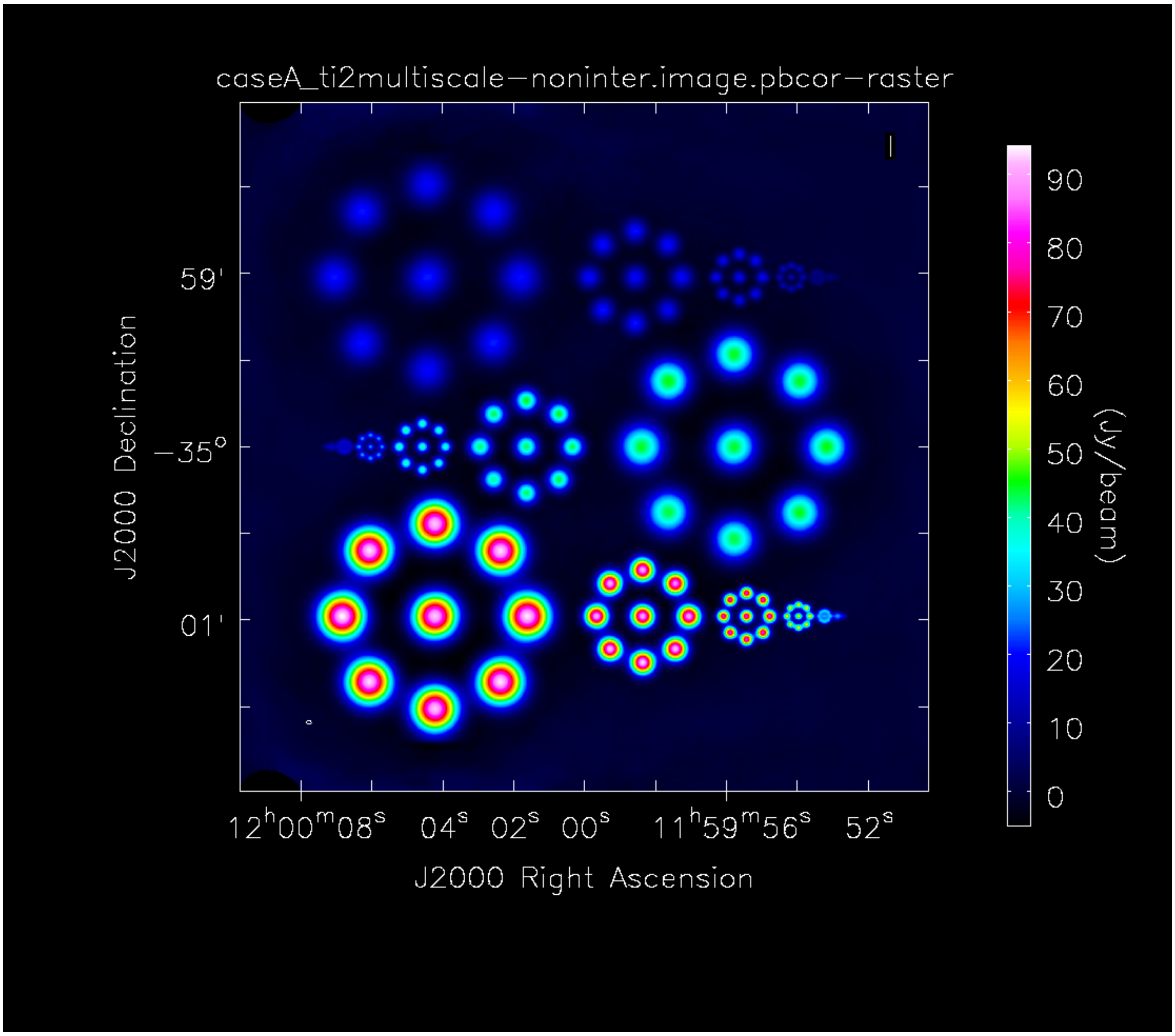

Figure 4.7: The end-result of simulating an observation of testimage 4.4 using configuration C43-3 with the BLD thinned to match the ideal "analytical" shape (case "A"). Like for C43-1, case A, the largest structures seem well recovered. Significant blurring sets in for Gaussian group number 4.

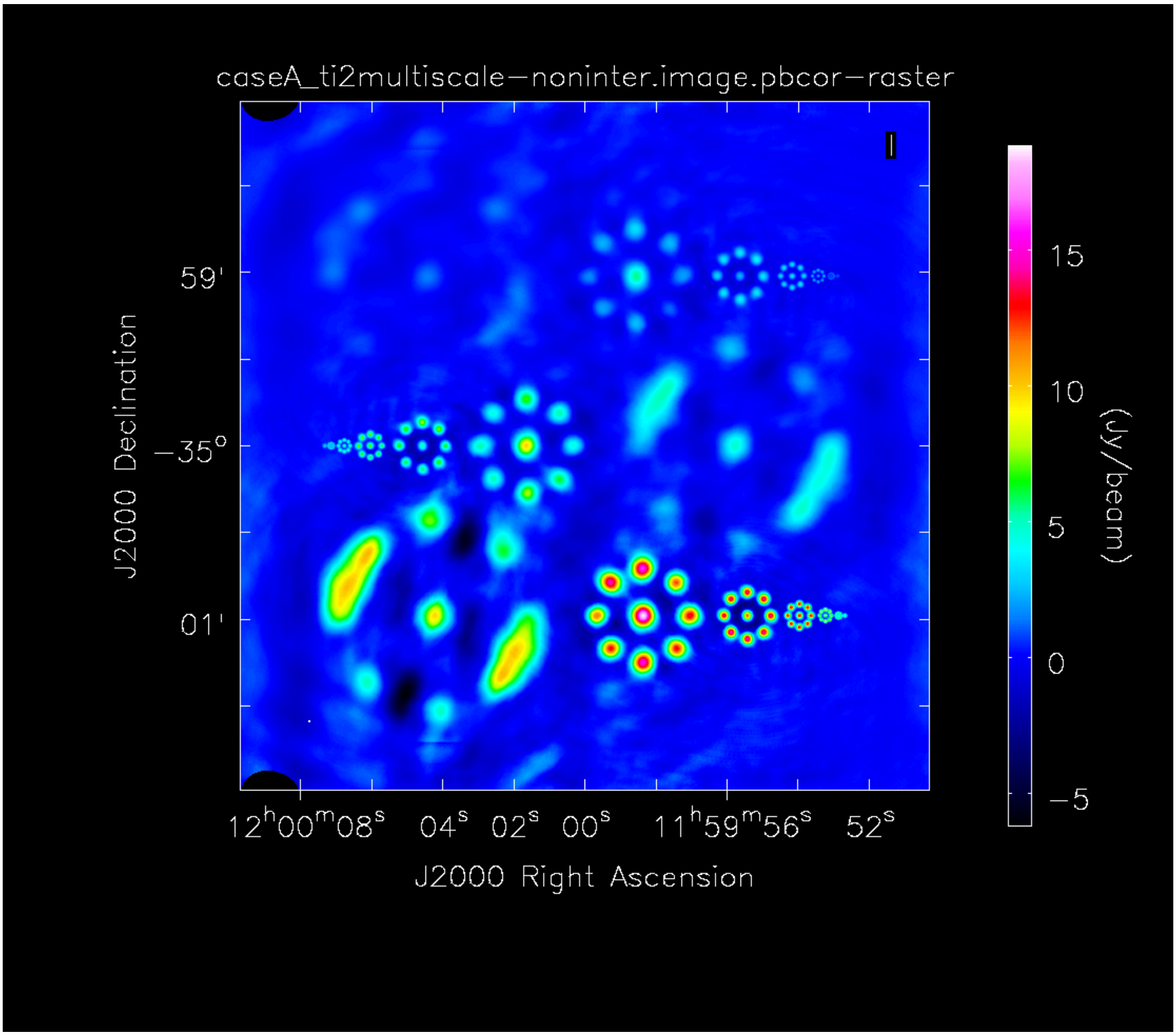

Figure 4.8: The end-result of simulating an observation of testimage 4.4 using configuration C43-5 with the BLD thinned to match the ideal "analytical" shape (case "A"). In this intermediate configuration, the largest Gaussians are hardly recovered. A rotational assymmetry in the recovery stems from corresponding assymmetries in the orientation of the shortest baselines. Also the second-largest group of Gaussians and the two smallest groups are not well recovered.

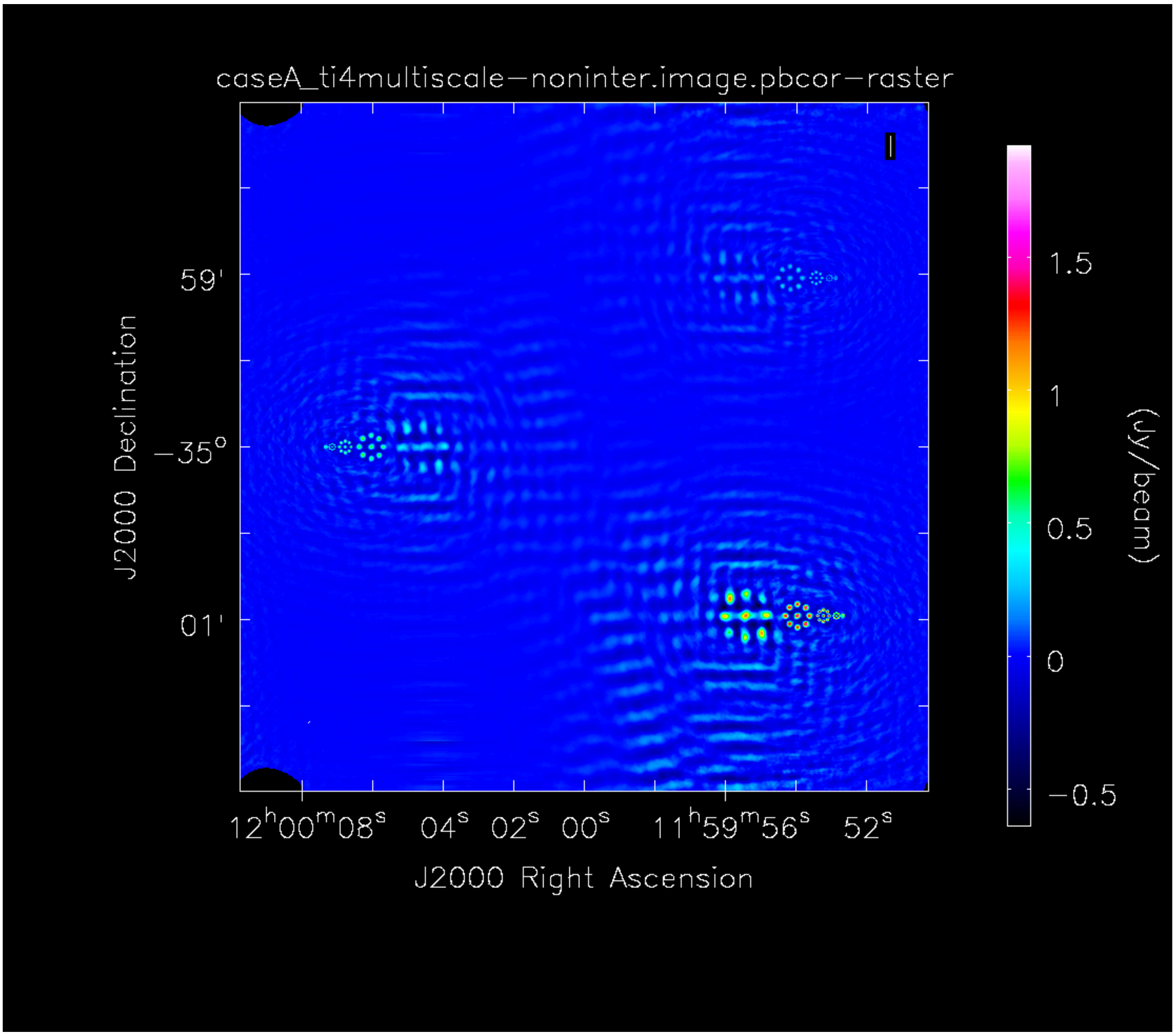

Figure 4.9: The end-result of simulating an observation of testimage 4.4 using configuration C43-7 with the BLD thinned to match the ideal "analytical" shape (case "A"). In this configuration, the two largest groups of Gaussians are not recovered at all. The third-largest group is distorted, the smallest group is blurred while groups 4, 5, and 6 are reasonably recovered. See also Fig. 4.10.

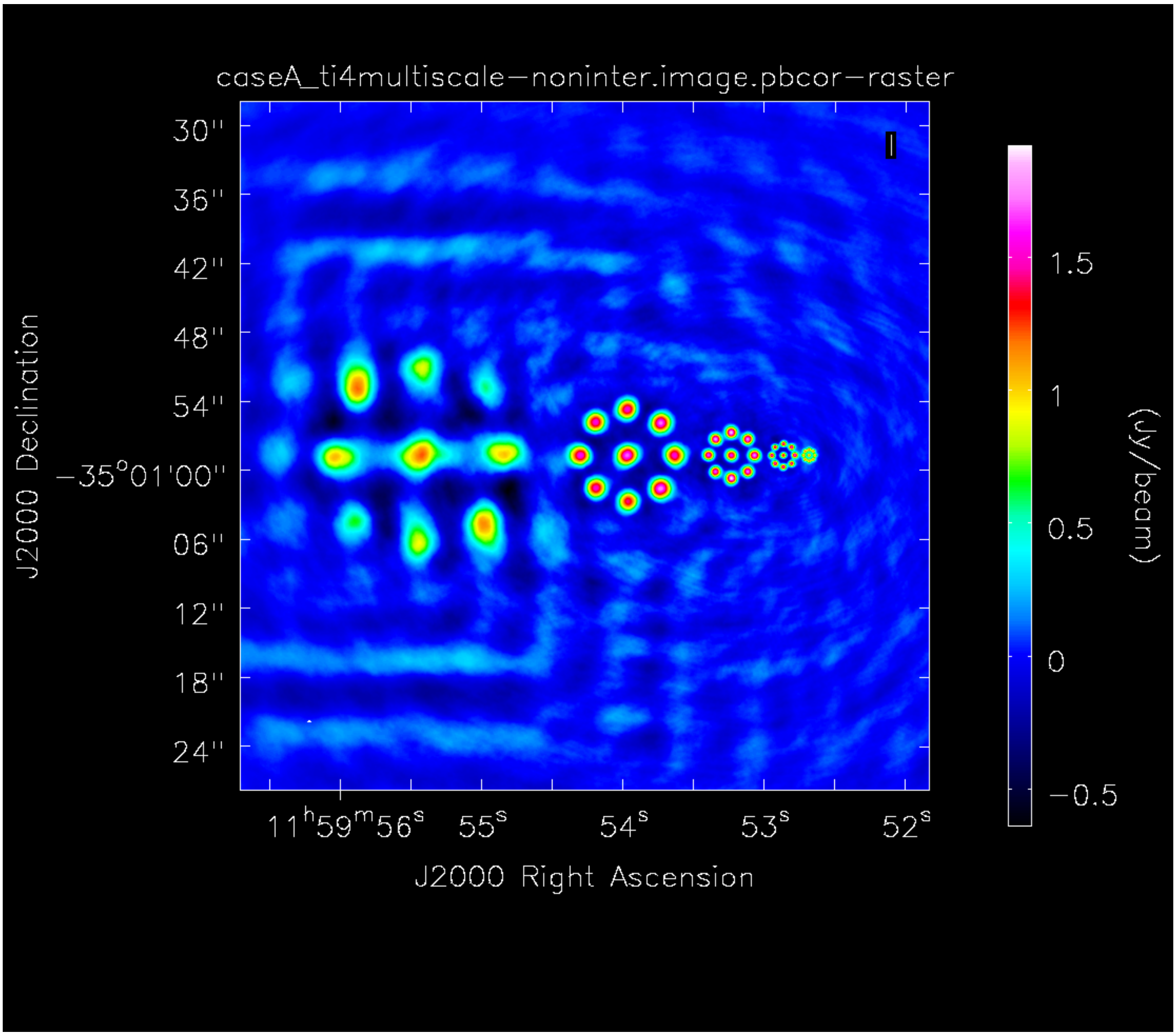

Figure 4.10: Detail of Fig. 4.9: the brightest groups of Gaussians which are not resolved out.

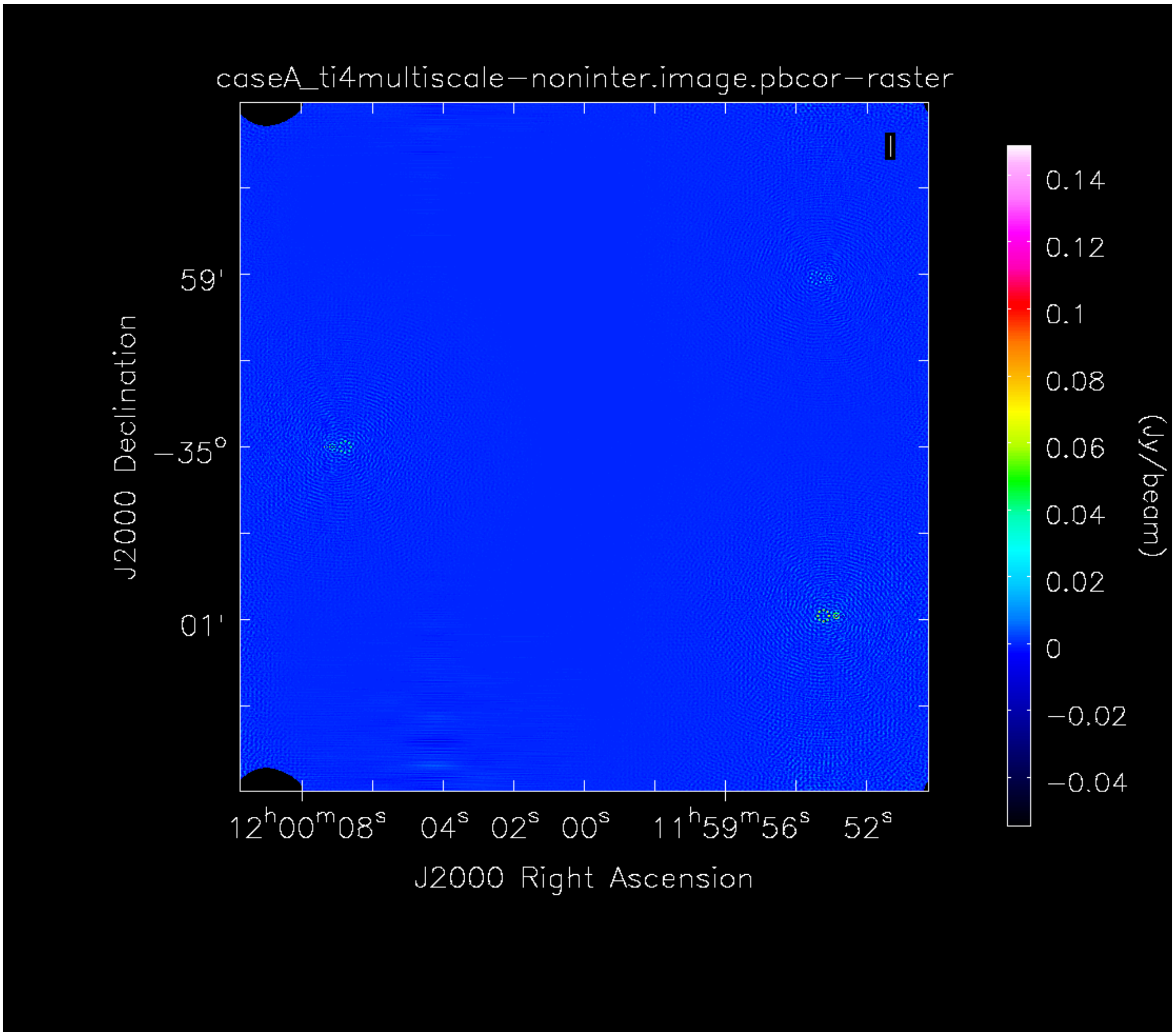

Figure 4.11: The end-result of simulating an observation of testimage 4.4 using configuration C43-9 with the BLD thinned to match the ideal "analytical" shape (case "A"). In this quite extended configuration, only the three smallest groups of Gaussians are recovered at all. The third-smallest group is distorted, in particular the central Gaussian is hardly visible. The two smallest groups are reasonably recovered. See also Fig. 4.12.

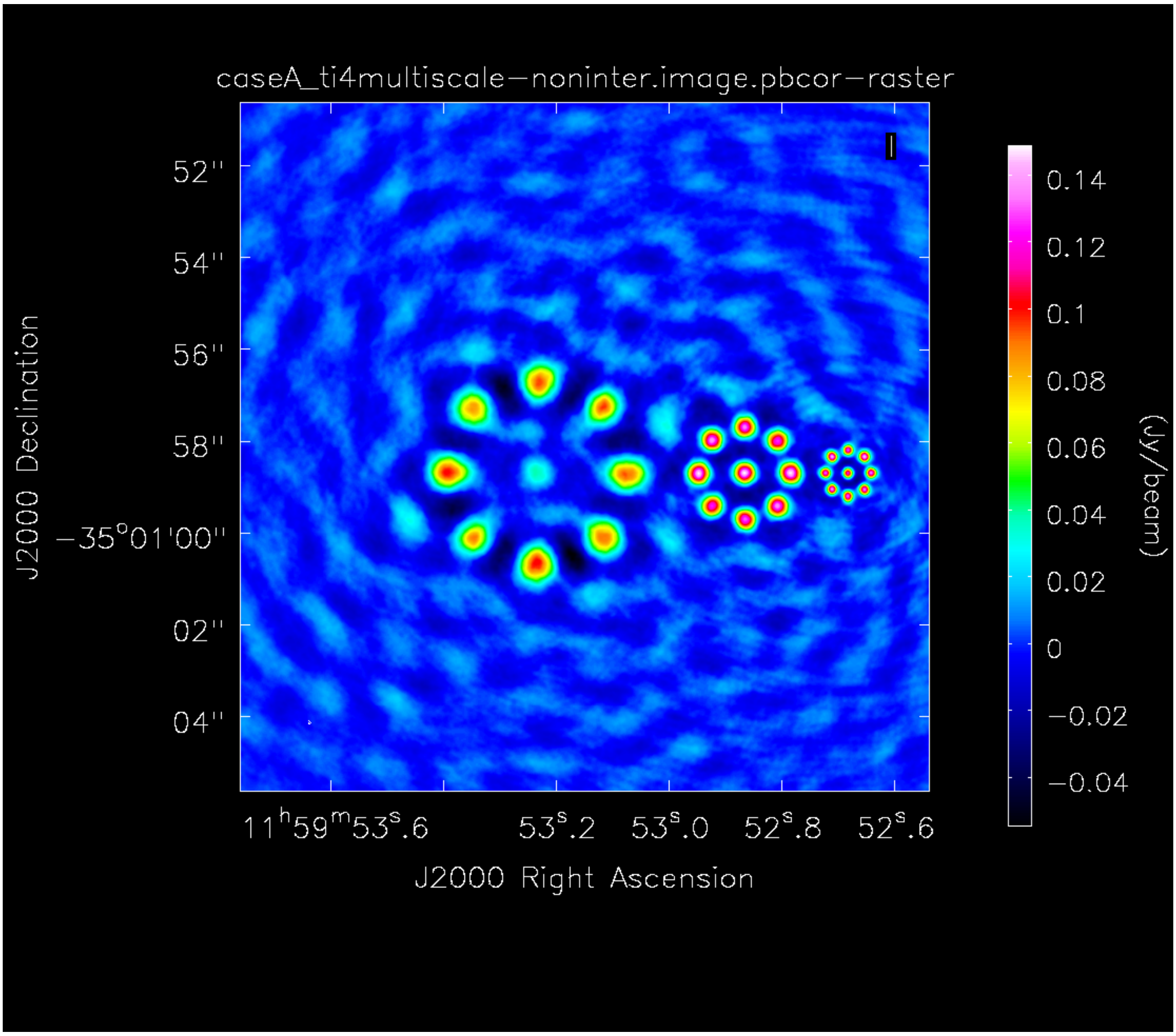

Figure 4.12: Detail of Fig. 4.11: the brightest groups of Gaussians which are not resolved out.

4.3.1 Beam sizes

Besides the images themselves, the deconvolution also provides restoring beams, which characterise the PSF. Tables 4.1 and 4.2 show the values obtained and a comparison to the values from the ALMA THB (Remijan et al. 2019). Corrected for elevation and frequency difference, the values are slightly smaller than the values we obtain for the native configuration except for C43-1. This is probably due to details of the simulation and not significant.

Case	A	B	C	D	E	F	G	I (native)
Config								
C43-1	3.47×2.72	3.40×2.68	3.41×2.66	3.48×2.69	3.56×2.78	3.43×2.65	3.40×2.63	3.44×2.79
C43-3	1.64×1.36	1.59×1.32	1.62×1.33	1.70×1.41	1.66×1.4	1.67×1.38	1.68×1.38	1.62×1.29
C43-5	0.65×0.59	0.63×0.57	0.63×0.57	0.66×0.61	0.67×0.61	0.65×0.59	0.65×0.59	0.64×0.56
C43-7	0.24×0.20	0.23×0.19	0.24×0.20	0.25×0.21	0.25×0.21	0.25×0.21	0.25×0.21	0.25×0.21
C43-9	0.064×0.057	0.060×0.054	0.064×0.057	0.067×0.060	0.065×0.058	0.067×0.059	0.068×0.060	0.069×0.059

Table 4.1: The beams sizes (arcsec) fitted by tclean for each of the 40 BLDs studied. The nominal simulation frequency is 115 GHz. The simulation DEC is -35° corresponding to an elevation of 78° at culmination. The simulation was covering a realistic hour-angle range of ± 1 h. The effective elevation is therefore closer to 65°.

Reference	Ideal BLD (Case A)	Native (Case I)	ALMA reference (THB, modified)
Config			
C43-1	3.07	3.10	3.23
C43-3	1.49	1.45	1.36
C43-5	0.620	0.600	0.521
C43-7	0.219	0.229	0.202
C43-9	0.0604	0.0638	0.0545

Table 4.2: The geometrical mean beam size θ_{res} (arcsec) for our ideal "analytical" BLD (case A), the native simulated BLD (case I), and the ALMA THB Cycle 7 value corrected to an elevation of 65° and a frequency of 115 GHz. The ALMA reference beams sizes (Remijan et al. (2019), Table 7.1) for 100 GHz are 3.38 arcsec (C43-1), 1.42 arcsec (C43-3), 0.545 arcsec (C43-5), 0.211 arcsec (C43-7), and 0.057 arcsec (C43-9) at zenith. The correction of $1/\sin(\mathrm{elevation})$ amounts to a size increase of 10%.

4.3.2 Pointspread functions

The pointspread functions (PSFs) for the BLDs studied here are obtained as a side-product of the deconvolution process from the CASA tclean task. In each of the figures in this section (Figs. 4.13 - 4.32), the central region of the PSF is shown together with a Gaussian fit to it, the residual of that fit, and the radial profile of the residual (azimuthal average, mininum, and maximum). For a discussion see section 4.5.

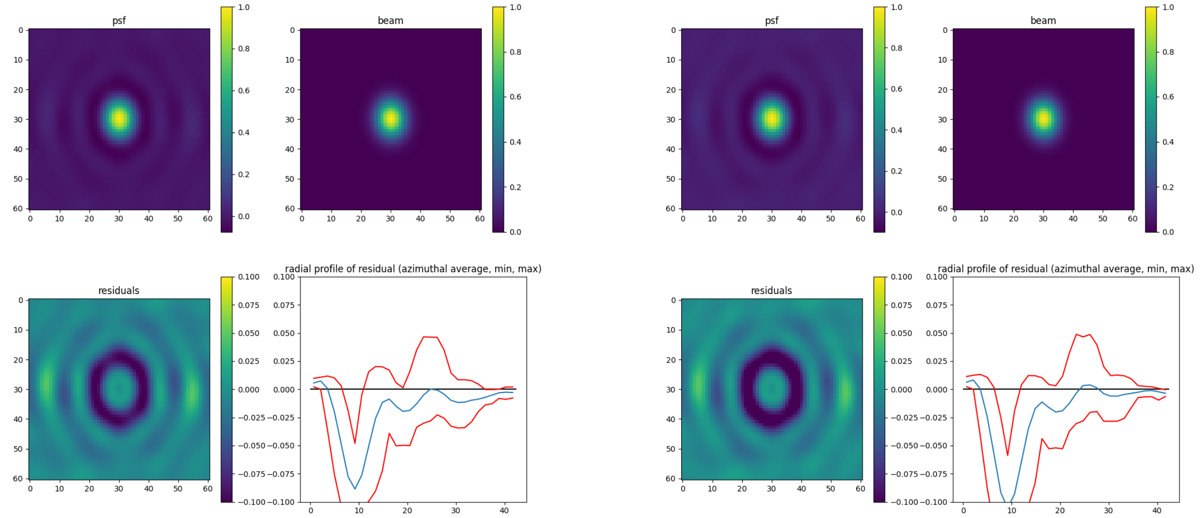

Figure 4.13: PSF, 2D Gaussian fit (beam), the fit residual, and the radial profile of it: **left:** for config C43-1, BLD case "A"; **right:** or config C43-1, BLD case "B".

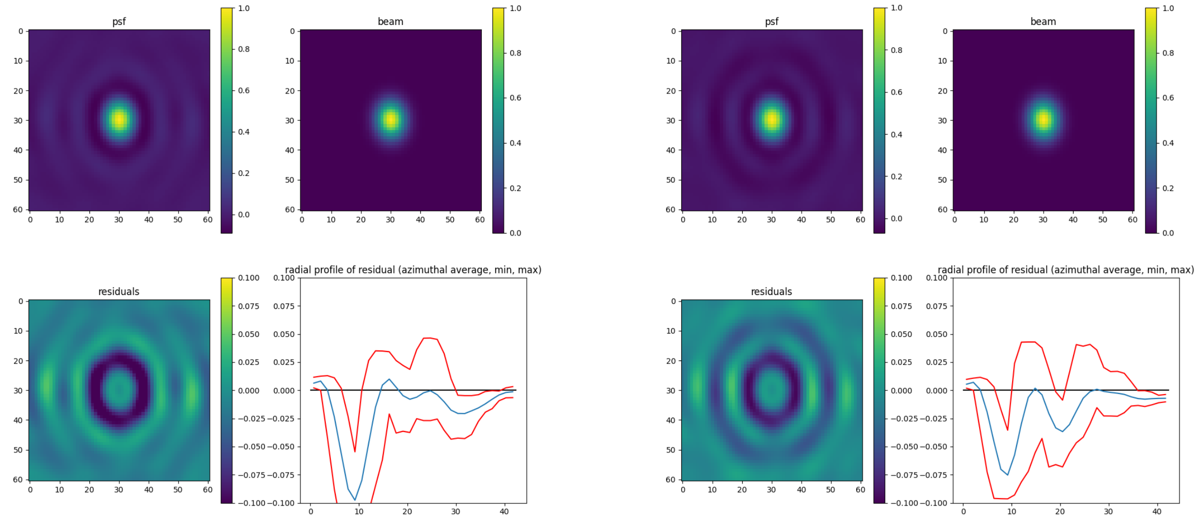

Figure 4.14: PSF, 2D Gaussian fit (beam), and the fit residual, and the radial profile of it: **left:** for config C43-1, BLD case "C"; **right:** or config C43-1, BLD case "D".

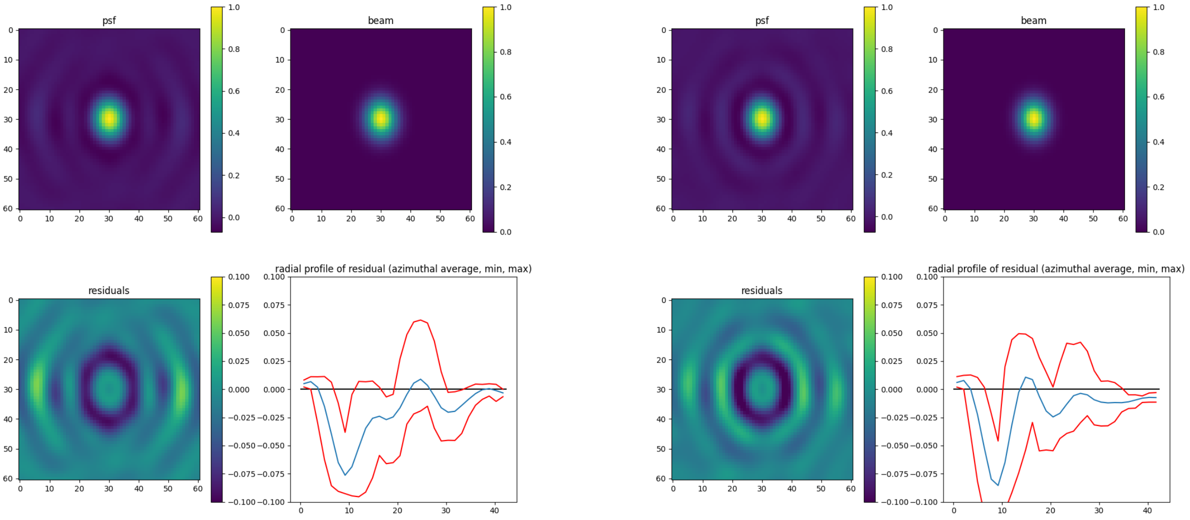

Figure 4.15: PSF, 2D Gaussian fit (beam), and the fit residual, and the radial profile of it: **left:** for config C43-1, BLD case "E"; **right:** or config C43-1, BLD case "F".

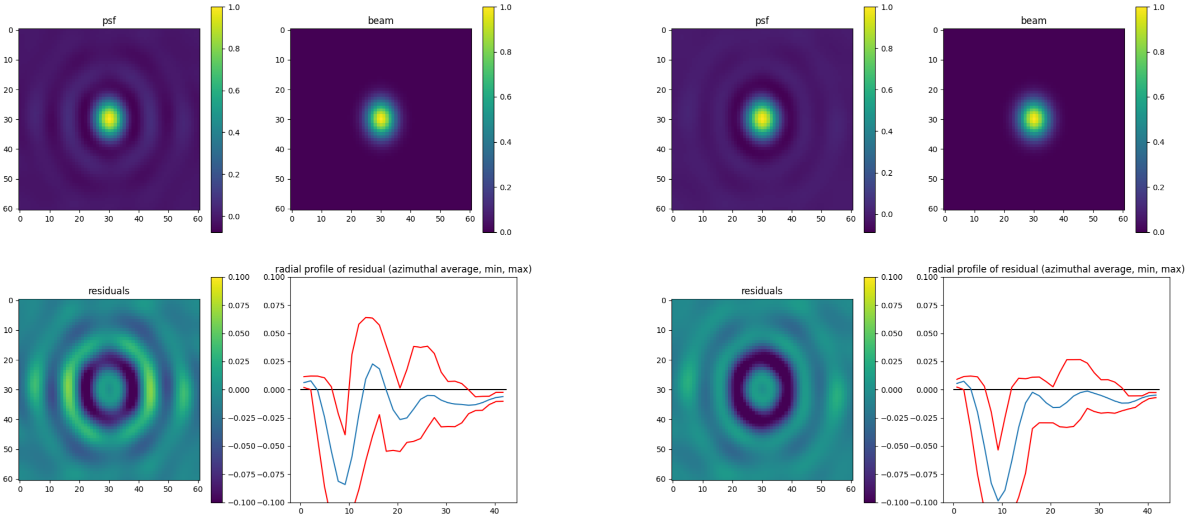

Figure 4.16: PSF, 2D Gaussian fit (beam), and the fit residual, and the radial profile of it: **left:** for config C43-1, BLD case "G"; **right:** or config C43-1, BLD case "I".

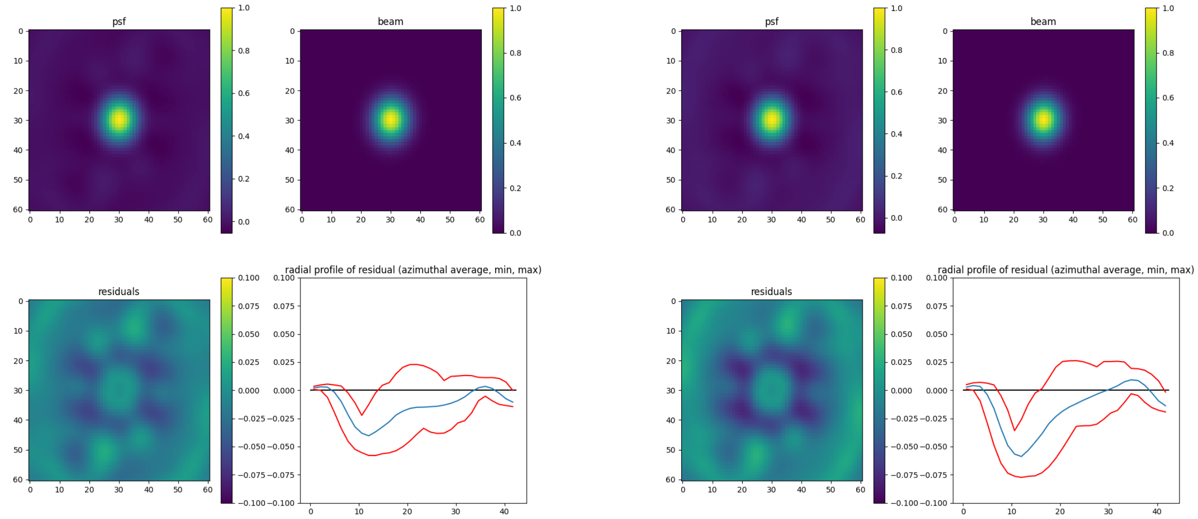

Figure 4.17: PSF, 2D Gaussian fit (beam), and the fit residual, and the radial profile of it: **left:** for config C43-3, BLD case "A"; **right:** or config C43-3, BLD case "B".

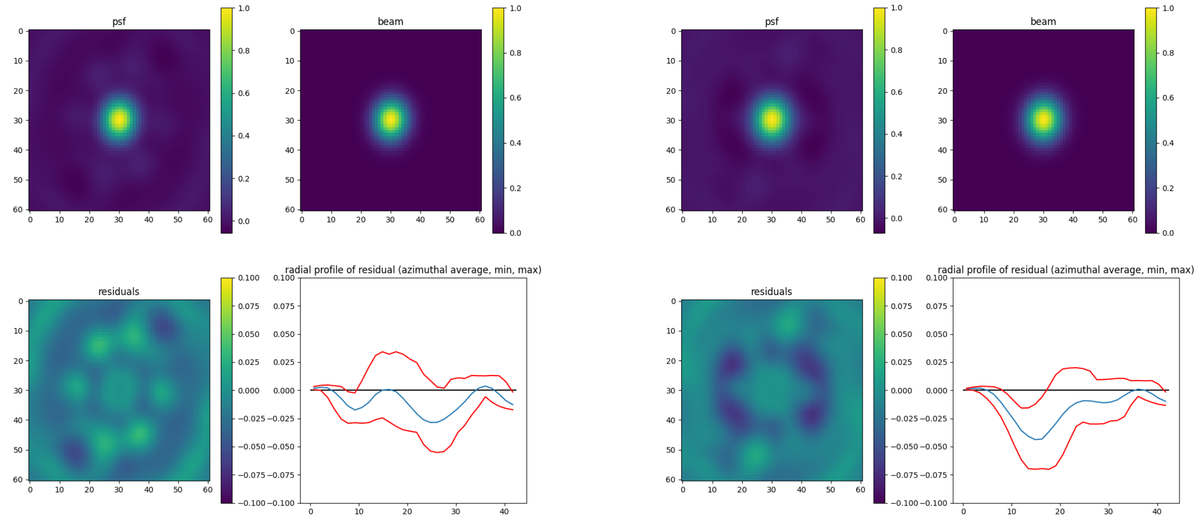

Figure 4.18: PSF, 2D Gaussian fit (beam), and the fit residual, and the radial profile of it: **left:** for config C43-3, BLD case "C"; **right:** or config C43-3, BLD case "D".

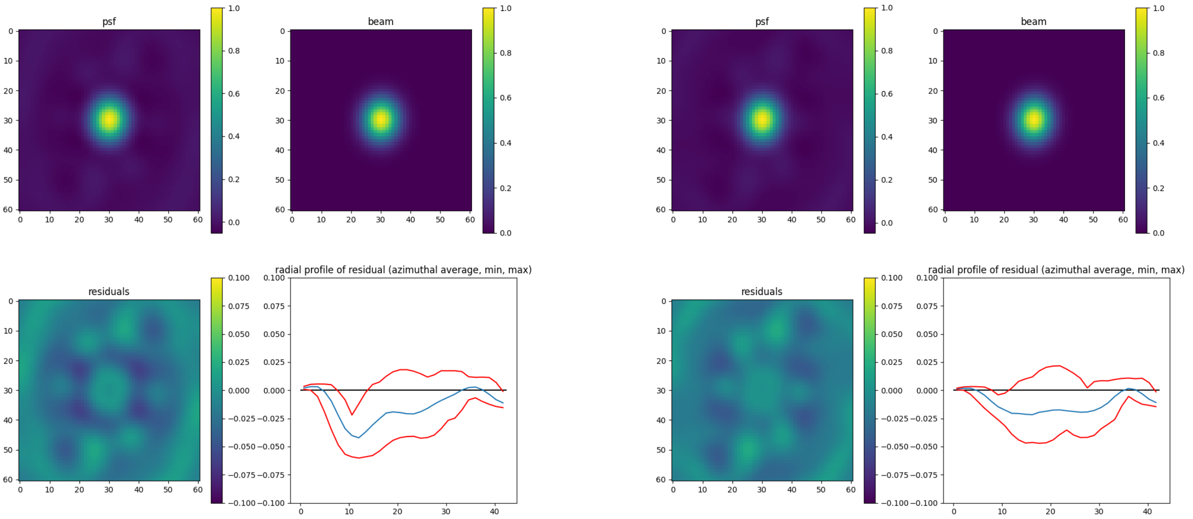

Figure 4.19: PSF, 2D Gaussian fit (beam), and the fit residual, and the radial profile of it: **left:** for config C43-3, BLD case "E"; **right:** or config C43-3, BLD case "F".

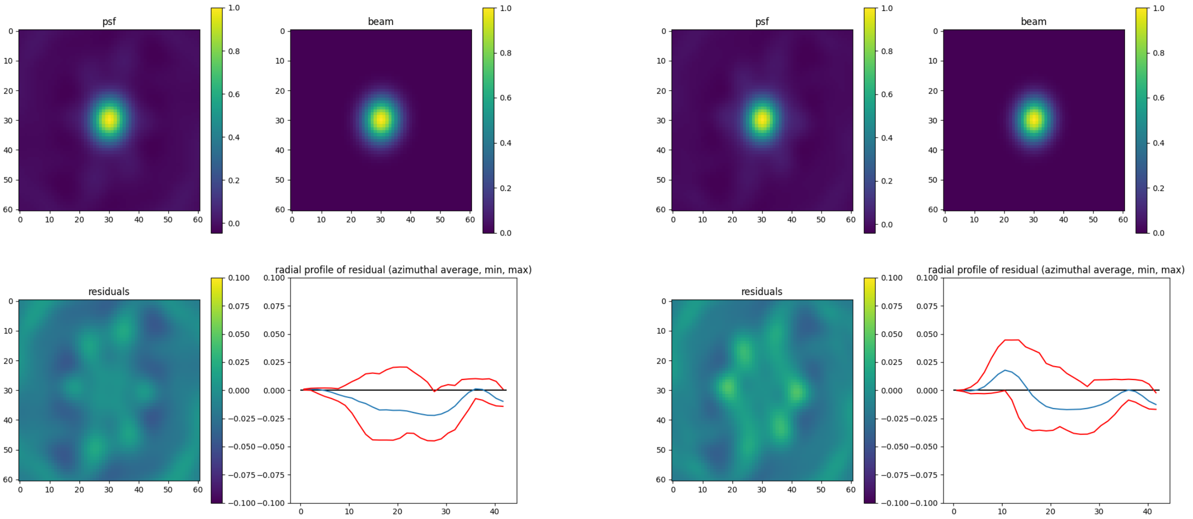

Figure 4.20: PSF, 2D Gaussian fit (beam), and the fit residual, and the radial profile of it: **left:** for config C43-3, BLD case "G"; **right:** or config C43-3, BLD case "I".

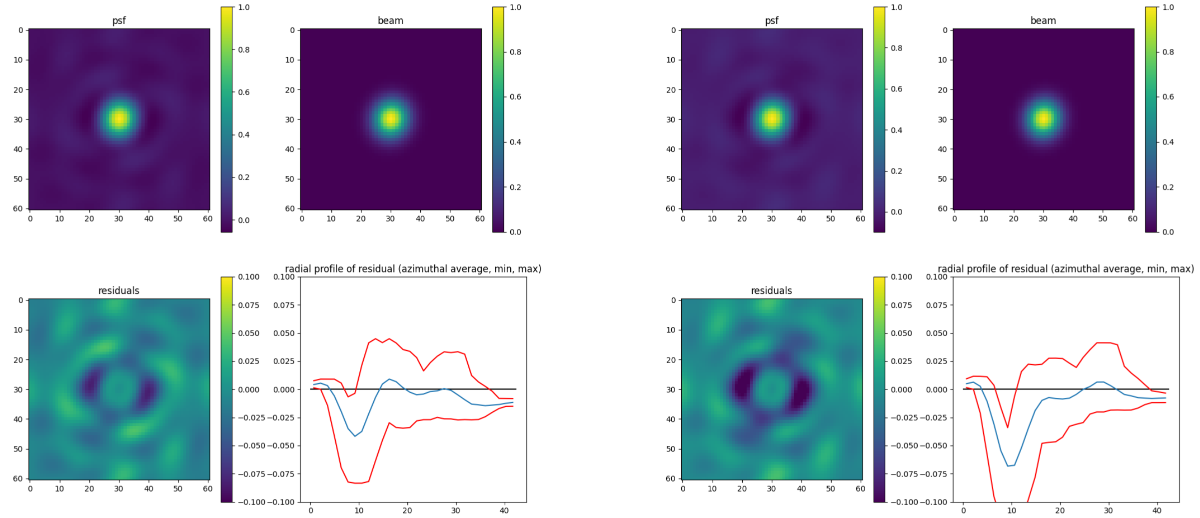

Figure 4.21: PSF, 2D Gaussian fit (beam), and the fit residual, and the radial profile of it: **left:** for config C43-5, BLD case "A"; **right:** or config C43-5, BLD case "B".

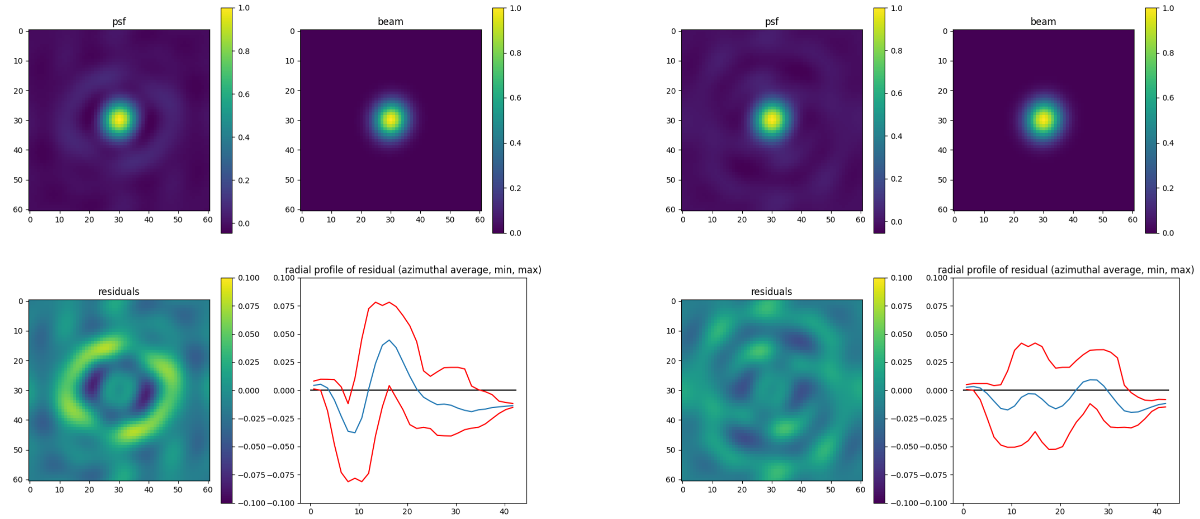

Figure 4.22: PSF, 2D Gaussian fit (beam), and the fit residual, and the radial profile of it: **left:** for config C43-5, BLD case "C"; **right:** or config C43-5, BLD case "D".

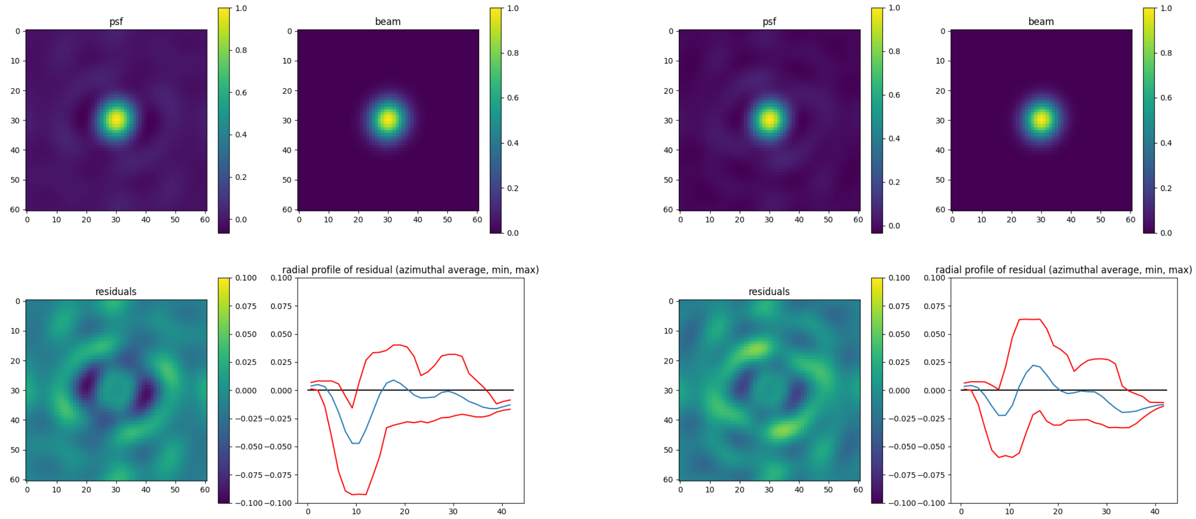

Figure 4.23: PSF, 2D Gaussian fit (beam), and the fit residual, and the radial profile of it: **left:** for config C43-5, BLD case "E"; **right:** or config C43-5, BLD case "F".

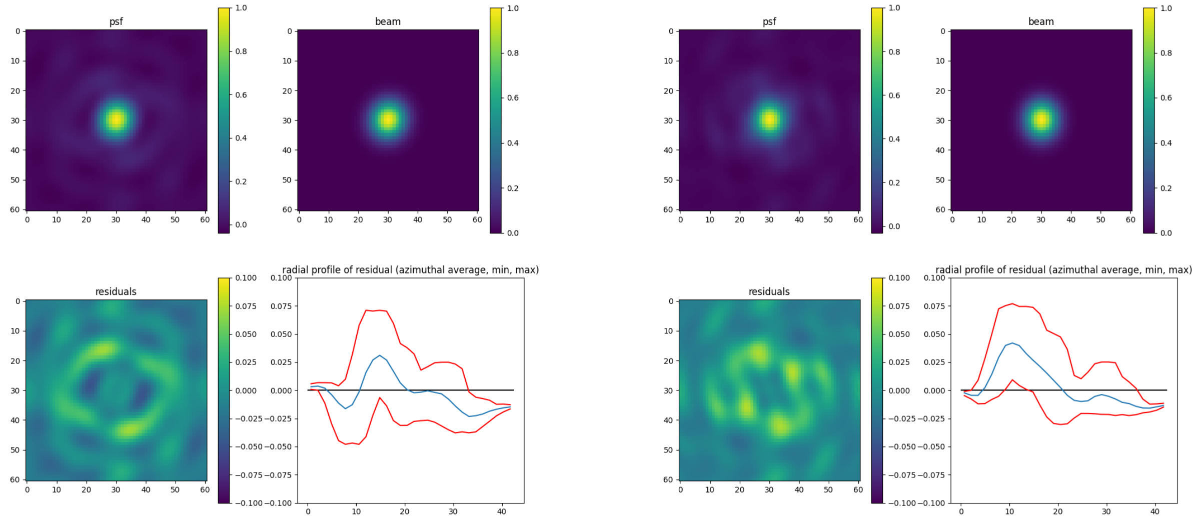

Figure 4.24: PSF, 2D Gaussian fit (beam), and the fit residual, and the radial profile of it: **left:** for config C43-5, BLD case "G"; **right:** or config C43-5, BLD case "I".

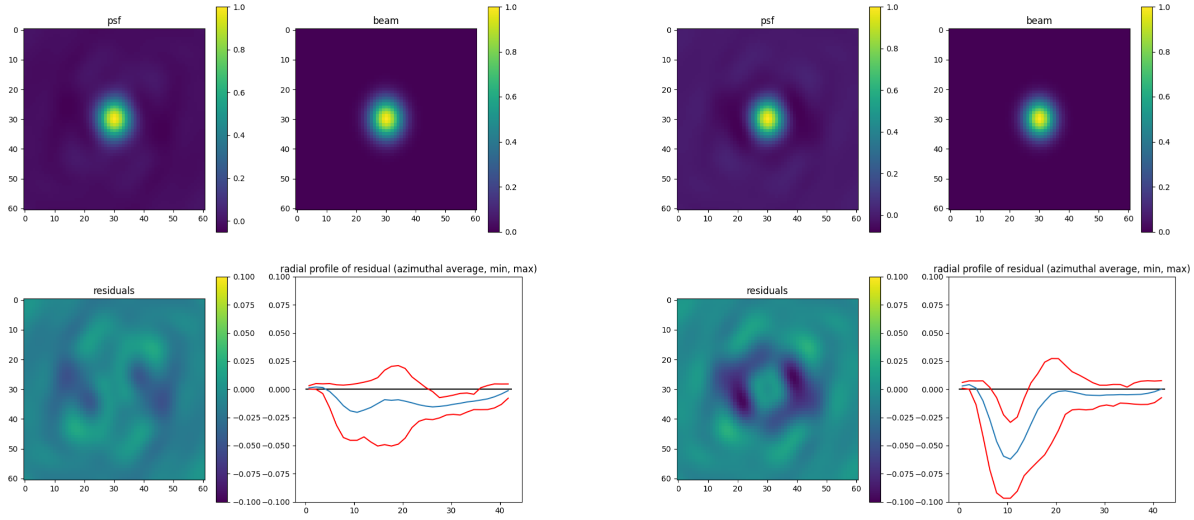

Figure 4.25: PSF, 2D Gaussian fit (beam), and the fit residual, and the radial profile of it: **left:** for config C43-7, BLD case "A"; **right:** or config C43-7, BLD case "B".

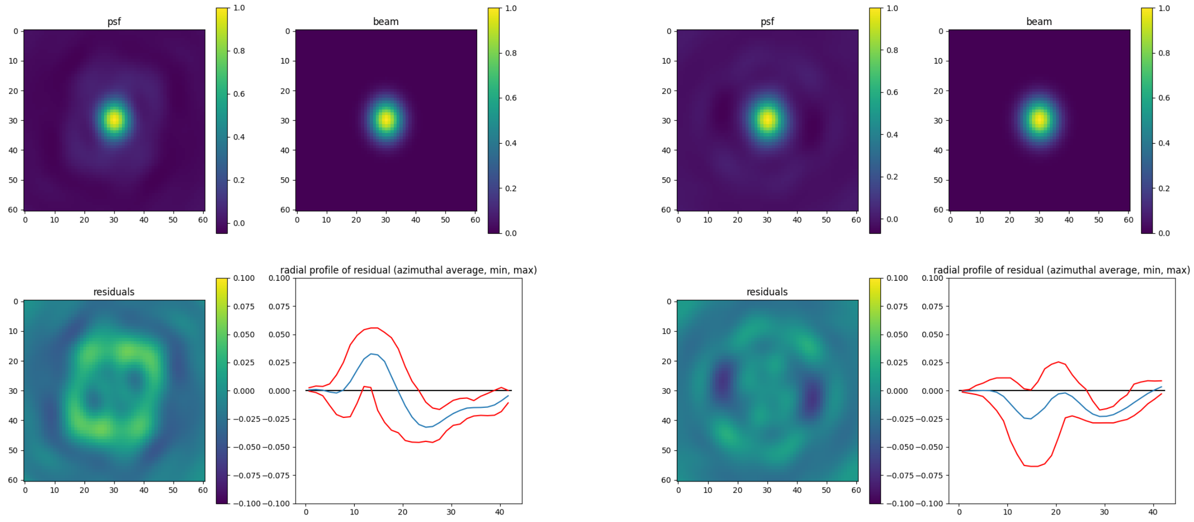

Figure 4.26: PSF, 2D Gaussian fit (beam), and the fit residual, and the radial profile of it: **left:** for config C43-7, BLD case "C"; **right:** or config C43-7, BLD case "D".

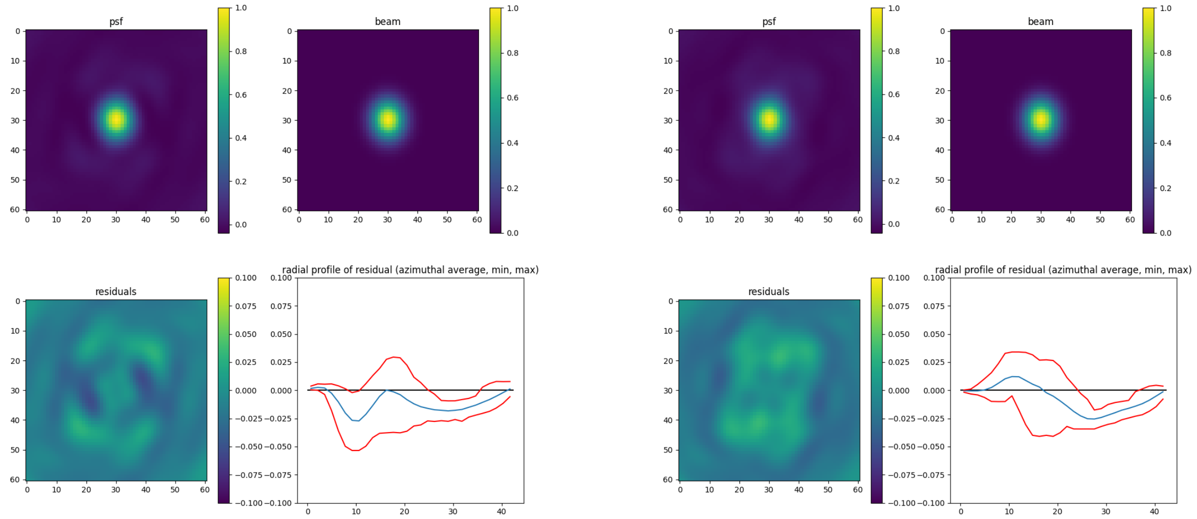

Figure 4.27: PSF, 2D Gaussian fit (beam), and the fit residual, and the radial profile of it: **left:** for config C43-7, BLD case "E"; **right:** or config C43-7, BLD case "F".

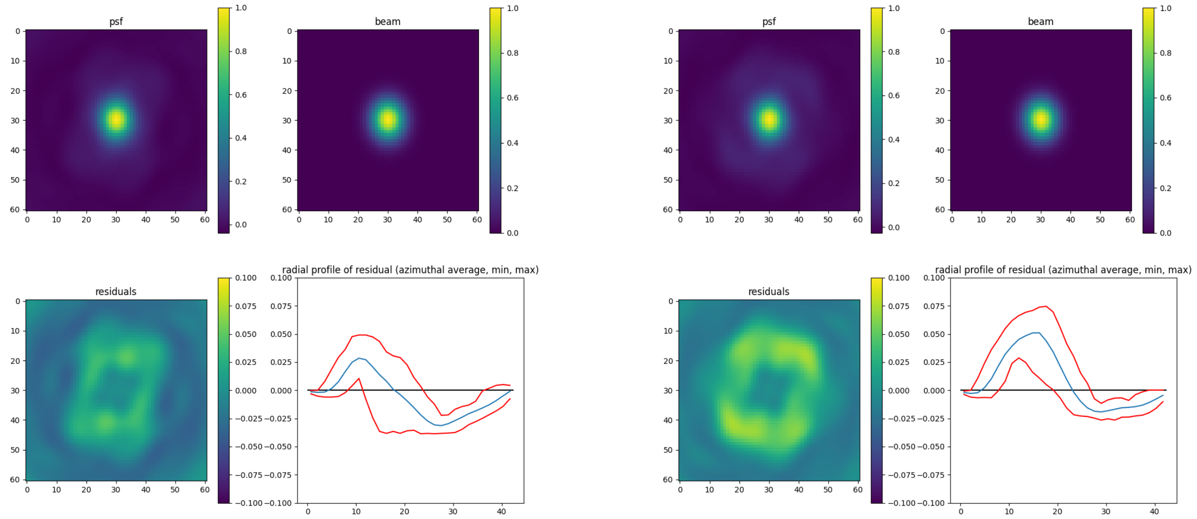

Figure 4.28: PSF, 2D Gaussian fit (beam), and the fit residual, and the radial profile of it: **left:** for config C43-7, BLD case "G"; **right:** or config C43-7, BLD case "I".

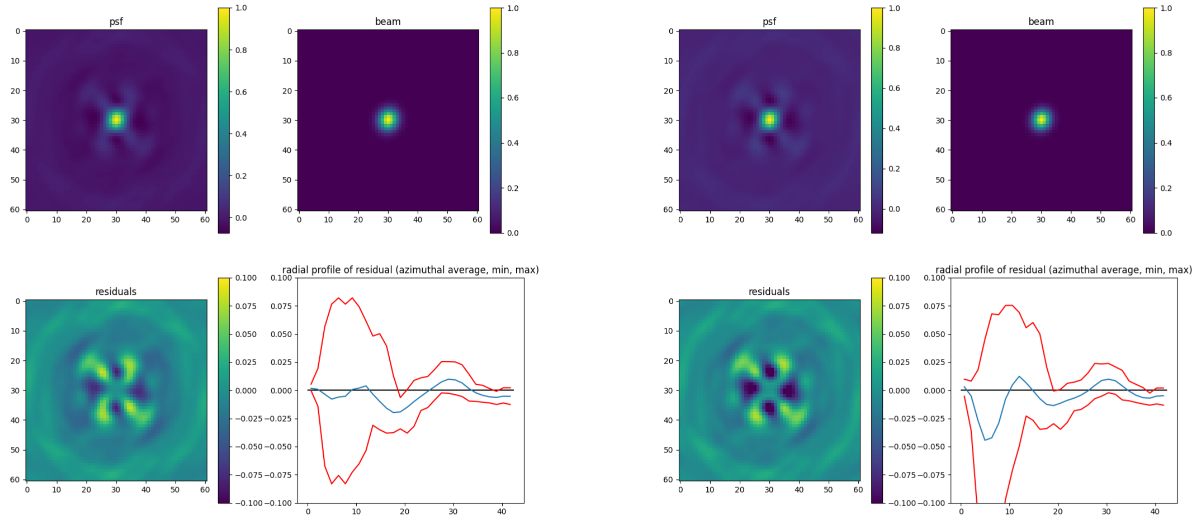

Figure 4.29: PSF, 2D Gaussian fit (beam), and the fit residual, and the radial profile of it: **left:** for config C43-9, BLD case "A"; **right:** or config C43-9, BLD case "B".

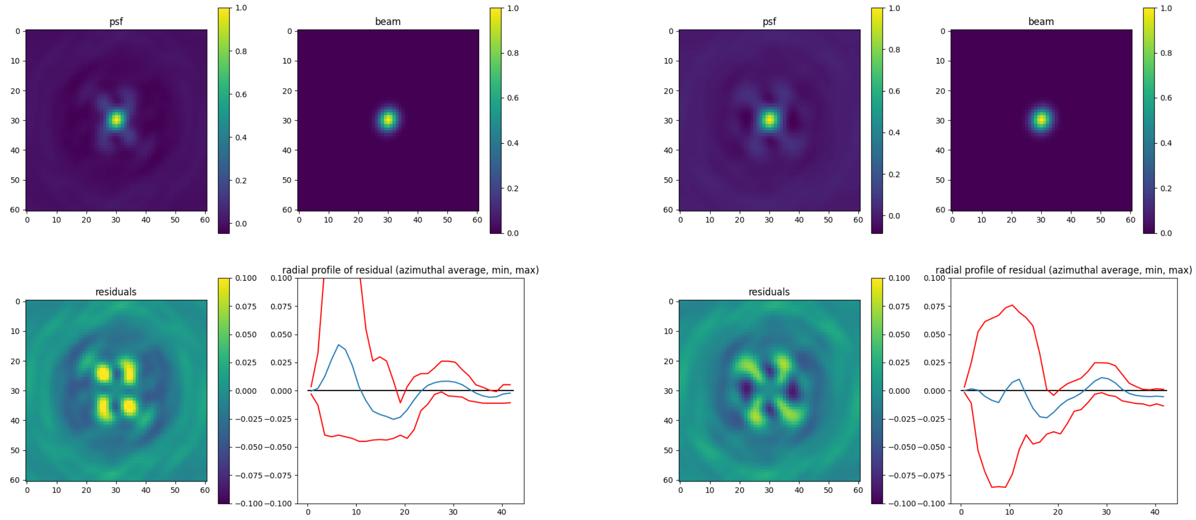

Figure 4.30: PSF, 2D Gaussian fit (beam), and the fit residual, and the radial profile of it: **left:** for config C43-9, BLD case "C"; **right:** or config C43-9, BLD case "D".

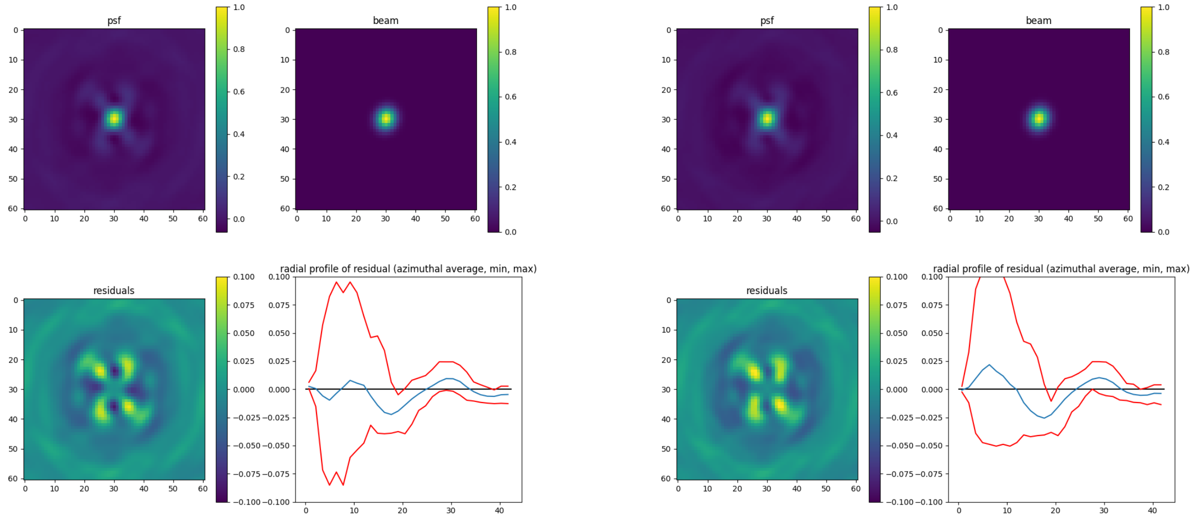

Figure 4.31: PSF, 2D Gaussian fit (beam), and the fit residual, and the radial profile of it: **left:** for config C43-9, BLD case "E"; **right:** or config C43-9, BLD case "F".

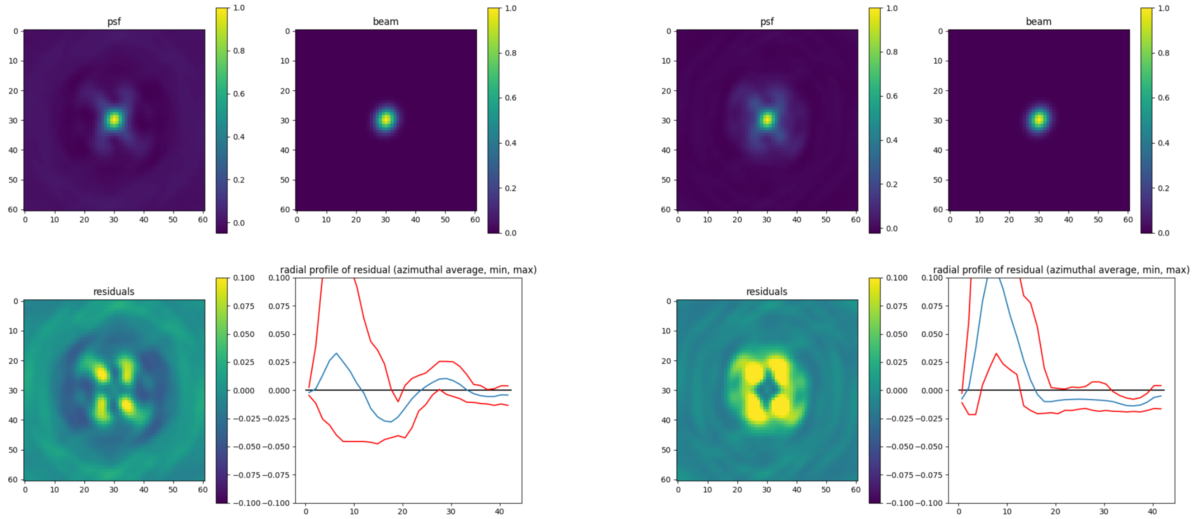

Figure 4.32: PSF, 2D Gaussian fit (beam), and the fit residual, and the radial profile of it: **left:** for config C43-9, BLD case "G"; **right:** or config C43-9, BLD case "I".

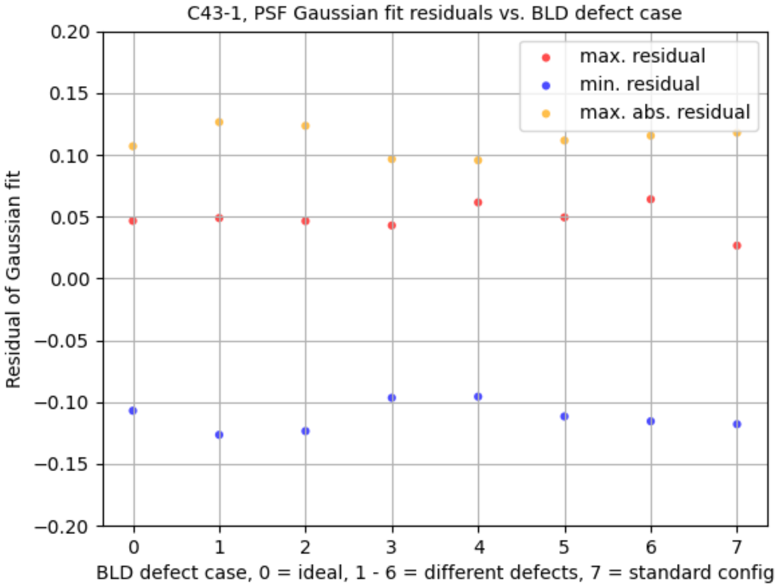

Figure 4.33: Left: The minimum, maximum, and maximum absolute residuals for a Gaussian fit to the PSF for base config **C43-1** (as shown in figures 4.13 - 4.16) plotted vs. the BLD case. For technical reasons, the cases are numbered 0-7 instead of A - G, I.

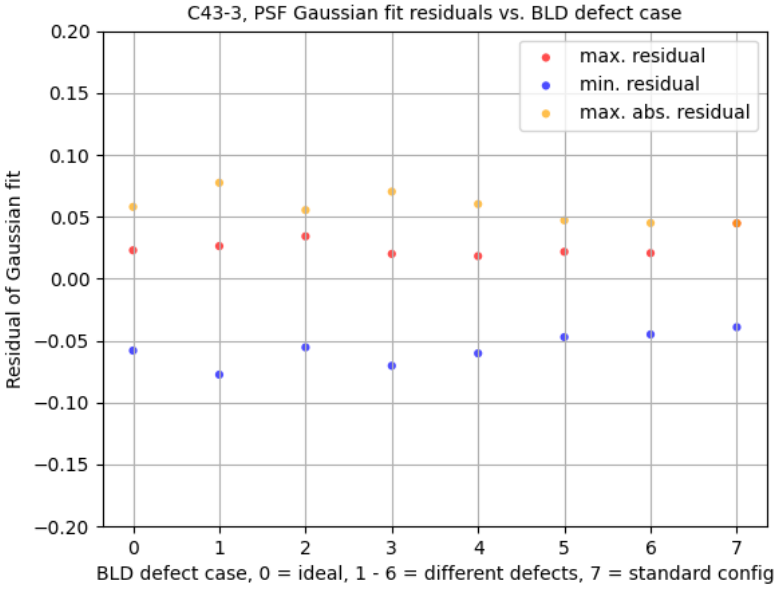

Figure 4.34: Left: The minimum, maximum, and maximum absolute residuals for a Gaussian fit to the PSF for base config **C43-3** (as shown in figures 4.17 - 4.17) plotted vs. the BLD case. For technical reasons, the cases are numbered 0-7 instead of A - G, I.

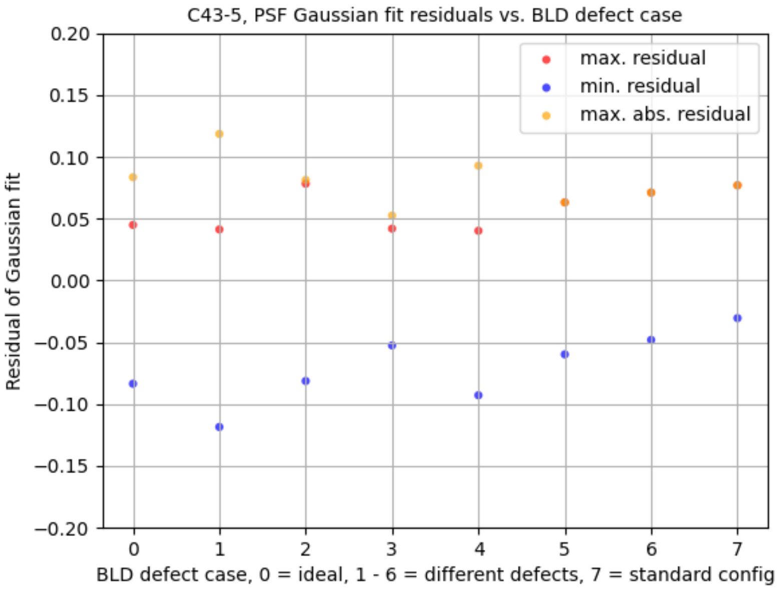

Figure 4.35: Left: The minimum, maximum, and maximum absolute residuals for a Gaussian fit to the PSF for base config **C43-5** (as shown in figures 4.21 - 4.24) plotted vs. the BLD case. For technical reasons, the cases are numbered 0-7 instead of A - G, I.

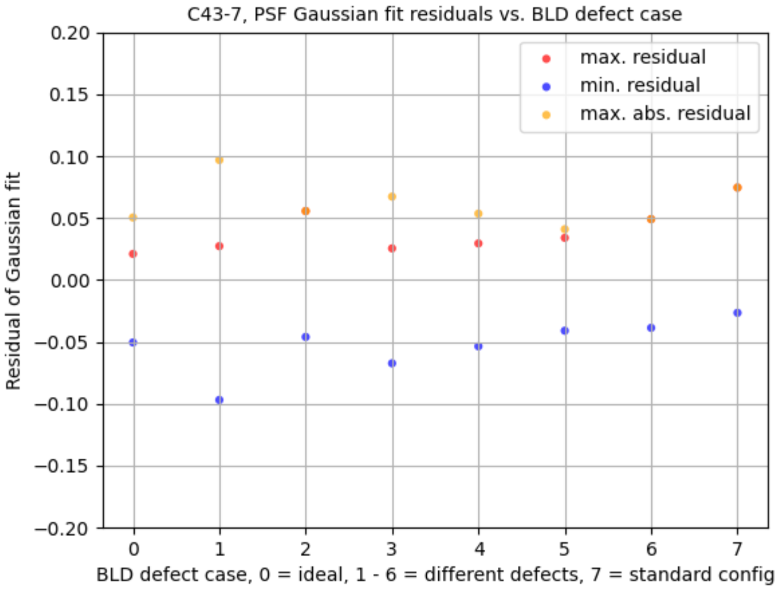

Figure 4.36: Left: The minimum, maximum, and maximum absolute residuals for a Gaussian fit to the PSF for base config **C43-7** (as shown in figures 4.25 - 4.28) plotted vs. the BLD case. For technical reasons, the cases are numbered 0-7 instead of A - G, I.

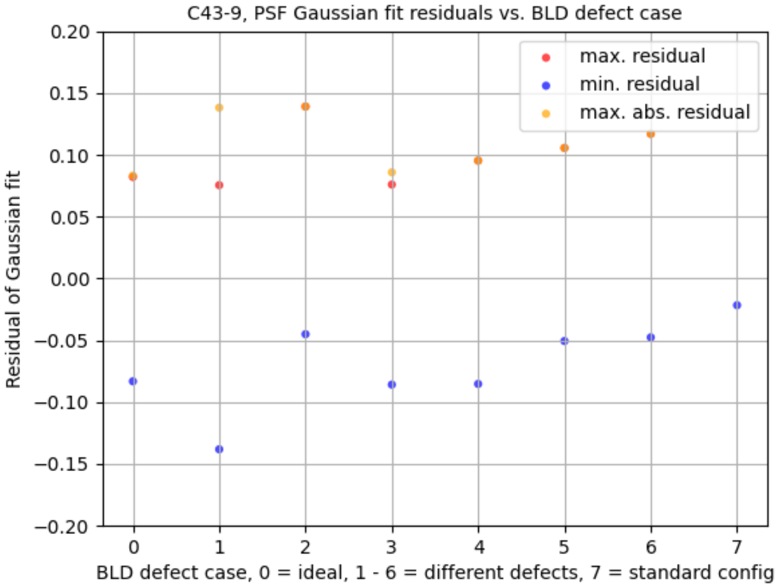

Figure 4.37: Left: The minimum, maximum, and maximum absolute residuals for a Gaussian fit to the PSF for base config **C43-9** (as shown in figures 4.29 - 4.32) plotted vs. the BLD case. For technical reasons, the cases are numbered 0-7 instead of A - G, I.

We discuss these results in section 4.5.

4.4 Evaluation of the output images

Using the CASA "imfit" task, we fit a Gaussian to each of the deconvolved Gaussians in the images obtained in the previous section. For each individual fit, the image is masked to only include a region of radius = 0.66 × the known FWHM of the original Gaussian around the known location of the original Gaussian. The resulting fit parameters can then be compared to the known original parameters of the Gaussians and the quality of the reconstruction be judged. Furthermore, we define a fidelity parameter and create fidelity maps.
When the FWHM of a Gaussian is given in the units of "pixels" in the following sections, this refers to the tclean pixel size as defined in section 4.3.

4.4.1 Flux reconstruction

The flux is reconstructed using the CASA imfit task. From the resulting flux a relative flux reconstruction error is computed as (measured flux - original flux)/original flux. For each group of nine Gaussians of the same original size and flux, this error is averaged.
The Figs. 4.38 - 4.41 show these average flux reconstruction errors as a function of the original size of the Gaussian for each of the five studied base configurations C43-1, 3, 5, 7, and 9 for the BLD case A (left hand side plot in each figure). The right hand side plot in each of these figures shows for comparison the flux reconstruction errors which were obtained by applying the same "imfit" flux reconstruction to the simulation input image regridded to the same resolution as the cleaned image. This "reference" plot represents the best possible outcome of the flux reconstruction given the finite image pixel size.

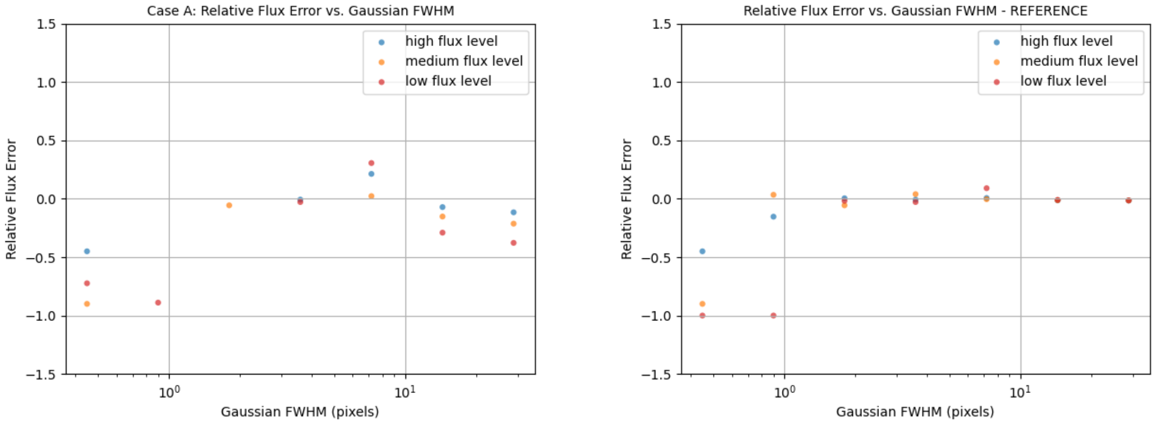

Figure 4.38: Left: The relative flux reconstruction error (measured flux - original flux)/original flux for config **C43-1 BLD case A**. Right: The same but measured in the simulation input image after regridding to the resolution of the cleaned image. The three colours indicate the three flux levels of the Gaussians in the simulation input image.

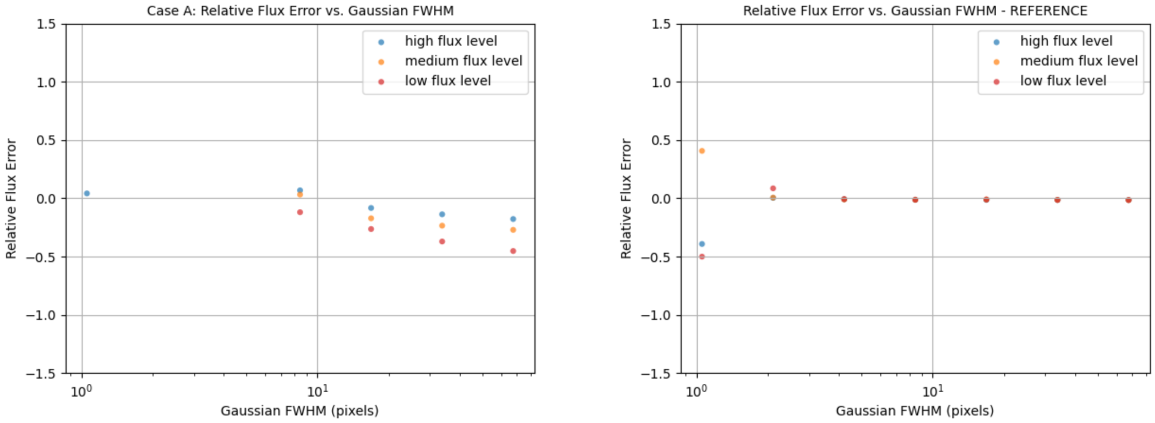

Figure 4.39: Left: The relative flux reconstruction error (measured flux - original flux)/original flux for config **C43-3 BLD case A**. Right: The same but measured in the simulation input image after regridding to the resolution of the cleaned image.

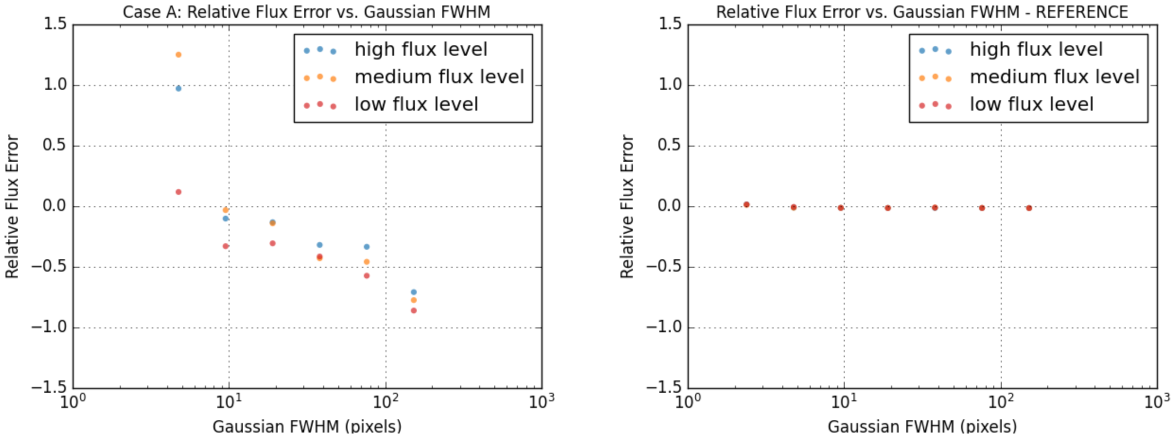

Figure 4.40: Left: The relative flux reconstruction error (measured flux - original flux)/original flux for config **C43-5 BLD case A**. Right: The same but measured in the simulation input image after regridding to the resolution of the cleaned image.

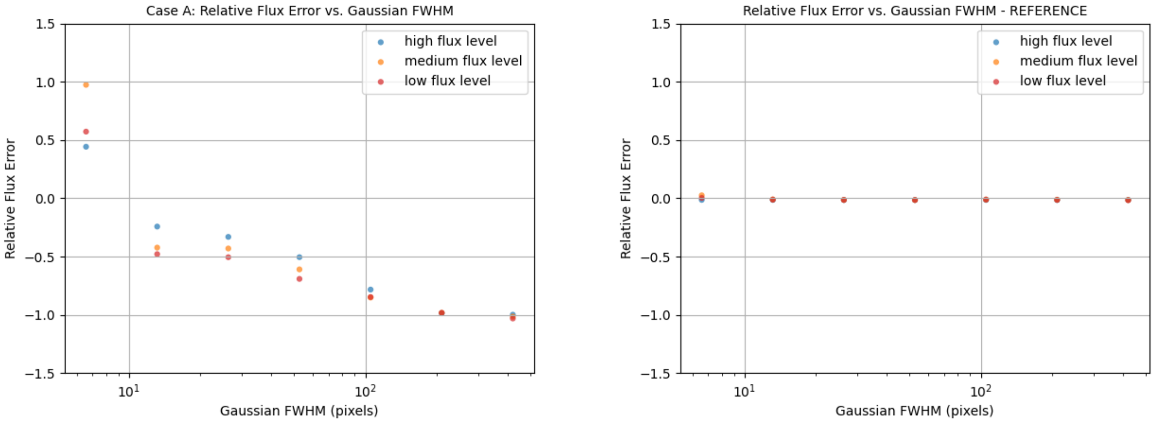

Figure 4.41: Left: The relative flux reconstruction error (measured flux - original flux)/original flux for config **C43-7 BLD case A**. Right: The same but measured in the simulation input image after regridding to the resolution of the cleaned image.

Figs. 4.38 - 4.41 show the results for BLD case A and the reference for all five base configurations. The same type of plots were also obtained for all other BLD cases: B - G, and I. Since showing these individual plots would bloat this report considerably and what we are really interested in is the *comparison* between the different cases, we condense the results into one plot per base configuration. In order to achieve this, we select for each base configuration the Gaussian size where the reconstruction is best, and then plot the parameter of interest (here the relative flux reconstruction error) vs. the BLD case. For technical reasons the cases are numbered 0 - 7 in the plots instead of being labeled A - G, I.

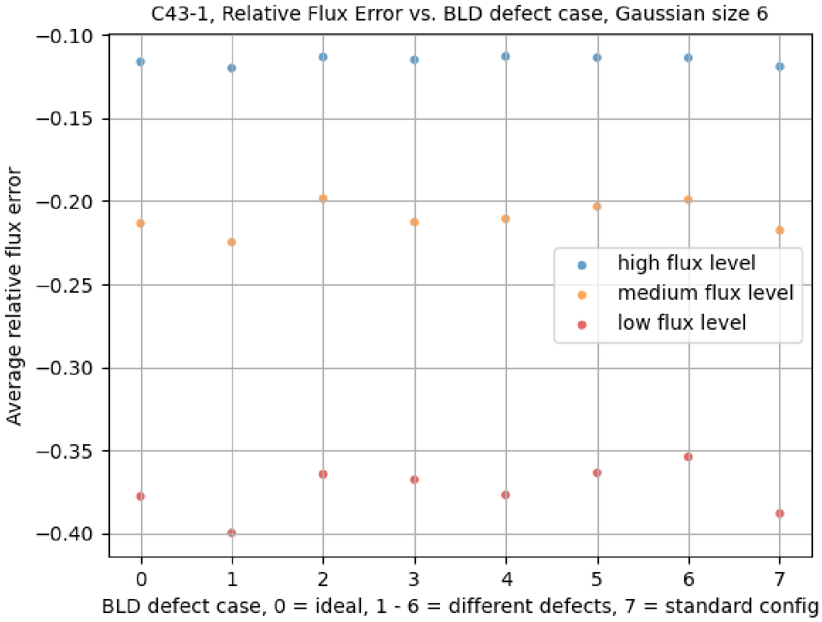

Figure 4.42: The relative flux reconstruction error (measured flux - original flux)/original flux for Gaussian size 6 (i.e. the largest Gaussian) for base config C43-1, plotted vs. the BLD case. For technical reasons the cases are numbered 0 - 7 instead of A - G, I. Note in this figure and all subsequent ones in this chapter that cases A - G all have the same total number of visibilities while case "I" (7) has by construction a higher number and thus higher sensitivity.

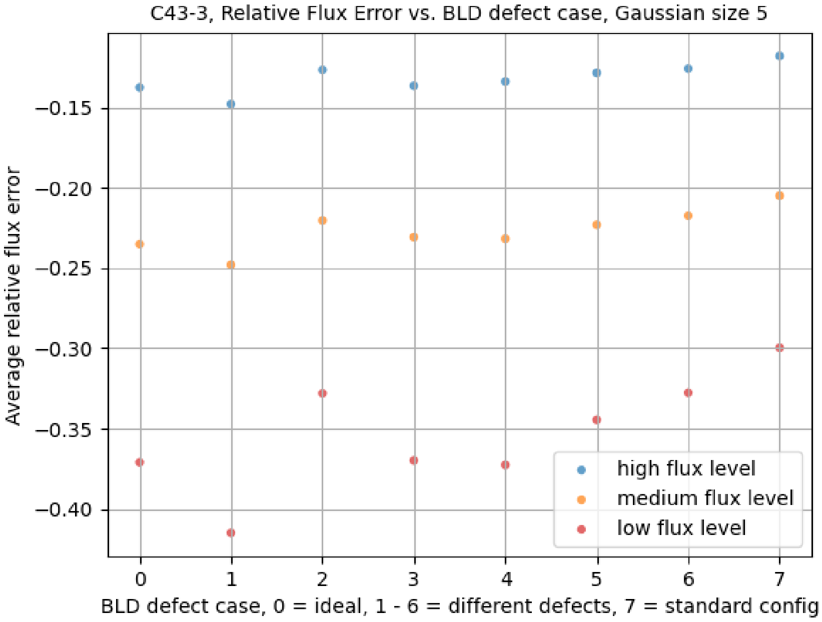

Figure 4.43: The relative flux reconstruction error (measured flux - original flux)/original flux for Gaussian size 5 (i.e. the second-largest Gaussian) for base config C43-3, plotted vs. the BLD case. For technical reasons the cases are numbered 0 - 7 instead of A - G, I.

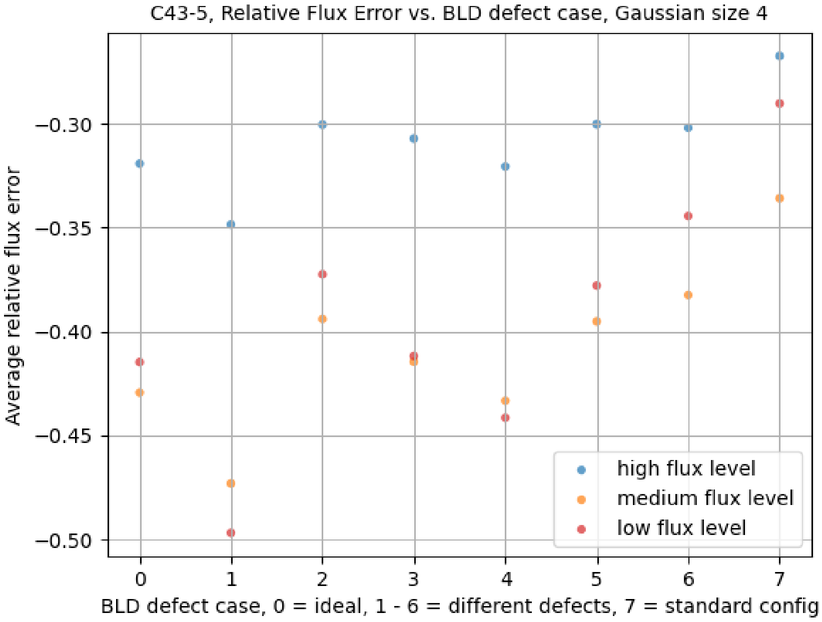

Figure 4.44: The relative flux reconstruction error (measured flux - original flux)/original flux for Gaussian size 4 (i.e. the fourth-smallest Gaussian) for base config C43-5, plotted vs. the BLD case. For technical reasons the cases are numbered 0 - 7 instead of A - G, I.

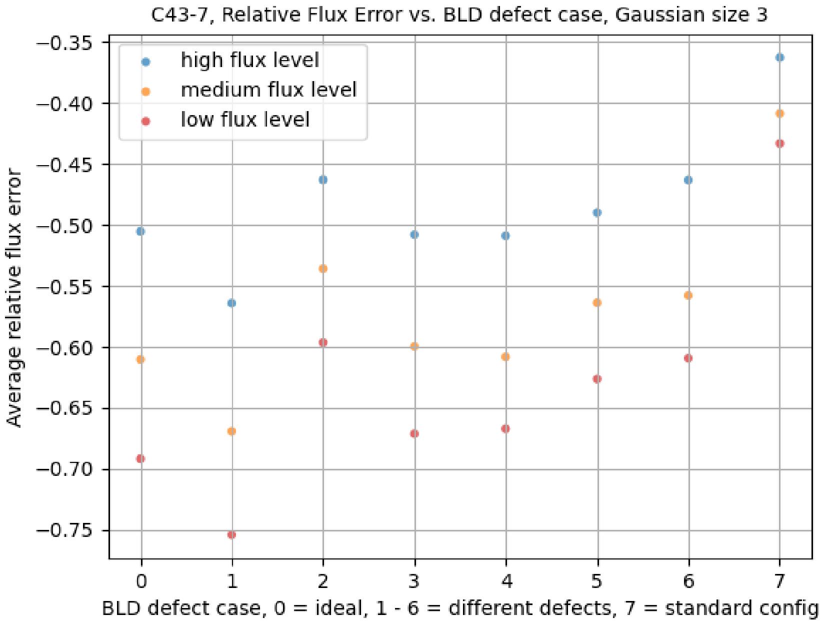

Figure 4.45: The relative flux reconstruction error (measured flux - original flux)/original flux for Gaussian size 3 (i.e. the third-smallest Gaussian) for base config C43-7, plotted vs. the BLD case. For technical reasons the cases are numbered 0 - 7 instead of A - G, I.

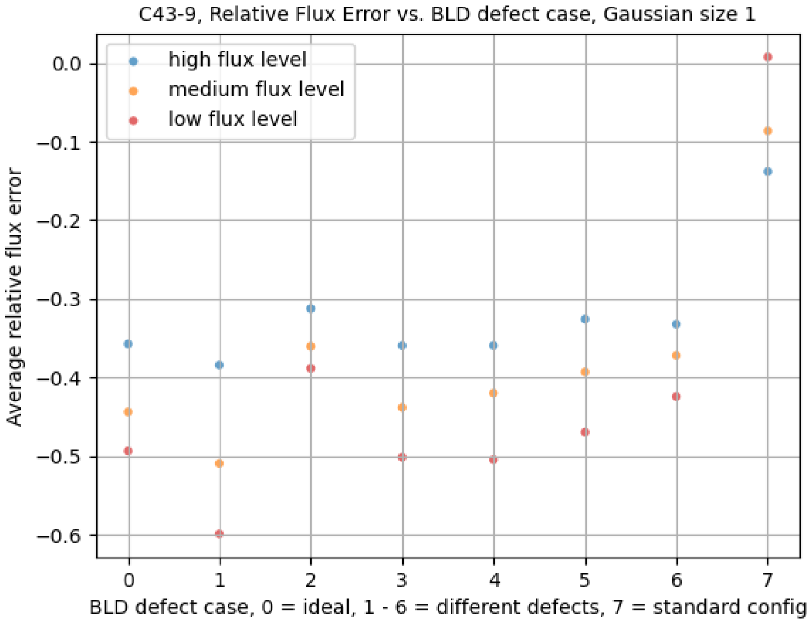

Figure 4.46: The relative flux reconstruction error (measured flux - original flux)/original flux for Gaussian size 1 (i.e. the smallest Gaussian) for base config C43-9, plotted vs. the BLD case. For technical reasons the cases are numbered 0 - 7 instead of A - G, I.

4.4.2 Position reconstruction

The position is reconstructed using the same CASA imfit procedure as in the flux reconstruction described above. From the resulting position a position reconstruction error is computed as the distance to the known original position of the individual Gaussian divided by the size of the FWHM of this original Gaussian. For each group of nine Gaussians of the same original size and flux, this error is averaged.

The Figs. 4.47 - 4.51 show these position reconstruction errors as a function of the original size of the Gaussian for each of the five studied base configurations C43-1, 3, 5, 7, and 9 for the BLD case A (left hand side plot in each figure). The right hand side plot in each of these figures shows for comparison the position reconstruction errors which were obtained by applying the same "imfit" procedure to the simulation input image regridded to the same resolution as the cleaned image. This "reference" plot represents the best possible outcome of the position reconstruction given the finite image pixel size.

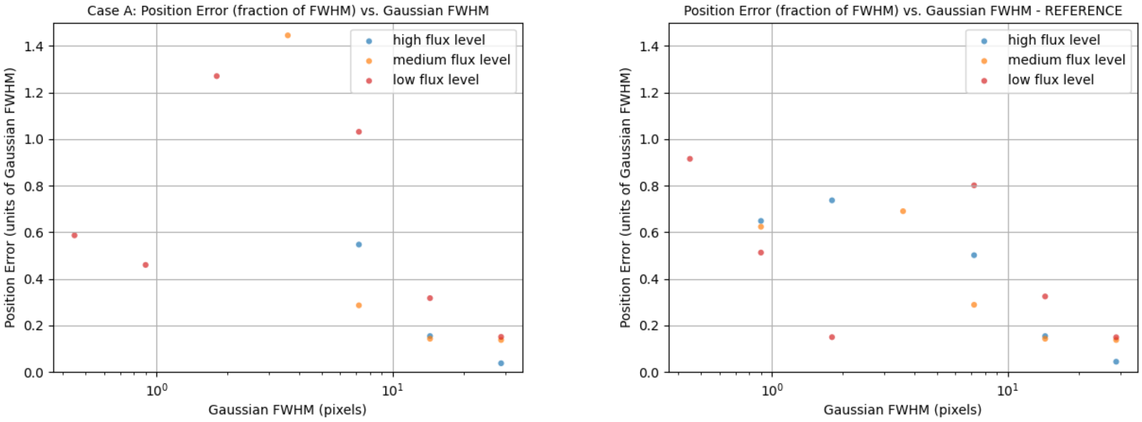

Figure 4.47: Left: The position error, i.e. 2D distance between the reconstructed and the known original position of each Gaussian, in units of the original Gaussian FWHM for config **C43-1 BLD case A**. Right: The same but measured in the simulation input image after regridding to the resolution of the cleaned image. The three colours indicate the three flux levels of the Gaussians in the simulation input image.

The results show, as one would expect, that the interferometer in each configuration has a range of angular scales where it reconstructs best. This range depends somewhat on the flux level of the observed object. The ideal image reconstruction shown on the right of each figure is only limited by the image resolution which leads to reconstruction problems at scales which are of the order of the pixel size or smaller.

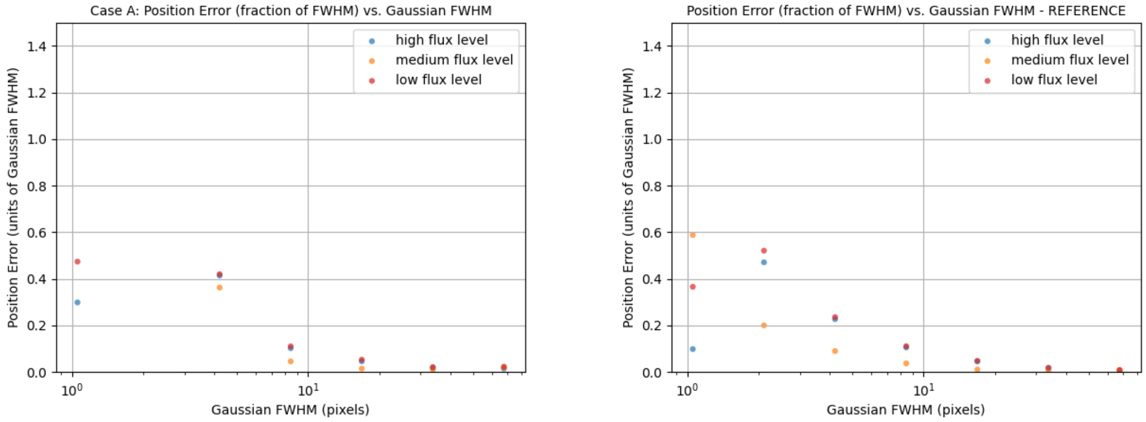

Figure 4.48: Left: The position error, i.e. 2D distance between the reconstructed and the known original position of each Gaussian, in units of the original Gaussian FWHM for config **C43-3 BLD case A**. Right: The same but measured in the simulation input image after regridding to the resolution of the cleaned image.

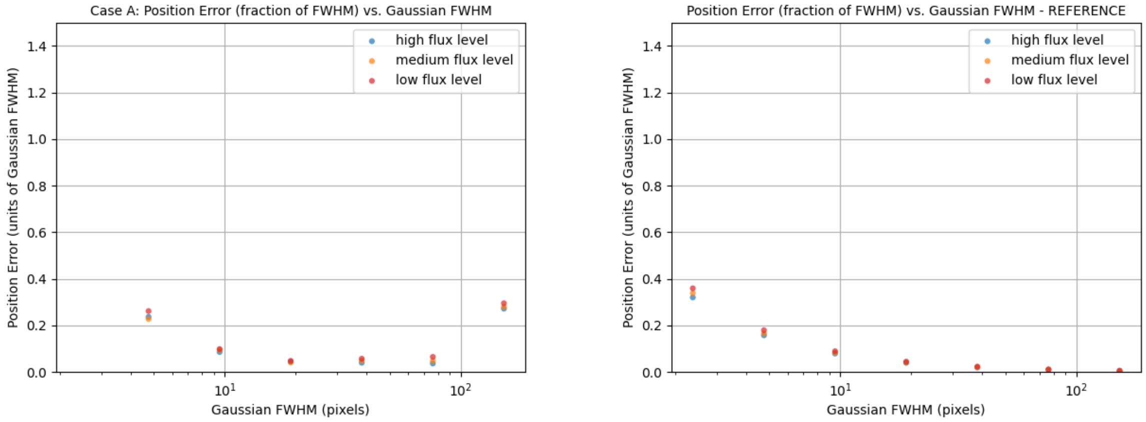

Figure 4.49: Left: The position error, i.e. 2D distance between the reconstructed and the known original position of each Gaussian, in units of the original Gaussian FWHM for config **C43-5 BLD case A**. Right: The same but measured in the simulation input image after regridding to the resolution of the cleaned image.

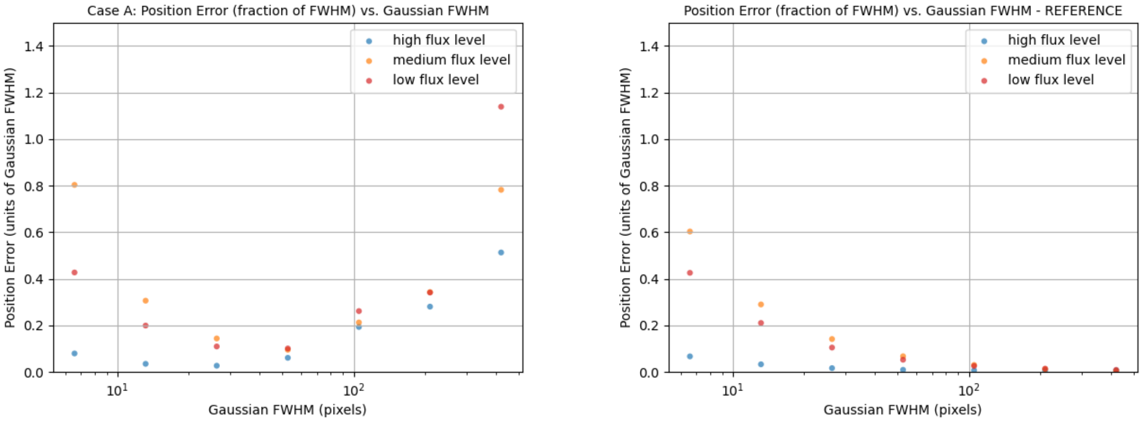

Figure 4.50: Left: The position error, i.e. 2D distance between the reconstructed and the known original position of each Gaussian, in units of the original Gaussian FWHM for config **C43-7 BLD case A**. Right: The same but measured in the simulation input image after regridding to the resolution of the cleaned image.

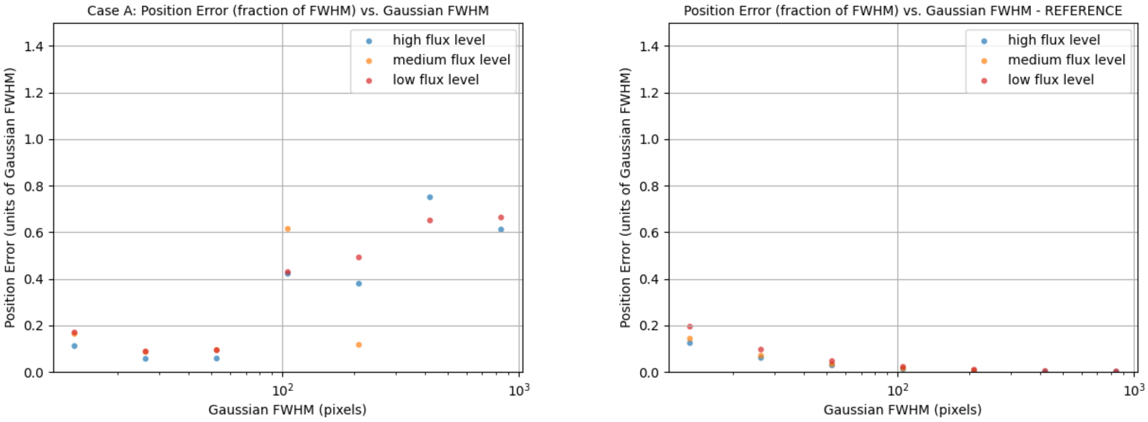

Figure 4.51: Left: The position error, i.e. 2D distance between the reconstructed and the known original position of each Gaussian, in units of the original Gaussian FWHM for config **C43-9 BLD case A**. Right: The same but measured in the simulation input image after regridding to the resolution of the cleaned image.

Figs. 4.47 - 4.51 show the results for BLD case A and the reference for all five base configurations. The same type of plots were also obtained for all other BLD cases: B - G, and I. As in the previous section, we avoid showing these individual plots and condense the results into one plot per base configuration by selecting for each base configuration the Gaussian size where the reconstruction is best, and then plot the parameter of interest (here the position reconstruction error) vs. the BLD case. Again, for technical reasons the cases are numbered 0 - 7 in the plots instead of being labeled A - G, I.

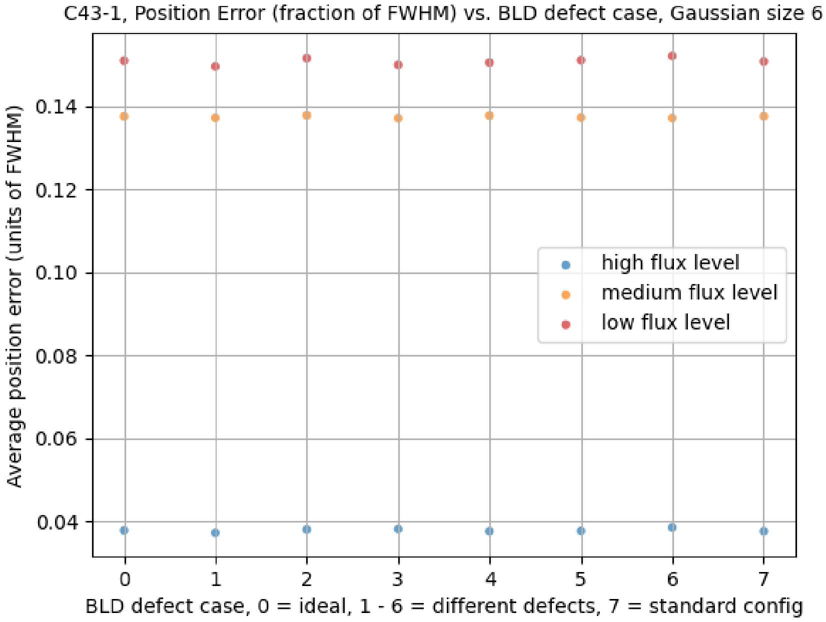

Figure 4.52: The position reconstruction error (distance to known original position in units of the known FWHM of the original Gaussian) for Gaussian size 6 (i.e. the largest Gaussian) for base config C43-1, plotted vs. the BLD case. For technical reasons the cases are numbered 0 - 7 instead of A - G, I.

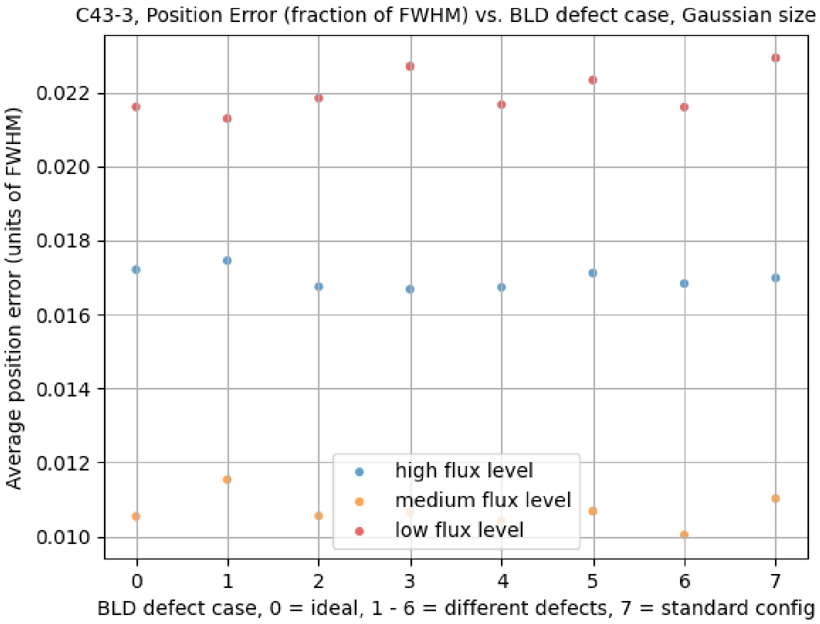

Figure 4.53: The position reconstruction error (distance to known original position in units of the known FWHM of the original Gaussian) for Gaussian size 5 (i.e. the second-largest Gaussian) for base config C43-3, plotted vs. the BLD case. For technical reasons the cases are numbered 0 - 7 instead of A - G, I.

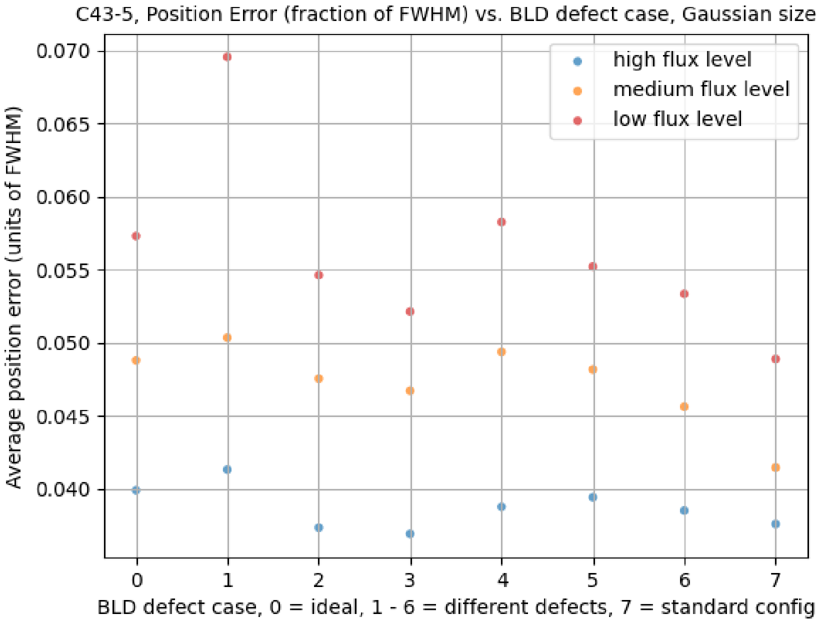

Figure 4.54: The position reconstruction error (distance to known original position in units of the known FWHM of the original Gaussian) for Gaussian size 4 (i.e. the fourth-smallest Gaussian) for base config C43-5, plotted vs. the BLD case. For technical reasons the cases are numbered 0 - 7 instead of A - G, I.

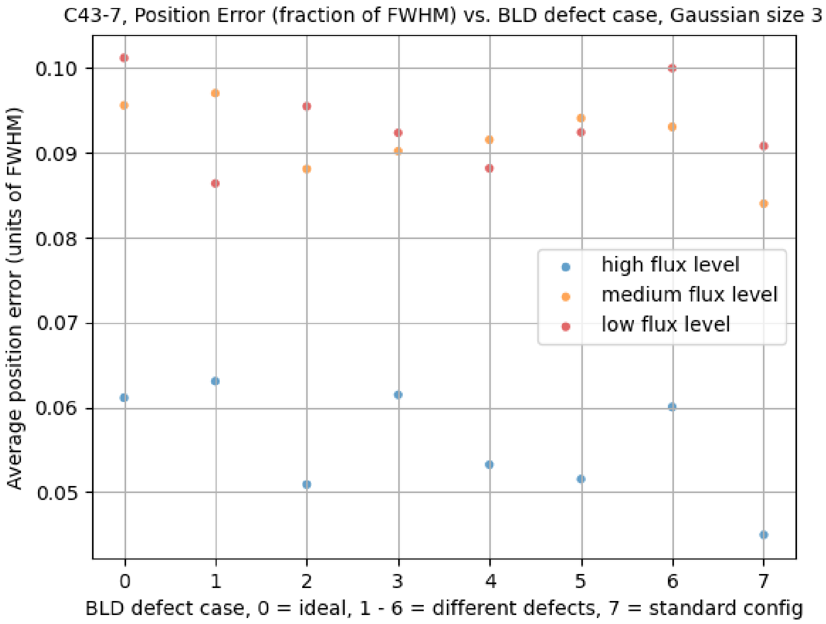

Figure 4.55: The position reconstruction error (distance to known original position in units of the known FWHM of the original Gaussian) for Gaussian size 3 (i.e. the third-smallest Gaussian) for base config C43-7, plotted vs. the BLD case. For technical reasons the cases are numbered 0 - 7 instead of A - G, I.

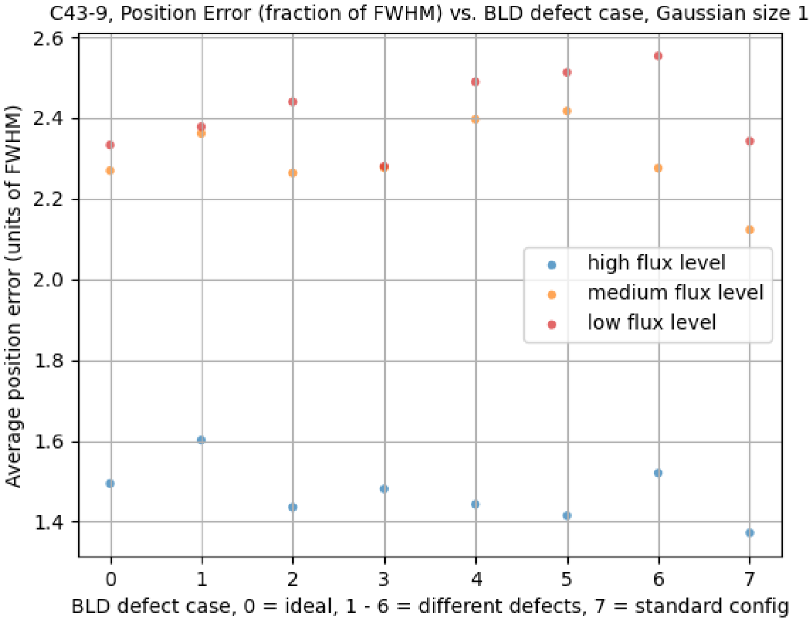

Figure 4.56: The position reconstruction error (distance to known original position in units of the known FWHM of the original Gaussian) for Gaussian size 1 (i.e. the smallest Gaussian) for base config C43-9, plotted vs. the BLD case. For technical reasons the cases are numbered 0 - 7 instead of A - G, I.

4.4.3 Shape reconstruction

In order to assess how well the shape of the Gaussians is reconstructed, we look at the ellipticity (defined as (difference major - minor axis)/minor axis) of the Gaussians after deconvolution which should be zero if there reconstruction were perfect.

The major and minor axis size of each Gaussian is measured using the same CASA imfit task procedure as in the position reconstruction described above. For each group of nine Gaussians of the same original size and flux, this ellipticity is averaged.

The Figs. 4.57 - 4.61 show these ellipticities as a function of the original size of the Gaussian for each of the five studied base configurations C43-1, 3, 5, 7, and 9 for the BLD case A (left hand side plot in each figure). The right hand side plot in each of these figures shows for comparison the ellipticity, which was obtained by applying the same "imfit" procedure to the simulation input image regridded to the same resolution as the cleaned image. This "reference" plot represents the best possible outcome of the shape reconstruction given the finite image pixel size.

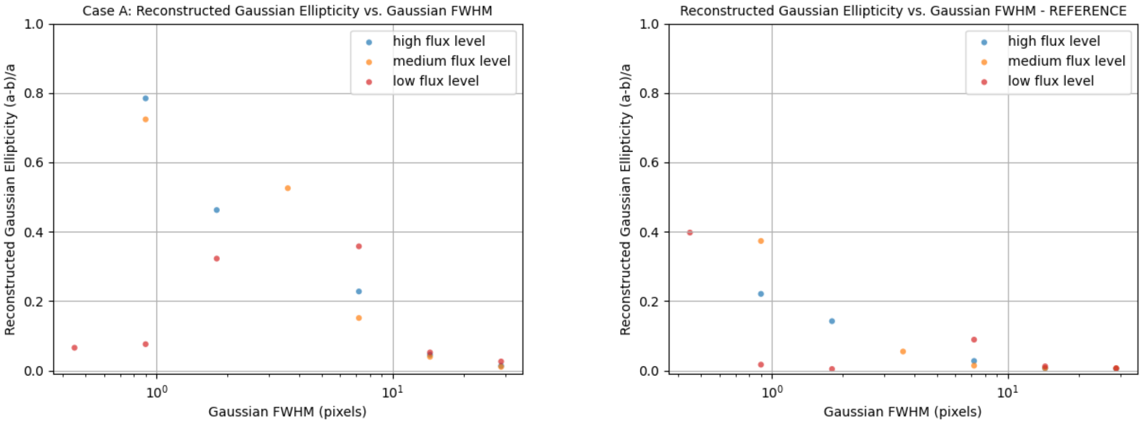

Figure 4.57: Left: The ellipticity (major - minor)/major of the reconstructed Gaussians for config **C43-1 BLD case A**. Right: The same but measured in the simulation input image after regridding to the resolution of the cleaned image. The three colours indicate the three flux levels of the Gaussians in the simulation input image.

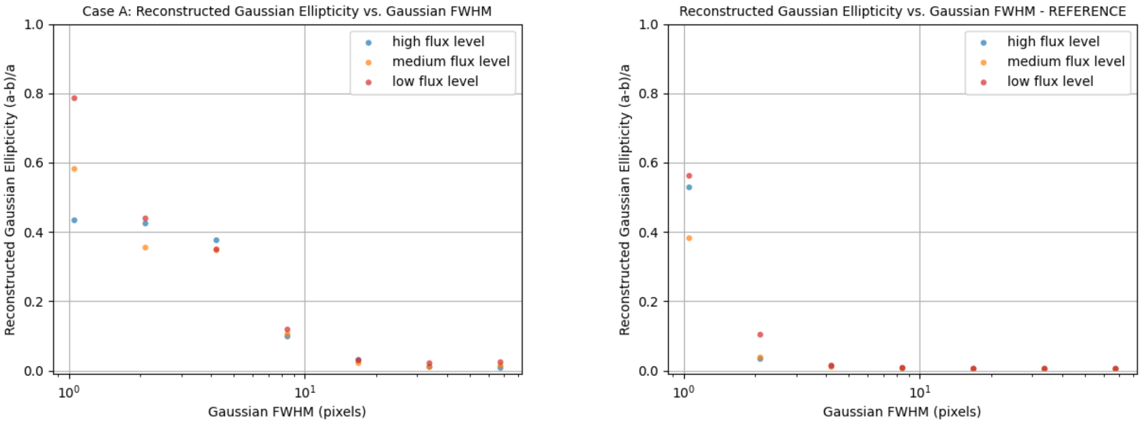

Figure 4.58: Left: The ellipticity (major - minor)/major of the reconstructed Gaussians for config **C43-3 BLD case A**. Right: The same but measured in the simulation input image after regridding to the resolution of the cleaned image.

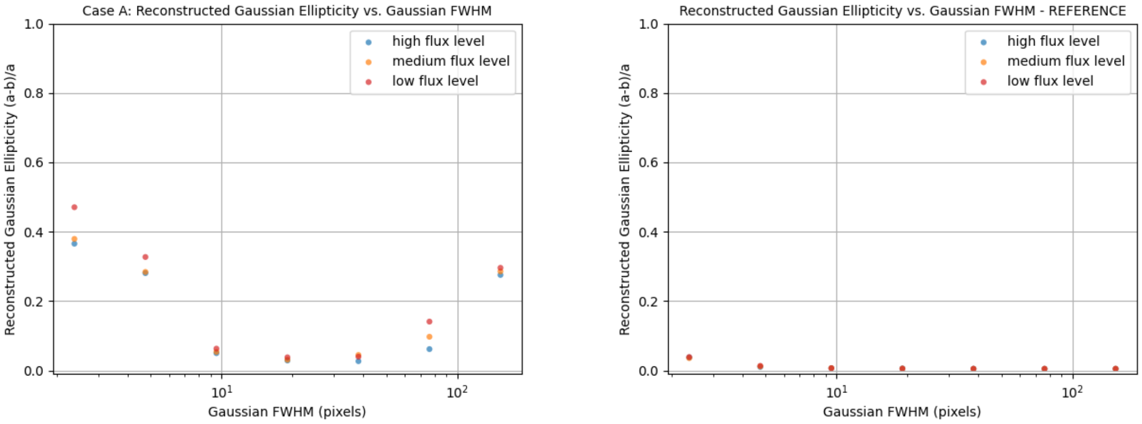

Figure 4.59: Left: The ellipticity (major - minor)/major of the reconstructed Gaussians for config **C43-5 BLD case A**. Right: The same but measured in the simulation input image after regridding to the resolution of the cleaned image.

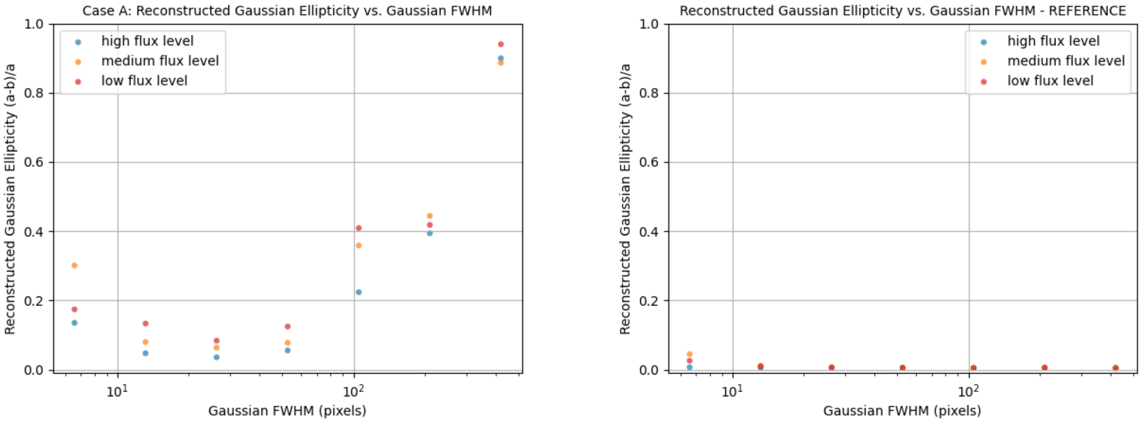

Figure 4.60: Left: The ellipticity (major - minor)/major of the reconstructed Gaussians for config **C43-7 BLD case A**. Right: The same but measured in the simulation input image after regridding to the resolution of the cleaned image.

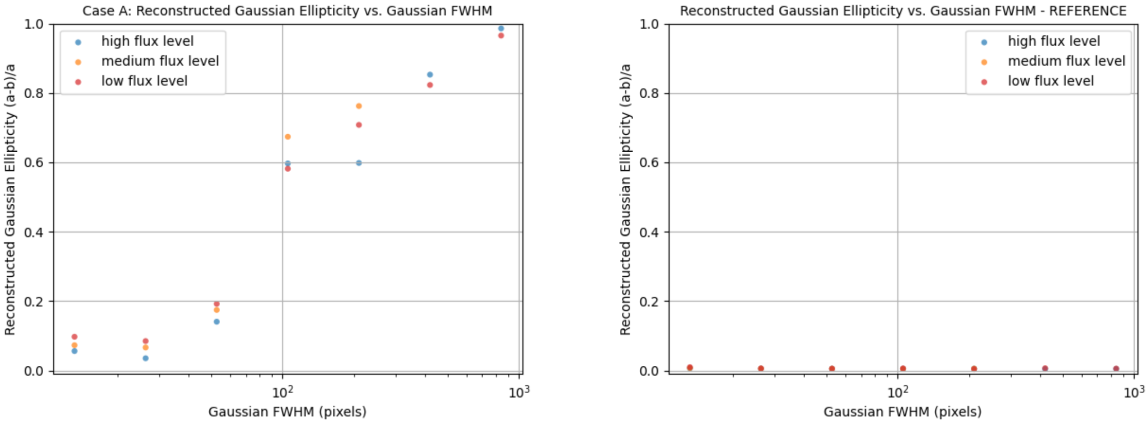

Figure 4.61: Left: The ellipticity (major - minor)/major of the reconstructed Gaussians for config **C43-9 BLD case A**. Right: The same but measured in the simulation input image after regridding to the resolution of the cleaned image.

Figs. 4.57 - 4.61 show the results for BLD case A and the reference for all five base configurations. The same type of plots were also obtained for all other BLD cases: B - G, and I. As in the previous sections, we avoid showing these individual plots and condense the results into one plot per base configuration by selecting for each base configuration the Gaussian size where the reconstruction is best, and then plot the parameter of interest (here ellipticity of the reconstructed Gaussians) vs. the BLD case. Also here, for technical reasons the cases are numbered 0 - 7 in the plots instead of being labeled A - G, I.

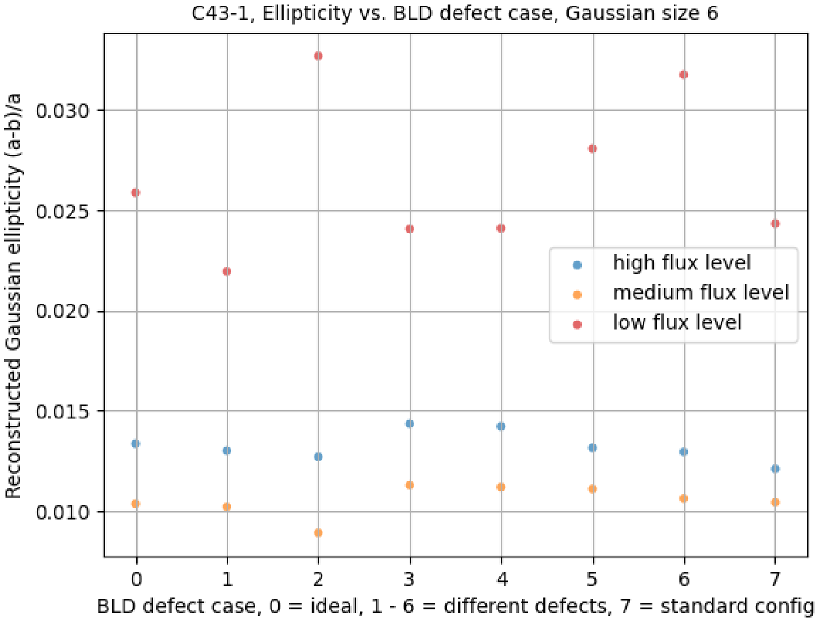

Figure 4.62: The ellipticity of the reconstructed Gaussians (expectation value is zero) for Gaussian size 6 (i.e. the largest Gaussian) for base config C43-1, plotted vs. the BLD case. For technical reasons the cases are numbered 0 - 7 instead of A - G, I.

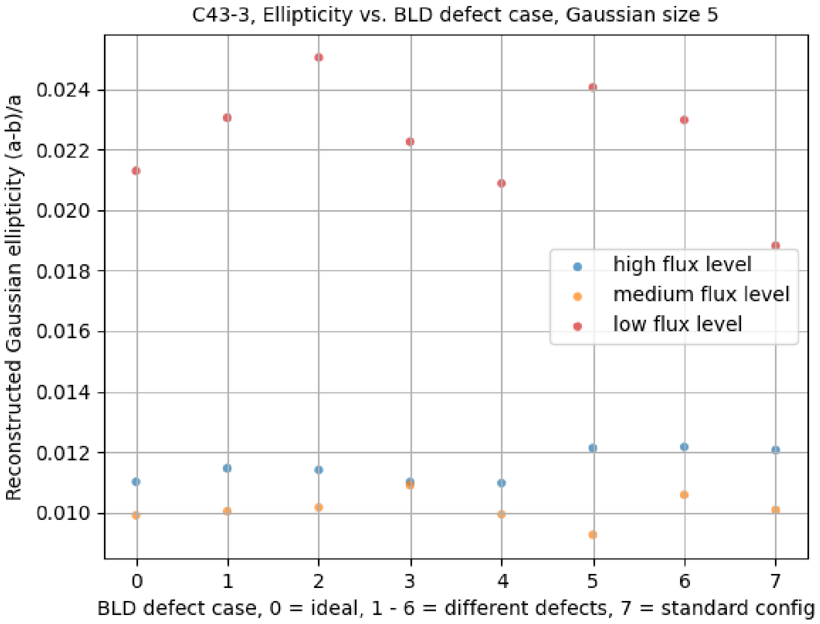

Figure 4.63: The ellipticity of the reconstructed Gaussians (expectation value is zero) for Gaussian size 5 (i.e. the second-largest Gaussian) for base config C43-3, plotted vs. the BLD case. For technical reasons the cases are numbered 0 - 7 instead of A - G, I.

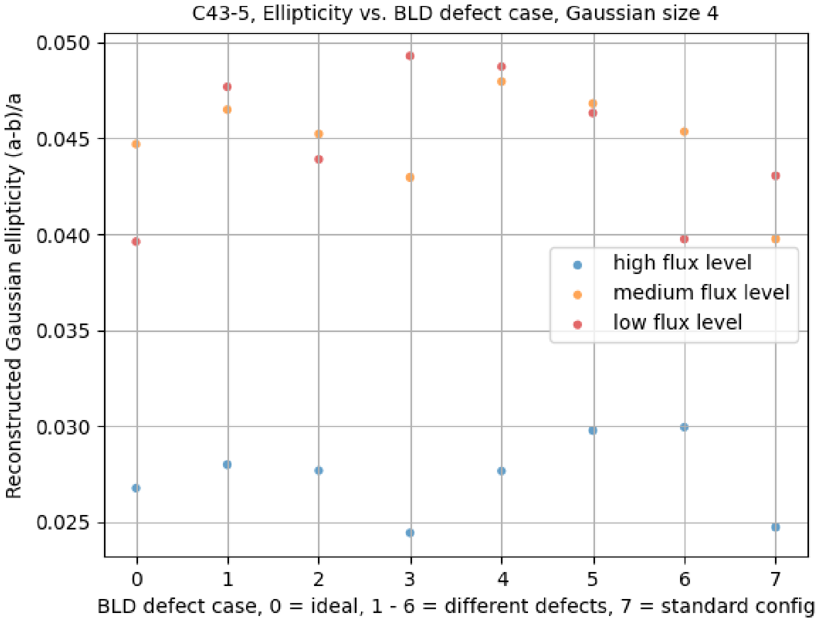

Figure 4.64: The ellipticity of the reconstructed Gaussians (expectation value is zero) for Gaussian size 4 (i.e. the fourth-smallest Gaussian) for base config C43-5, plotted vs. the BLD case. For technical reasons the cases are numbered 0 - 7 instead of A - G, I.

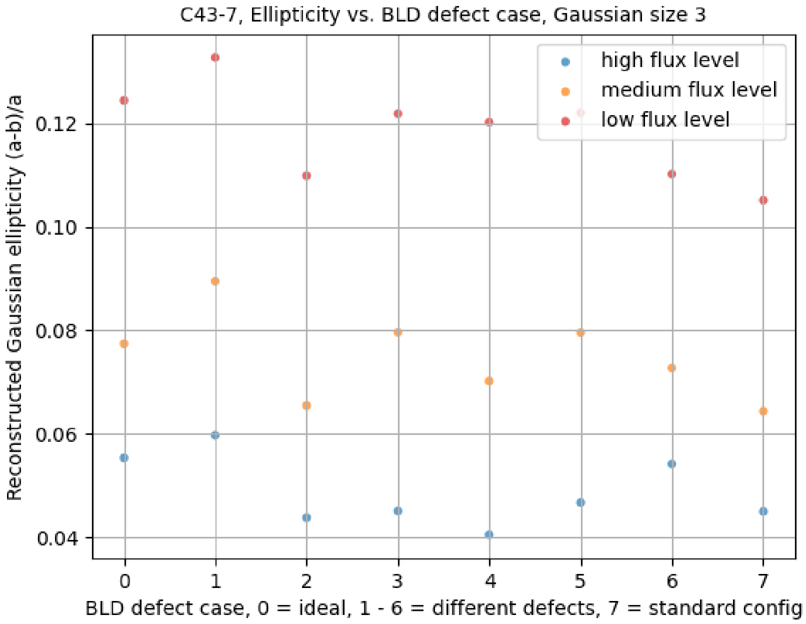

Figure 4.65: The ellipticity of the reconstructed Gaussians (expectation value is zero) for Gaussian size 3 (i.e. the third-smallest Gaussian) for base config C43-7, plotted vs. the BLD case. For technical reasons the cases are numbered 0 - 7 instead of A - G, I.

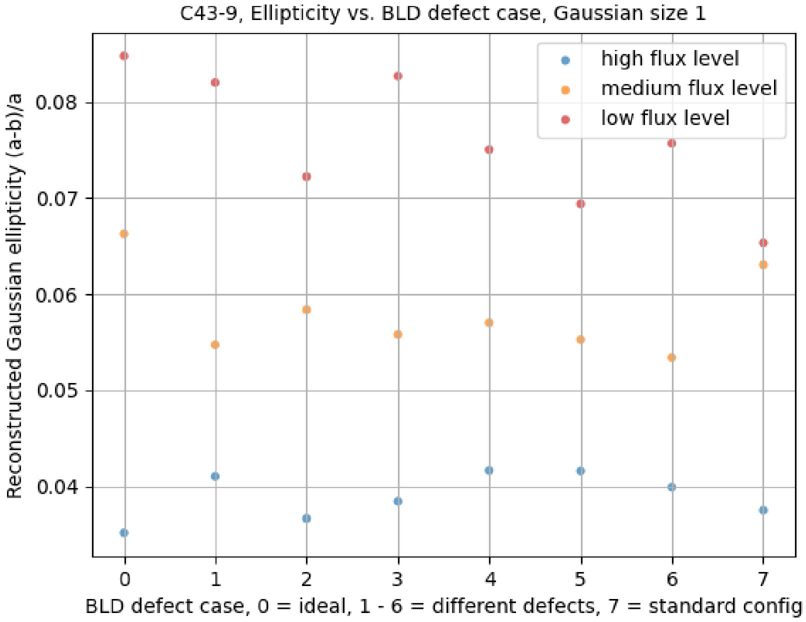

Figure 4.66: The ellipticity of the reconstructed Gaussians (expectation value is zero) for Gaussian size 1 (i.e. the smallest Gaussian) for base config C43-9, plotted vs. the BLD case. For technical reasons the cases are numbered 0 - 7 instead of A - G, I.

4.4.4 Fidelity

We study the fidelity of the deconvolved images by defining

$$\text{fidelity} = |\text{reference}|/|\text{reference} - \text{image}| + 1$$

In the CASA task "immath", this corresponds to the "expr" value

```
abs(IM1)/abs(IM1 - IM0)+1.
```

The "reference" image is the original simulation input image regridded to the same resolution as the deconvolved image.

Fig. 4.67 shows a map of the (natural) log of this fidelity for the native ALMA configuration C43-5 (case I) while the subsequent plots Figs. 4.68 - 4.74 show the corresponding fidelity maps for C43-5 BLD cases A - G. The figures show the natural logarithm of the fidelity. So 1.0 means a discrepancy to the reference of 58%, 2.0 a discrepancy of 16%, 3.0 a discrepancy of 5%, 6.0 a discrepancy of 0.2%.

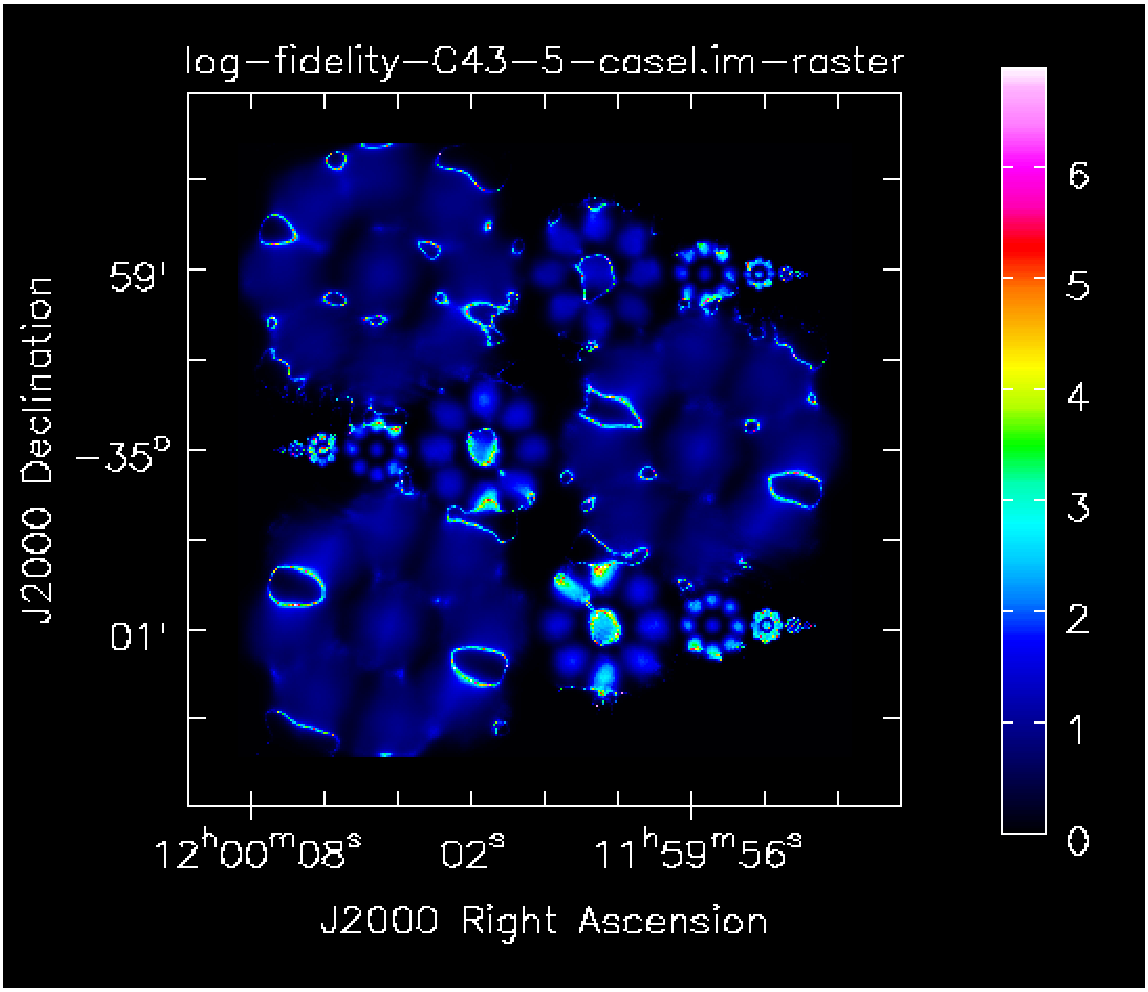

Figure 4.67: The log image fidelity of the cleaned image for config **C43-5 BLD case I**, i.e. the native ALMA configuration without modification, w.r.t. the simulation input image regridded to the same resolution.

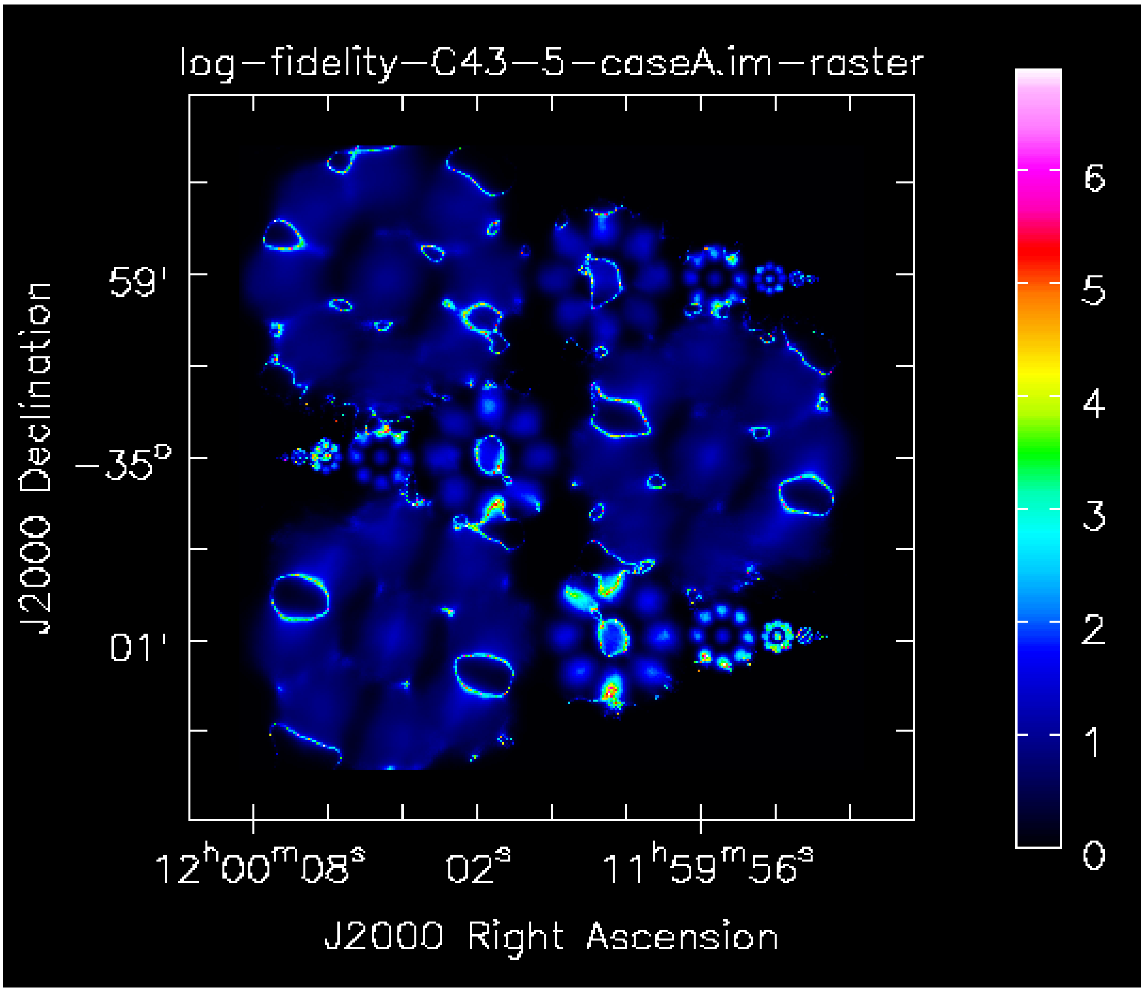

Figure 4.68: The log image fidelity of the cleaned image for config **C43-5 BLD case A** w.r.t. the simulation input image regridded to the same resolution.

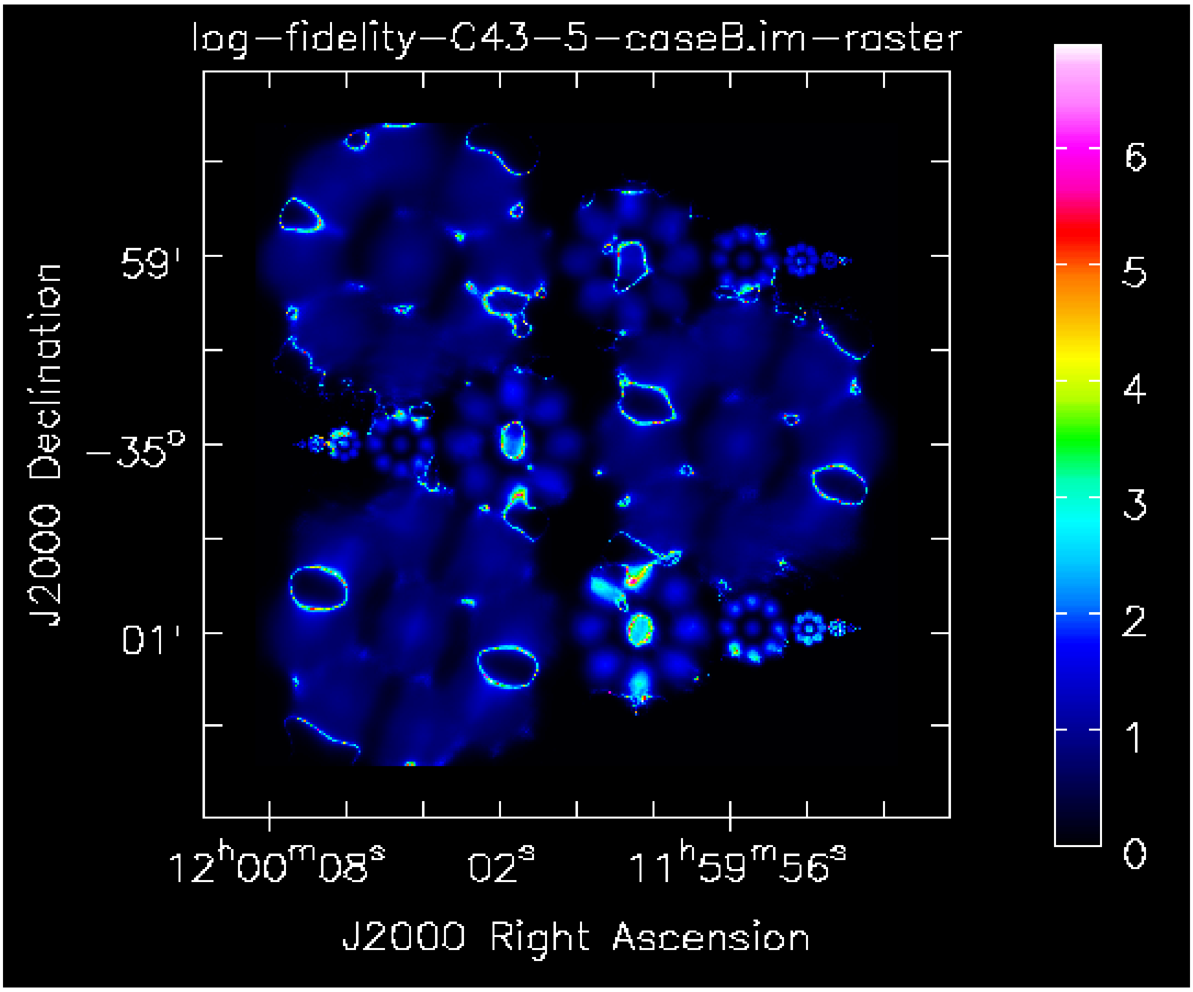

Figure 4.69: The log image fidelity of the cleaned image for config **C43-5 BLD case B** w.r.t. the simulation input image regridded to the same resolution.

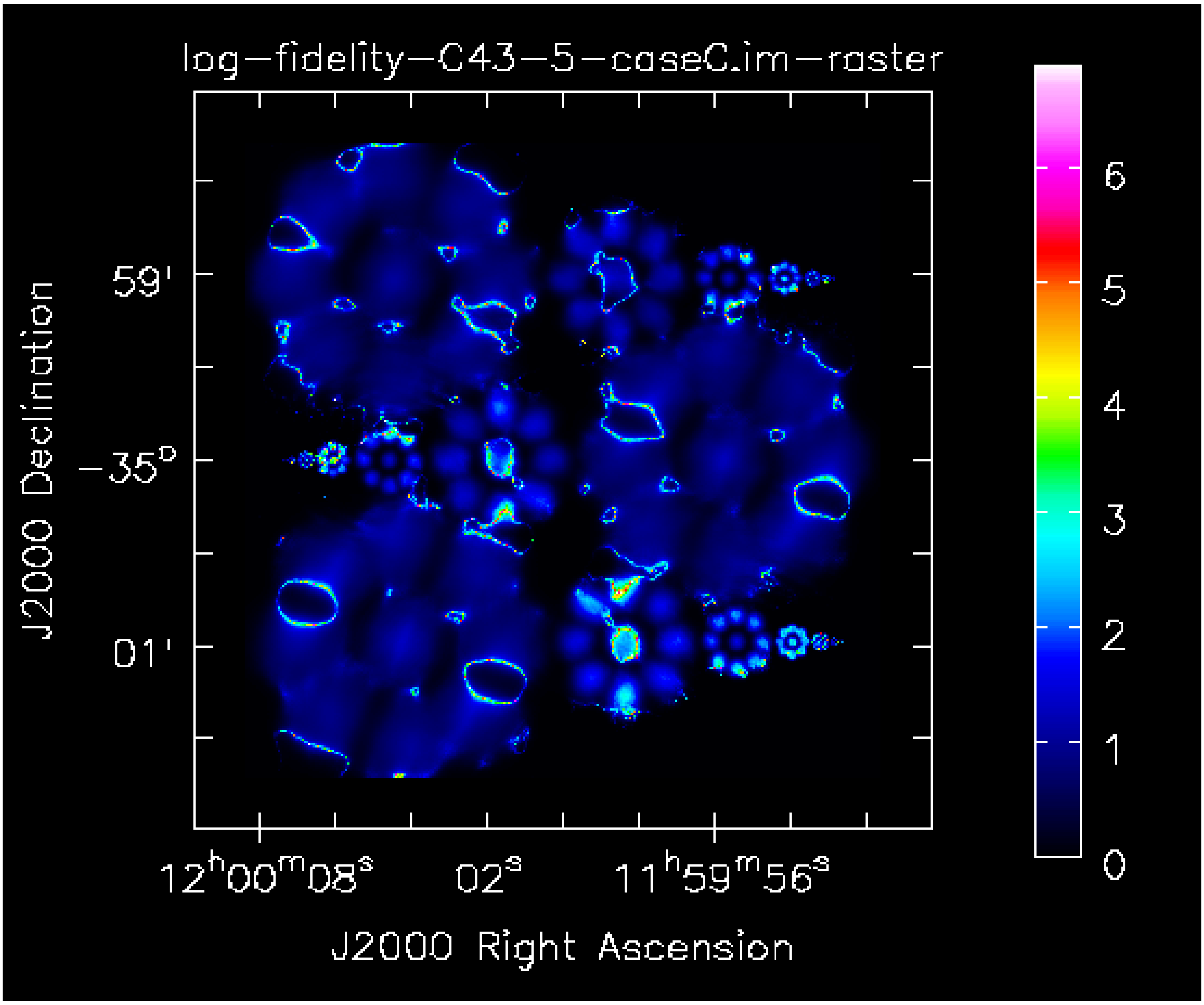

Figure 4.70: The log image fidelity of the cleaned image for config **C43-5 BLD case C** w.r.t. the simulation input image regridded to the same resolution.

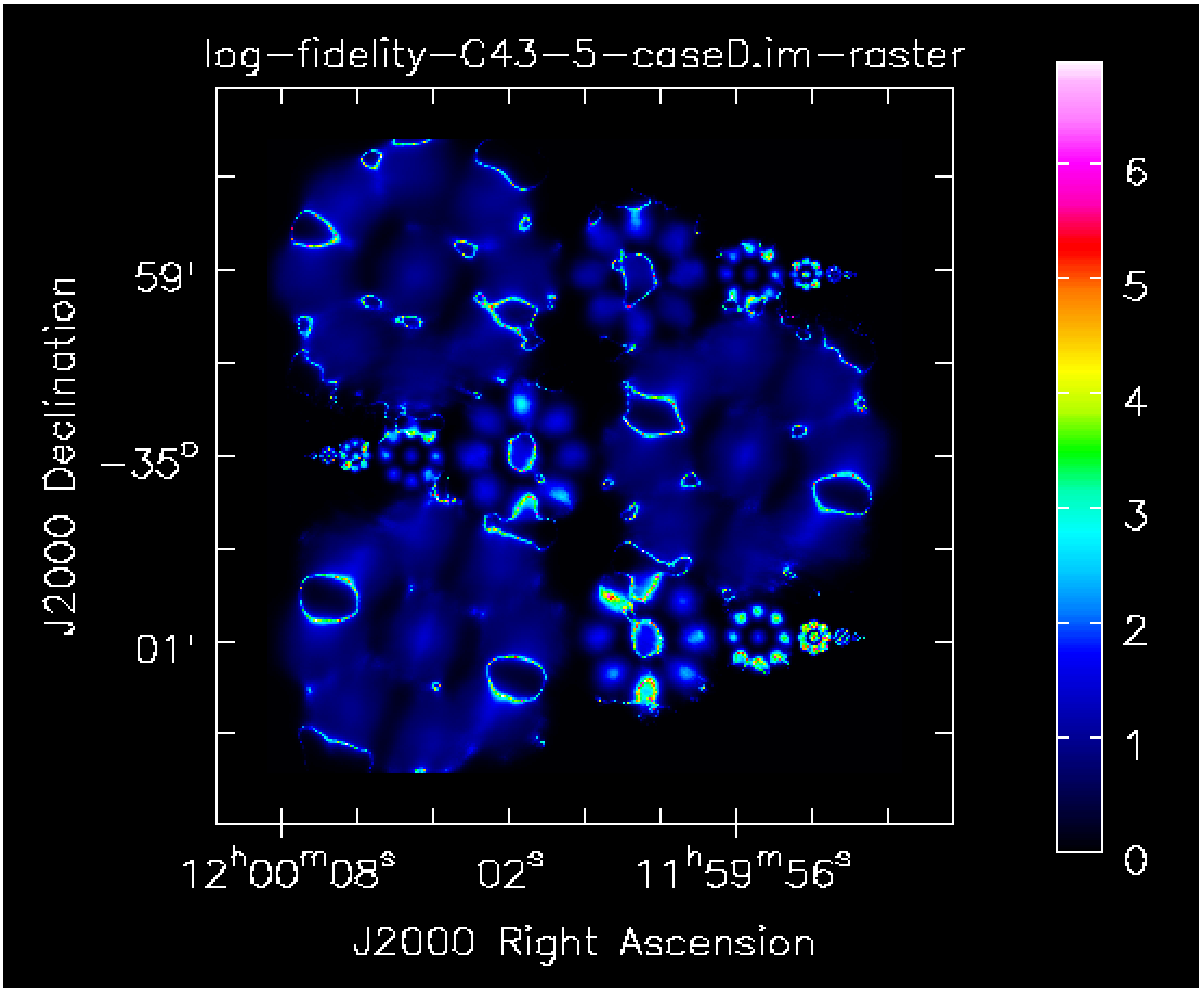

Figure 4.71: The log image fidelity of the cleaned image for config **C43-5 BLD case D** w.r.t. the simulation input image regridded to the same resolution.

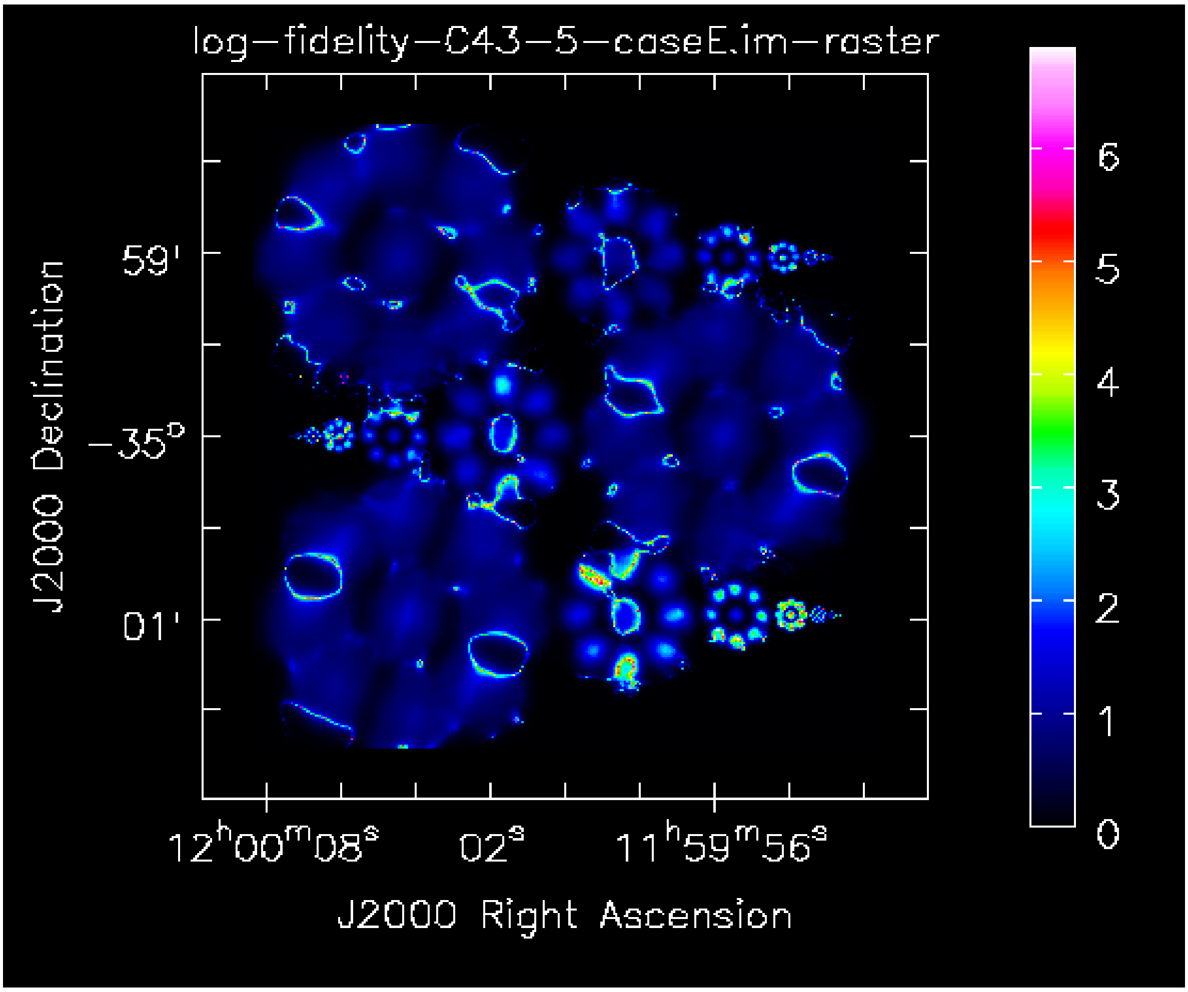

Figure 4.72: The log image fidelity of the cleaned image for config **C43-5 BLD case E** w.r.t. the simulation input image regridded to the same resolution.

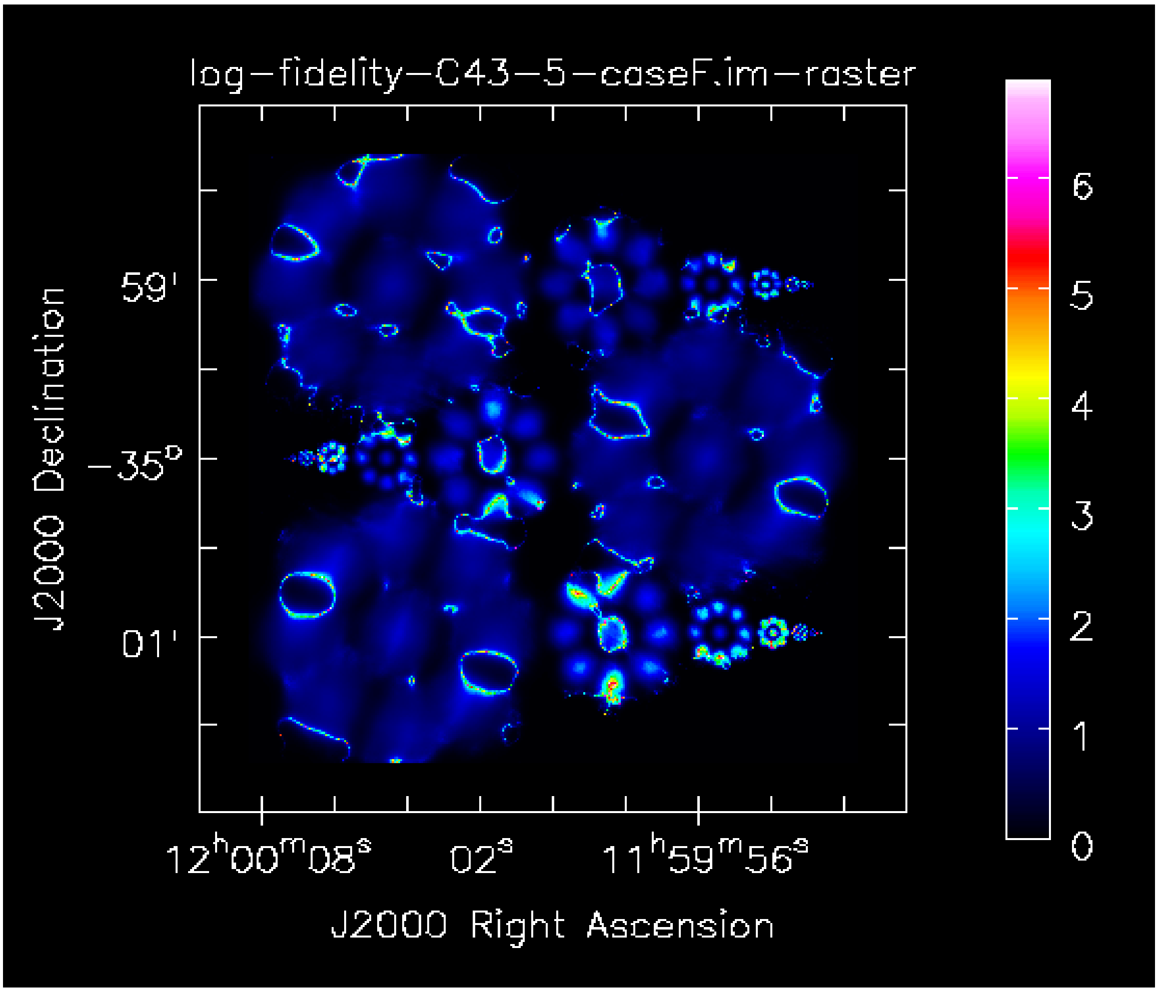

Figure 4.73: The log image fidelity of the cleaned image for config **C43-5 BLD case F** w.r.t. the simulation input image regridded to the same resolution.

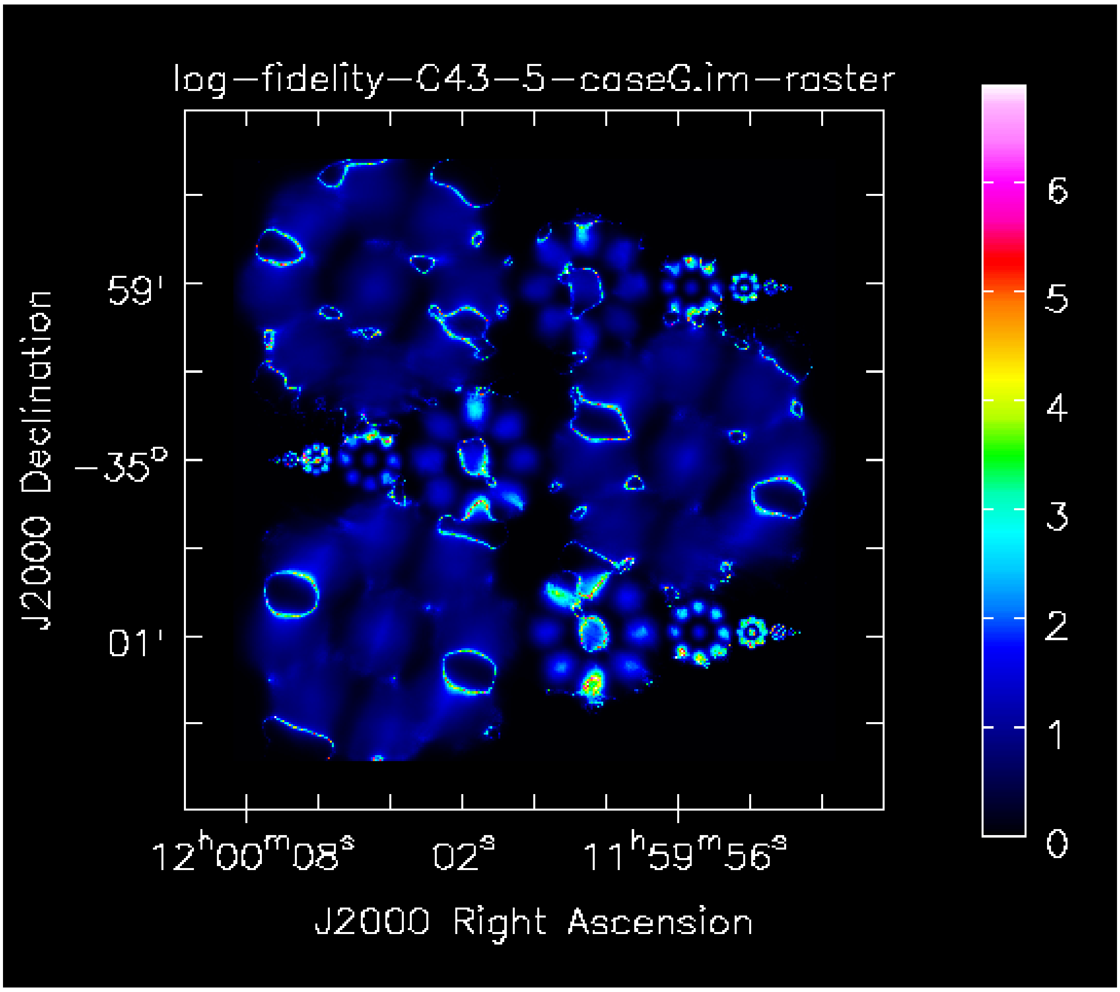

Figure 4.74: The log image fidelity of the cleaned image for config **C43-5 BLD case G** w.r.t. the simulation input image regridded to the same resolution.

4.5 Discussion - impact of BLD shape on imaging

The aim of this sub-study was to quantify the impact of deviations of the BLD shape from the ideal on the final imaging product, i.e. the deconvolved image as it would be delivered to the ALMA user.

As described in sections 4.1 - 4.3, we have investigated the *impact of deformations of the BLD shape of the order of 40% (corresponding to the standard QA2 sensitivity margin of ca. 20%) in different BL ranges* on the PSF shape and the flux, position, and shape reconstruction of Gaussian shaped objects over a range of flux (i.e. SNR) levels and the essentially full range of angular scales accessible to ALMA in a realistic setting of a large 12-m mosaic observation at average elevations of 65° with five different base configurations: C43-1, 3, 5, 7, and 9.

For understanding the results, it is important to understand that in applying deformations to the BLD, we are *keeping the overall sensitivity constant.* This means that we are not testing what happens when we *omit* sensitivity at a certain angular scale range[3], but we are testing what happens when we *redistribute* sensitivity from one angular scale range to the rest of the BLD. So, e.g., in case B we are taking away ca. 20% sensitivity from the shortest baselines and spreading it over the longer baselines (following the ideal shape). Consequently, we are actually going to see an *improvement* in the image quality, compared to case A, for smaller angular scales! The negative effect which the BLD defect in case B introduces, is only to be expected at the large angular scales where the sensitivity was lowered. Similarly, in the other defect cases C - G, we should expect an improvement at all angular scales except the ones where the sensitivity was reduced. We demonstrate this more clearly in an additional investigation in section 4.6 below.

With respect to the PSF shape, we investigated how well it agrees with an ideal Gaussian shape and found that the BLD defects we applied do not introduce a clear deterioration of the residuals of a Gaussian fit in all base configurations (see section 4.3.2). Apparently, a change in sensitivity of ca. 20% in a range constituting ca. 20% of the total BL range is tolerable. If any deterioration is visible, it occurs mostly for defects at the lower end of the BLD, i.e. cases B and C (see figures 4.33 - 4.37).

In agreements with the findings concerning the PSFs and the theoretical expectations described above, the results presented in section 4.4 demonstrate that the *impact of the introduced BLD defects on the image quality is small*, especially for the highest flux level. While of course the reconstruction accuracy for a given Gaussian size and flux depends strongly on the base configuration used, the BLD shape deformations we applied did not change the reconstruction parameters significantly. Also the image fidelity does not seem to change systematically with the deformations.

We attribute this result also to the fact that the image deconvolution with CASA has now reached a sufficiently sophisticated level to be able to make up for BLD defects of the order of 40% as investigated here. This is good news for ALMA as it means that defects of this order in the observations can be accommodated by offline analysis.

We must caution however, that we have only studied a test case which is made up of relatively benign geometrical shapes. Astronomical objects with more complex shapes containing sharper features will be more difficult to deconvolve and the better the PSF, the more one will be able to trust the deconvolution result.

---

[3] It is clear that the image quality deteriorates when you reduce overall sensitivity. And a reduction in overall sensitivity would not pass the present standard QA2. The question we are trying to answer is about the right *relative* sensitivity between angular scale ranges.

Our result could therefore be used for defining a limiting case of still acceptable BLD shapes: the missing visibility seconds in an individual BL histogram bin should not amount to more than 40% in the intermediate BL bins, i.e. in bins 2 - 9 the filling fraction could be required to be $\geq$ 60% if the imaging quality is important for the science goal.

In this context it also needs to be mentioned that the "analytical" BLD shape approximates the ALMA C6/7 configurations but with certain deviations, in particular a certain underexposure in the intermediate bins which corresponds roughly to our case F. This will need to be taken into account when defining the limiting case for operations.

Another aspect which we were not able to study here in detail is the possibility of adjusting a mal-shaped BLD by *offline reweighting*, i.e. adjusting the WEIGHT column of the MS based on the filling fraction value for the BL bin of the given visibility. This will of course come at the cost of a loss of overall sensitivity but some first attempts showed very promising results and we recommend to further look into this possibility in a future study. Software prototypes are included in the `assess_ms` and `thinms` modules (see appendix B).

4.6 Sanity check with more extreme BLD defects

Given that the defects introduced in cases B - G only had mild consequences on image quality, we extended the study to a more extreme set of cases where we double the size of the defect. We name these new BLD defect cases B2 - G2:

BLD Case B2: "analytical" shape but 80% reduced in bins 1 and 2 of the ten equidistant bins of the QA metric (as defined in 3.3) from zero to the max. BL.

BLD Case C2: like Case B2 but 80% reduced in bins 3 and 4 instead of 1 and 2.

BLD Case D2: like Case B2 but 80% reduced in bins 5 and 6 instead of 1 and 2.

BLD Case E2: like Case B2 but 80% reduced in bins 7 and 8 instead of 1 and 2.

BLD Case F2: "analytical" shape but 40% reduced in bins 3, 4, 5, 6.

BLD Case G2: "analytical" shape but 60% reduced in bins 3, 4, 5, 6.

With these case definitions, we only study one base configuration, C43-7, in order to keep the parameter space small for this "sanity check". The MeasurementSets for the cases were obtained using otherwise the same procedures as for cases B - G and also the subsequent evaluation was done the same way. Figures 4.75 - 4.77 show the BLDs of the six new cases (plotted in blue) compared to the ideal BLD shape which corresponds to the original case A. Note that these plots use the non-equidistant binning as described in section 3.1 in order to show more details on the short spacings.

In the following we concentrate on the relative flux error of the reconstruction of the Gaussian objects in the input image as a tracer of overall image reconstruction quality.

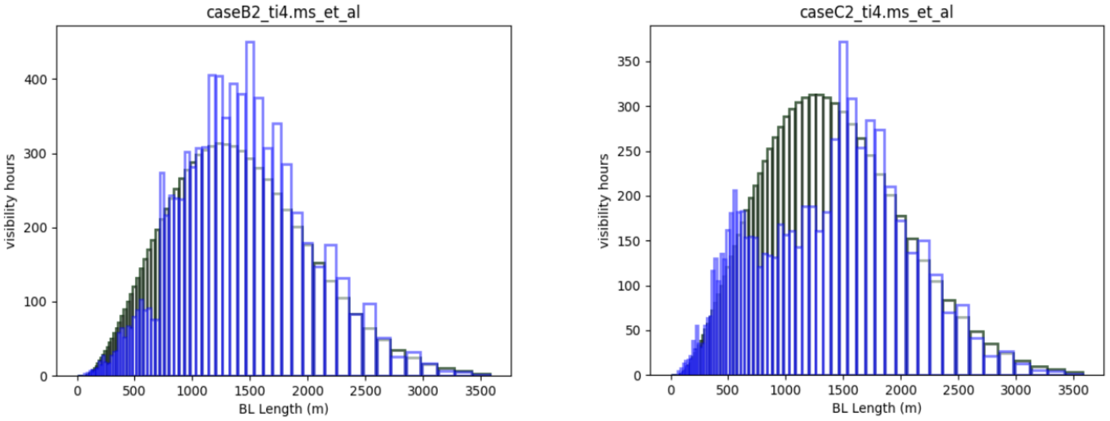

Figure 4.75: Left: The BLD for the ideal case (black), which corresponds to C43-7 case A, and for **C43-7 case B2** (blue). Right: Same as on the left but blue is config **C43-7 BLD case C2**.

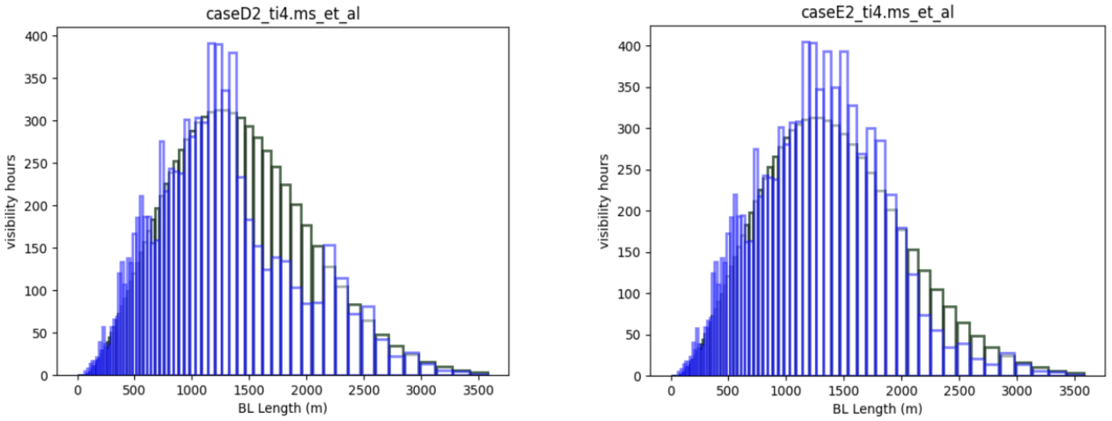

Figure 4.76: Left: The BLD for the ideal case (black), which corresponds to C43-7 case A, and for **C43-7 case D2** (blue). Right: Same as on the left but blue is config **C43-7 BLD case E2**.

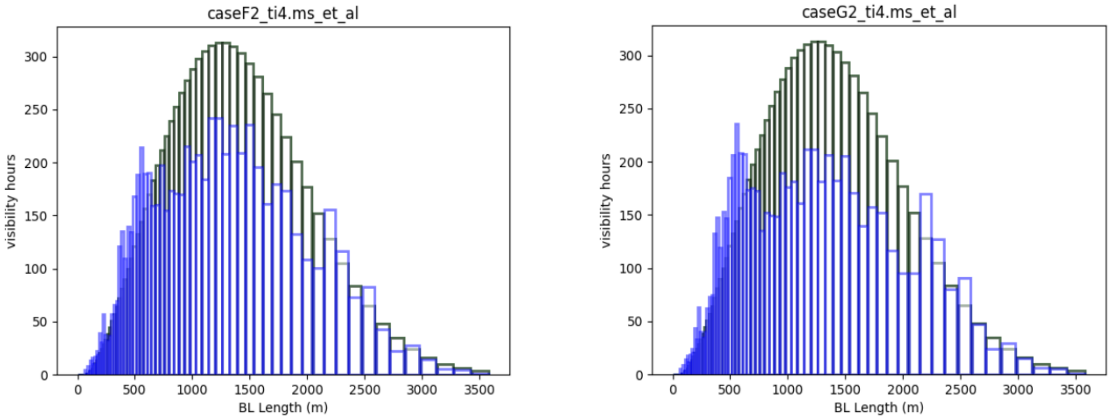

Figure 4.77: Left: The BLD for the ideal case (black), which corresponds to C43-7 case A, and for **C43-7 case F2** (blue). Right: Same as on the left but blue is config **C43-7 BLD case G2**.

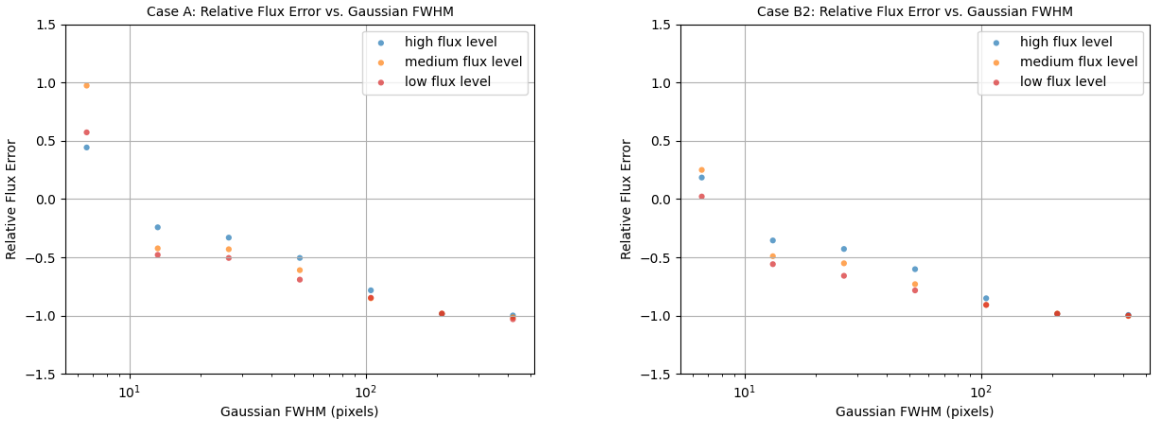

Figure 4.78: Left: The relative flux reconstruction error (measured flux - original flux)/original flux for config **C43-7 BLD case A** (same as the left side of fig. 4.41, repeated here for convenience). Right: The same but for config **C43-7 BLD case B2**.

Figure 4.78 shows the relative flux error obtained with the original C43-7 case A (plotted vs. the angular size of the Gaussian) and the same for the new case B2 described above. As one would expect from a lowering of the sensitivity at the shorter baselines, the relative flux error is worse for all Gaussians except the smallest one. For the smallest Gaussian, on the other hand, the reconstruction has greatly improved since sensitivity was redistributed to these scales. The two largest Gaussians are not reconstructed at all because the configuration does not have any sensitivty at these scales, and that does not change when we switch from case A to case B2.

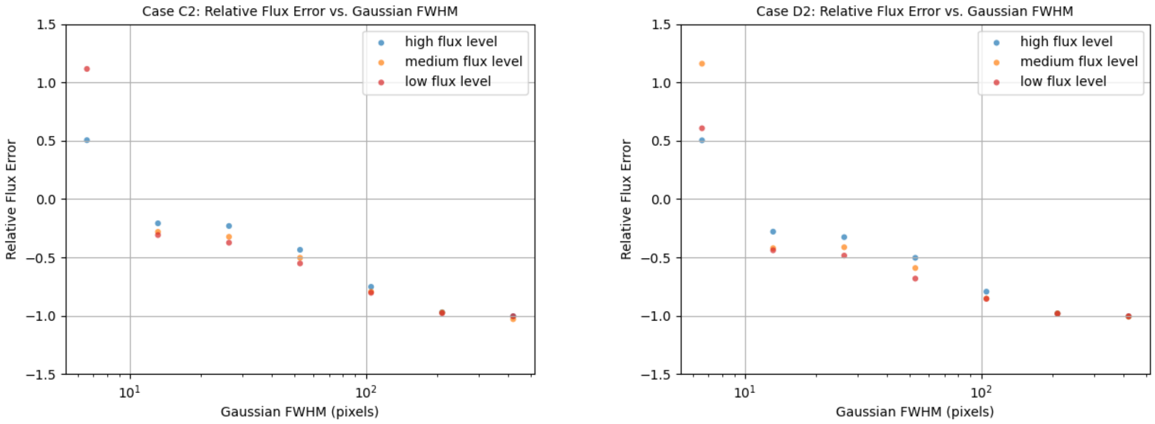

Figure 4.79: Left: The relative flux reconstruction error (measured flux - original flux)/original flux for config **C43-7 BLD case C2**. Right: The same but for config **C43-7 BLD case D2**.

Figures 4.81 and 4.80 show the corresponding plots for cases C2 - E2. Also they can be understood like the plot for case B2. As the defect wanders up in baseline length (down in angular scale), the larger Gaussians are reconstructed better.

Finally, for cases F2 and G2, which are not a continuation of the B2, C2, D2, E2 sequence but are two cases with a broad defect at intermediate BLs (G2 is 50% deeper than F2), we see that the corresponding strong improvement of the sensitivity at the shorter baselines below the defect leads to a small improvement in the reconstruction of the Gaussians 4, 5, and 6 (the second,

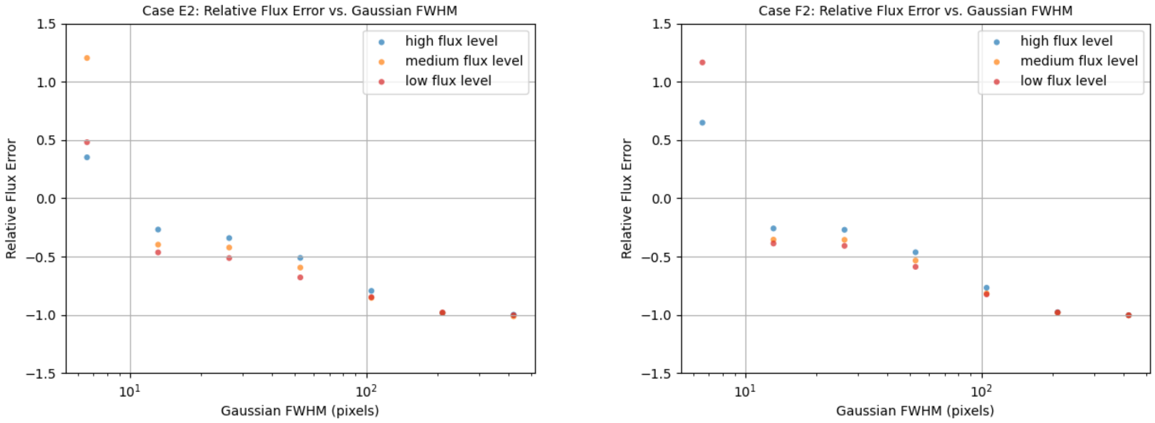

Figure 4.80: Left: The relative flux reconstruction error (measured flux - original flux)/original flux for config **C43-7 BLD case E2**. Right: The same but for config **C43-7 BLD case F2**.

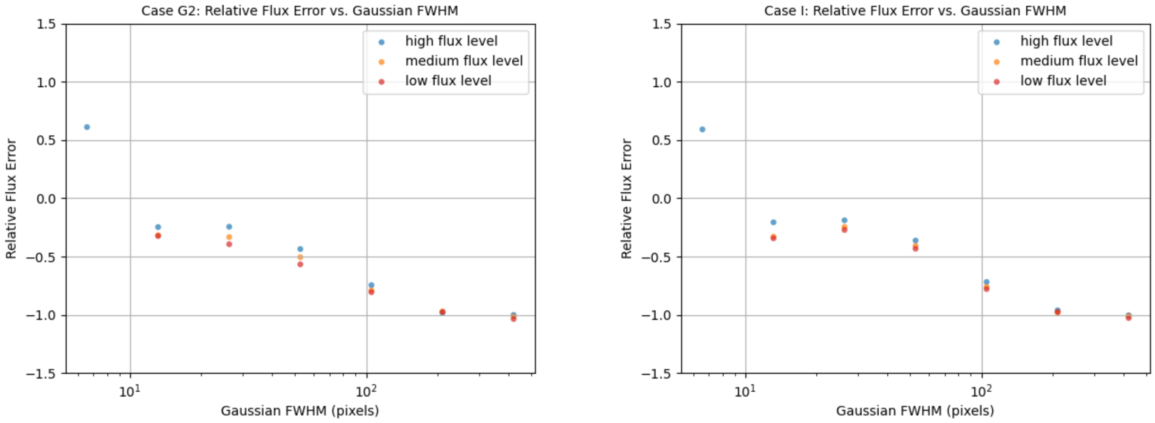

Figure 4.81: Left: The relative flux reconstruction error (measured flux - original flux)/original flux for config **C43-7 BLD case G2**. Right: The same but for config **C43-7 BLD case I**, i.e. the unmodified ALMA configuration.

third, and fourth smallest). The smallest Gaussian is not reconstructed well and not at all for the two fainter flux levels.

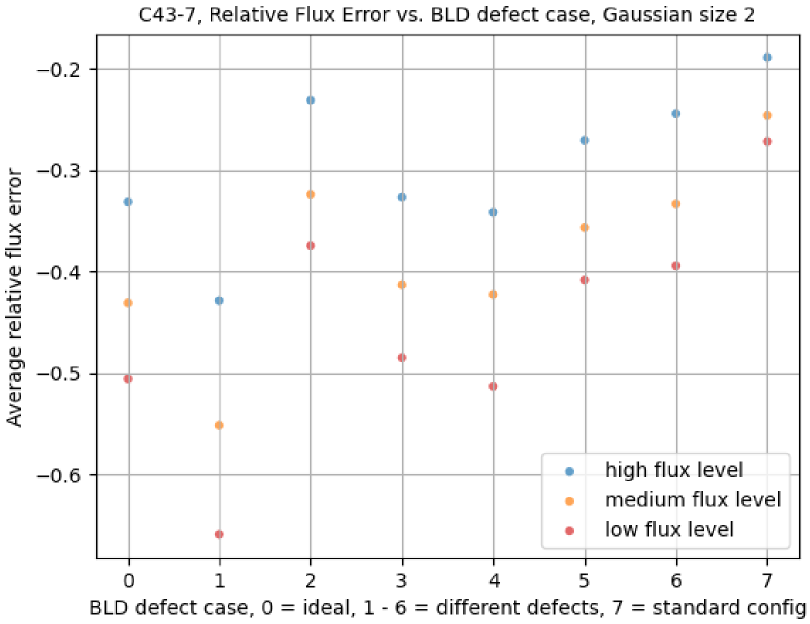

Figure 4.82: The relative flux reconstruction error (measured flux - original flux)/original flux for Gaussian size **2** (i.e. the second-smallest Gaussian) for base config C43-7, plotted vs. the BLD case. For technical reasons the cases are numbered 0 - 7 instead of A, B2, C2, D2, E2, F2, G2, I.

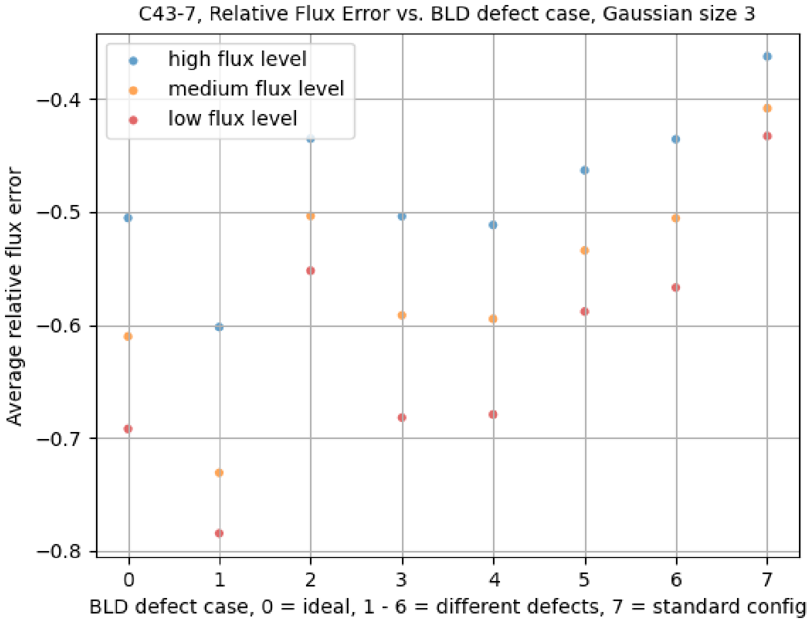

Figure 4.83: The relative flux reconstruction error (measured flux - original flux)/original flux for Gaussian size **3** (i.e. the third-smallest Gaussian) for base config C43-7, plotted vs. the BLD case. For technical reasons the cases are numbered 0 - 7 instead of A, B2, C2, D2, E2, F2, G2, I.

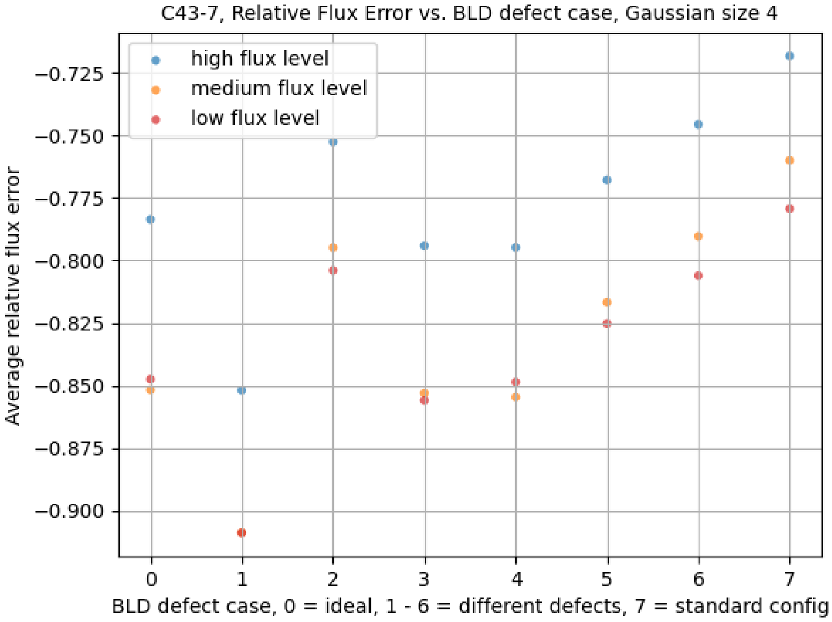

Figure 4.84: The relative flux reconstruction error (measured flux - original flux)/original flux for Gaussian size **4** (i.e. the fourth-smallest Gaussian) for base config C43-7, plotted vs. the BLD case. For technical reasons the cases are numbered 0 - 7 instead of A, B2, C2, D2, E2, F2, G2, I.

Figures 4.82 - 4.84 show the relative flux error again for a fixed Gaussian size (second smallest, third smallest, and fourth smallest respectively) as a function of defect case. For all three Gaussian sizes, case B2 (= 1 on the horizontal axis in the plots), which is the case of a strong lack of sensitivity at the shortest baselines, deteriorates the reconstruction the most.
Case C2 (=2), which under-emphasizes the baselines near the peak of the ideal BLD, performs best, while D2 and E2 (3 and 4) perform essentially like A for the angular scales relevant for these three Gaussian sizes. F2 and G2, the cases of a broader flattening of the BLD, also perform better than A but not quite as good as C2.
This indicates that there may still be an opportunity to further tune our ideal BLD shape. To judge this better we also need to look again at the PSF sidelobe levels (and it should also be followed up in a future study using more complex input images as already mentioned in the previous section). The sidelobes can be seen for cases B2 - E2 in comparison to cases B - E in figures 4.85 to 4.88. The deterioration from the doubling of the defect size is clearly visible and especially large for B2 and C2. The shorter spacings are particularly crucial for PSF health. Figure 4.89 shows again for comparison the PSFs of the ideal and the native BLD. Of all BLDs shown in this section, the ideal BLD (case A) has the most Gaussian PSF. Performance in terms of flux recovery can only be improved over "A" at the expense of worsening the PSF.

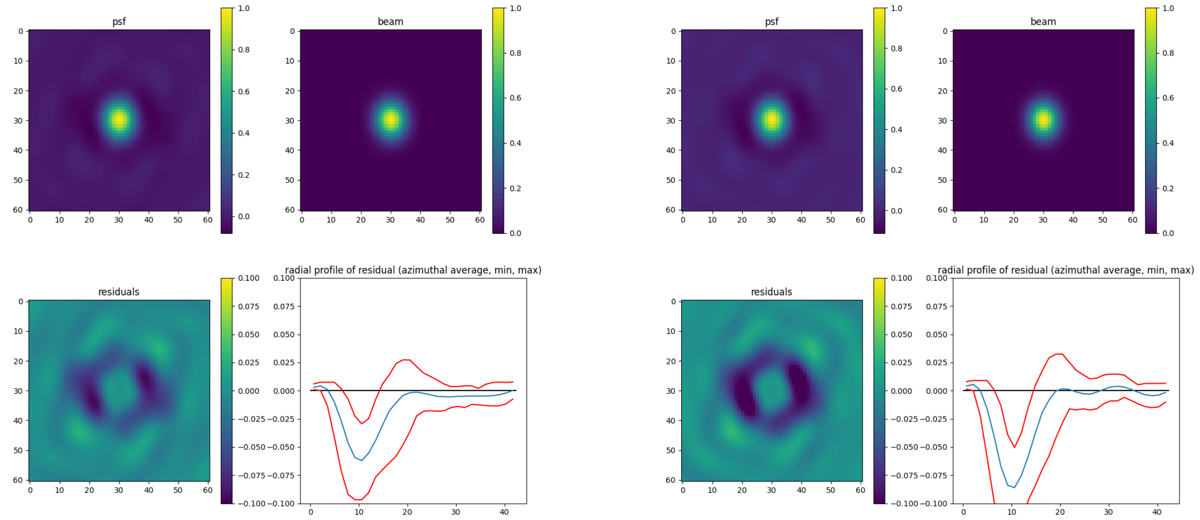

Figure 4.85: PSF, 2D Gaussian fit (beam), the fit residual, and the radial profile of it: **left:** for config C43-7, BLD case "B"; **right:** or config C43-7, BLD case "B2".

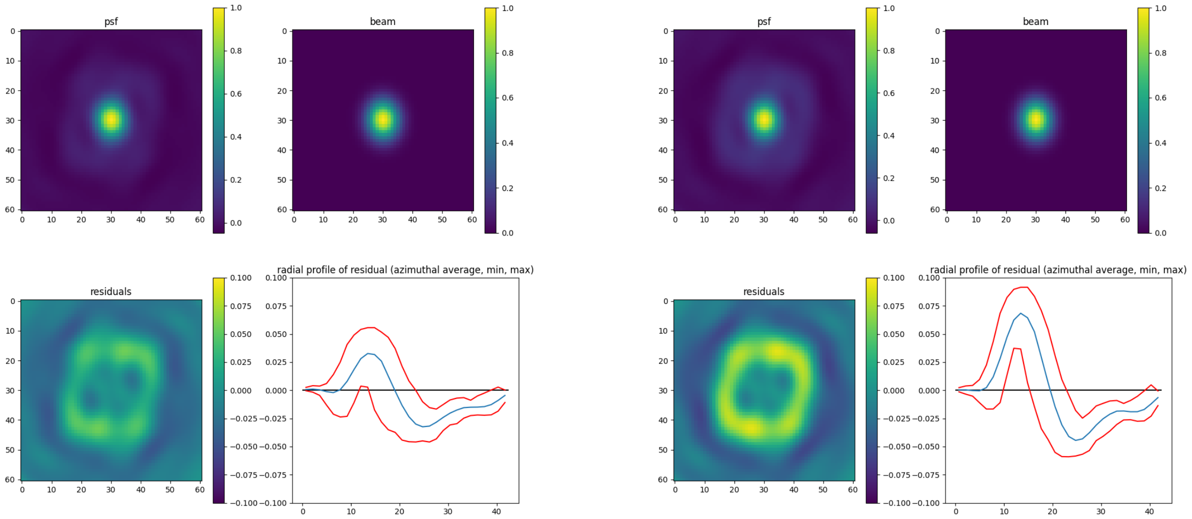

Figure 4.86: PSF, 2D Gaussian fit (beam), the fit residual, and the radial profile of it: **left:** for config C43-7, BLD case "C"; **right:** or config C43-7, BLD case "C2".

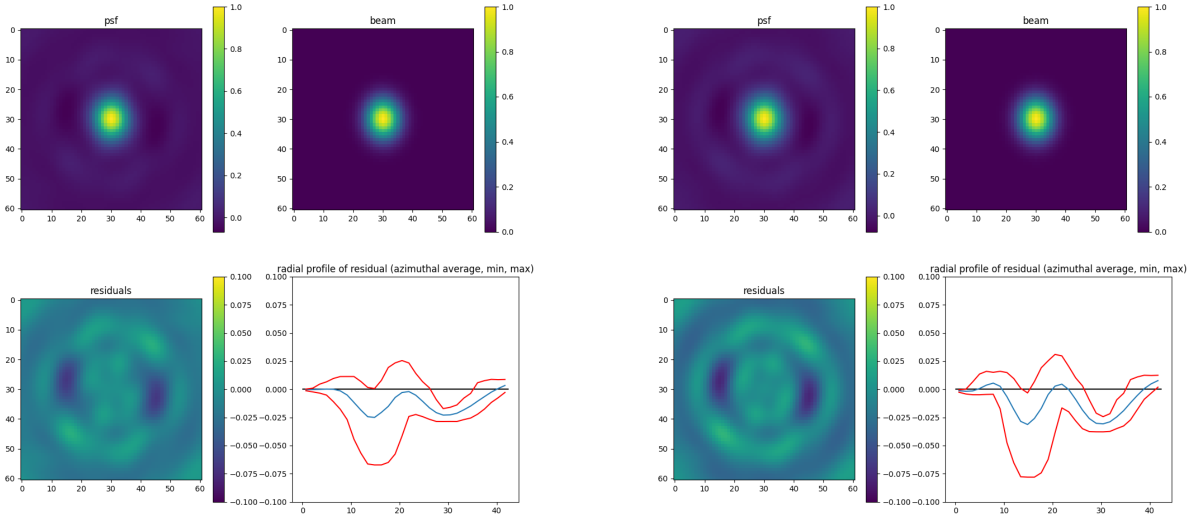

Figure 4.87: PSF, 2D Gaussian fit (beam), the fit residual, and the radial profile of it: **left:** for config C43-7, BLD case "D"; **right:** or config C43-7, BLD case "D2".

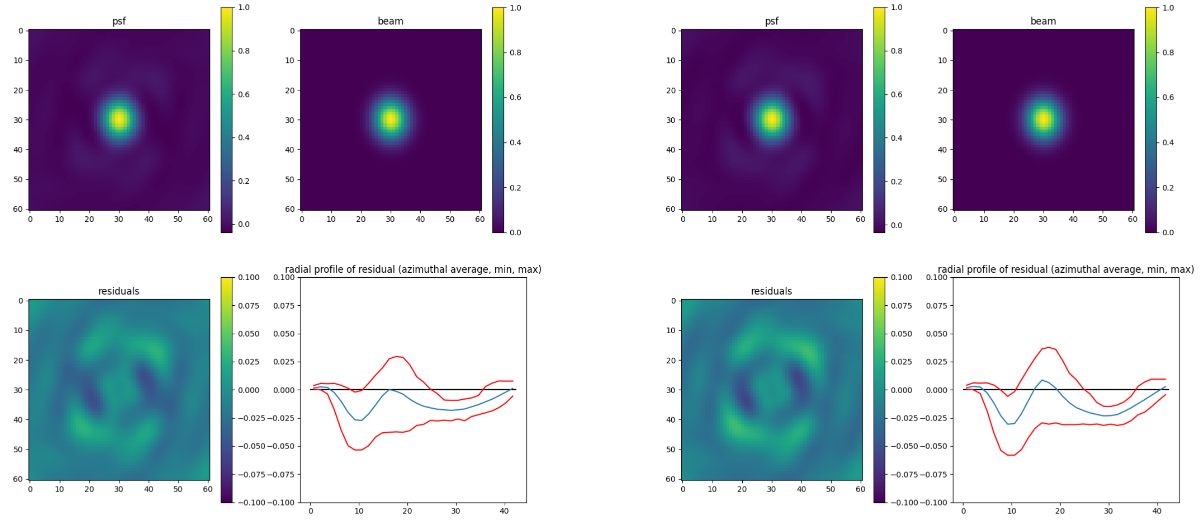

Figure 4.88: PSF, 2D Gaussian fit (beam), the fit residual, and the radial profile of it: **left:** for config C43-7, BLD case "E"; **right:** or config C43-7, BLD case "E2".

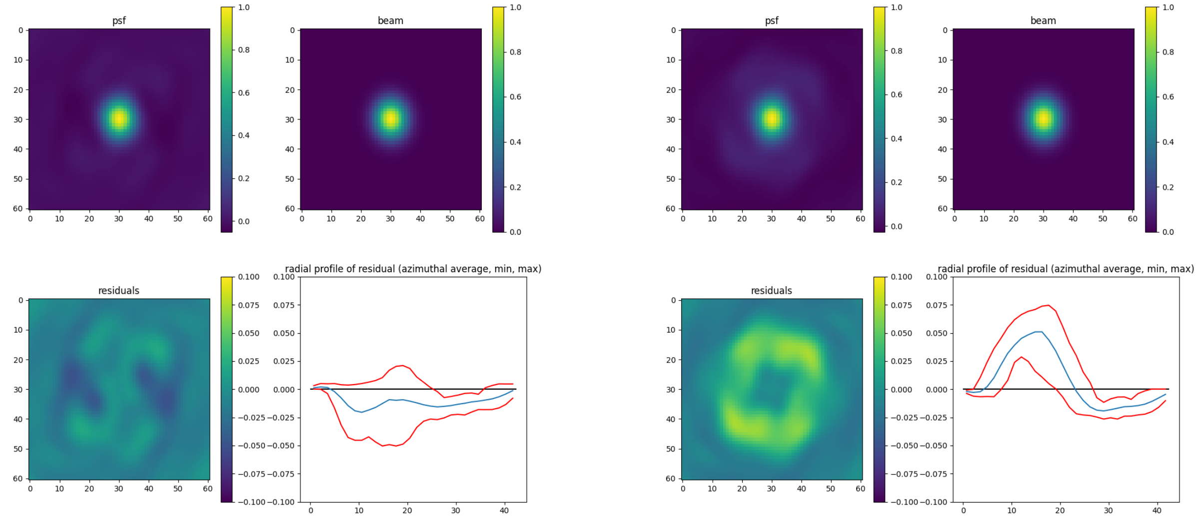

Figure 4.89: PSF, 2D Gaussian fit (beam), the fit residual, and the radial profile of it: **left:** for config C43-7, BLD case "A"; **right:** or config C43-7, BLD case "I". These two figures were already shown in figures 4.25 (left) and 4.28 (right) and are shown here again for conveniently comparing them to the figures above.

5 Development of a BLD assessment tool: "assess_ms"

One of the main goals of this study was to develop a prototype for a software tool to judge the quality of the uv coverage of a given observation. With "assess_ms" we have developed such a tool. It offers already a quite wide range of functionality and serves to demonstrate how such a tool could be used in operations. The main point it is still lacking is the full handling of the T_{sys} information (in order to achieve a full implementation of the "Execution Fraction" as it is used in scheduling). Once the detailed tuning of the QA parameters for failing an MOUS because of its BLD is completed, they can be inserted in this tool and used in production.

5.1 Requirements for assess_ms

1. Since the tool will handle MSs, it is best to implement it as a CASA Python module. The tools is then a call to a function/method of that module from the CASA command line.

2. The tool is to take a set of calibrated MSs which belong to a given observation, e.g. a set of uncalibrated MSs from an incomplete MOUS during scheduling, or a single MS in QA0, or the calibrated MSs for a fully observed MOUS in the QA2 context, and analyse their BLD to determine whether it is sufficiently near to the expectation. The expectation is defined by the science goal parameters AR, LAS, and exposure time.

3. While the LAS is a single number, the AR is typically specified by the user as range of acceptable values, i.e. AR_{min} and AR_{max}.

4. Since the determination of the expected BLD has some computational cost and only a limited number of histograms can be plotted on top of each other, we want to perform the expectation calculation only at discrete values of the AR which we want to specify explicitly on the command line.

5. Since the L80 (defined as the 80th percentile of the BL distance in meters) still plays an important role in the scheduling context, we want to be able to compute it automatically and add the corresponding AR to the list of ARs to test. (In our study, it turned out that the L80 is indeed a good estimator of the AR when using our "analytical" BLD shape.)

6. If an MOUS has multiple targets, we need to inspect only one target at a time, i.e. also the target name needs to be specified, the representative target.

7. Since we are only interested in testing the shape of the BLD, we also need to inspect only one spectral channel at a time, i.e. also a reference frequency needs to be specified which would typically be the center of the representative spectral window. Strong differences between the BLDs of different channels can only be caused by extensive flagging and that would in turn be caught by the sensitivity requirements imposed by QA2.

8. For a QA0/2_PASS decision, we want the user to be able to choose between different criteria (conditions) to be applied with a default (the standard QA2_PASS condition).

9. The user should be able to select between different ways of calculating the expected BLD shape: our "analytical" and our "FD" method, the former being the default.

10. MSs have a high data volume and there are situations where a user may want to re-assess a given observation without having to keep the MSs on disk which belong to it. We therefore need a functionality to store the observed BLDs as histogram objects in a file and re-load them in a new assess_ms session.

11. The tool should produce intelligible log output both in the CASA logger and in the terminal.

12. The tool should produce diagnostic BLD plots as png files which can be included in web pages.

13. The plots and all other file output should be stored in a given directory, the "storage directory".

14. For test purposes, it should be possible to disable the application of weights in the determination of the observed BLD.

All these requirements are fulfilled by our present implementation. See the next section.

5.2 Implementation of assess_ms

Throughout this study and also for this tool we have used CASA 6, i.e. Python 3. assess_ms was implemented as a standard CASA Python application similar to the "analysisUtils" or the calibration script generator "almaqa2csg". It works both under CASA 5.8 and 6.1 and is under version control in the JAO CVS repository. Present version (7 July 2021) is 1.40. The detailed list of functions in the module and their parameters is given in Appendix B. A usage example which also shows the plots is given in section 5.3.

Histogramming and plotting is completely based on our "mshistotools" module which in turn is based on matplotlib. mshistotools implements histogramming in an object-oriented way defining 1D and 2D histogram objects (see Appendix B).

Noteworthy implementation details of assess_ms concern the determination of the histogram binning, the handling of multiple input MSs, and the handling of previously stored BLDs.

Concerning the determination of the binning, the longest baseline of the observation needs to be determined. In the case of multiple input MSs, this means that before any histogramming can take place, all MSs need to be opened and the longest baseline needs to be found. Based on

that, the common binning for the joint BLD can then be set. Then all MSs need to be opened again to actually perform the filling of the BLD histogram.
However, for the determination of the ten bins for the calculation of the filling fractions, the upper edge of the highest bin must be determined from the maximum baseline length *of the expectation*. Observed baselines longer than that maximum expected baseline are thus ignored in the shape assessment, i.e. treated as an added bonus - an important feature of our method.
Internally, both a fine-binned version of histograms and the more coarse display version of the histograms is kept.
In the case of multiple MSs, care needs to be taken in the field selection since the Field ID of the science target may be different between MSs when certain calibrators are present or absent. Selection needs to use names.
The storage of histogram objects is implemented via pkl files. This has worked very well and enabled us to reprocess a large number of MOUSs, when needed, in relatively short time without having to access the MSs again.

5.3 Recommended standard usage of assess_ms in QA2

Here we show an example of how assess_ms could be used in QA2 and what it produces. As example we choose the MOUS uid://A001/X133d/X19e0 from Cycle 6 (2018.1.01055.L MWC_480_b_06_TM1). It has six QA0_PASS EBs. The acceptable range of AR values is 0.08 arcsec - 0.12 arcsec, the requested LAS is 4.0 arcsec. The representative frequency is 265.88 GHz. The planned observation time on-target is 9906 s.
This information is fed into assess_ms via the following command lines[1]:

```
from assess_ms import *
assess_ms(storagedir='uid___A001_X133d_X19e0_MWC_480_b_06_TM1_qa2',
          ar_asec_range=[0.08, 0.12], time_s=9906, las_asec=4.,
          freq_ghz=265.88, ar_asec_to_test=[0.08, 0.12],
          vis=['uid___A002_Xdfcc3f_X3b32.ms.split.cal',
          'uid___A002_Xe014a2_X3caa.ms.split.cal',
          'uid___A002_Xe014a2_X414a.ms.split.cal',
          'uid___A002_Xe03886_X11879.ms.split.cal',
          'uid___A002_Xe03886_X1781.ms.split.cal',
          'uid___A002_Xe03886_Xc8ff.ms.split.cal'])
```

The first parameter "storagedir" defines the name of the directory to be created for holding all output files.
The parameter "ar_asec_to_test" defines the AR values for which the expectation should be calculated and the comparison with the observed BLD should be performed. We typically choose the two borderline cases AR_{min} and AR_{max} and, by default, assess_ms adds the AR derived from the L80 of the observed BLD to this list (parameter "useL80" is True).
Launching the above command in CASA (in the directory containing the six MSs) then produces the following terminal output:

---

[1] Note that the contents of the JAO CVS repository directory `AIV/science/ArrayConfiguration/beamWG` needs to be in the path for the import of the modules needed by assess_ms to work.

```
    *** Begin assess_ms
Version: $Id: assess_ms.py,v 1.40 2021/07/07 09:31:15 dpetry Exp $
**** determine the binning of the expectation based on the input MSs ****
MS uid___A002_Xdfcc3f_X3b32.ms.split.cal has the longest baselines: 5883.564528585881 m
Field IDs for uid___A002_Xdfcc3f_X3b32.ms.split.cal:  [3]
**** filling observed Baseline Length Distribution histograms for EB uid___A002_Xdfcc3f_X3b32.ms.split.c
Field IDs for uid___A002_Xdfcc3f_X3b32.ms.split.cal:  [3]
**** filling observed Baseline Length Distribution histograms for EB uid___A002_Xe014a2_X3caa.ms.split.c
Field IDs for uid___A002_Xe014a2_X3caa.ms.split.cal:  [3]
**** filling observed Baseline Length Distribution histograms for EB uid___A002_Xe014a2_X414a.ms.split.c
Field IDs for uid___A002_Xe014a2_X414a.ms.split.cal:  [3]
**** filling observed Baseline Length Distribution histograms for EB uid___A002_Xe03886_X11879.ms.split.
Field IDs for uid___A002_Xe03886_X11879.ms.split.cal:  [3]
**** filling observed Baseline Length Distribution histograms for EB uid___A002_Xe03886_X1781.ms.split.c
Field IDs for uid___A002_Xe03886_X1781.ms.split.cal:  [3]
**** filling observed Baseline Length Distribution histograms for EB uid___A002_Xe03886_Xc8ff.ms.split.c
Field IDs for uid___A002_Xe03886_Xc8ff.ms.split.cal:  [3]
*** observed L80 is 1274.0 m equivalent to AR = 0.1047850974388149 arcsec.
**** Computing the expectations, one for each AR ... ****
totalvis from_ex:  8945049.371999959
...
**** Storing observations and expectations ****
**** Summary plot 'expectation min AR', 'expectation max AR', 'observation' ****
```

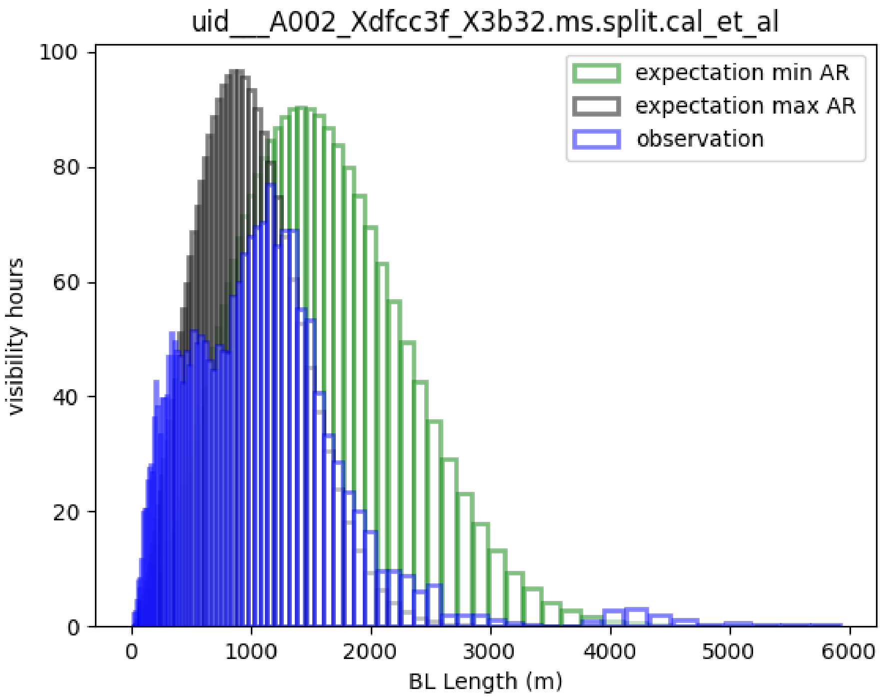

Figure 5.1: Example of an "observation and expectation" plot produced by the assess_ms application. See section 5.3.

Up to this point, the processing takes the larger part of the total processing time since all MSs have to be opened and a selection on the intent, field, SPW, etc. has to be carried out and then the UVW coordinates be read and the expectations computed. Finally the histogram objects are stored and the first plot is produced showing the observed BLD and the expected BLDs for AR_{min} and AR_{max} (see Fig. 5.1).
After this, the procedure begins to perform the quality assessment looping over all AR values in the list (in our case these are three values: AR_{min}, AR_{max}, and the AR derived from the L80). The boundaries of the "ten bins" for the computation of the filling fractions are displayed:

```
tenbin_bins  [14.0, 504.0, 994.0, 1484.0, 1974.0, 2464.0, 2954.0, 3444.0, 3934.0, 4424.
```

The result of each assessment is printed to the terminal and the logger:

```
    fill_frac_tenbin [ 3.06004509  0.97487101  0.78095971  0.37517929  0.18845677  0.14
  0.08124576  0.15407071  6.26459622 10.        ]
Total visibility seconds observed:          8274619.584
Total visibility seconds expected for AR 0: 8945049.371999972
43*(43-1)/2 * T_obs (visibility seconds): 8945049.372000001
WARN assess_ms::::casa Dataset is QA fail for  AR=0.08 arcsec according to condition "c
WARN assess_ms::::casa    Reasons:
WARN assess_ms::::casa     Filling fraction below 0.6 in range 50% - 60% : 0.1421
WARN assess_ms::::casa     Filling fraction below 0.6 in range 60% - 70% : 0.0812
WARN assess_ms::::casa     Filling fraction below 0.6 in range 30% - 40% : 0.3752
WARN assess_ms::::casa     Filling fraction below 0.6 in range 70% - 80% : 0.1541
WARN assess_ms::::casa     Filling fraction below 0.6 in range 40% - 50% : 0.1885
...
fill_frac_tenbin [ 1.81638139  0.78778735  0.54170171  0.82604742  1.15057397  1.297782
  1.94532641  4.02975175 10.         10.        ]
Total visibility seconds observed:          8274619.584
Total visibility seconds expected for AR 1: 8945049.37200002
43*(43-1)/2 * T_obs (visibility seconds): 8945049.372000001
2021-07-07 10:39:27 WARN assess_ms::::casa Dataset is QA fail for  AR=0.12 arcsec accor
2021-07-07 10:39:27 WARN assess_ms::::casa    Reasons:
2021-07-07 10:39:27 WARN assess_ms::::casa     Filling fraction below 0.6 in range 20%
...
fill_frac_tenbin [2.14058142 0.79717205 0.6414427  0.82743315 0.77613223 0.74236015
 1.10580336 2.06152989 3.98763565 5.24416001]
Total visibility seconds observed:          8274619.584
Total visibility seconds expected for AR 2: 8945049.372000022
43*(43-1)/2 * T_obs (visibility seconds): 8945049.372000001
Dataset is QA pass for _L80_ AR=0.104785 arcsec according to condition "c"
Overall result: QA PASS
```

and the return value of assess_ms is True. In addition a number of diagnostic plots are produced. As one can see from the output, the assessment deems the observation a PASS for the AR derived from the L80. As one can see already from 5.1, the observed BLD (blue) is somewhere near the middle between the two extreme expected BLDs for the min. and max. AR values.

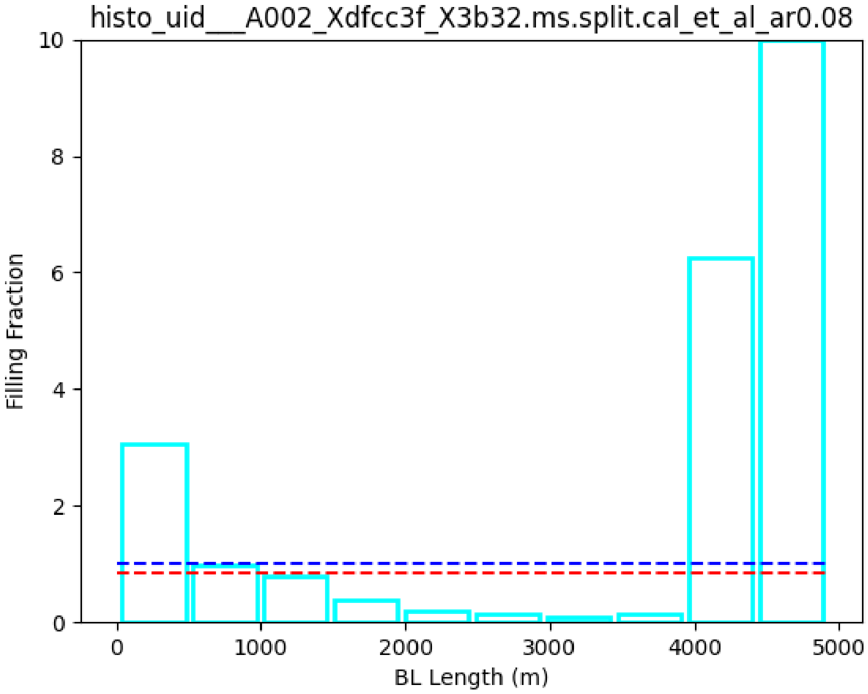

Figure 5.2: The filling fraction plot for the minimum AR for the example MOUS. For this AR, the FF is too far below 1.0 in the intermediate bins and so would result in a FAIL decision.

The result thus makes sense (the L80 is close to the average value of AR_{min} and AR_{max} in this case) and also indicates that the L80 is in this case a good estimator of the achieved AR.
Figs. 5.2 - 5.4 show the filling fraction plots for the three AR values tested in this assess_ms run.
Finally, Figs. 5.5 and 5.6 show two other potentially useful types of plots which assess_ms produces at the moment.

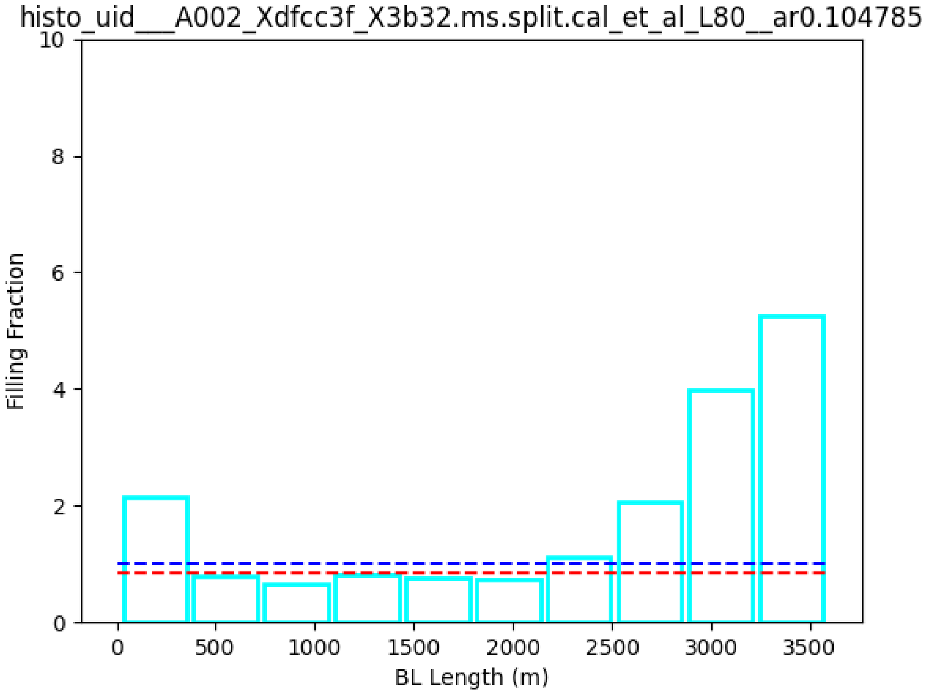

Figure 5.3: The filling fraction plot for the AR derived from the L80 of the example MOUS. Here, the FF is sufficiently high in all bins. This would result in a PASS decision.

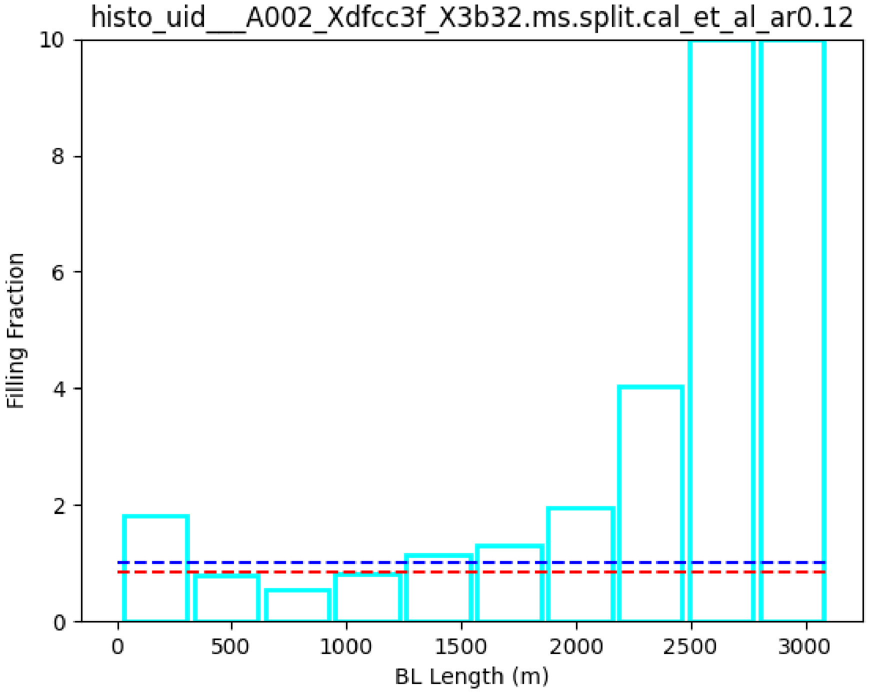

Figure 5.4: The filling fraction plot for the maximum AR for the example MOUS. See text.

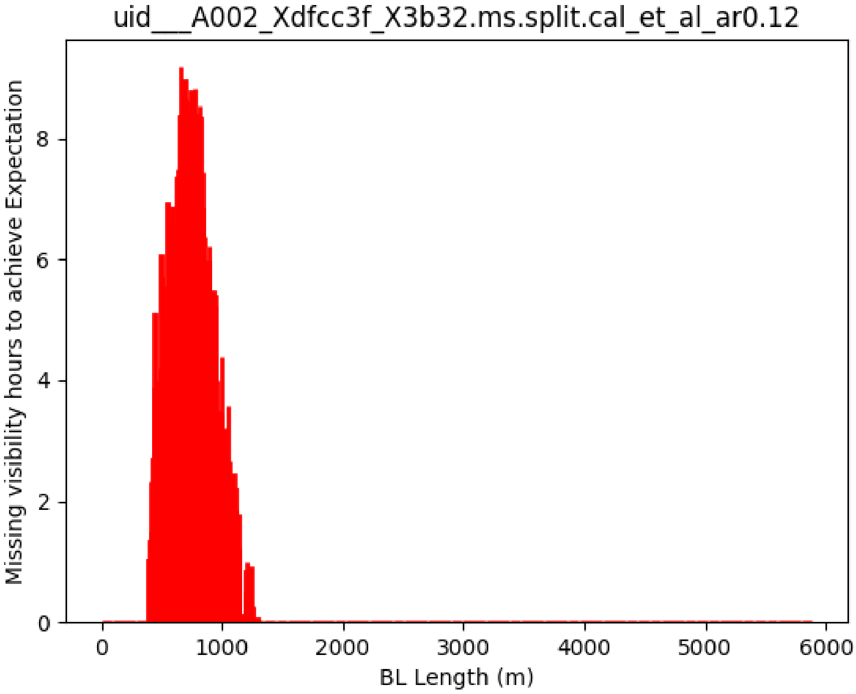

Figure 5.5: The missing visibilities plot for the maximum AR for the example MOUS. This plot shows how many visibility hours would be needed to be added in each bin to the observed BLD in order to match the expectation. In other words, this plot shows the expected BLD of the missing observation which would have to carried out to make the MOUS pass for the given AR.

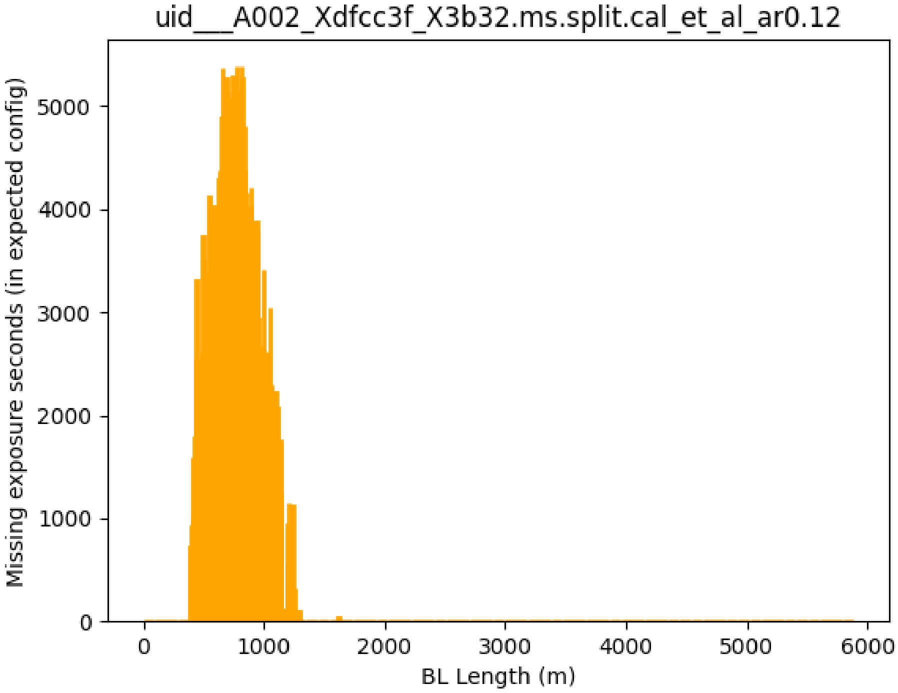

Figure 5.6: The missing exposure plot for the maximum AR for the example MOUS. Similar to Fig. 5.5 but instead of visibilities, what is shown is the missing exposure time to achieve the expected BLD for the given AR.

5.4 Future improvements

An important addition to `assess_ms` is the inclusion of the T_{sys} information in the calculation of the expectation and thus the filling fraction (FF) such that the FF becomes fully equivalent to the "execution fraction" used in scheduling and QA.

Furthermore, we would like to give the user (i.e. the QA analyst) the option to obtain the science goal parameters automatically from the ALMA database rather than having to look them up and type them in the command line.

Finally, one could attempt to accelerate the computation of the expected BLD to the point that it is possible to apply standard χ^2 minimisation techniques to fit the expected shape to the observed BLD. The AR and LAS would then become fit parameters which could be compared to the science goal parameters. However, such an approach would still require the nominal expected BLD to be computed and plotted to inform the analyst and quantify the deviation of the observation from it.

6 Evaluation of real data: properties of the sample

For testing the UV approach for quality evaluation of MOUS we ran the quality checks on a sample of 581 MOUS from Cycles 6 and 7 out of which 524 are TM1 MOUS and 57 TM2 MOUS. *In this chapter and chapter 7 we show the results of the analysis for the TM1 MOUS only.* The combination of TM1 and TM2 MOUS into a single GOUS is analysed in chapter 8. For the analysis performed in this chapter, we separated the sample of TM1 MOUS in two sets (see Table 6.1), those that do not require further MOUS in the corresponding GOUS (Set 1) and those that require a TM2 MOUS in the corresponding GOUS (Set 2). The separation in two sets is intended to disentangle effects due to general operational constraints that affect both sets and the potential lack of short BLs needed to meet the LAS expectations that should affect only Set 2 (since such BLs are expected to be filled with the respective TM2 MOUS, see chapter 8). After removing from the sample MOUS that do not have pipeline results available, the remaining number of TM1 MOUS is 369/102 for Sets 1/2, respectively. Out of the 369 MOUS of Set 1, 95/274 have been observed in Cycle 6/Cycle 7, respectively. Out of the 102 MOUS of Set 2, 96/6 have been observed in Cycle 6/Cycle 7, respectively. A list of all the MOUS in Set 1 and 2 is provided in Appendix A. For reference, Table 6.2 provides a list of all the properties that we have looked at and refer to in the following sections.

6.1 General properties

Figs. 6.1–6.2 show the distribution of the Set 1 and Set 2 MOUS per configuration together with some general properties of the sample. When looking at these figures it should be kept in mind that these properties are not necessarily those of the sample of a full ALMA Cycle, although we expect that they are quite representative. As expected, Set 2 does not include any MOUS in the most compact configurations. In addition, the median on-source time for one-execution

	Number of MOUS		
	Total	Cycle 6	Cycle 7
Set 1 (GOUS with only TM1 MOUS)	369	95	274
Set 2 (GOUS with TM1 and TM2 MOUS)	102	96	6

Table 6.1: Definition of sets 1 and 2. Note that for Set 2 in this chapter we only evaluate the TM1 MOUS. We evaluate the combination of the TM1 and TM2 MOUS in chapter 8.

Table 6.2: List of analysed sample properties

Property	Abbreviation
C43 configuration	confign
C43p7 configuration	confign2
Representative frequency (GHz)	freq
Representative bandwidth (Hz)	bwf
Number of requested executions	execount
On-source time (seconds)	times
AR normalised to 100 GHz (arcseconds)	arnorm
Ratio of LAS to L80 AR	las2ar
Number of antennas of the MOUS (averaged over all SB executions)	avgant
Elevation of the source at the start of the observation for the MOUS (averaged over all SB executions, degrees)	avgelev
Fractional AR	far
Relative EF (ratio of EF to number of requested executions)	efrel
Number of pads in the real array matching those of a given C43 configuration	padsin43
Number of pads in the real array matching those of a given C43p7 configuration	padsin43p7
Number of pads in the real array that do not match the corresponding C43 configuration	extrapads
Number of pads in the real array that do not match the corresponding C43p7 configuration	extrapads2
Ellipticity of the QA2 beam	bellipticity
Robust factor used by the pipeline in QA2	robustt
Ratio of the AR obtained in QA2 and the L80 AR	ratioar
Ratio of achieved to requested RMS	rmsratio

SBs is larger in this set compared to Set 1.

6.2 Properties as a function of configuration

Figs. 6.3–6.8 show further characteristics of sets 1 and 2. In each figure, the left, middle and right columns show the properties of the full sample (left column) and as a function of array configuration, where "configuration" is either the C43 (middle column) or the C43p7[1] (right column) configuration that is best-matched by the antenna pads used during the observation.

6.2.1 PI requests

When looking at the PI requests for Set 1 (Fig. 6.3), it is interesting that the requested on-source time per MOUS is longer for MOUS observed in extended configurations (6 to 10). These MOUS also request a higher ratio of LAS to AR (LAS2AR), despite the fact that the MOUS included in this set have been chosen not to have a TM2 pair and consequently the requests of intrinsically large LAS2AR ratios are excluded (the few MOUS with LAS2AR values >20 for this set correspond to GOUS that also include a MOUS in the 7M and/or TP arrays). For Set 2 (Fig. 6.4), the LAS2AR ratios are larger, as expected, but also the median on-source times, likely due to this Set being dominated by MOUS in extended configurations. In contrast, the majority of MOUS request only one execution per MOUS, similarly to those of Set 1.

---

[1] See sect. 7.4 for how the C43 and C43p7 configurations are defined.

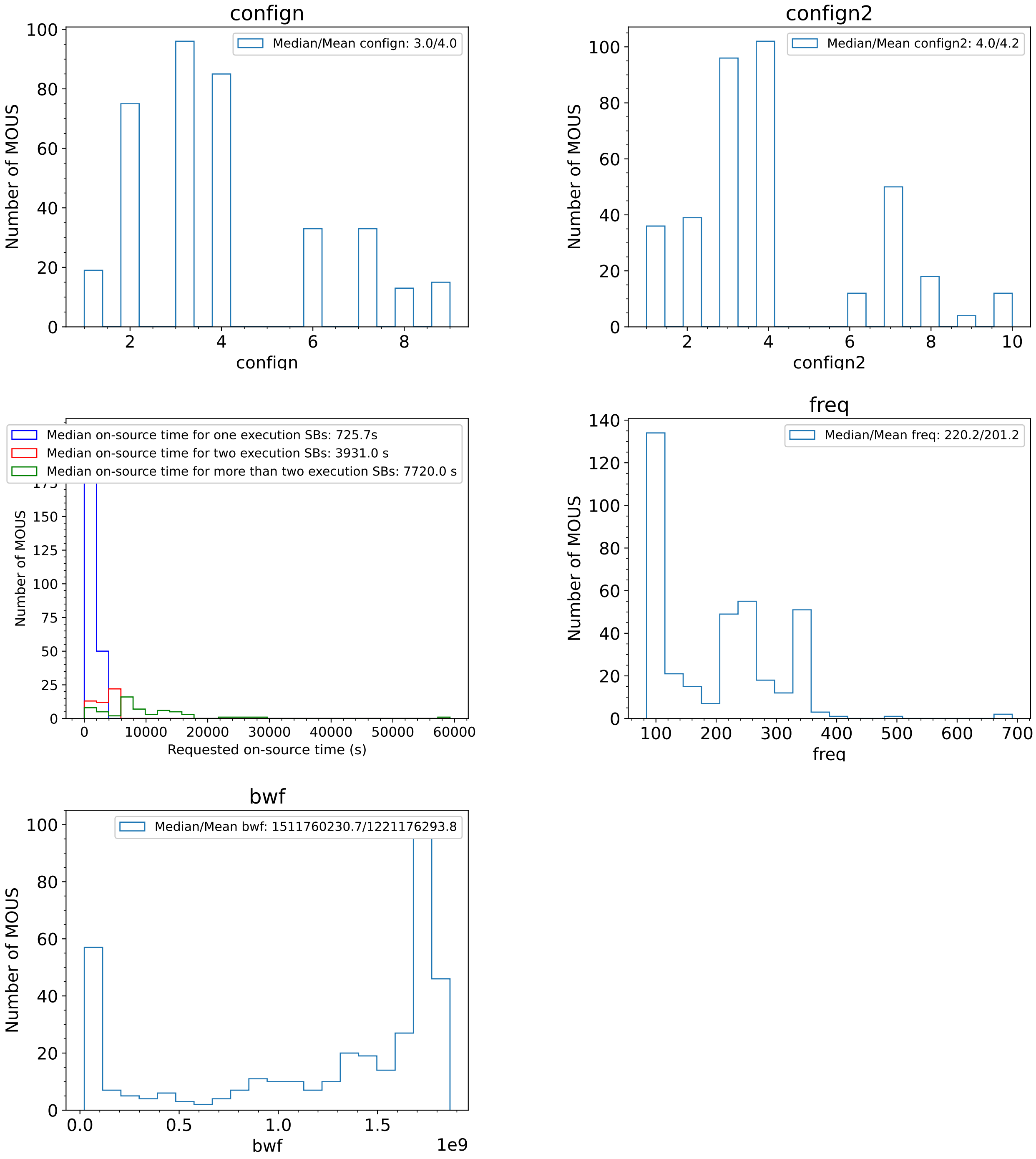

Figure 6.1: General characteristics of the Set 1 MOUS sample on which the UV methods have been tested. From left to right and top to bottom: C43 and C43p7 configurations that are better matched to each MOUS, on-source time per execution as a function of number of executions, representative frequency (in GHz) and representative bandwidth (in Hz).

6.2.2 Scheduling properties

Next we look at the scheduling properties of the MOUS or the conditions under which the MOUS were scheduled. For Set 1 (Figs. 6.5–6.6), the median number of antennas used is 45,

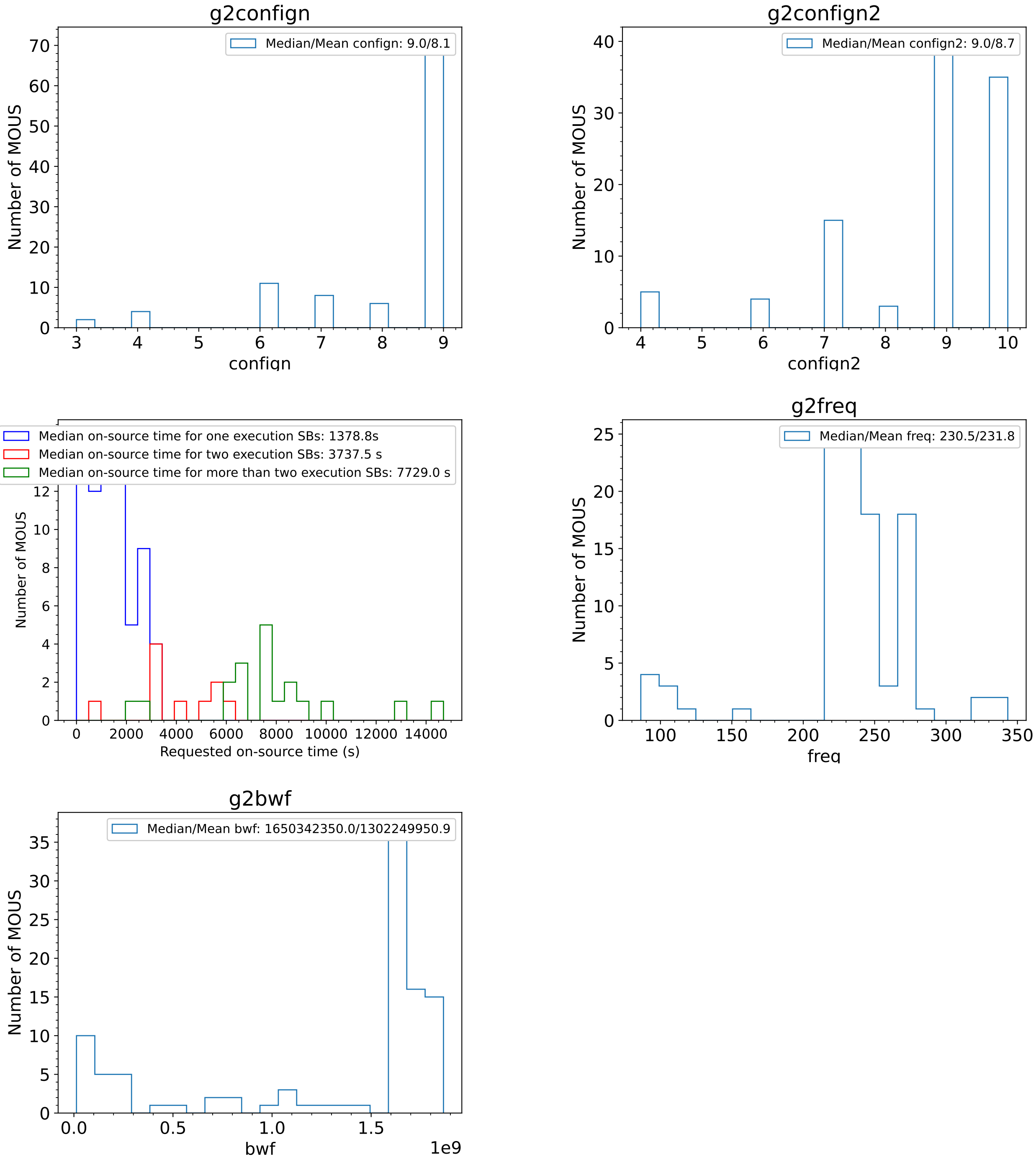

Figure 6.2: Same as Fig. 6.1 but for Set 2.

the median elevation is 58° and there is a significant fraction of MOUS that are scheduled close to or below a Fractional Angular Resolution (FAR)[2] of zero, indicating that in general MOUS are scheduled in a configuration that matches the minimum AR request or that even has a characteristic AR that is finer than the minimum AR request (we note that this only happens when more than 43 antennas are included in the array and the minimum AR request can be

---

[2] FAR $= \frac{(AR_{array} - AR_{min})}{(AR_{max} - AR_{min})}$

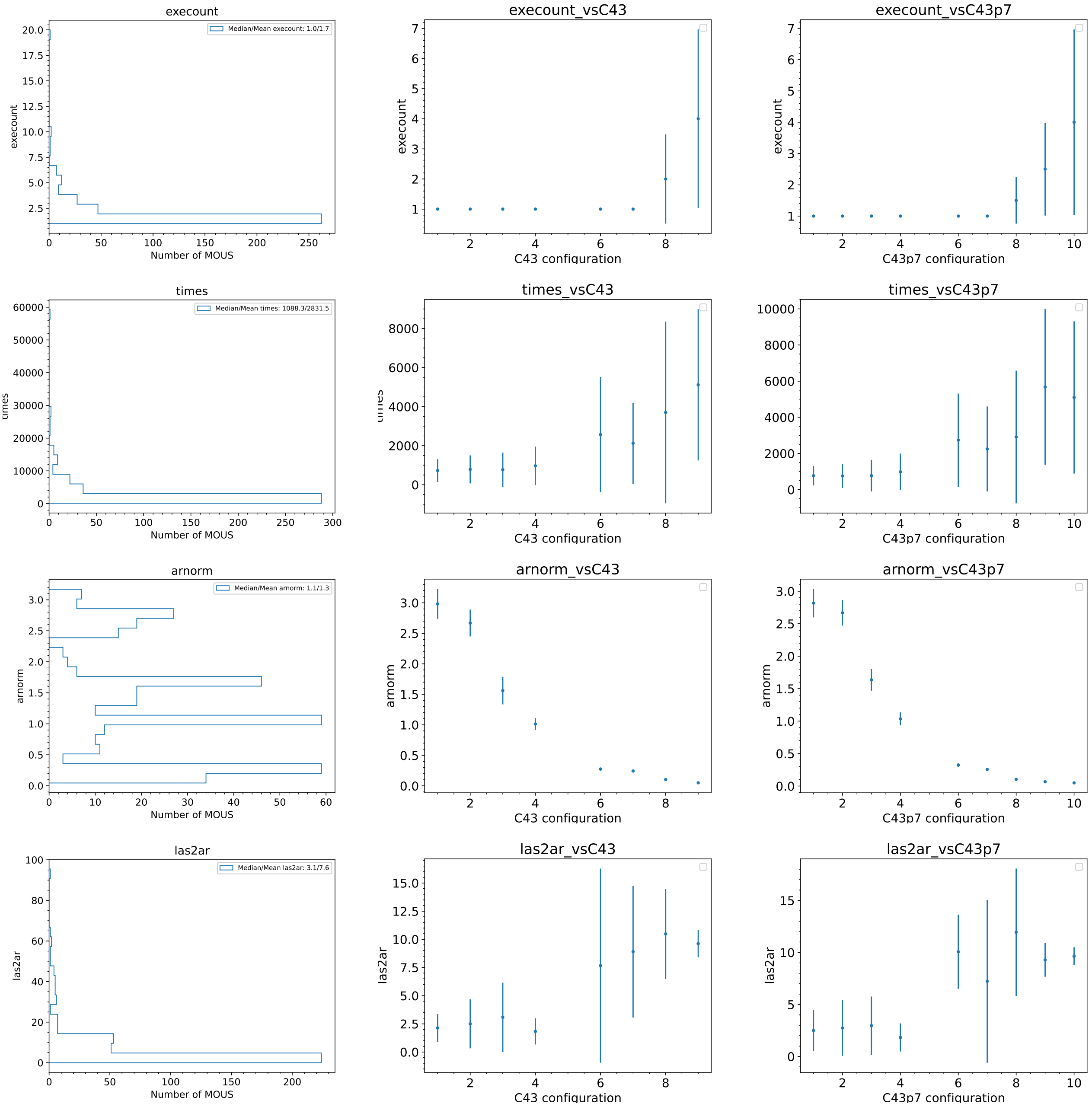

Figure 6.3: PI requested parameters of the Set 1 sample on which the UV methods have been tested. From top to bottom: number of requested executions, total on-source time in seconds, AR normalised to 100 GHz and ratio of LAS to AR.

fulfilled with the most inner 43 antennas). Interestingly, a majority of MOUS show a relative Execution Fraction (EF) that is significantly larger than one. This is especially the case for MOUS consisting of one-execution SBs, for which the final EF is often close to 1.5 (this may be due to the presence of antennas in the array beyond the minimum of 43 or to a T$_{sys}$ lower than

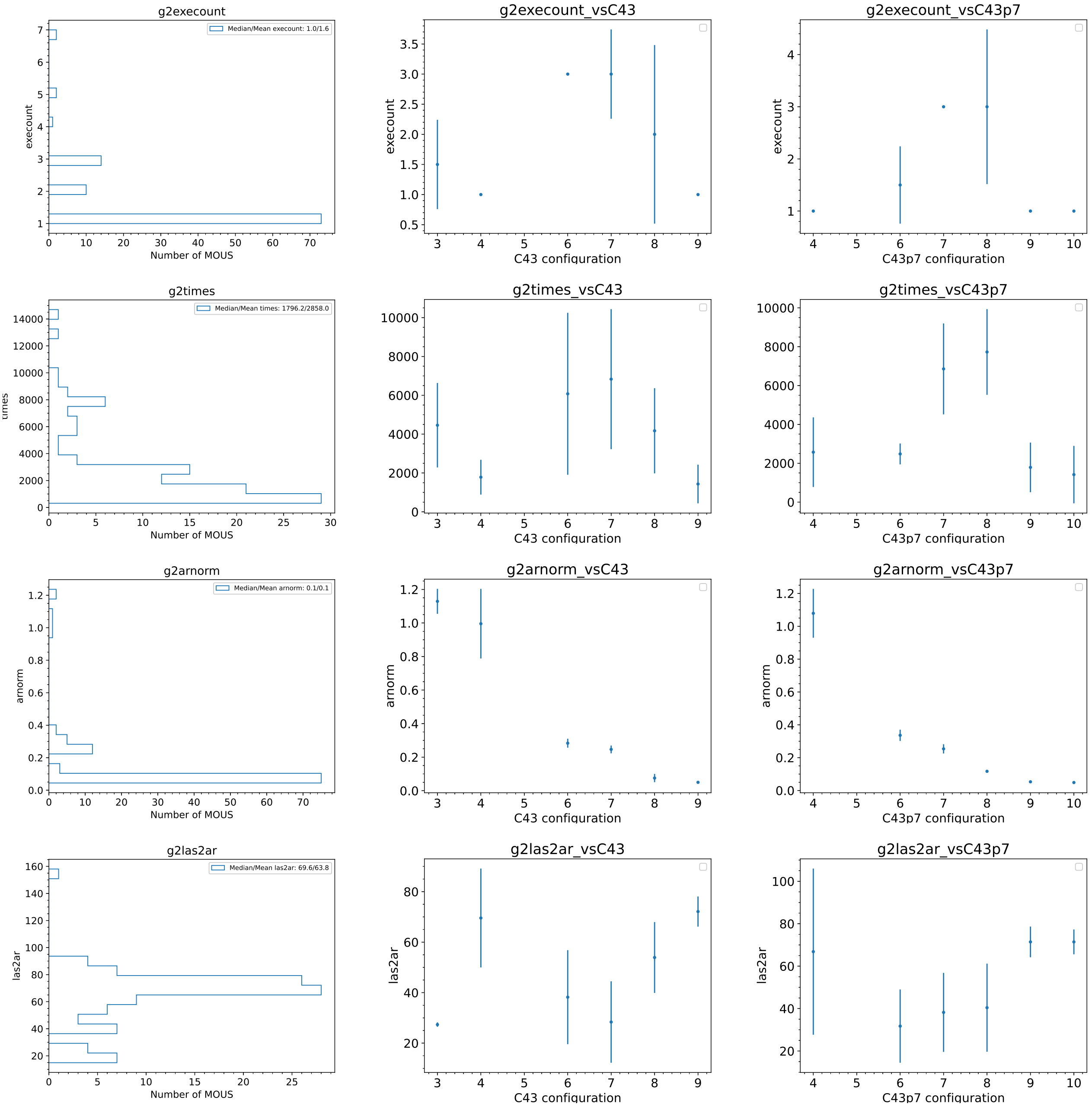

Figure 6.4: Same as Fig. 6.3 but for Set 2.

the one used by the OT for sensitivity calculations[3]). In terms of match of the real arrays to the pre-defined configurations, extended configurations show a worse match to the pre-defined nominal configurations (Fig. 6.6). For example, for the three more extended configurations the

---

[3] We investigated the relative effect of number of antennas and T_{sys} in the final RMS by plotting the ratio of achieved vs requested RMS ($RMS_{achieved/requested}$) against the number of antennas used. For MOUS with more than 45 antennas there was a trend of decreasing $RMS_{achieved/requested}$ with increasing number of antennas. However, the spread of $RMS_{achieved/requested}$ values was large within each sample of MOUS with the same number of antennas and its median value was <0.8 overall (even for samples with less than 43 antennas), indicating that the most significant factor leading to a high EF is a real value of T_{sys} lower than the one used by the OT for sensitivity calculations.

median number of pads that match one of the C43 configurations is below 36 and more than 10 extra pads that do not match the configuration are included in the array. When matched to one of the C43p7 configurations, we observe the same effect, namely the number of pads that match a C43p7 configuration are ∼42–44 for the compact and intermediate configurations but drops to <38 for the two more extended configurations, resulting in no extra pads in the array for the three more compact configurations but more than six extra pads for the two more extended configurations.

For Set 2 (Figs. 6.7-6.8), the median number of antennas used is only slightly larger (46 vs 45 in Set 1). However, it is clear that the effect that was observed in Set 1 for the MOUS in extended configurations dominates the overall sample here. Consequently, the median number of pads that match a given C43 configurations is only 34 for Set 2 (compared to 38 for Set 1) and the median number of pads that match a given C43p7 configurations is only 38 for Set 2 (compared to 43 for Set 1). Interestingly, Set 2 MOUS seem to be scheduled in a narrower FAR range compared to Set 1. While Set 1 was peaking at FAR ∼ 0.1, indicating scheduling close to the minimum requested AR, the distribution of FAR was broad, smoothly extending all the way from -0.5 to 1. Instead, for Set 2, the distribution shows the majority of MOUS being scheduled at FAR between 0.1 and 0.25. This may be due to this set being a less even sample in terms of configurations or requested AR (note that MOUS from the large project 2018.1.00659.L largely dominate the sample, see Table A.2). A further difference is that for Set 1, there is a significant number of MOUS with a relative EF between 1 and 1.5, while for Set 2, the distribution is more significantly dominated by MOUS with a relative EF of 1.5, resulting in a median value of 1.5 compared to 1.3 for Set 1.

6.2.3 QA2 properties

Finally, the scheduling properties have an effect on the QA2 characteristics of the sample. For example, comparing Set 1 (Fig. 6.9) and Set 2 (Fig. 6.10), a robust value of 1.0 has to be used more often in Set 2 (see "robustt") resulting in a worse match between the AR recovered during QA2 and the L80 prediction (see "ratioar"). Large beam ellipticities may be also reflecting the low elevation of some observations. For example, for Set 1, MOUS scheduled in configuration C43p7-9 have been observed at low elevation, which results in beams with larger ellipticity in that set. Instead, MOUS scheduled in the same configuration in Set 2 have been observed at higher elevations and their beam ellipticity is also smaller. This could indicate that large beam ellipticities are only due to low elevations, although the shape of each particular configuration should also play a role (see Fig. 7.9 in the Cycle 7 ALMA THB (Remijan et al. 2019)). Interestingly, and although in general the achieved RMS is below the requested RMS for both Sets 1 and 2, the achieved RMS seems to be comparatively higher for MOUS scheduled in the C43p7-9 configuration in Set 1 and in the C43p7-8 configuration in Set 2. This may be partially linked to the larger number of executions requested in the extended configurations resulting in a relative EF closer to one, as opposed to those in more compact configurations with a median relative EF significantly above one. This effect is only slightly noticeable in Set 1 and needs further study. For Set 2, the median relative EF for MOUS scheduled in C43p7-8 is ∼0.6, significantly lower than for other configurations, but this does not seem to result in a significantly higher rmsratio for that particular configuration.

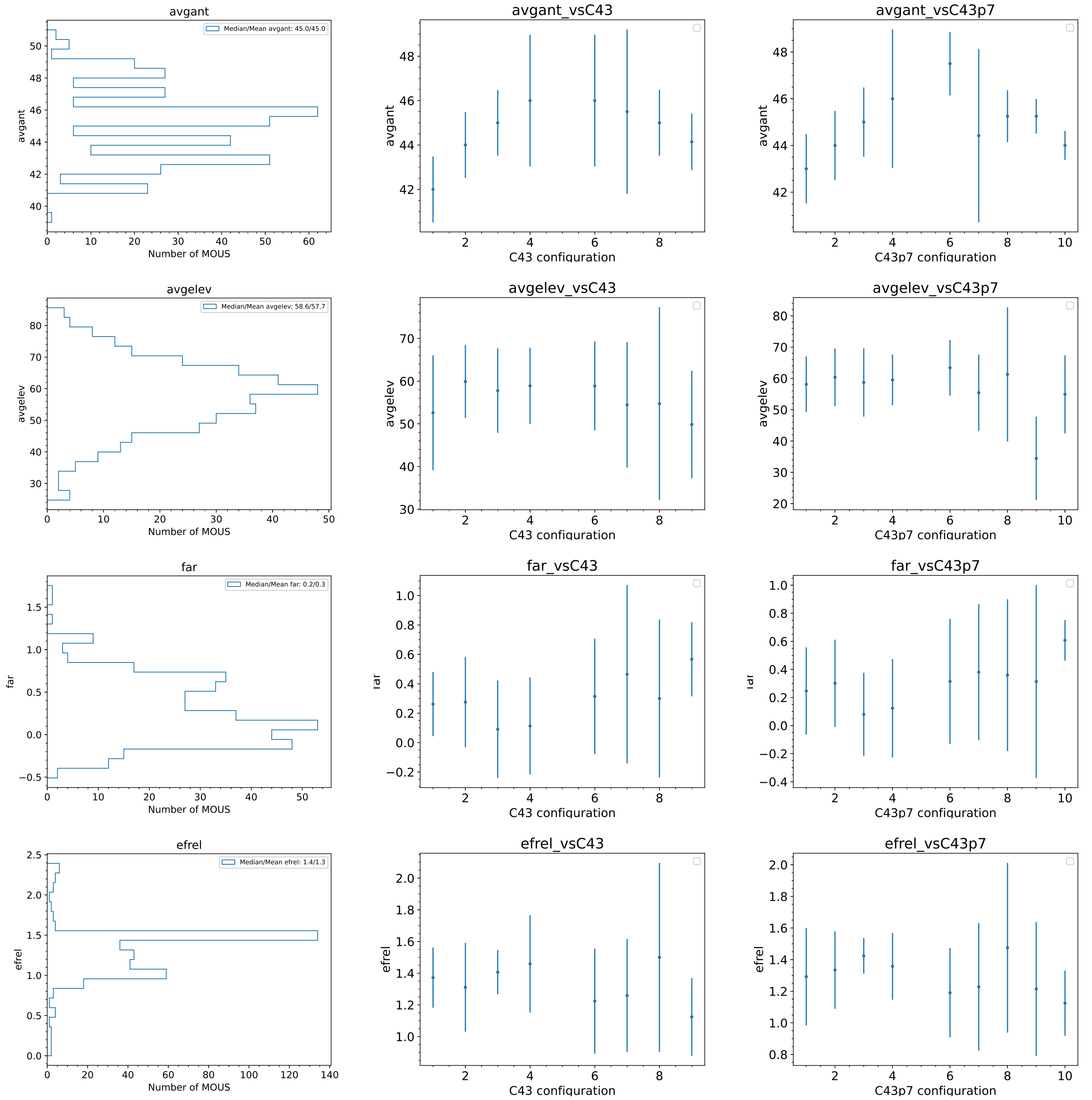

Figure 6.5: Scheduling characteristics (I) of the Set 1 sample on which the UV methods have been tested: average number of antennas in the array, average elevation of the SB executions, FAR and relative execution fraction (or total execution fraction divided by number of requested executions).

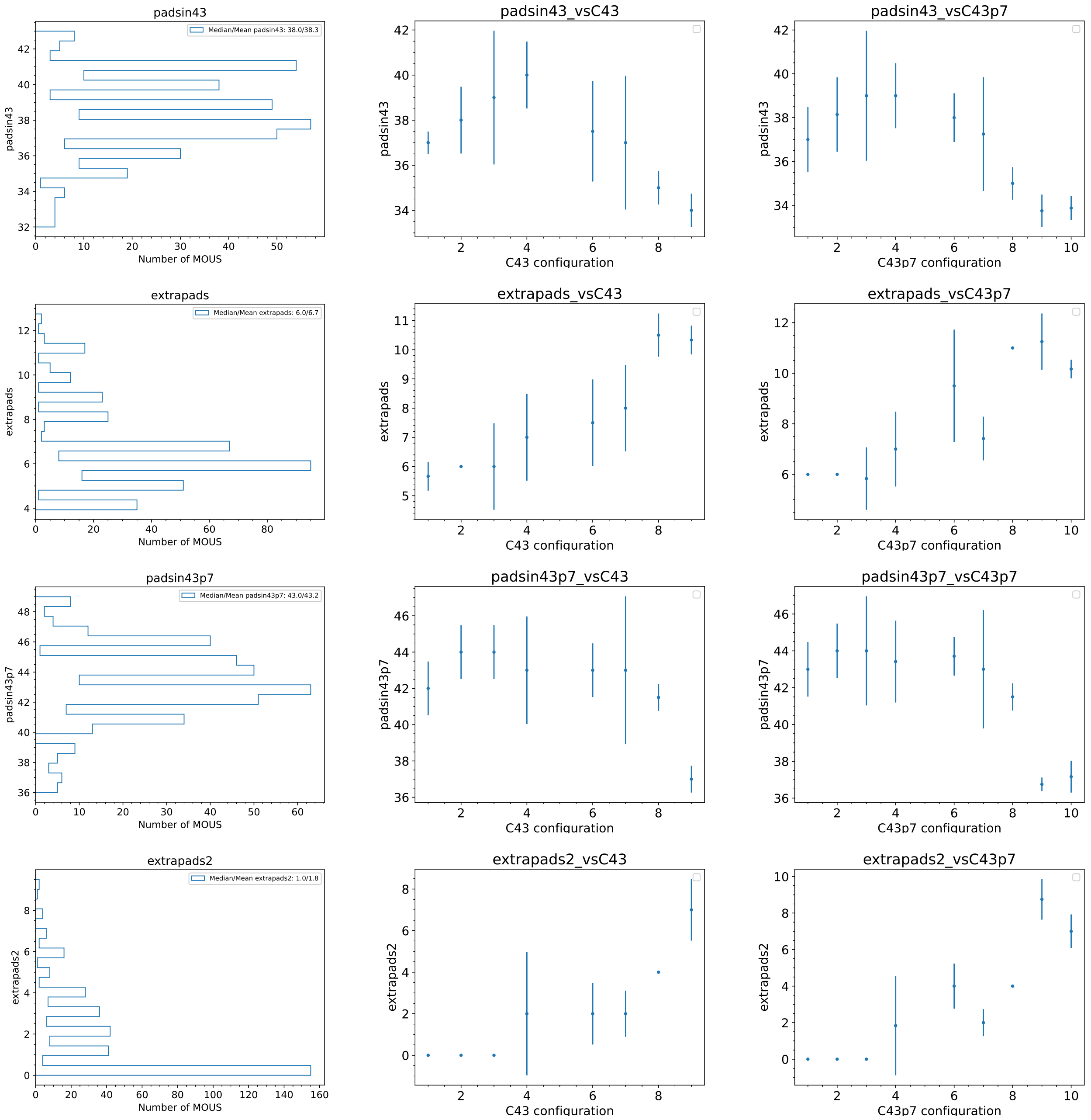

Figure 6.6: Scheduling characteristics (II) of the Set 1 sample on which the UV methods have been tested: number of pads matching a C43 configuration, number of pads that do not match the selected C43 configuration, number of pads matching a C43p7 configuration and number of pads that do not match the selected C43p7 configuration.

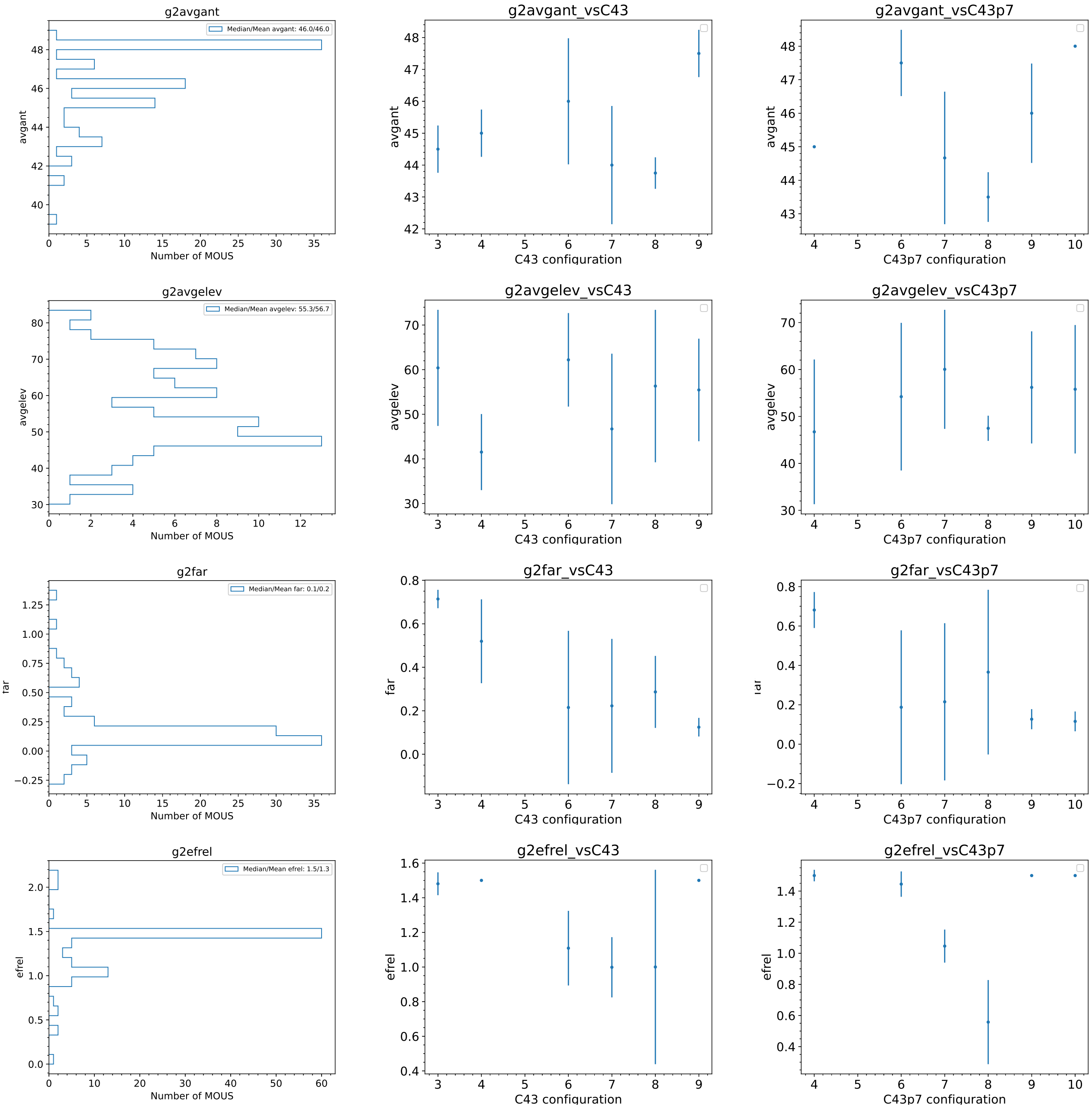

Figure 6.7: Same as Fig. 6.5 but for Set 2.

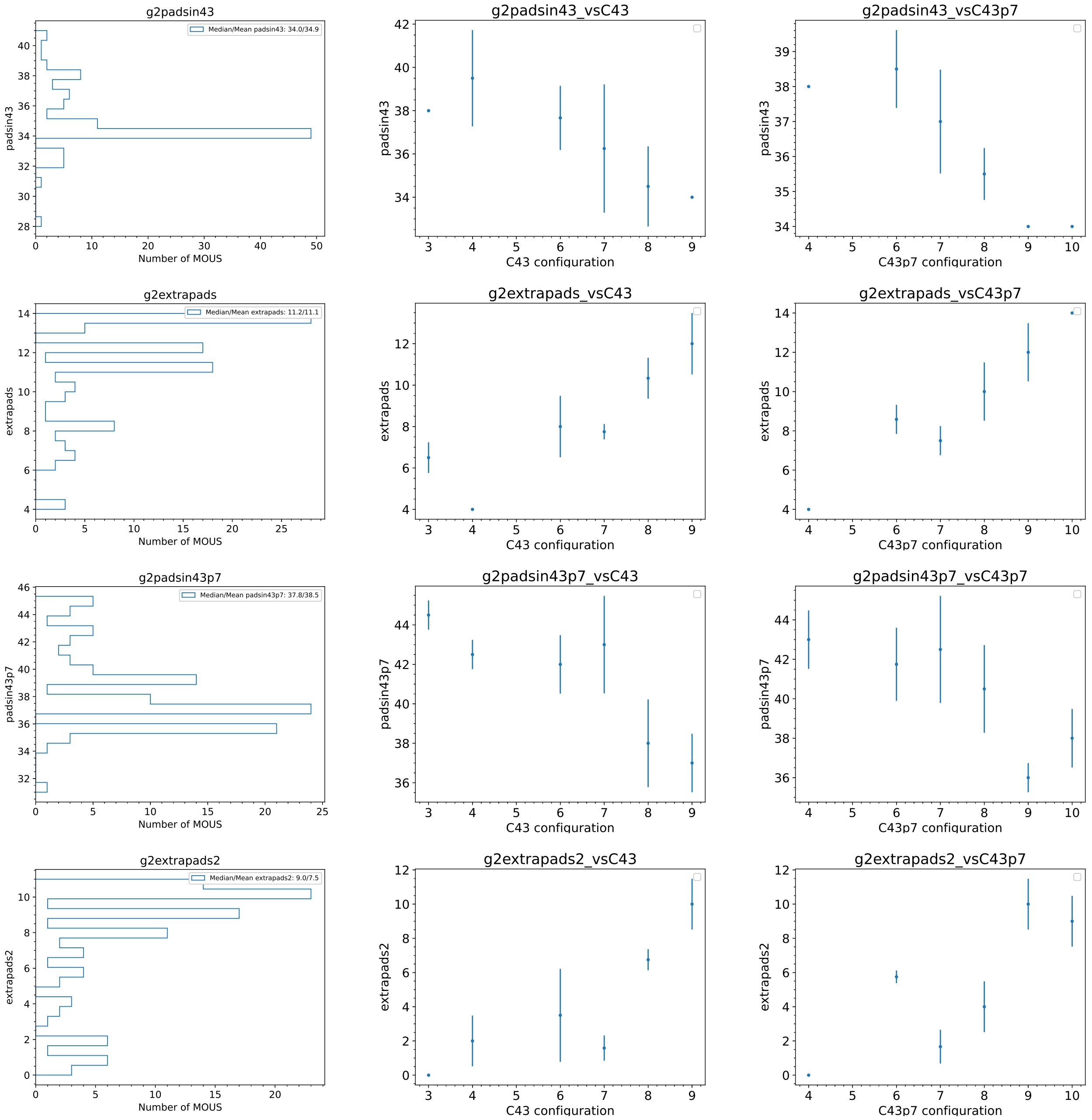

Figure 6.8: Same as Fig. 6.6 but for Set 2.

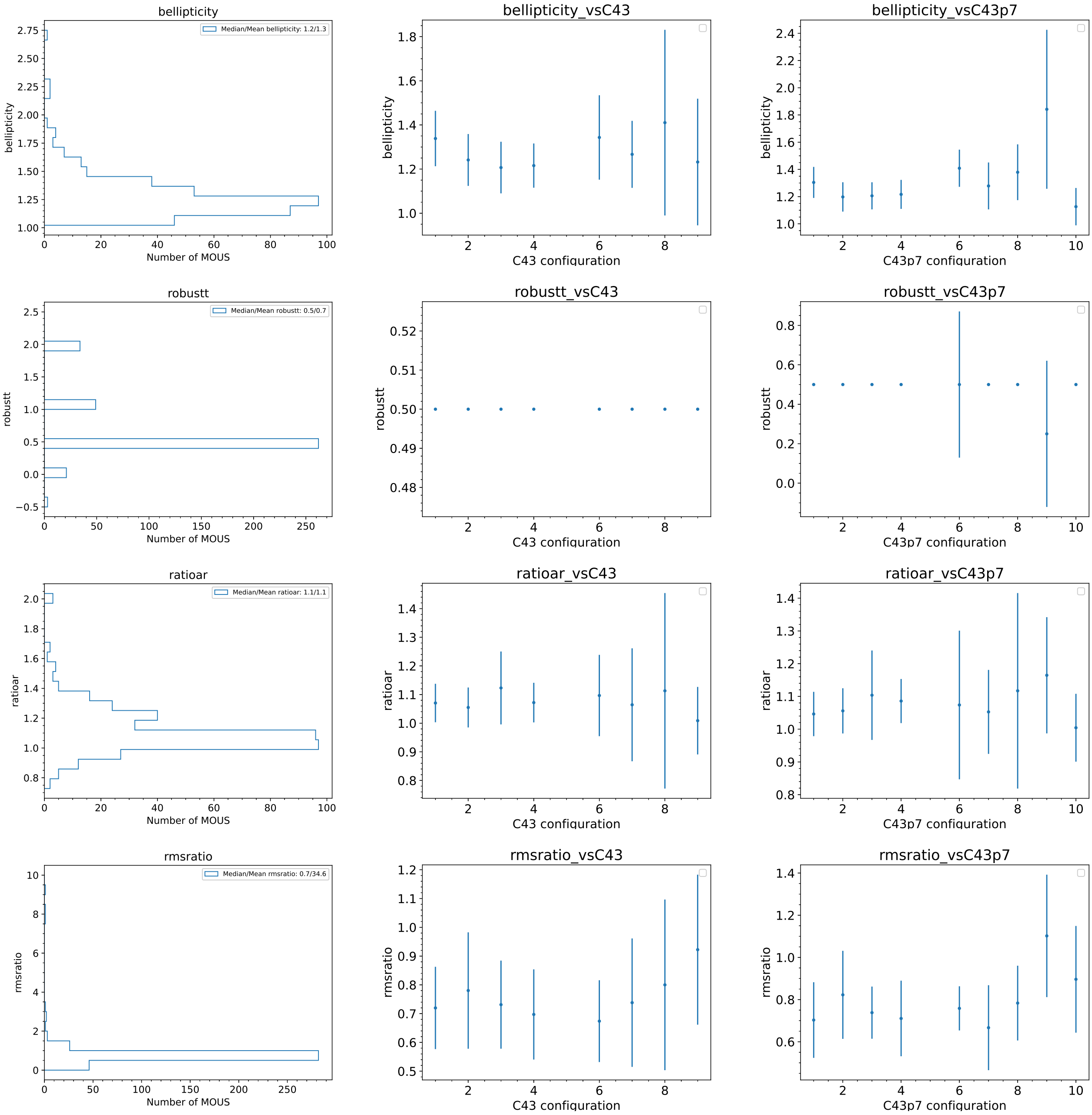

Figure 6.9: QA2 characteristics of the Set 1 sample. From top to bottom: synthesized beam ellipticity, robust value used by the pipeline for imaging, ratio between the AR recovered by QA2 and the AR estimated with the L80 method and ratio between achieved and requested RMS.

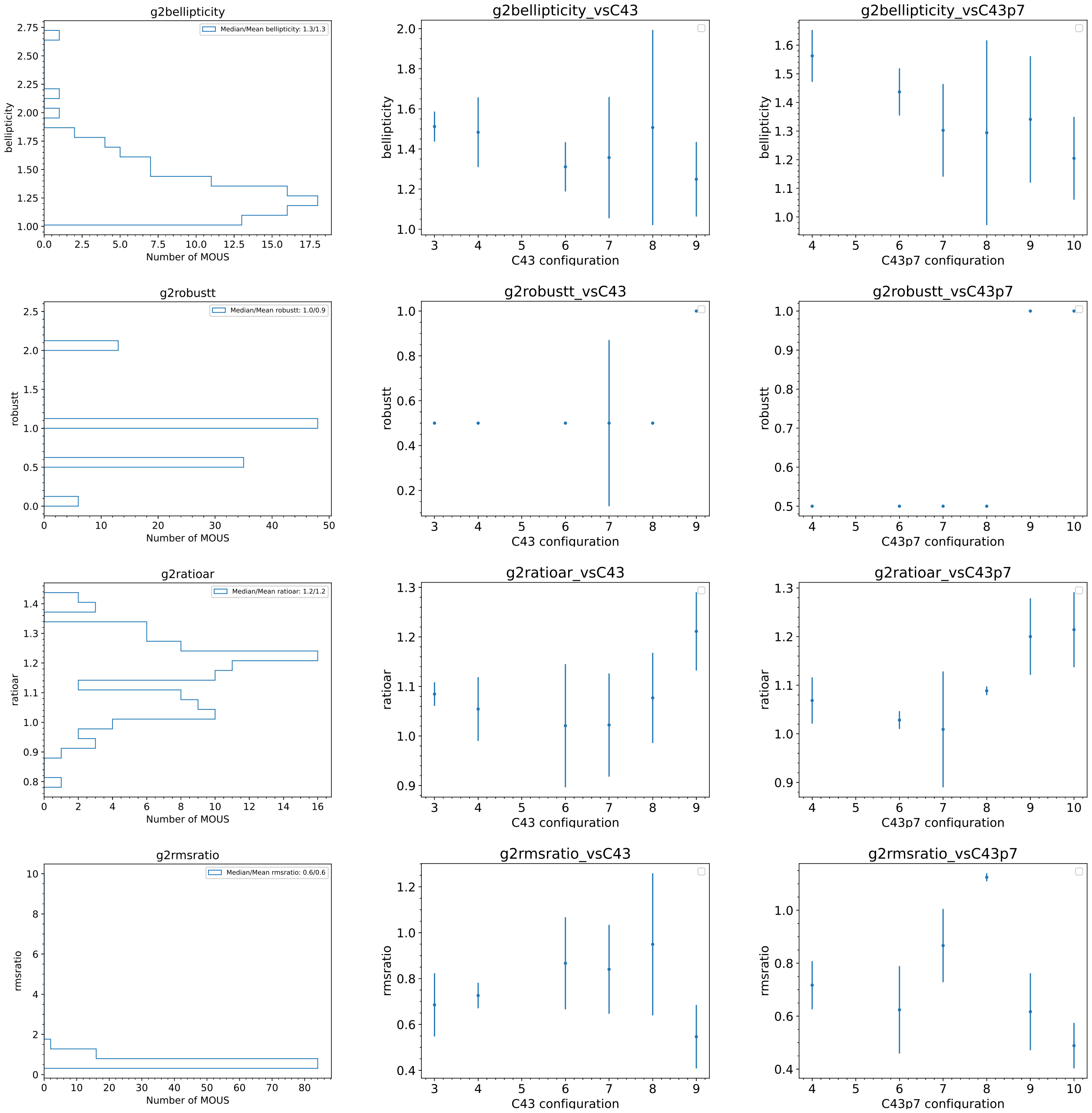

Figure 6.10: Same as Fig. 6.9 but for Set 2.

7 Evaluation of real data: results

The observed BLD for a given MOUS may deviate from the expected one due to a variety of operational constraints. First, as shown in chapter 6, the real arrays often differ from the C43 configurations. For example, for configurations 8–9 the median number of pads in the real arrays that match the corresponding C43 configuration is below 36, as opposed to the expected 43 (see Fig. 6.6). While up to ten extra pads are used to reach the minimum requested number of antennas in the array, such antennas may add baselines with lengths that differ from those of the antennas missing in the original configurations, thus contributing to a mismatch of observed vs. expected BLD. Moreover, deviations of the observed BLD with respect to the expected one may be exacerbated if such extra pads contribute to reaching the requested RMS in exposure times shorter than those originally estimated by the OT. In addition, the elevation of the observed source or the observing time may contribute to significant deviations from the observed BLD to the one expected based on sources transiting at an elevation of 70° or on-source times of one hour, as those used for the design of the configurations.

In this chapter we evaluate the effect of operational constraints on the match of the observed to expected BLD with the aim of identifying any potential parameter that leads to worse matches, therefore likely resulting in images of lower quality (see chapter 4). As in previous chapter, we perform the evaluation for sets 1 and 2 separately since for Set 2, in addition to mismatches due to operational constraints we expect a deficit of short BLs due to the fact that the TM2 MOUS have not yet been added to fulfill the LAS request (this effect is evaluated in chapter 8).

For the evaluation, we calculate the BLD expected for each MOUS based on the requested AR, LAS and on-source time and examine how this expectation matches the observed BLD. Most of the results in this chapter are based on the comparison to the expectation from the analytic method ("ana" hereafter), since this method provides in general a significantly better match to the observed BLDs compared to the filled dish method ("fd" hereafter, see sect. 3.2 for a description of both methods). In addition, and since in general the requested AR is actually a range of ARs rather than a single value, we used the L80 AR for the observed BLD (that is, excluding all flagged BLs) as an input to calculate the expected BLD. We discuss the advantages, caveats, and potential improvements to such approach in sect. 7.3.

For evaluating the match of observed to expected BLDs we use the four plots extracted following the methods outlined in sect. 3.3. As explained in the corresponding chapter, each bin of the BLD indicates the coverage for a set of angular scales. For example, the first bins indicate whether the LAS has been met and the last bin whether the AR has been met. If the match of the BLD to the expectation were perfect, the FFs for all bins would be equal to one, that is, the figures below would show straight horizontal lines (the perfect match is indicated in the FF plots with a dashed horizontal line at FF=1 for comparison with the real match). A constant FF per bin but different from one would still indicate a perfect match in terms of shape but an overall low/high RMS. A relatively flat distribution except for the last bin, which has a FF significantly above the other bins may indicate that the AR of the set is actually finer than the one used for estimating the expectations. Instead, a relatively flat distribution except for the first bin, which has a FF significantly above the other bins, and the last bin, which has a FF below the other bins, may indicate that the AR of the set is actually coarser than the one used for estimating the expectations. In the plots that use as a marker the difference of observed and expected visibilities instead of the FF, the perfect match is indicated with a dashed horizontal line with a value of zero, that is, the perfect match results when the observed and expected visibilities are equal and thus their difference is zero.

7.1 Comparison of observed vs expected BLD

Each of the following subsections examines the effect of one parameter or a set of related parameters in the match of observed to expected BLDs.

7.1.1 Configuration effects

The first parameter we evaluate is the "design" of the configurations. While operational procedures are expected to have an effect in the BLD match to expectations (see subsections following this one), the most important effect is expected to result from how well the C43 configurations match the analytical expectation (see also sects. 7.5 and 7.4). Any BLD mismatch that is observed globally for a specific configuration is likely to be related to the design of that configuration, although for extended configurations there is a relatively large number of pads that are not matched during operations, complicating the interpretation of the results for these configurations (see sect. 7.1.2).
Figs. 7.1-7.2 show that there is a clear difference in the quality of BLD match among configurations. Compact configurations (C43–1 to C43–4) show in general a better match of the BLD compared to more extended configurations (C43–6 to C43–9). This is especially noticeable when looking at the total number of visibility hours missing for extended configurations at medium length bins (2-3). An exception is C43–9, which shows a strange behaviour in the sense that in Set 1, it behaves similarly to other extended configurations in terms of missing visibility hours in intermediate bins but in Set 2 it rather behaves similarly to the compact configurations. The reason for this is not fully understood but could be related to the low number of pads matching the nominal configuration (only 34 out of 43) and the extra pads varying between Set 1 and Set 2. When looking at the FF plots, it is noticeable that extended configurations show a larger excess of long baselines and very short baselines and a deficit at intermediate baselines. This is most noticeable for C43–8 in both sets and indicates that the BLD of such configuration is somehow more elongated than the analytical expectation compared to other configurations. In addition, for C43–9, the AR that best matches the BLD seems to be coarser than the L80 AR.
Next we evaluate to which extent the BLD match shows the largest deficit in terms of FF in a large number of bins. In principle, an excess of BLs at any given bin should not be detrimental since such BLs could be down-weighted in the imaging process. However, it is likely that the deficits in some BL ranges will increase together with excesses in other BL ranges, thus resulting in a sensitivity lower than requested for the BL ranges that show deficits. To evaluate the deficits we compute the number of bins that show a FF lower than 85% (tbin85) and than 60% (tbin60)

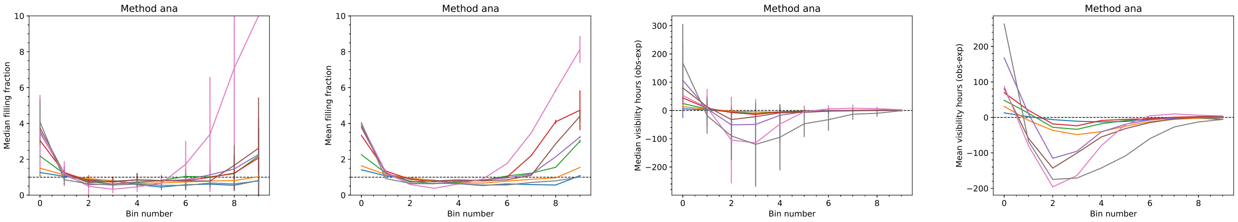

Figure 7.1: Selection on C43 "configuration" according to pad match for Set 1. Blue, orange, green, red, purple, brown, pink and grey correspond to groups 0, 1, 2, 3, 5, 6, 7 and 8, respectively. Groups 0–9 correspond to nominal configurations C43–1 to C43–10, respectively.

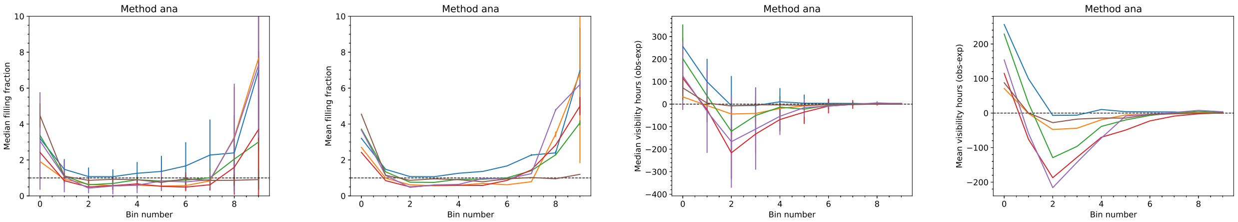

Figure 7.2: Same as Fig. 7.1 for Set 2. Blue, orange, green, red, purple and brown correspond to Groups 2, 3, 5, 6, 7 and 8, respectively.

compared to one. Figs. 7.3-7.4 show the results of such parameters as a function of configuration. When looking only at deficits instead to the global BLD match, configurations 1, 8 and 9 are worst in terms of number of bins with a low FF. As expected, many of the deficits are small and at least for Set 1 large deficits (below 60% FF) are limited to one bin in median, except for configurations 1, 8 and 9. For Set 2, configurations 4, 7 and 8 show in median more than 2 bins with a large deficit. Table 7.1 shows the impact that such deficits may have in the QA of MOUS if a minimum limit is requested on the deficit for all bins of the BLD.

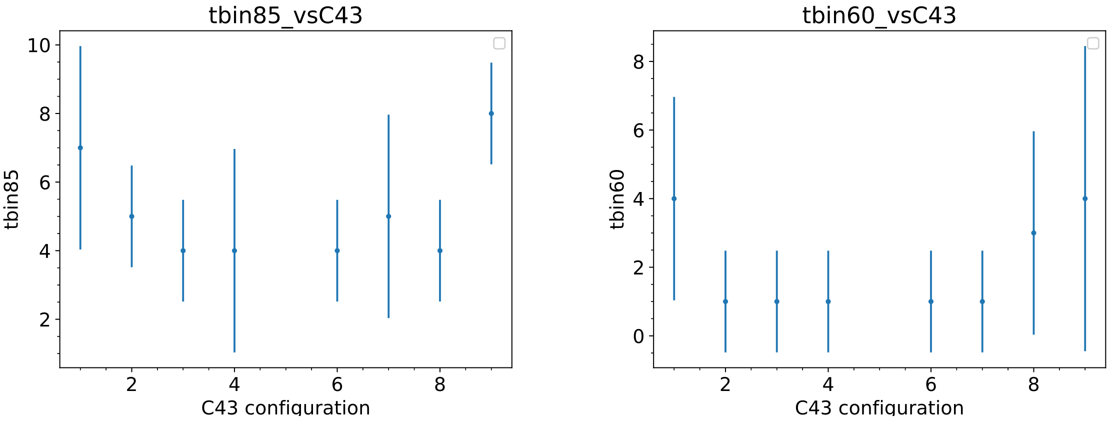

Figure 7.3: Number of BLD bins that show a FF below 85% (left) and 60% (right) for Set 1.

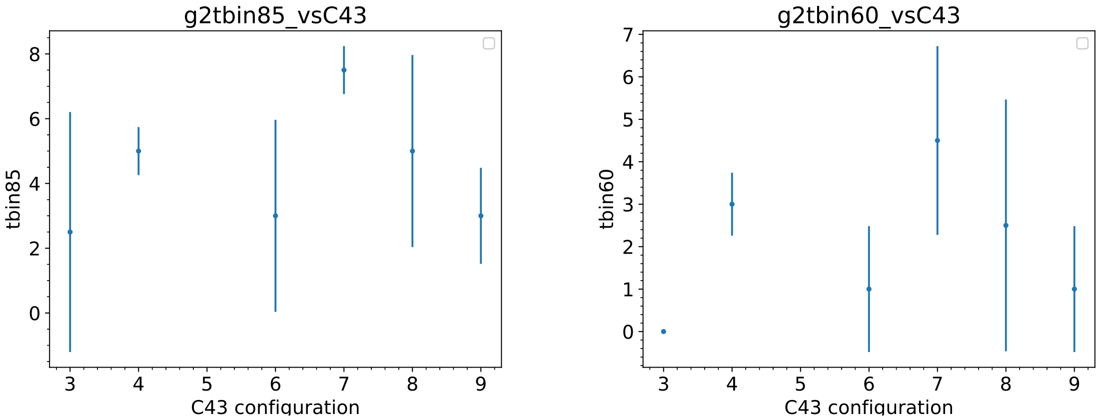

Figure 7.4: Same as Fig. 7.3 but for Set 2.

Table 7.1: Number(fraction) of MOUS that have more than 0, 2 or 4 BLD bins with a FF less than unity.

Number of MOUS	Number of bins < 0.85 FF			Number of bins < 0.60 FF			Number of bins < 0.35 FF		
	>0	>2	>4	>0	>2	>4	>0	>2	>4
Set 1									
369	343 (92.9%)	310 (84.0%)	175 (47.4%)	229 (62.0%)	95 (25.7%)	45 (12.1%)	54 (14.6%)	14 (3.8%)	7 (1.9%)
Set 2									
102	93 (91.2%)	80 (78.4%)	38 (37.2%)	67 (65.7%)	22 (21.6%)	9 (8.8%)	7 (6.9%)	2 (2.0%)	2 (2.0%)

7.1.2 Effect of number of antennas, pad distribution and relative EF

The imaging expectations for ALMA have been generated using configurations of 43 antennas with fixed positions for the antennas, following the nominal C43 configurations. However, in reality, since Cycle 6, the number of antennas in the array when doing observations is typically larger (see Figs. 6.5 and 6.7). This can affect the match of the BLD due to several reasons. First, the EF is currently calculated with a formula (see ALMA THB) that takes into account the number of antennas in excess of 43 and the values of T$_{sys}$ compared to the values estimated by the OT at the declination of the source and for a fixed PWV (the maximum value under which the observations can be carried out at the representative frequency). This means that for an array with more than 43 antennas, the requested RMS will be typically reached in a shorter exposure time than planned. While in the end, the average FF of the BLD should match that of the expectation, there will be bins with lower and higher FFs than the corresponding expectation depending the BLs added to the real distribution by the extra antennas. For example, if the extra antennas add short BLs, there will be an excess of these BLs and a deficit in medium to long BLs to reach the same RMS (we note that a relative EF, EF divided by the number of executions, of unity may also be reached due to a low T$_{sys}$, in which case the shape of the BLD would not be affected, only its absolute normalisation).

Second, and perhaps more importantly, as shown in Figs. 6.6-6.8, some antennas are not placed in the pads of the nominal C43 configurations and extra pads are used (note that this may result in a mismatch of the observed vs expected BLD also in the case that only a total of 43 antennas are available).

Finally, when extra antennas are available, the scheduler may discard some for the calculation of the L80 AR. For example, a given SB may be scheduled in a configuration that is slightly more extended than requested if there are extra antennas in the array adding to long BLs that could be discarded for the AR estimate. In such a case, the fractional angular resolution (FAR) will be negative (see Fig. 6.5) and we expect that robust parameters larger than 0.5 will have to be used during imaging to recover the PI requested AR. The effect in the BLD could be that the FFs will be below/above expectation for short/long BLs, respectively. A variation of this case is that when the scheduler discards antennas at short BLs resulting in a FAR > 1, but that case rarely occurs.

In what follows we evaluate these three effects. Looking at the average number of antennas, for Set 1, Group 0 shows the best BLD match as expected. For Set 2 however, the best match seems to be that of Group 1, which may be due to the fact that the BLD of Groups 0 seems to have a slightly coarser representative AR than that of the corresponding L80, thus resulting in a large excess of short BLs. When looking at the mean visibility hours it is also clear that for Group 2 the excess of antennas results in an overall higher sensitivity and a lower number of missing visibility hours in the intermediate bins. This is also observed when looking at the relative EF ("efrel"), but in contrast to Figs. 7.5-7.6, in Fig. 7.7-7.8 Group 2 (corresponding to high values of efrel) does not seem to show a significantly worse match compared to Group 1, indicating that the high EF are perhaps caused mainly by values of T_{sys} lower than those considered for the estimates rather than the total number of antennas. A similar effect is observed when looking at the ratio of achieved vs requested RMS. A larger relative EF is expected to be directly correlated with a lower ratio of achieved vs requested RMS (“rmsratio”, Figs. 7.9-7.10). Thus, if the group selection were similar, we would expect Group 0 in the “rmsratio” selection to behave like Group 2 in the previous EF selection. However, from the number of MOUS that belong to each group it is already clear that the selection is not one-to-one as e.g. in the “rmsratio” selection the majority of MOUS in Set 1 belong to the group with an achieved RMS similar or better than requested (Group 0) but are probably distributed in groups 1–2 (relative EF >= 1) in the “efrel” selection. In contrast, an almost one-to-one match between relative EF and RMS ratio is observed in Set 2, for which the BLD match of Group 2 in the “efrel” selection is similar to that of Group 0 in the “rmsratio” selection.

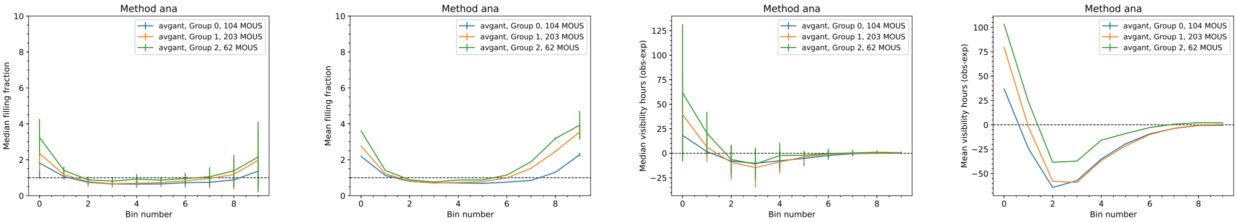

Figure 7.5: Selection on the average number of antennas for Set 1. Groups 0–2 correspond to <=43, in (43:47] and >47, respectively.

Next, we examine the effects of the second factor, namely that of the pad match to the nominal C43 configurations and the extra pads used in the arrays. Figs. 7.11-7.18 show the number of

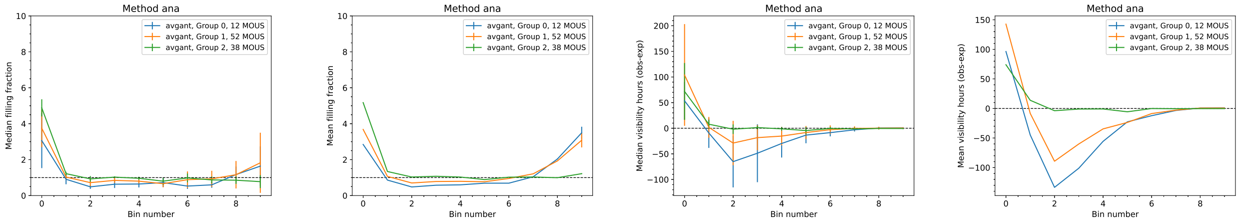

Figure 7.6: Same as Fig. 7.5 but for Set 2. Groups 0–2 correspond to <=43, in (43:47] and >47, respectively.

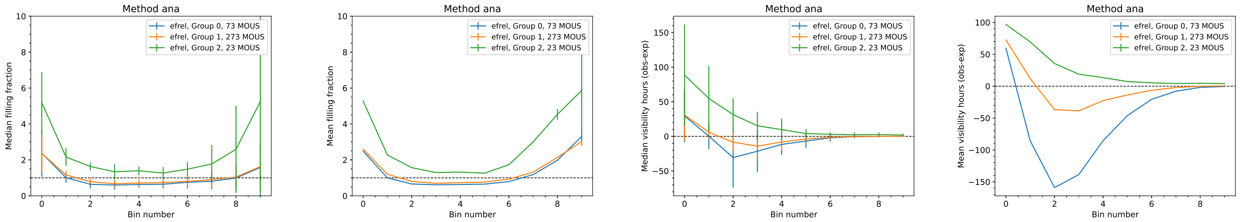

Figure 7.7: Selection on relative EF (EF/Number of requested executions) for Set 1. Groups 0–2 correspond to a relative EF <=1, 1 < EF <=1.5 and EF >1.5, respectively.

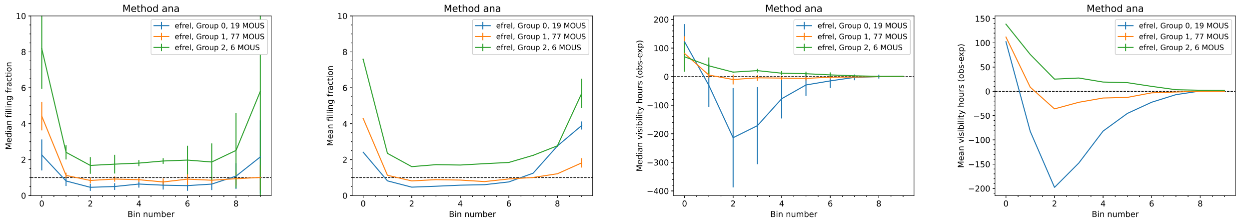

Figure 7.8: Same as Fig. 7.7 but for Set 2. Groups 0–2 correspond to a relative EF <=1, 1 < EF <=1.5 and EF >1.5, respectively.

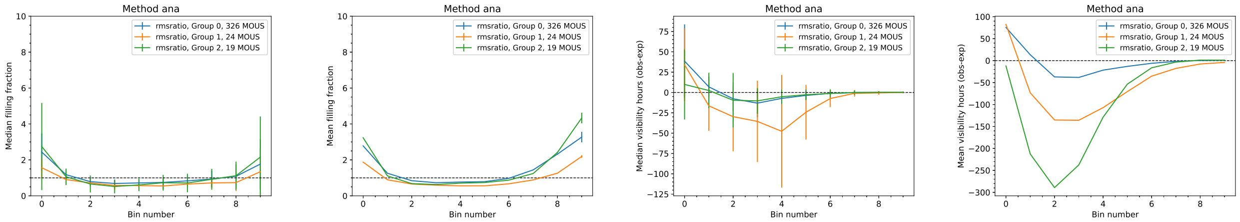

Figure 7.9: Selection on the ratio of achieved to requested RMS for Set 1. Groups 0–2 correspond to ratios of achieved to requested RMS of <=1, in (1:1.2] and >1.2, respectively.

pads that match a given nominal C43 or C43p7 configuration and the number of extra pads used. These quantities are related although they do not correlate one-to-one. For example, the fact that there are a low number of pads matching the pads of the nominal configuration is usually related to a high number of extra pads. However, there may be a high number of extra pads also due to having a high total number of antennas (even if there is a high number of pads matched to those of the nominal configurations). As shown in Figs. 6.6 and 6.8, extended configurations

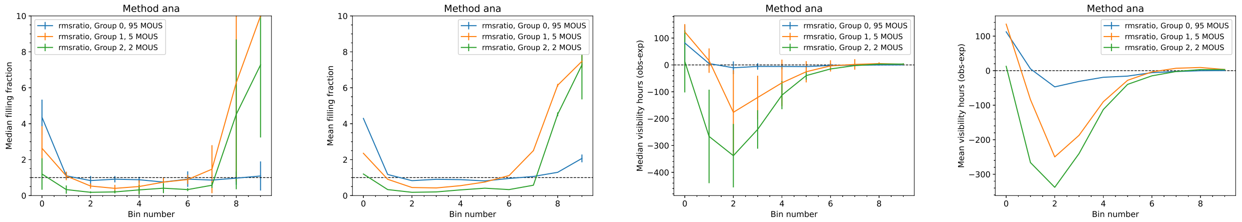

Figure 7.10: Same as Fig. 7.9 but for Set 2. Groups 0–2 correspond to ratios of achieved to requested RMS of <=1, in (1:1.2] and >1.2, respectively.

have both a low number of pads that match those of the corresponding nominal configurations and a high number of extra pads. In contrast, the more compact configurations have a low number of extra pads even in cases when there is a low number of pads that coincide with those of the nominal configurations. Configurations with intermediate BLs such as C43-4 are those with a higher number of pads matching those of the nominal configurations and an intermediate number of extra pads. Figs. 7.11-7.18 show that the number of extra pads influences the match of the BLD. For Set 1, Group 0, which corresponds to less than 6 extra pads, has a better match compared to groups 1–2. It is also apparent that for Group 2 the BLD has a representative AR, which is coarser than the L80 AR. Interestingly, MOUS with more pads matching those of the C43 and C43p7 nominal configurations (Group 2) show a large deviation from the analytical expectation. This is likely related to the fact that such MOUS have also more extra antennas. However, this effect has to be further studied as a function of configuration and disentangling the effects of having in general more antennas in the array by looking at subsets of MOUS with the same number of antennas but with different number of pad matches to the C43 configurations.

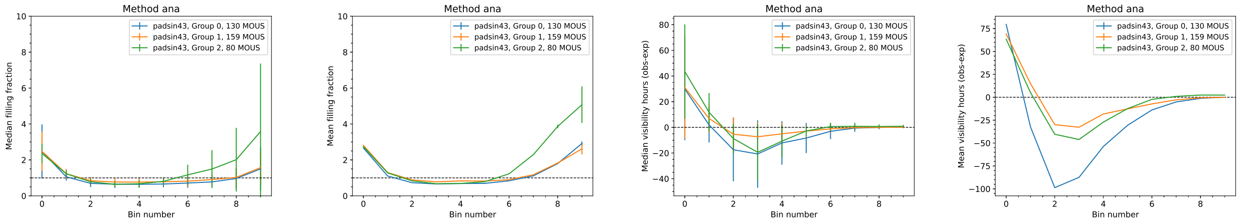

Figure 7.11: Selection on number of pads that match those of a C43 configuration for Set 1. Groups 0–2 correspond to <=37, in (37:40] and >40, respectively.

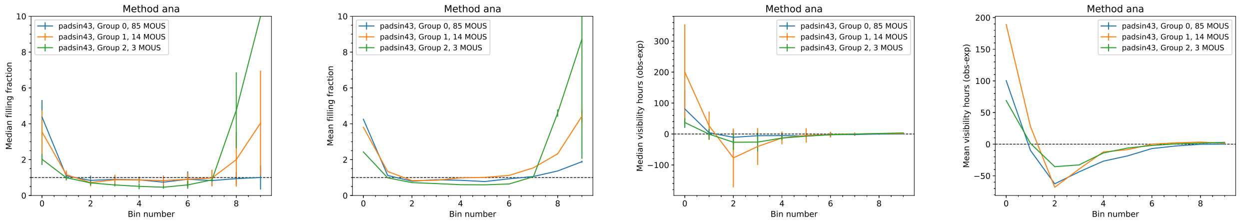

Figure 7.12: Same as Fig. 7.11 but for Set 2. Groups 0–2 correspond to <=37, in (37:40] and >40, respectively.

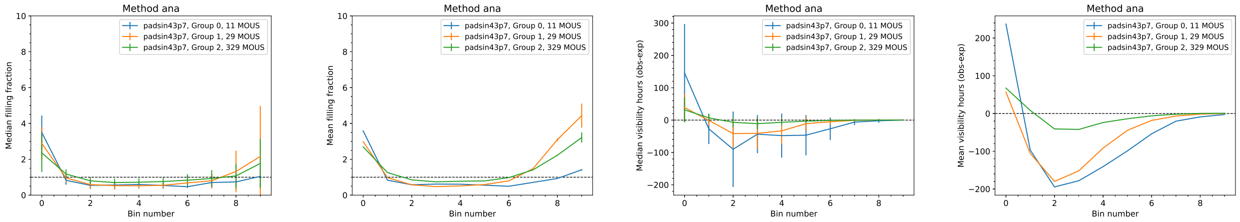

Figure 7.13: Selection on number of pads that match those of a C43p7 configuration for Set 1. Groups 0–2 correspond to <=37, in (37:40] and >40, respectively.

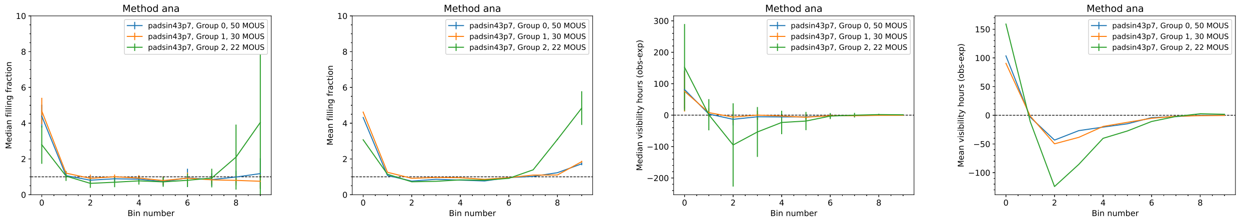

Figure 7.14: Same as Fig. 7.13 but for Set 2. Groups 0–2 correspond to <=37, in (37:40] and >40, respectively.

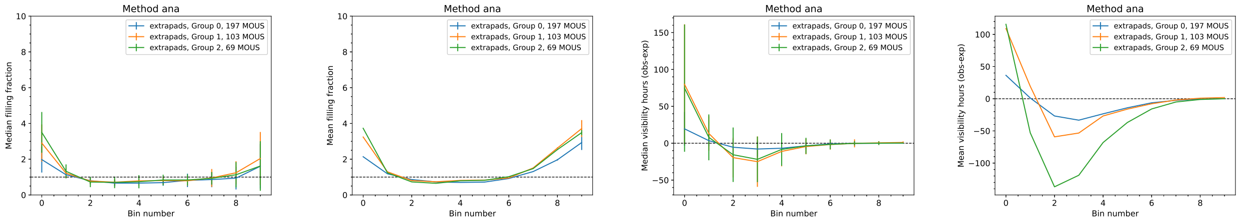

Figure 7.15: Selection on number of pads that add to those of the C43 configurations for Set 1. Groups 0–2 correspond to <6, 7-8 and >8, respectively.

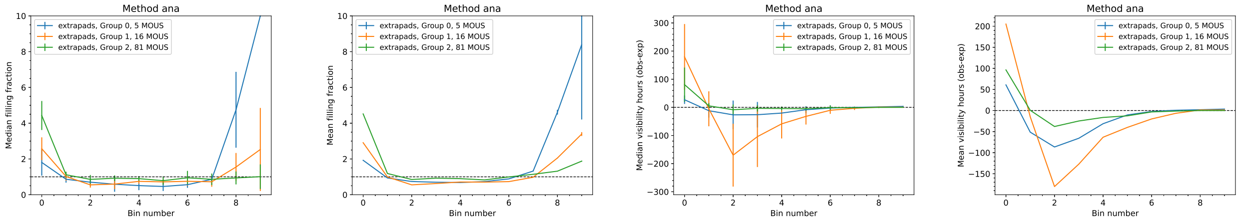

Figure 7.16: Same as Fig. 7.15 for Set 2. Groups 0–2 correspond to <6, 7-8 and >8, respectively.

Finally, we look at the effect of having antennas in the BLD that are not considered by the scheduler to estimate the L80 AR. We identified those cases by selecting on FAR. For both sets, MOUS in Group 1 show the better BLD match. This is expected since Group 1 corresponds to the MOUS for which the scheduler did not discard any antennas in the calculation of the array AR to match the requested AR. Group 0 shows a relatively good match for both sets, indicating that the effect of observing with FAR<1 is not very significant. The worst matches corresponds to FAR>1, which implies that the MOUS was scheduled in a configuration too

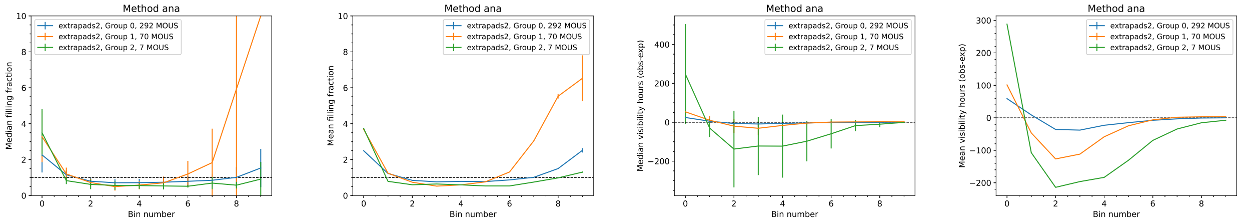

Figure 7.17: Selection on number of pads that add to those of the C43p7 configurations for Set 1. Groups 0–2 correspond to <3, 4-7 and >7, respectively.

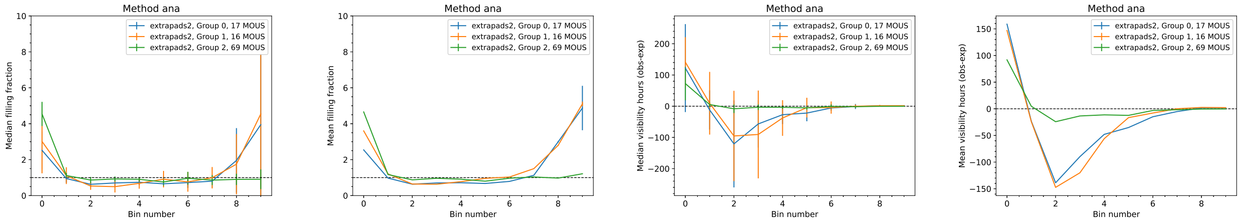

Figure 7.18: Same as Fig. 7.17 for Set 2. Groups 0–2 correspond to <3, 4-7 and >7, respectively.

compact compared to the requested one. Although it may seem puzzling that in that case the excess does not occur at short BLs but rather at long BLs and over several bins, this could be explained by the fact that a match to the L80 AR does not really capture whether the MOUS was scheduled in a configuration adequate for the SB or not. It simply indicates how well the L80 AR describes the BLD and in this particular case, the L80 AR seems to be coarser than the real BLD representative AR, which may be due to a badly formed configuration. Cases with FAR>1 are rare, and correspond to <4 and 2% of the total number of MOUS for sets 1–2, respectively, in our sample.

Regarding the robust value used by the pipeline, for Set 1 the best match is achieved for MOUS that can be imaged with a robust parameter of 0.5. Those that have to be imaged with larger robust factors are probably associated to MOUS observed with an excess of antennas at long baselines (due to either an FAR<0 or perhaps due to extended configurations not matching a large number of pads). The effect is more visible as the robust parameter increases. Interestingly, for Set 2, the best match seems to be achieved for Group 1. The L80 AR seems too coarse compared to the real BLD for Group 0 and too fine for Group 2.

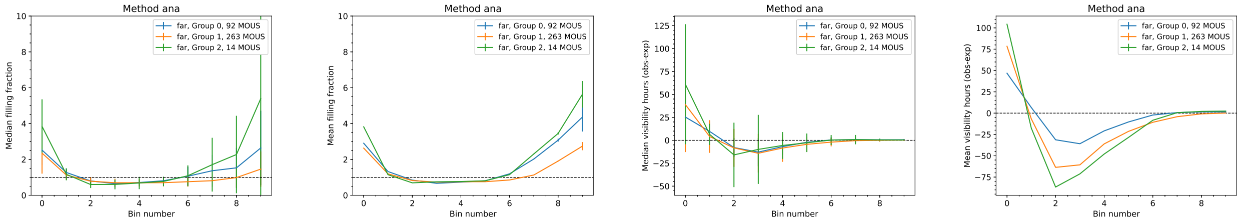

Figure 7.19: Selection on FAR for Set 1. Groups 0–2 correspond to <=0, in (0:1] and >1, respectively.

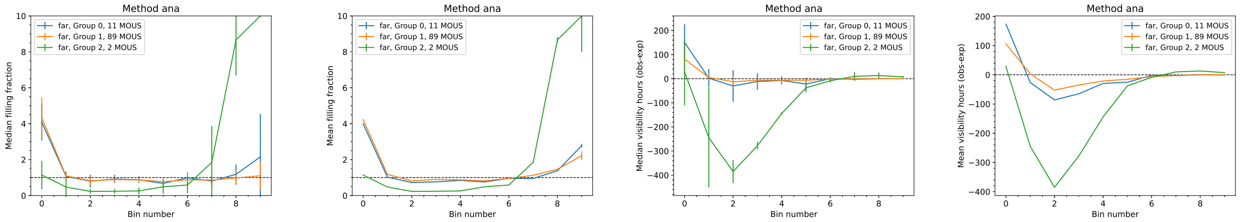

Figure 7.20: Same as Fig. 7.19 for Set 2. Groups 0–2 correspond to <=0, in (0:1] and >1, respectively.

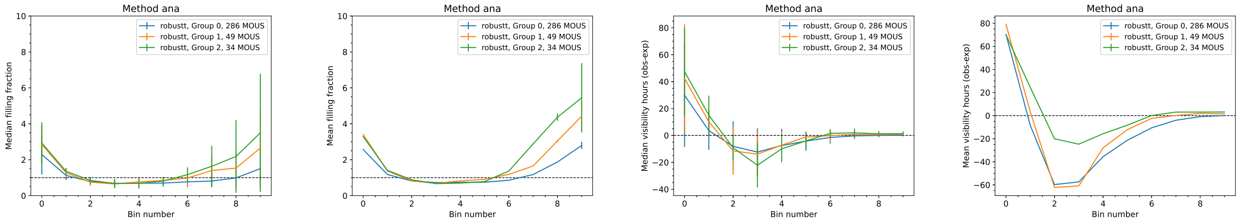

Figure 7.21: Selection on robust parameter used for imaging by the pipeline for Set 1. Groups 0–2 correspond to <=0.5, 1 and >1, respectively.

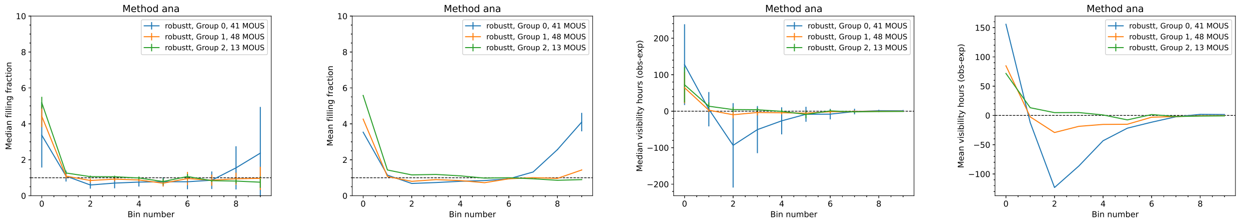

Figure 7.22: Same as Fig. 7.21 for Set 2. Groups 0–2 correspond to <=0.5, 1 and >1, respectively.

7.1.3 Effect of short exposure times

While most of the imaging expectations for ALMA have been generated using relatively long exposure times (1 hour or longer), ALMA observations are generally shorter (see Fig. 6.3 and Fig. 6.4). In our sample, the vast majority of MOUS consist of one- execution SB and the median on-source time for the full sample in Set 1 is only 23 minutes, with the most prominent peak at 5 minutes. CASA simulations performed by the scheduling WG showed that the angular resolution of a given observation is higher by a few percent (up to 10%) when increasing the on-source time from less than one minute (e.g. that used for some mosaics) to one hour due to the additional UV coverage provided by Earth rotation. Thus, we evaluate the BLD match for MOUS with different number of executions and on-source time to determine if the short exposure times also have a significant effect in the final BLD, besides on the AR. For example, one might expect that longer exposure times will result in BLDs that better match the ideal expectation due to a higher UV coverage.

Looking first at the number of executions, the overall median FF is lower for Group 2 compared to Groups 0-1. This is more clearly seen in Set 1 and is likely due to the relative EF being lower for MOUS with more than two executions since in the latter case the EF can be better adjusted by reducing the final number of executions. This results in a significant deficit of visibility hours at bins ∼1–5. In addition, for Set 2 the L80 AR seems to be coarser than that of the real BLD for Groups 1-2. This could indicate that as the number of executions increases the real BLD matches a finer AR expectation.

Regarding on-source time, although there do not seem to be significant differences among groups, the best match seems to be achieved for Group 0, namely an on-source time below 300 s, which would indicate that the UV coverage gained with longer exposure times does not necessarily contribute to a better BLD match. This needs further study, as it seems contradictory with general ideas on UV coverage for interferometers. For Set 2 the L80 AR seems to be coarser than that of the real BLD for Group 2, consistently with what is found for the number of executions. In summary, the most significant effect of long exposure times or a large number of executions seems to be that the relative EF is lower. There is no obvious worsening of the match for short on-source times, but given the low number of MOUS of this group, this effect should be studied further.

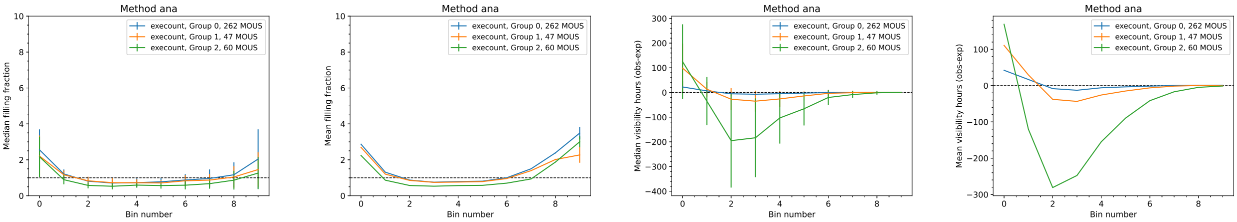

Figure 7.23: Selection on requested number of executions (execount) per MOUS for Set 1. Groups 0–2 correspond to a number of executions =1, = 2 and >2, respectively.

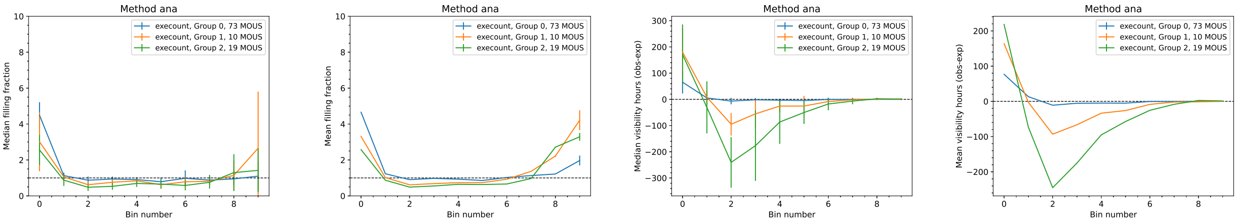

Figure 7.24: Same as Fig. 7.23 for Set 2. Groups 0–2 correspond to a a number of executions =1, = 2 and >2, respectively.

7.1.4 Effect of elevation and beam ellipticity

While most of the imaging expectations for ALMA have been generated using a declination of -23 degrees and a source transiting, the range of declinations spans between -80 and +45 degrees and not all the observations are executed at the target transit.

In average, the elevation of ALMA observations in our sample is 58/55° for sets 1/2, respectively (see Fig. 6.5 and Fig. 6.7). CASA simulations performed by the scheduling WG (QA2 beam failures analysis) showed that the AR of a given observation is up to 30% coarser for observations performed at low elevations (e.g. for a declination of 30° and HA = -3 compared to a declination

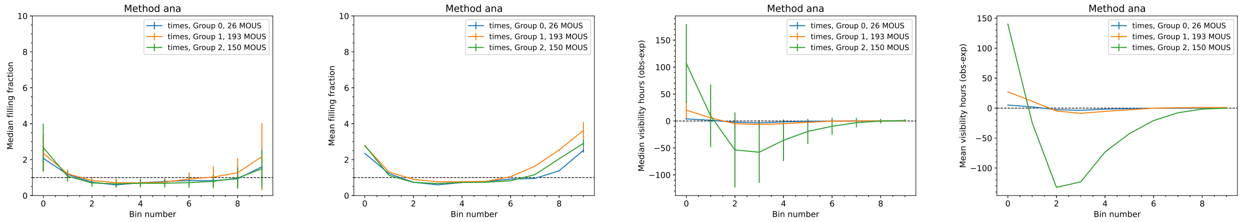

Figure 7.25: Selection on on-source time for Set 1. Groups 0–2 correspond to on-source times <=300 s, in (300:1800] s and >1800 s, respectively.

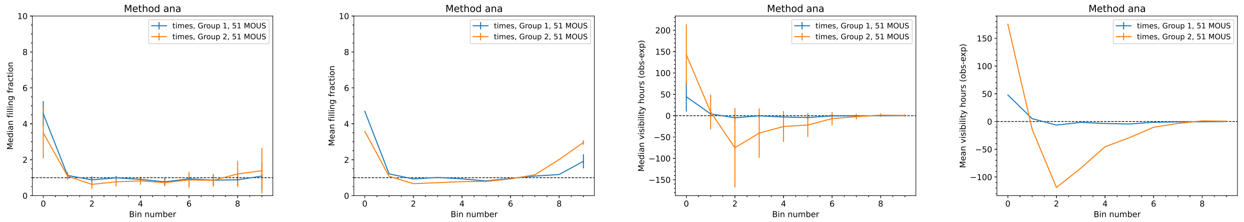

Figure 7.26: Same as Fig. 7.25 for Set 2. Groups 0–2 correspond to on-source times <=300 s, in (300:1800] s and >1800 s, respectively.

of -23° and HA = 0). Since Cycle 7, the ALMA scheduler takes into account the elevation of the target and the on-source time to schedule an observation so that targets at low elevations and with short on-source times should be observed at more extended configurations to reach the same resolution than targets at high elevations. Thus, the purpose of evaluating the BLD match for MOUS with different elevation (given by a combination of declination and HA) is to determine if at lower elevations the match is worse due to the BLD being skewed towards shorter baselines. This could be visible for C43p7-9 in Set 1 since according to Fig. 6.5 those MOUS have been observed at the lowest elevations. Since a skewed distribution will also result in more elliptical beams, selecting on the ellipticity of the beam obtained in QA2 should also reveal some differences among the selected groups. However, it is not clear at which value of the ellipticity such differences would arise. While large beam ellipticities are generally associated to low elevations, the design of the configurations is also an important factor. For example, Fig. 7.9 of the THB (Remijan et al. 2019) indicates that the ellipticity is larger at -23° (zenith at the ALMA site) than at -40° or at 10°, although the exact values are different for each configuration.

Looking first at the effect of target elevation, the best BLD match is found for Group 1, or MOUS observed between 40 and 70° of elevation. This is in agreement to expectations since the configurations have been designed to have more circular beams and thus closer to ideal expectations for elevations close to 60-70°. In contrast, at low elevations (Group 0) the L80 AR seems to be coarser than that of the real BLD in both sets.

Looking at beam ellipticity, for both sets, the worse match is found for Group 2, or MOUS with the largest ellipticity, as expected. For this group the L80 AR seems to be coarser than that of the real BLD, consistent with the finding that the group of MOUS observed at lower elevation suffers from the same issues (see above). However, it is interesting that in absolute terms, for Set 2, Group 0 presents a larger deficit of visibility hours at intermediate bins.

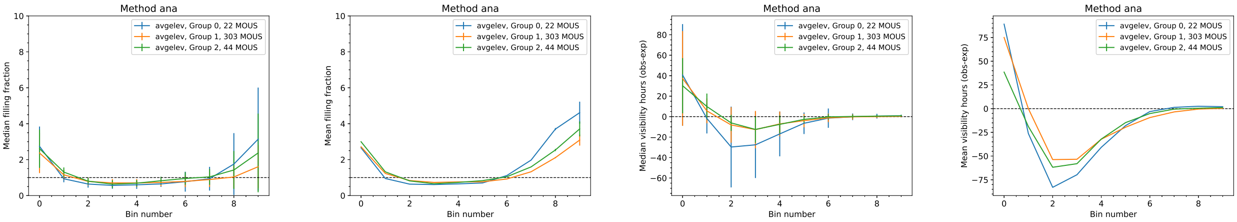

Figure 7.27: Selection on the average elevation for Set 1. Groups 0–2 correspond to an elevation <=40°, in (40°:70°] and >70°, respectively.

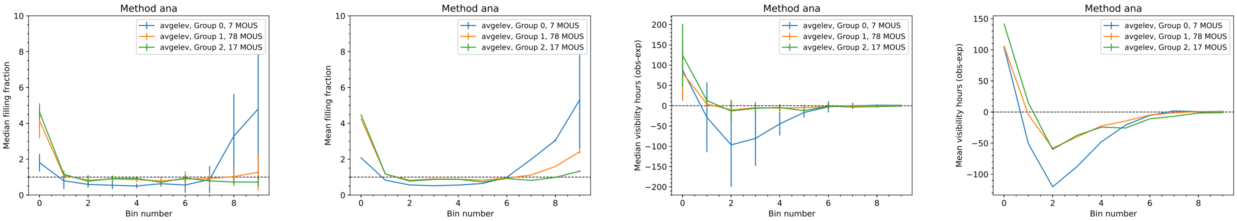

Figure 7.28: Selection on the average elevation for Set 2. Groups 0–2 correspond to an elevation <=40°, in (40°:70°] and >70°, respectively.

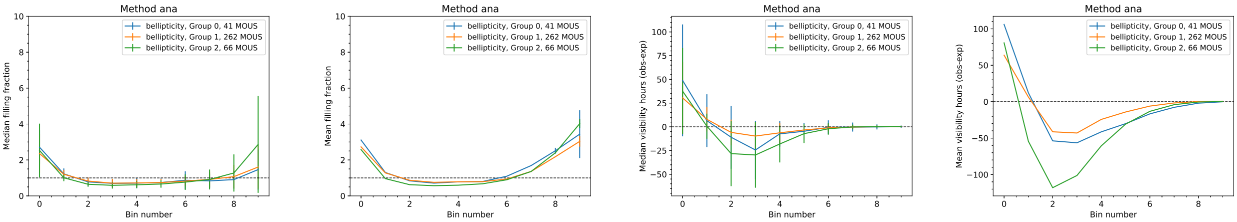

Figure 7.29: Selection on the beam ellipticity for Set 1 where the ellipticity has been calculated based on the QA2 beam. Groups 0–2 correspond to an ellipticity <=1.1, in (1.1,1.5] and >1.5, respectively.

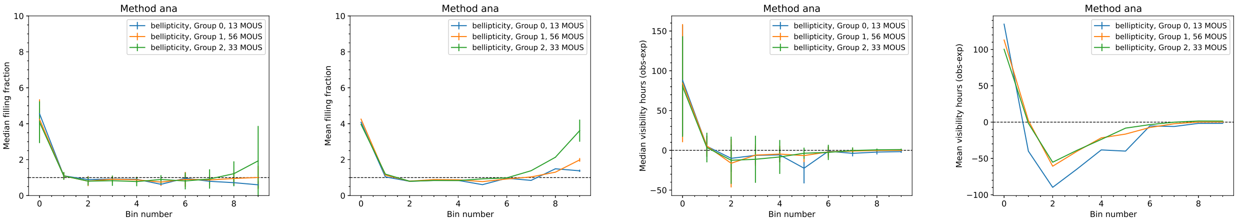

Figure 7.30: Selection on the beam ellipticity for Set 2 where the ellipticity has been calculated based on the QA2 beam. Groups 0–2 correspond to an ellipticity <=1.1, in (1.1,1.5] and >1.5, respectively.

7.1.5 Effect of a large LAS

We expect that SGs requesting a large ratio between LAS/AR (>∼18) will not be met with observations in one configuration only. We test this in chapter 8.

7.2 Large deviations of observed vs expected BLD and their causes

In this section we show a few examples of especially bad matches of the observed BLD and the expected one and their potential causes. They are intended to highlight the worse matches that can be obtained with the current operational constraints and that may result in imaging issues but still won't be identified with the current QA2 procedures.
All the examples shown correspond to MOUS that have passed QA2. Fig. 7.31 indicates that the origin of the bad BLD matches is likely different. For example, for SB 8982-610_a_03_TM1, the abrupt change of number of BLs at 100-150 m is likely caused by flagging due to shadowing. In contrast, SB SMC_YSO_b_07_TM1 has a tail of BLs at long BL lengths, which seem a left-over from a previous more extended configuration and SBs IRAS_165_a_06_TM1 and DL_Tau_a_03_TM1 show BLDs that are far more elongated than the analytic expectations.

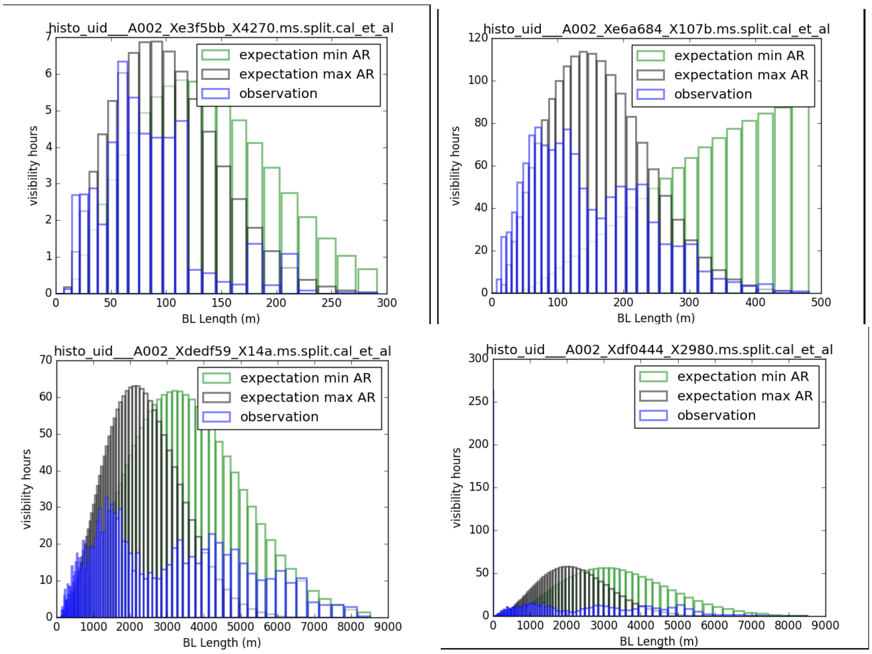

Figure 7.31: Observed BLD (blue) compared to expected distribution for the minimum expected AR (green) and the maximum expected AR (grey). From top to bottom: MOUS corresponding to SBs 8982-610_a_03_TM1 (extreme flagging due to shadowing causing a significant drop of BL between ∼120-160 m), SPT0348_a_03_TM1, SMC_YSO_b_07_TM1, IRAS_165_a_06_TM1, DL_Tau_a_03_TM1.

7.3 AR match to the BLD

A key parameter for the BLD match is the AR used to calculate the expectation. However, previous studies (see Scheduling WG reports 1 and 2[1]) have shown that the L80 AR does not always match the AR obtained in QA2. Fig. 7.32 shows an example of a BLD that is not well

---

[1] https://confluence.alma.cl/display/DSOSCHED/Data+quality

Table 7.2: Examples of MOUS with a few bins of the BLD reaching FF below 60%.

Project code	SB name	C43/C43p7/OT	EF	On-source time	Lowest FF	# bins with < 0.6 FF
2019.1.01136.S	8982-610_a_03_TM1	2/2/2	1.0	111.3	0.1	4
2019.1.00779.S	SPT0348_a_03_TM1	3/3/345	1.2	6531.5	0.4	5
2019.1.00534.S	SMC_YSO_b_07_TM1	4/4/4	1.0	1814.0	0.2	6
2018.1.01656.S	IRAS_165_a_06_TM1	8/8/8	1.0	6912.6	0.2	3
2018.1.00614.S	DL_Tau_a_03_TM1	8/8/8	1.0	6313.8	0.1	5

match to expectations when the L80 AR is used. In constrast, Fig. 7.33 shows a case for which the QA2 AR differs significantly from the L80 AR and while the latter shows a good match to the BLD, the former clearly is coarser than the representative AR of the BLD. A systematic study of the changes of the L80 AR as a function of source elevation and configuration is needed to understand when the L80 AR predictions have systematic deviations from the representative AR of the BLD (see also sect. 7.5).

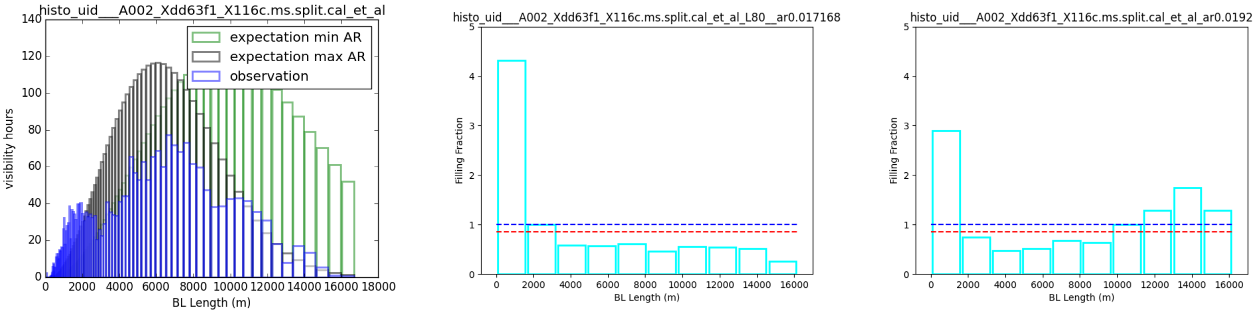

Figure 7.32: Left: Observed BLD (blue) compared to expected distribution for the minimum expected AR (green) and the maximum expected AR (grey). Middle: match of the BLD for the corresponding L80 AR. Right: match of the BLD for the AR that best represents the AR of the observed BLD. The distributions correspond to SB W_Hya_a_06_TM1. The blue and red horizontal dashed lines in the middle and right plots mark a FF=1 and a FF=0.85, respectively.

7.4 ALMA configuration design and practicalities

The configurations in use for ALMA have been re-designed from the original 28 (+ 28 north-south extensions) 50-antenna configurations ("C50") requiring 4 moves between each configurations and covering all angular scales reachable with the 12-m array in order to reflect the availability of X(<50) antennas. For imaging optimization the ACDC algorithms was used, an ALMA developed brute-force variant of the principles established with the APO algorithm (Boone 2001, 2002), most notably a Gaussian aperture target uv distribution. For Cycle 4, 9 40-antenna configurations ("C40") were devised from every third C50 with 12 antenna moves allowed between them. For Cycle 5 10 43-antenna configurations ("C43") were devise extending

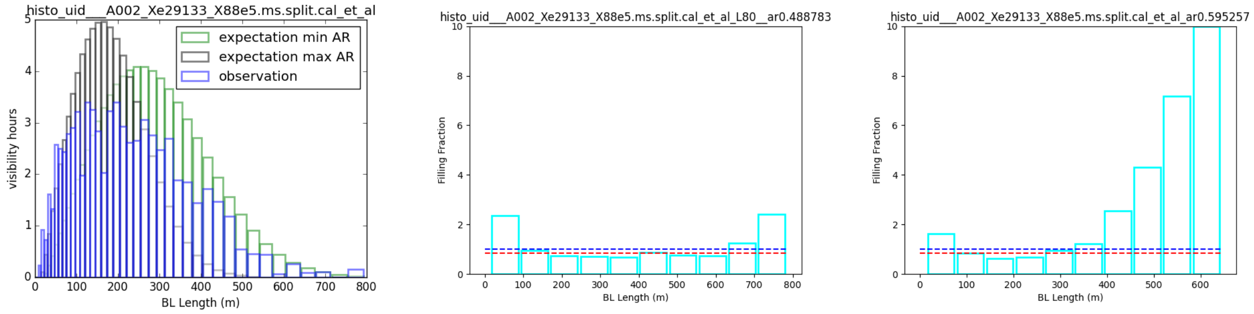

Figure 7.33: Left: Observed BLD (blue) compared to expected distribution for the minimum expected AR (green) and the maximum expected AR (grey). Middle: match of the BLD for the corresponding L80 AR. Right: match of the BLD for the QA2 AR. The distributions correspond to SB Serpens_a_06_TM1. The blue and red horizontal dashed lines in the middle and right plots mark a FF=1 and a FF=0.85, respectively.

up to 16 km, but restricting the number of moves for C43-1 to C43-8 to 8 in order to help operations, and are still in use as of Cycle 8. The remaining 7 antennas were assigned to low priority pads typically belonging to the next compact configuration in order not to afford extra moves ("C43p7"). For an overview of the resulting properties of the aforementioned configurations Figure 7.34 shows the cumulative 1D length distributions of all baselines.

The design algorithm can provide highly regularly shaped and spaced configurations even with a reduced number of antennas and even slightly improved compared to the ALMA C50 standard configurations as is demonstrated with the C40 configuration. The differences that can be seen between the configurations show that C40 are most concentrated in length / uv space with regular Gauss-like distributions. The move restrictions introduced in Cycle 5 resulted in a progressive stretch of the configurations from more compact to extended, apart from the longest baseline configuration 9 and 10 affording more moves. In addition the C43p7 configurations when all antennas are considered (or removed from the array in an un-prioritised way) stretch further in uv-scales, with C43p7-X effectively providing hybrid C43-X-1 + C43-X configurations. The effect is a flattening of the Rayleigh 1D distributions compared to the C-40 examples, which needs to be considered in relation to the analytical expectation function.

7.5 Match of the nominal configurations to analytical expectations

The results in Sects. 7.1-7.2 highlight the effect that some operational parameters have in the final BLD distribution of a given observation and its match to an ideal BLD distribution. However, as already pointed out in sect. 7.1.1, even the nominal configurations will differ from the ideal BLD distributions. While in sect. 7.1.1 we used real data averaged over a given configuration to already pinpoint differences between configurations, in this section we go a step further and show examples of the BLD match of the C40 and C43 nominal configurations to the analytic expectations for different positions of astronomical targets. This evaluation intends to explore what are the best BLD matches that we can aim at (free of other operational constraints) and helps setting a limit for the minimum FF that we want to ensure with the QA method

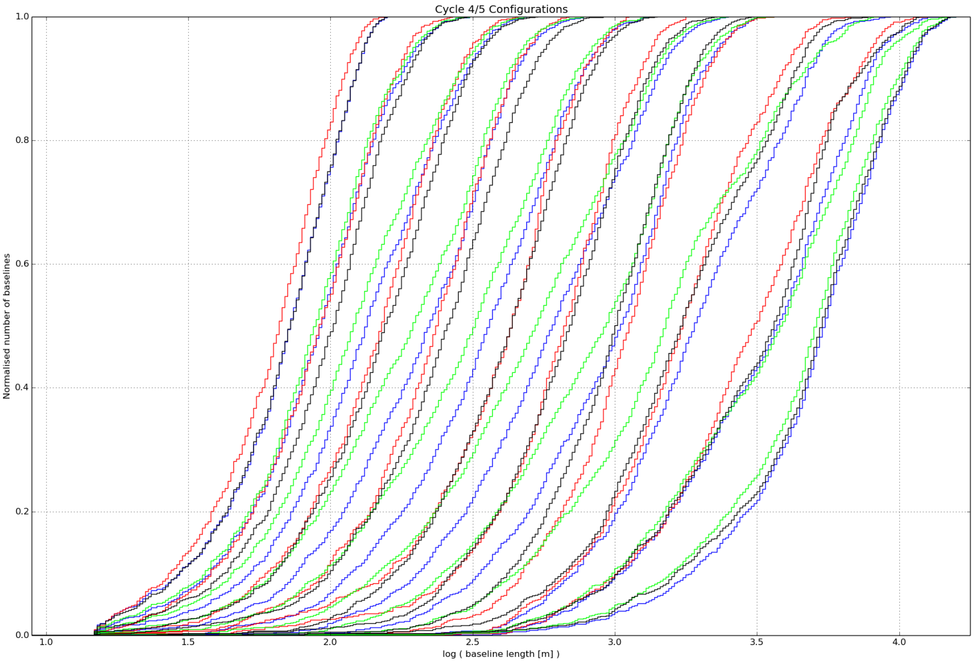

Figure 7.34: Cumulative baseline length distributions for the ALMA configurations C40 (red), C43 (blue), C43p7 (green) and C50 (black); see text for details.

investigated in this report. Comparing the C40 and C43 configurations is instructive since the C43s resulted from limiting the number of moves between configurations compared to those of the C40s. Such move limitation resulted partially in more elongated configurations (see sect. 7.4), which are likely at the origin of the excesses observed at short BL and long BLs and the deficits at intermediate BLs, although clearly further operational constraints have made such excesses/deficits more prominent in some cases.
Figs. 7.35-7.40 show the BLDs of configurations 3, 7 and 9 (both for C40 and C43 designs and for a series of declinations and hour angles of observation) compared to the analytical expectation based on the AR that best matches the BLD and the L80 AR (see also Table 7.3). We observe the following:

- Except for C43-3 (Fig. 7.36), the L80 AR is finer than the AR that results in a best match to the BLD.
- For the AR that results in a better BLD match, the match of the C40s is in general better than that of the C43s. However, there are differences between the compact and extended configurations with C40-3 having an almost perfect match but C40-9 showing already excesses at short and long baselines.
- While all the C43 configurations show an excess at short and long baselines due to their elongated shape compared to analytic expectations, there are differences in the depth of the deficits, these being less prominent for C43-7 compared to C43-3 and C43-9.

Conf.	Number of bins < 0.85 FF				Number of bins < 0.60 FF			
	Dec/HA -20°/-1	Dec/HA -20°/1	Dec/HA -40°/-1	Dec/HA 0°/-1	Dec/HA -20°/-1	Dec/HA -20°/1	Dec/HA -40°/-1	Dec/HA 0°/-1
C40-3	0	0	0	1	0	0	0	1
C43-3	3	3	3	3	0	0	0	0
C40-7	1	0	2	4	0	0	0	1
C43-7	1	2	1	1	0	0	0	0
C40-9	4	4	4	5	1	1	0	1
C43-9	3	3	3	3	0	0	0	0

Table 7.3: Number of bins with less than 0.85 and 0.60 FF for the examined configurations, source declinations and hour angles of observation when the BLD is matched to that of the expected BLD for the representative AR. A caveat is that we have used the same AR for all the source positions of a given configuration. Therefore, if the BLD for a given configuration is very sensitive to the position in the sky of the observed source, this will cause a large number of bins with deficits for positions for which the representative AR of the BLD has significantly changed. For example, this is the case for C40-7, for which a representative AR of $0.225''$ is adequate for a declination of -20° but not for a declination of 0°, which is represented by a coarser AR (see Fig. 7.37).

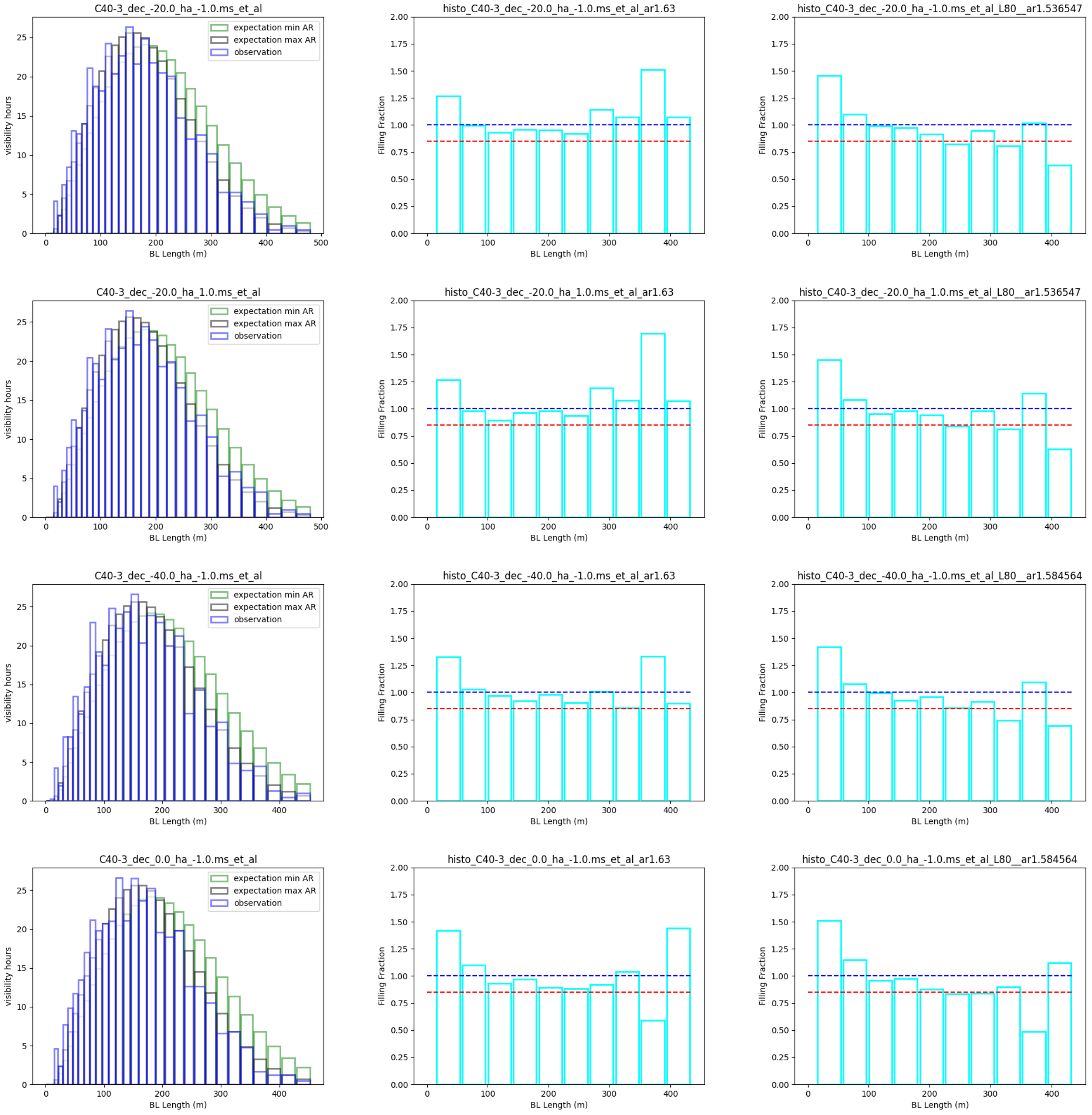

Figure 7.35: Observed BLD (blue) compared to expected distribution for minimum (green) and maximum AR (grey) and an observation of 30 minutes with the C40-3 nominal configuration. Middle and right: match of the BLD for an observation of 30 minutes with the C40-3 nominal configuration for a fixed AR (see the specific AR in the plot) and for the L80 AR (right). From top to bottom: source with a declination of -20° and at HA = -1 h, source with a declination of -20° and at HA = 1 h, source with a declination of -40° and at HA = -1 h and source with a declination of 0° and HA = -1 h. Minimum and maximum AR are 1.42 and 1.63″, respectively. The blue and red horizontal dashed lines in the middle and right plots mark a FF=1 and a FF=0.85, respectively.

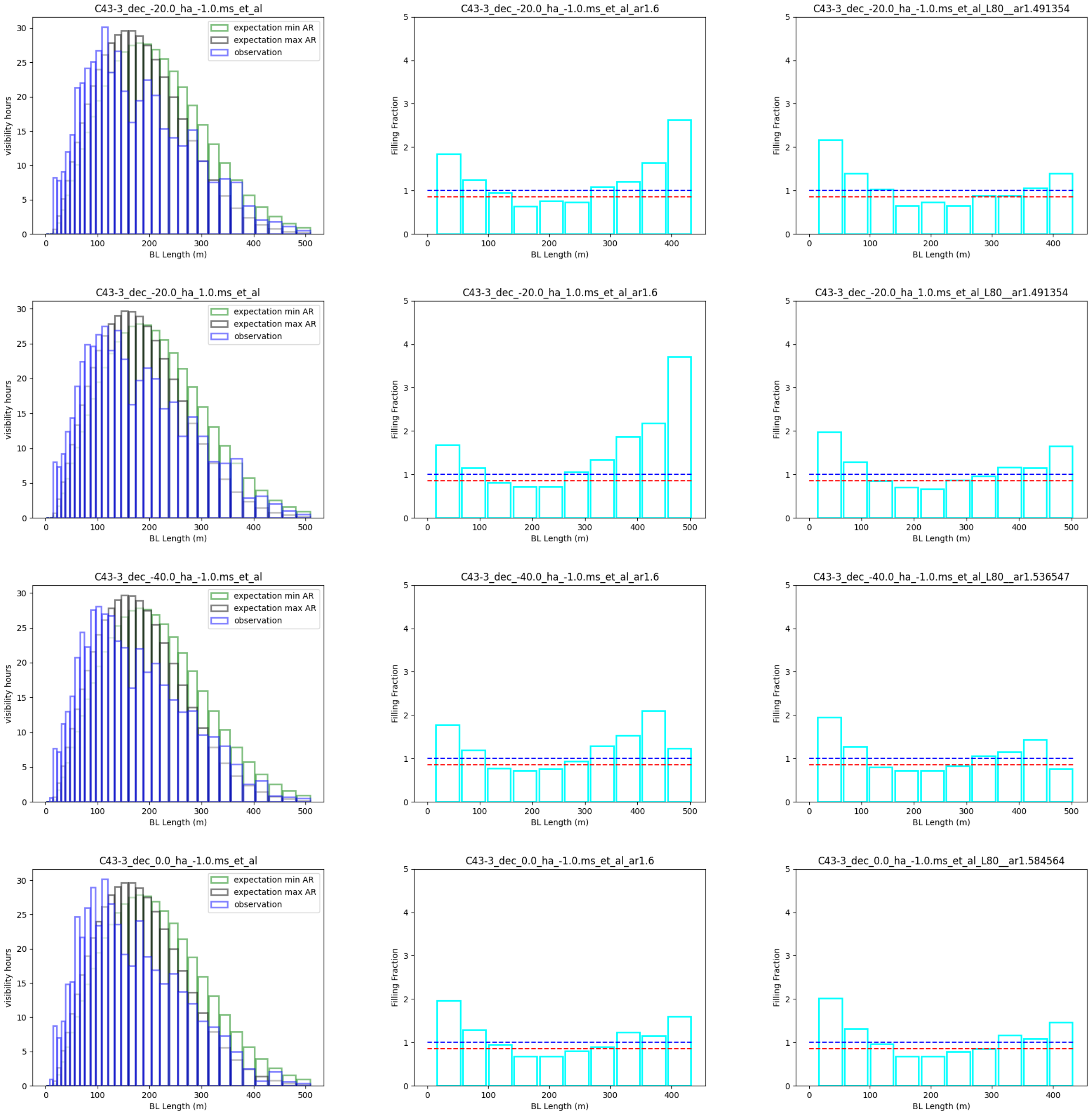

Figure 7.36: Same as Fig. 7.35 but for the nominal configuration C43-3. Minimum and maximum AR are 1.42 and 1.63″, respectively.

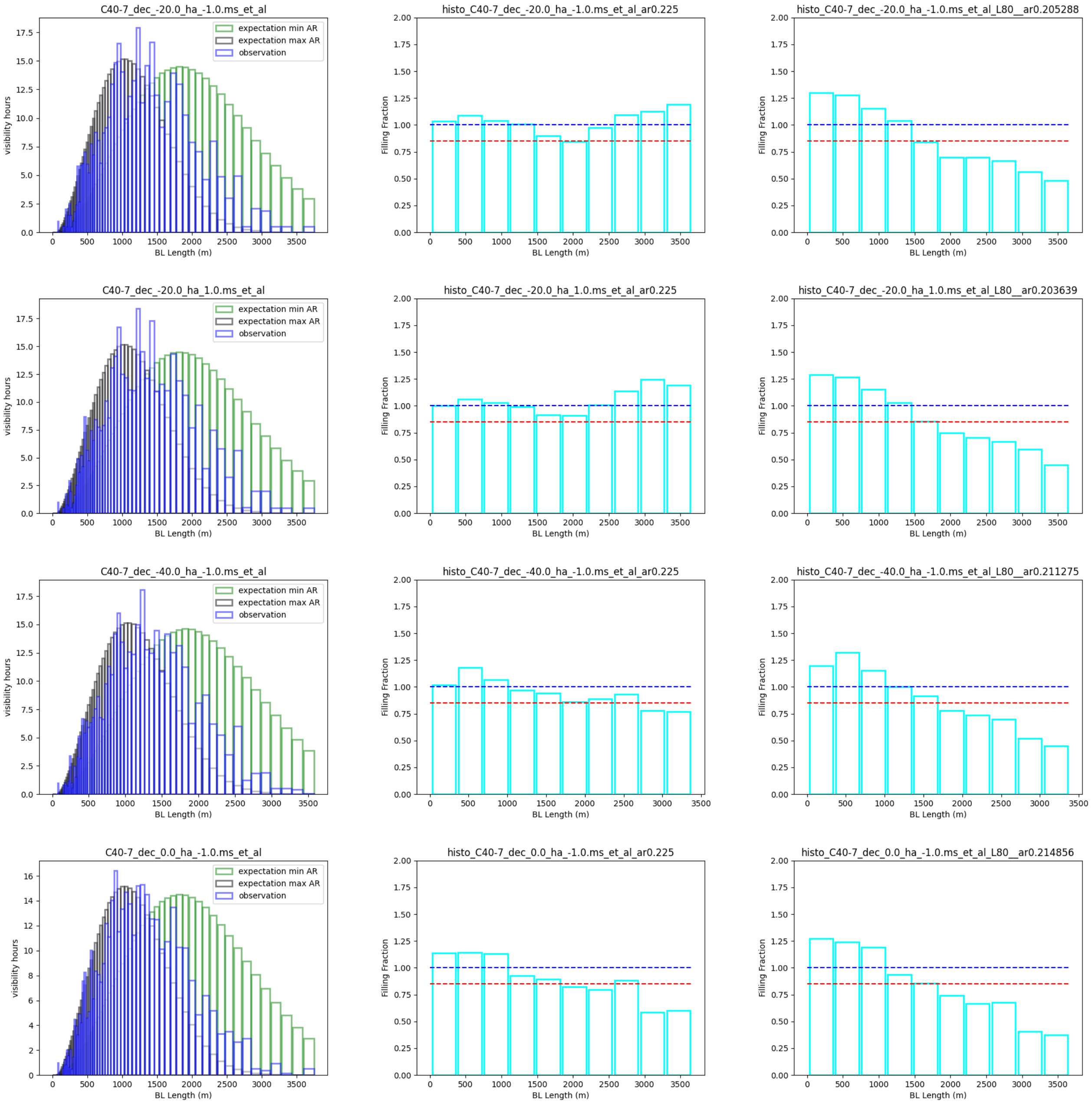

Figure 7.37: Same as Fig. 7.35 but for the nominal configuration C40-7. Minimum and maximum AR are 0.168 and 0.273″, respectively.

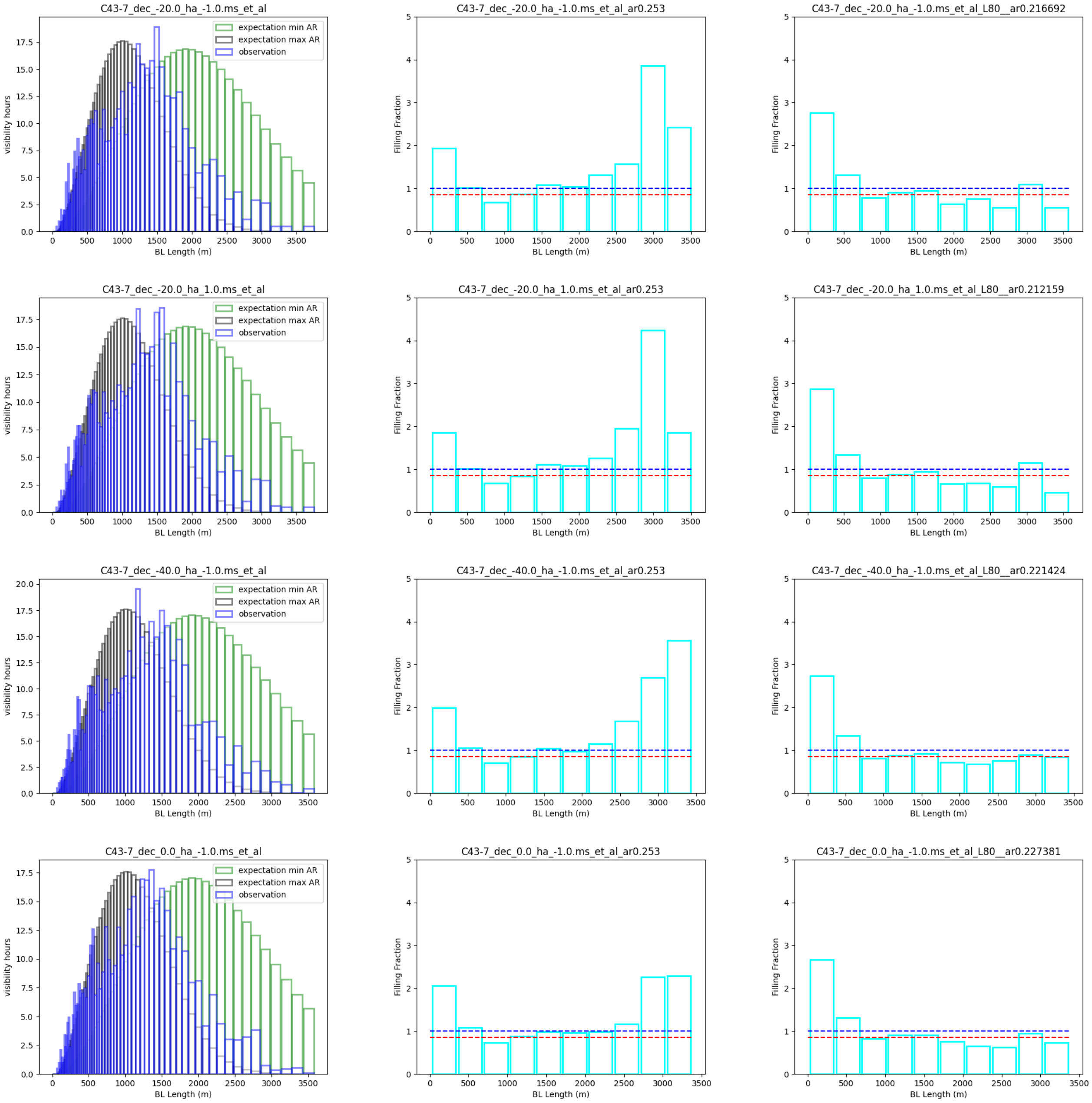

Figure 7.38: Same as Fig. 7.36 but for the nominal configuration C43-7. Minimum and maximum AR are 0.16 and 0.274″, respectively.

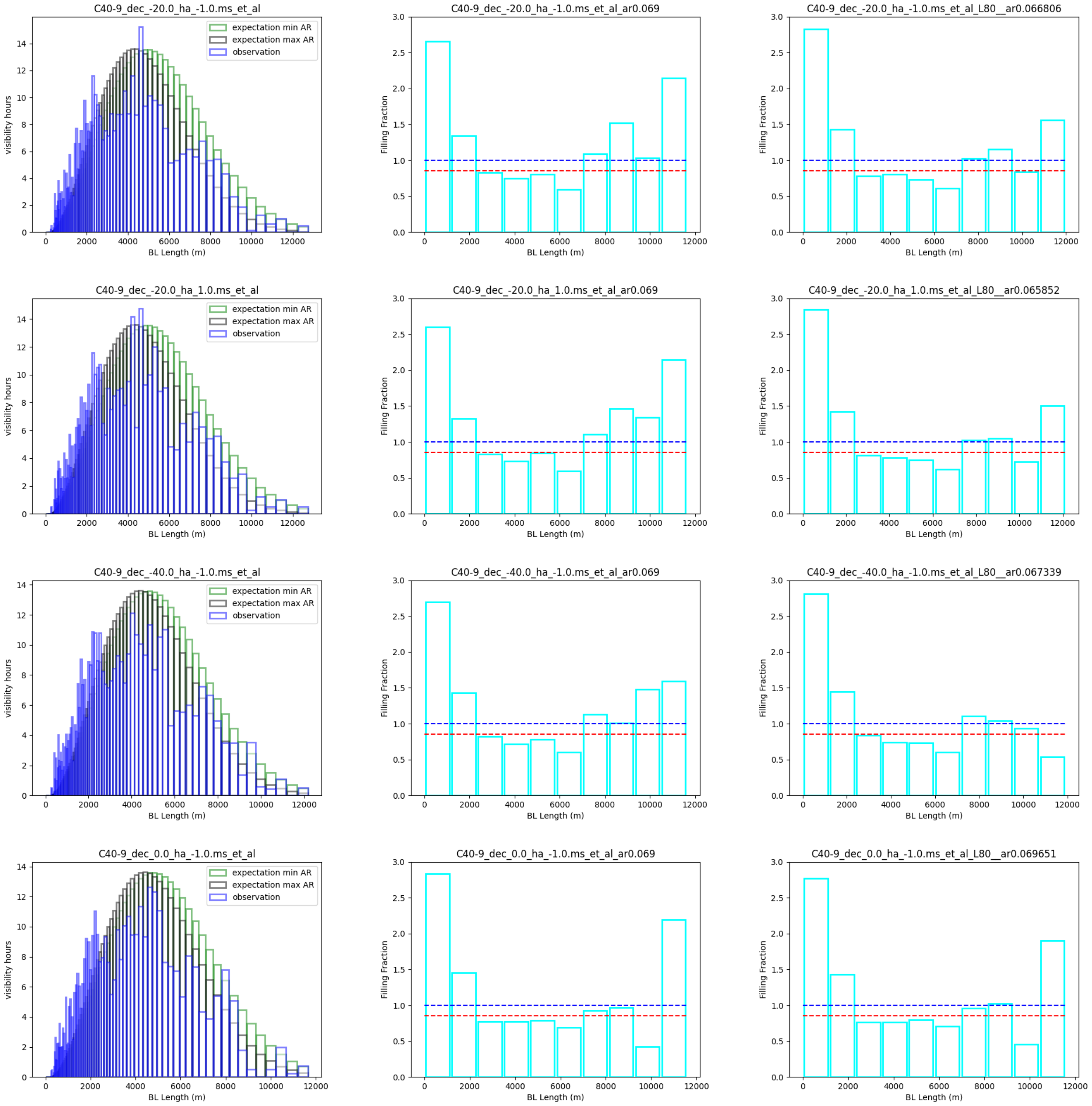

Figure 7.39: Same as Fig. 7.35 but for the nominal configuration C40-9. Minimum and maximum AR are 0.062 and 0.071″, respectively.

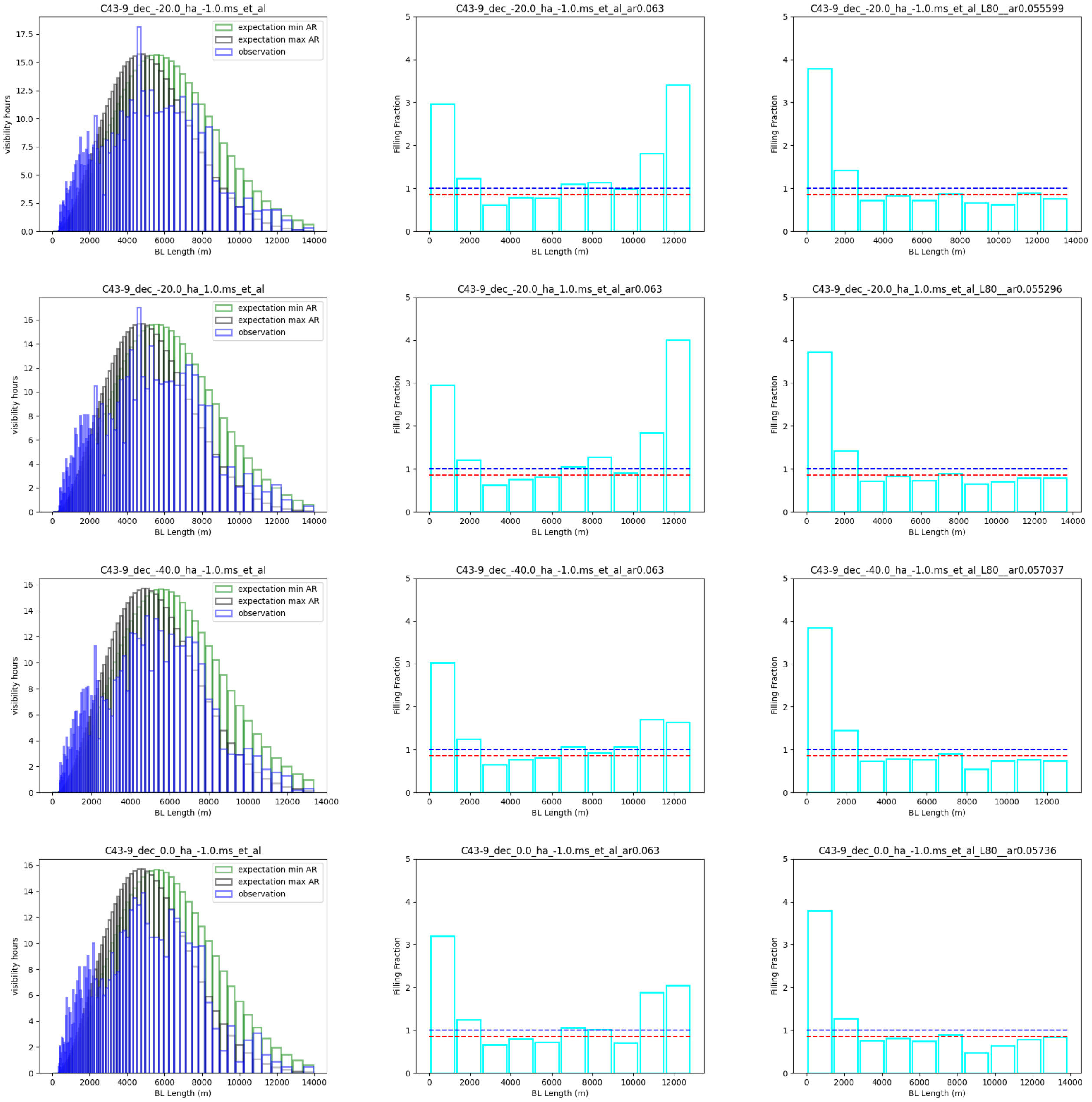

Figure 7.40: Same as Fig. 7.36 but for the nominal configuration C43-9. Minimum and maximum AR are 0.055 and 0.065″, respectively.

7.6 Summary

The results of sect. 7.5 highlight the need of making a systematic comparison of the BLD match for all the nominal configurations and a range of source declination and HA of observation for determining how the BLD differs as a function of different observational parameters. It is expected that at least for the compact configurations the C43s are a worse representation of the analytic BLD compared to the C40s as it is observed for configuration 3. This effect is amplified during real operations due to observational constraints but some parameters have a stronger effect than others. For example, based on the results of this chapter, the BLD match is not improved for MOUS with a higher number of executions or longer on-source times.

In addition, it is clear that the L80 AR is not always representative of the AR of the BLD. In this sense, it is important to explore alternatives to determine the AR such as fitting the BLD with an iterative method that searches the best match of the observed and ideal BLD.

We note here that the design of the ALMA operational configurations was driven by the desire to provide good imaging results with short, single executions and some consideration of longer tracks for the LB configurations, but no attempt was made to provide optimization over combinations of configurations. Indeed, the majority (>80%) of SGs in ALMA projects require executions in a single configuration only. For the BLD approach this means that the task of providing good uv coverage over executions in different configuration may be more challenging, implementing the approach could be more rewarding by possibly elevating the need for modified configurations to be designed and used specifically for multi-configuration imaging.

8 Evaluation of BLD match for GOUS with TM1/TM2 MOUS

We evaluated the suitability of the TM2 configuration to fill the short baselines of GOUS for which observations in two configurations were scheduled to match the SG requested AR and LAS. Table 8.1 lists the GOUS used for the evaluation.

Table 8.1: Properties of the GOUS sample

Project code	SB name	OT Conf.	Int. time
2019.1.01132.S	NGC1482_b_03_TM1	4	2963.42
	NGC1482_a_03_TM2	1	2116.7
2019.1.01034.S	DEEP2_33_a_06_TM1	5	2207.42
	DEEP2_33_a_06_TM2	2	574.46
2018.1.00452.S	B335_b_06_TM1	6	1572.38
	B335_b_06_TM2	3	393.02
2018.1.01055.L	MWC_480_b_06_TM1	7	9905.924
	MWC_480_b_06_TM2	4	2842.36
2018.1.00659.L	RW_Sco_d_06_TM1	8	489.788
	RW_Sco_d_06_TM2	5	120.86
2018.1.00659.L	SV_Aqr_d_06_TM1	8	1923.164
	SV_Aqr_d_06_TM2	5	423.26
2018.1.00659.L	U_Her_a_06_TM1	8/9	798.236
	U_Her_a_06_TM2	5/6	181.34
2018.1.00659.L	U_Del_a_06_TM1	8/9	1759.868
	U_Del_a_06_TM2	5/6	393.02

8.1 Methods

For the evaluation we added the visibilities of the two MOUS belonging to each GOUS. Then we compared the result to an expectation calculated by using the AR expected for the TM1 MOUS, the LAS requested by the SG and the sum of the on-source time of the TM1 and TM2 MOUS. We used CASA 6.1 and assess_ms v1.35 for analysis.

8.2 Results

Figs. 8.1–8.2 show the observed BLDs for the MOUS corresponding to the TM1 configuration (left) and for the full GOUS (right) compared to the expected BLDs for the minimum and maximum AR in the AR range. The expectation curves have the same shape for the TM1 MOUS and the GOUS but the overall normalization is lower for the former due to their shorter on-source time. In general, the TM2 MOUS do not seem to be adequate to complement the TM1 in the sense that they add BLs where there are already enough (mostly in the first bin of the BLD). A potential reason for this may be that with the growing number of antennas and the range of AR requested by PIs, the configurations that complement themselves in order to reach a given set of AR and LAS are not uniquely determined any longer.

Figs. 8.3-8.4 show the FF for a subset of the GOUS in Table 8.1 for the MOUS corresponding to the TM1 configuration (left) and for the full GOUS (right) with respect to the BLD expected for the QA2 AR of the TM1 MOUS and the LAS of the corresponding GOUS. The coverage of short angular scales does not show a significant improvement when the full GOUS is considered.

Fig. 8.5 shows the match of the observed BLD for the TM1 configuration only to the analytic expectation generated with the requested AR/LAS for Set 2/1, that is, for the MOUS that belong to a GOUS that includes a TM1/TM2 pair or TM1 configuration only, respectively. It is remarkable that the excess of short BLs is already larger for Set 2 than for Set 1, despite the fact that the corresponding TM2 MOUS has not been added yet. Another interesting remark is that in all analyses performed in sect. 7.1, Set 2 does not show a significant deficit of short BLs in general compared to Set 1.

A more thorough analysis is needed to determine how to best proceed in cases for which the LAS is not met uniquely with one configuration. An evaluation of the BLD as performed in this study may be the first step in this direction.

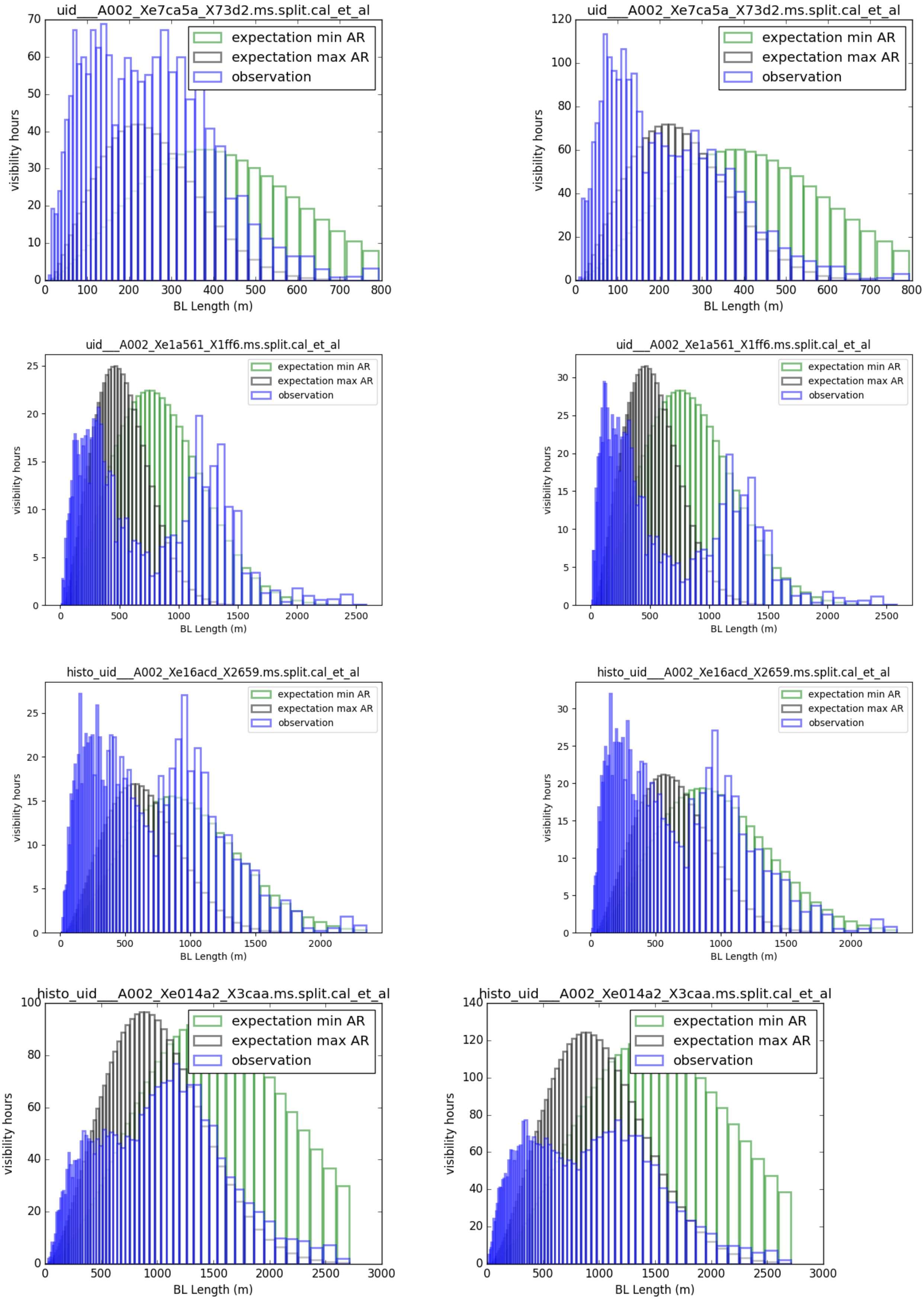

Figure 8.1: Observed BLD (blue) for TM1 (left) and TM1+TM2 (right) compared to expected distribution for the minimum expected AR (green) and the maximum expected AR (grey). From top to bottom: NGC1482_a/b_03, DEEP2_33_a_06 and B335_b_06 and MWC_480_b_06.

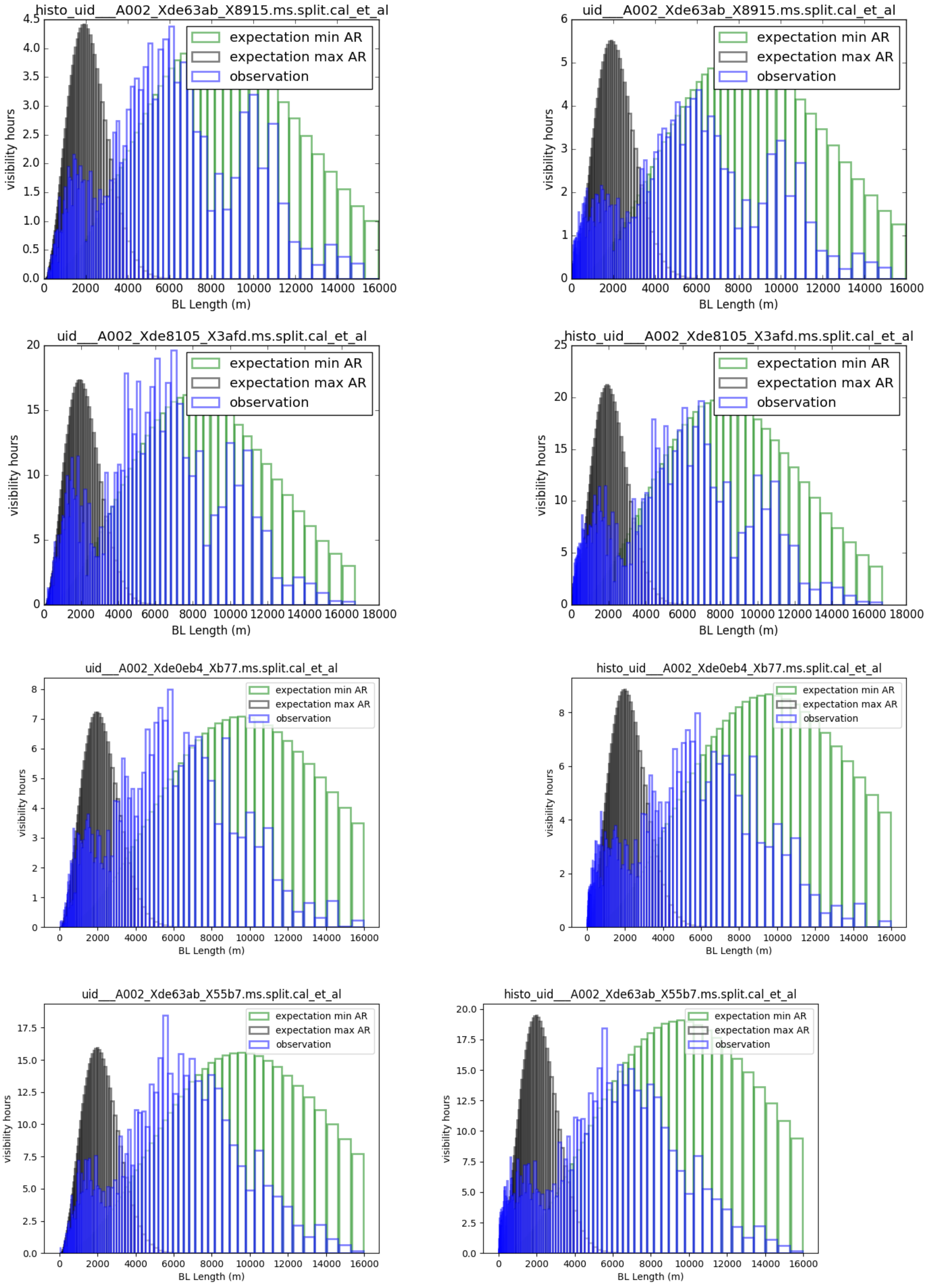

Figure 8.2: Continuation from Fig. 8.1. From top to bottom: RW_Sco_d_06, SV_Aqr_d_06, U_Her_a_06 and U_Del_a_06.

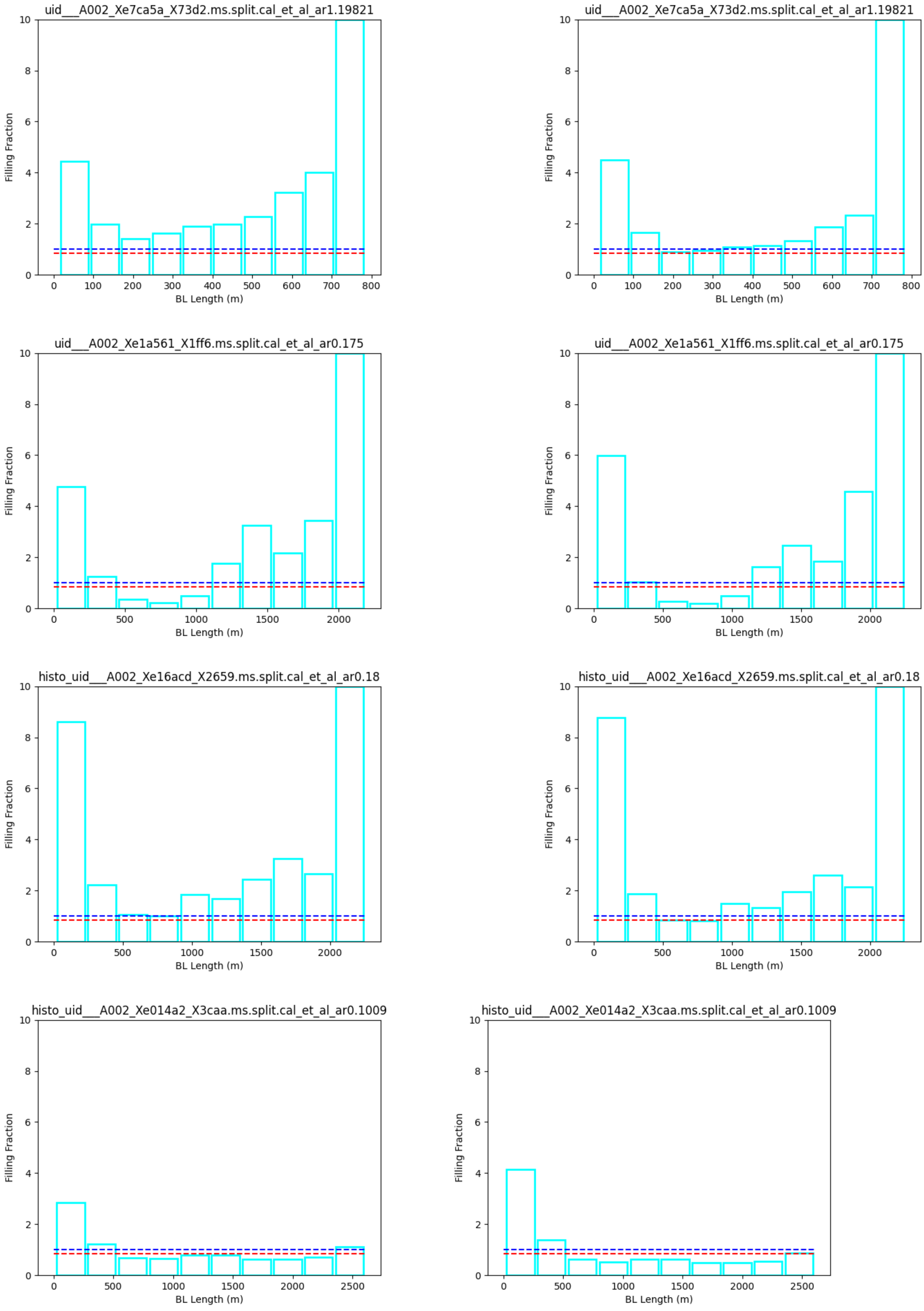

Figure 8.3: FF for TM1 (left) and TM1+TM2 (right). From top to bottom: NGC1482_a/b_03, DEEP2_33_a_06 and B335_b_06 and MWC_480_b_06. For calculating the expected AR we used the QA2 AR. The blue and red horizontal dashed lines mark a FF=1 and a FF=0.85, respectively.

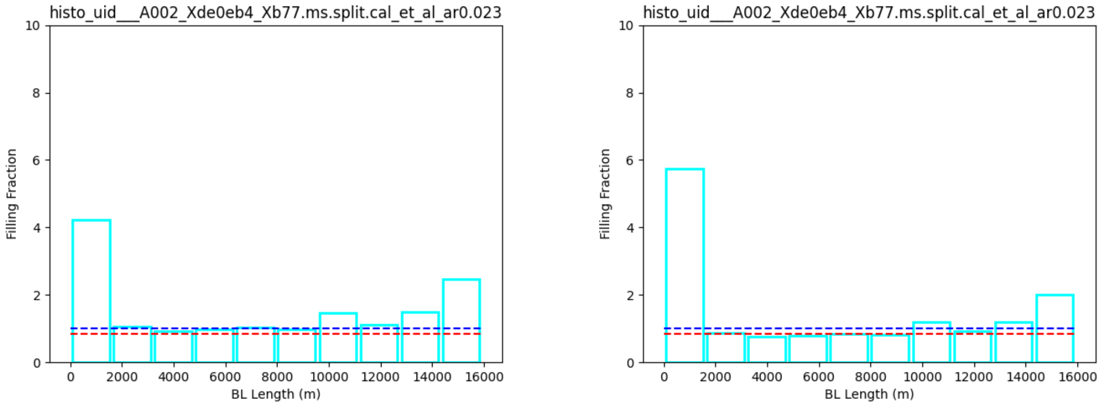

Figure 8.4: Continuation from Fig. 8.3. From top to bottom: U_Her_a_06.

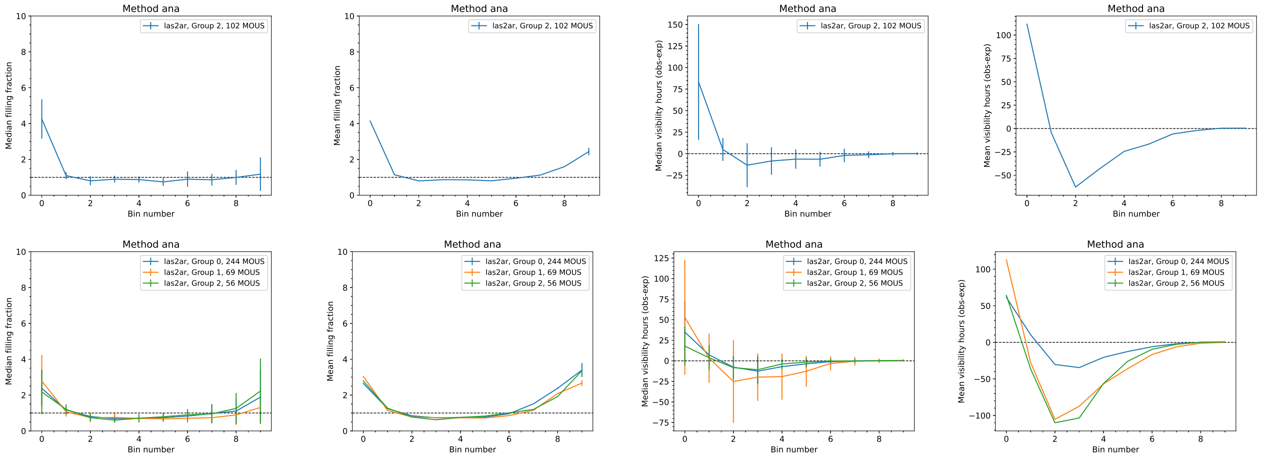

Figure 8.5: Upper row: selection on the ratio of LAS/AR where AR is calculated via the L80 formula for Set 2. Group 2 corresponds to an LAS2AR >12. Lower row: selection on the ratio of LAS/AR where AR is calculated via the L80 formula for Set 1, for which all MOUS have LAS2AR <15. Similarly to Figs. 7.5–7.30, horizontal lines refer to a FF of one (left and middle-left panels) and to the same number of observed and expected visibility hours (middle-right and right panels).

9 Scheduling

This chapter highlights how Scheduling could proceed if a BLD scheme was to be used.

The Scheduling task is central to the optimisation of the observatory operation because it is the moment when the data quality is determined and can only be adjusted in very moderate terms afterwards. This is true for meeting all scheduling conditions. Here we particularly investigate the imaging quality in terms of uv coverage determined by the projected baseline visibilities collected during the observation depending on the antenna positions in the array and the astronomical target source position.

Even though it is so important, the Scheduling task is last to be addressed, after PI request and OT, configuration planning, reduction and related quality assurance, so that it can incorporate all backward and forward constraints in the optimal way. In other words, the Scheduling task has to be optimised with respect to the final reduced data and reconstructed images considering the quality assurance criteria based on the PI request, or otherwise it would be incomplete.

We therefore have not yet arrived at a detailed Scheduling concept in this development study, and certainly not at a concrete implementation suggestion. We have considered some relevant scheduling aspects already and describe them in the following in this chapter.

9.1 Scheduling-relevant immediate lessons learned

It is the main idea, of course, of this investigation to evaluate where the data quality can be improved. In principle this starts with the configurations determined by the pad layout, an algorithm following design principles to optimize imaging, but also practicalities in operations related to an affordable number of relocation antenna moves and imperfections in the available array due to maintenance and repair of antenna failures. The evaluation extends via long term scheduling and planning with the OT configuration prediction to Dynamic Scheduling, where finally the data quality is fixed and has to be justified against time and conditions in relation to all projects. The task is complex with many parameters and priority weighting functions entering, but a detailed imaging component to the equation is missing without tracking the complete uv information for every project. A later adapted weighting is a repair operation with the cost of loss in sensitivity. From the above investigations on BLD of past ALMA data and on the baseline weighting with resulting imaging performance we can draw already important conclusions for relevant aspects to be considered in Scheduling.

How will this study help to simplify the selection of SBs to execute, based on what the PI requests, what the current array looks like, and the history of previous executions of the SB (if any)?

To start with, the BLD approach allows us to evaluate to a good approximation *before* the execution in the most detail possible what that angular scale coverage will be and how it relates to the request of the PI in quantitative terms. Currently executions happen largely based on pre-determined OT configuration choices with a check on the current vs. requested angular resolution (L80), but not on a comparison over the full range of requested scales.

As chapters 6 and 7 show, the vast majority of all, but in particular TM1, data sets shows a significant excess in filling fraction for the first two bins. So the second(ary) TM2 executions would not be needed. In particular, for Set 1 (see chapters 6 and 7), 98%(76%) of the MOUSs show an excess in the first(first and second) bin. For the MOUSs that show an excess in the first two bins, the mean excess is 2.98 and 1.35 FF in the first and second bin, respectively. For Set 2, 98%(72%) show an excess in the first(first and second) bin. For the MOUSs that show an excess in the first two bins, the mean excess is 4.72 and 1.28 FF in the first and second bin, respectively. This implies that for Set 2, even before adding the TM2, the excess in short BLs is similar or even larger to that of Set 1. Thus when the BLD scheduling approach is implemented, the majority of TM2 executions can be avoided or considerably shortened, with a considerable saving potential of observing time on the 12-m array.

There is at least one clear example, where only 16% shadowing in a compact configuration seems to cause a rather severe outlier case in the BLD (see Fig. 7.31, SB 8982-610_a_03_TM1). Thus, the predicted uv coverage would need to consider the impact of shadowing correctly in order to prevent such cases and offer optimized solutions.

In the imaging simulations it had been found that a robust evaluation of the imaging quality based only on a weighting adjustment of the 1D component (BLD) of the uv coverage distribution is difficult to determine. Rather the orthogonal axis of azimuthal variation in coverage also contributes to the quality and adds scatter and uncertainty to the results. Quite directly, the beam ellipticity and individual beam sidelobes depend on it. And, the filling of a whole uv track, which for several executions ALMA rarely facilitates in consecutive executions, can only be optimized against HA and the varying arrays, when the 2D uv information is available. While it is still unclear how much can be achieved in Scheduling to fill uv holes, the concept of filling sufficiently all uv pixels is clear.

For single execution SBs the benefit of the BLD approach, particularly when extended to 2D, is that all factors determining the uv based imaging quality, that is actual array with eventual irregularities, hour angle together with declination and observation duration can be considered correctly and factored into the scheduling weights depending on criticality. Specifically it is always possible to optimize coverage between two competing executions for different SBs or different execution times of one SB. As an intuitive example, imagine an array that happens to be elongated in the NW-SE direction, when clearly for a northern target later executions with a positive HA would be preferred over early negative HA executions for a more circular beam.

Finally we have found extreme cases of sub-optimal BLD, also caused by incomplete arrays, which can happen during relocation periods and antenna recovery phases. There the approach rather than optimising scheduling between SBs with different imaging requirements could use the algorithm to recognize such situations and decide against scheduling imaging projects but instead those with the least stringent imaging requirements, detection experiments, point sources, certain line studies, etc.

9.2 Scheduling based on BLDs

9.2.1 An Example from the Scheduler Prototype

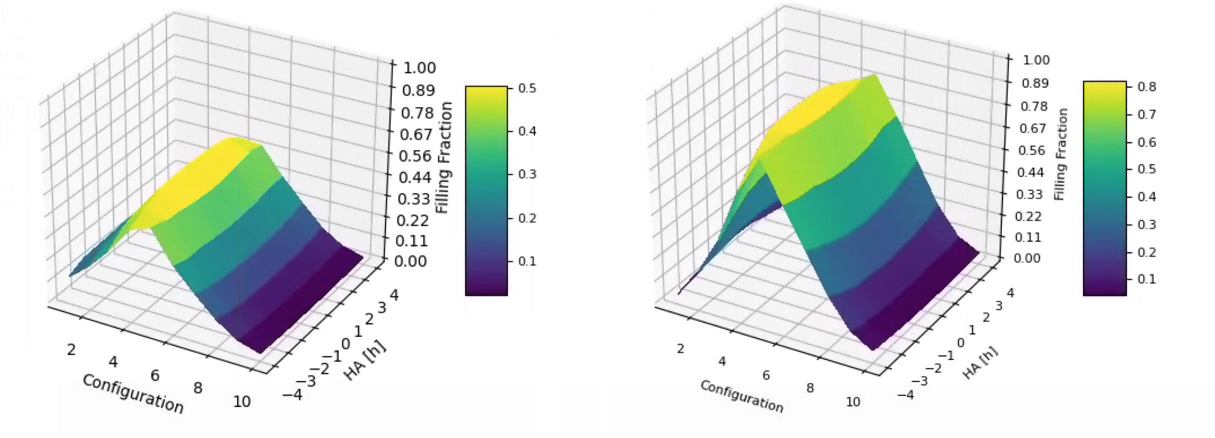

Figure 9.1: An ALMA observation requiring two scheduling block executions in Band 7 with an angular resolution of 0.3 arcseconds can be scheduled optimally in configuration C-4 at hour angles between -2h and +2h, with C-5 also allowed in the second execution. The scheduling options are given as the achieved total filling fractions on the z-axis as a function of configuration on the x-axis and hour angle on the y-axis. This scheduling projection assumes for the second execution that the first execution has been scheduled with maximal total filling fraction. The filling fraction of the second execution refers to the remainder of the first, resulting in over 90% completion of the observation.

ALMA distinguishes long and short term scheduling tasks relating to project pressure over seasonal conditions, e.g. weather pattern, day/night phase conditions, configuration schedule, and the daily aspects, e.g. available antenna array, actual weather conditions. In the following we describe our new scheduling approach, which aims at maximising the filling fraction in the relevant bins and quantifies execution completion in terms of filling the expected BLD in order to avoid scale based re-weighting at reduction, which reduces sensitivity of the data and efficiency of the observing:

1 - Determine expected BLD: Given the science goal parameters of target Declination (DEC), requested sensitivity, LAS, and AR range (i.e. minimum and maximum acceptable AR), the expected BLD of the MOUS is calculated.

2 - Find best-matching ALMA configuration and observation hour angle: Based on a library of BLDs created from detailed simulations of observations with different ALMA array configurations (see description below, this is different from what is described in section 3.2.2), find the optimal ALMA configuration C_{opt} and observation hour angle HA_{opt} which achieve the highest total filling fraction f_a. This is illustrated by Fig. 9.1.

3 - Observe first/next EB: When the array is moved into C_{opt} and weather conditions are appropriate, schedule the SB for execution at HA_{opt}.

4 - Compare observed BLD with expected BLD: Using, e.g., the metric described in section 3.3, determine whether the first EB already fulfills the expectation for the MOUS. If it is "pass", declare the observation complete. When applying the metric, iterate over the whole range of expected BLDs, from the smallest AR value up to the largest.

5 - Determine the remaining necessary observations, i.e. new expected BLD: In case step (4) results in a fail, i.e. the latest EB did not complete the observation, *subtract* the BLD of the latest EB from the expected BLD for the MOUS and declare the remainder the new expected BLD.

6 - Re-iterate from step 2: with the new expected BLD go back to step (2) and determine a new best configuration and HA. Repeat the loop until the observation is declared complete in step (4) or the observing period for the given SB has ended.

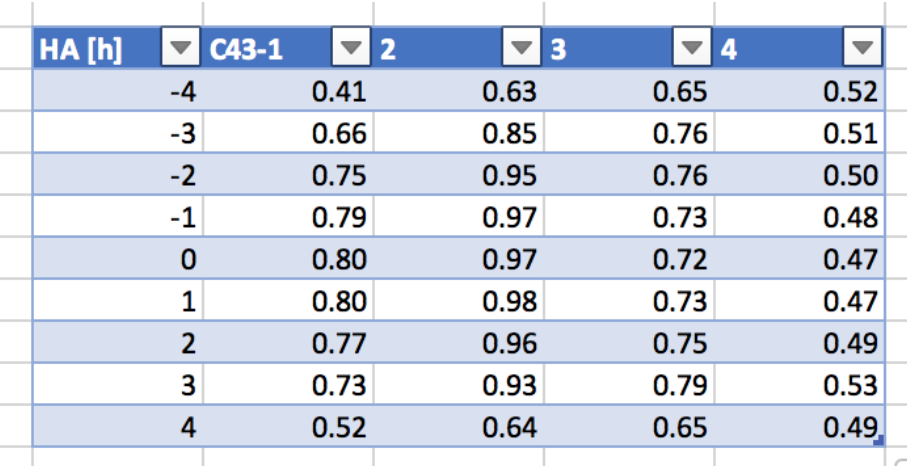

HA [h]	C43-1	2	3	4
-4	0.41	0.63	0.65	0.52
-3	0.66	0.85	0.76	0.51
-2	0.75	0.95	0.76	0.50
-1	0.79	0.97	0.73	0.48
0	0.80	0.97	0.72	0.47
1	0.80	0.98	0.73	0.47
2	0.77	0.96	0.75	0.49
3	0.73	0.93	0.79	0.53
4	0.52	0.64	0.65	0.49

Figure 9.2: Table of filling fractions determined by the scheduling algorithm for a PI angular resolution request targeting C43-2 with a single execution.

The library of simulated BLDs needed in step (2) of the algorithm is obtained by running a simulator for the generation of ALMA visibility data for a complete range of observatory configurations (presently ALMA has ten nominal configurations numbered 1 to 10), target declinations (DECs in steps of a few degrees), and possible observation hour angles (HAs). In our study, a prototype of this library was created from a suite of 900 simulations with the CASA task `simobserve` for each of the 10 ALMA configurations on a grid of Declination (in steps of 10 degrees) and hour angle (steps of 1 h above elevations of 30 degrees centered on culmination). Figure 9.1 shows the result of the process in step (2) of the above algorithm for a particular example, and Figure 9.2 shows a table of the overall filling fraction, summed over bins, as a function on configuration and HA for a PI request targeting C43-2.

9.2.2 Aspects for Implementation

An even more accurate scheduling could be achieved by complementing the library of simulated BLDs by simulations of the *hybrid* configurations which the array assumes *in between* the nominal

configurations (since only few antennas can be moved per day). Furthermore, during real time scheduling, the actually available antenna array could be considered. In reality we have seen that at least for extended configurations the pads differ in a large amount.
This will vary over the course of the day due to antenna maintenance tasks, problems with antennas or receiver bands, etc. The historic data show on average 6 arrays per day, but peak rates are higher and should not have an impact on the scheduling quality, still. Thus, a fast simulation and evaluation algorithm will be needed. From the simulations run for the creation of the library we estimated approx. 10 s per single evaluation task on one node of the JAO science cluster, but we see possibilities for further speed-up through analytical approaches outside CASA. Further, the number of possible SBs per scheduling slot (or HA per execution) to evaluate for imaging can be reduced by applying other scheduling criteria first, and the calculations can happen in the background to update scheduling queries in advance, and can be iterative, i.e. improve the estimation of the BLD as delta variations over the current array, assuming that only some baselines will change with the new array.
As we have seen from examples of past data it could be necessary to simulate the real array performance rather accurately, for example shadowing should be taken into account as even for modest loss in sensitivity (generally considered acceptable) the impact on the BLD can be substantial. The QA0 evaluation in addition can take data flagging into account and precisely quantify the success of the observation against the prospective goal of filling the BLD. Further, the T_{sys}, given the current atmospheric conditions and HA/elevation, needs to be included in order to allow the BLD approach to replace the current "baseline" execution fraction (based on number of antennas) by the detailed uv matching fraction to give the overall observing efficiency per scheduled execution, but considering correctly the scale coverage.
The scheduling decision will be complicated through the balance in the weighting scheme between the different criteria for scheduling priority[1] and how to include imaging in this [2]. Further, the decision will have to take into account future expectations of execution at different HA and available arrays / next configurations with their associated BLD, so for example when later projected baselines provide a better BLD match it should be considered, or when moving towards more extended configurations the shorter baseline part needs to be filled sufficiently with high priority, while the longer baselines can be left for upcoming arrays, the opposite when moving antennas inwards. In fact, such detailed evaluation may allow a rolling and truly smooth (in terms of angular scale) re-location process, eventually abandoning the idea of discrete configurations.
The main advantage of the iterative scheduling approach w.r.t. observing efficiency is that the additional BL coverage is tailored exactly to the deficit existing. Note that in reality, the image quality aspects, which are implied by the condition on the BLD, can only be one factor in the scheduling together with other ones imposed by the rules of the observatory:

- If the observation of the SB has to be completed by a certain date, e.g. by the end of the observing cycle, this means that the number of available configurations is steadily

---

[1] The scheduling weighting scheme refers to the process through which a global scheduling priority is determined for each SB at any given moment based on several factors that include the requested AR but also other important factors such as the requested frequency. This scheduling weighting scheme should not be confused with weighting of particular BLs within a BLD to achieve better images.

[2] We note that regardless of whether the shape of the BLD is considered for scheduling following the results of this study, the scheduling weighting scheme will be evaluated by the 'Development of decision Support Tools for Scheduling at ALMA' project, which has as one of its objectives 'to describe and translate the Scheduling problem into a multi-objective function that can be optimised'.

reduced as the cycle progresses until, near the end, there is only one left. In order to still pass the condition of the BLD metric, it may then be necessary to use a sub-optimal configuration and make up for this by increasing the observation time. This will result in an "over-exposure" at certain BL lengths (which can, however, be compensated for by offline re-weighting).

- If one or more EBs have already been observed and the algorithm determines a new C_{opt} for the next EB which will only be arrived at much later in the cycle, it may be advisable to give the PI the choice whether to indeed wait or relax the requirements. Alternatively, the observatory can decide, based on quantitative assessment, to achieve the completion by investing additional observing time in a sub-optimal configuration.

A List of the Cycle 6/7 MOUSs investigated in this study

Table A.1: Set 1

Project code	MOUS ID	SB name	EC	C43	C43p7	NC (OT)
2018.1.00597.S	uid://A001/X133d/X1082	SDSS_J23_a_06_TM1	1	7	7	C43-7
2018.1.00597.S	uid://A001/X133d/X1086	SDSS_J23_a_04_TM1	1	7	7	C43-7
2018.1.00663.S	uid://A001/X133d/X13ac	P1329+22_a_03_TM1	1	8	8	C43-8
2018.1.00699.S	uid://A001/X133d/X1461	IRAS_001_a_05_TM1	2	7	7	C43-6
2018.1.00699.S	uid://A001/X133d/X1469	IRAS_201_a_05_TM1	1	6	7	C43-6
2018.1.00699.S	uid://A001/X133d/X146d	IRAS_161_a_05_TM1	2	6	6	C43-6
2018.1.00699.S	uid://A001/X133d/X1471	IRAS_160_a_05_TM1	1	6	6	C43-6
2018.1.00699.S	uid://A001/X133d/X1475	IRAS_015_a_05_TM1	2	6	7	C43-6
2018.1.00745.S	uid://A001/X133d/X14e8	G24.78+0_a_06_TM1	5	8	8	C43-8
2018.1.00397.S	uid://A001/X133d/X1ac4	NGC3862_a_06_TM1	1	7	7	C43-7
2018.1.00397.S	uid://A001/X133d/X1ac8	NGC4061_a_06_TM1	2	7	7	C43-6
2018.1.00397.S	uid://A001/X133d/X1acc	NGC4261_a_06_TM1	1	6	7	C43-7
2018.1.00536.S	uid://A001/X133d/X1f3e	2MASSJ04_a_07_TM1	2	8	8	C43-8
2018.1.00591.S	uid://A001/X133d/X2187	CKL1_a_03_TM1	4	6	6	C43-6
2018.1.00591.S	uid://A001/X133d/X218b	CKL1_a_06_TM1	2	8	8	C43-8
2018.1.00638.S	uid://A001/X133d/X21cf	R_Aqr_a_06_TM1	2	9	10	C43-10
2018.1.00638.S	uid://A001/X133d/X21d3	R_Aqr_a_09_TM1	2	7	7	C43-7
2018.1.00638.S	uid://A001/X133d/X21db	R_Aqr_b_06_TM1	1	6	7	C43-6
2018.1.00717.S	uid://A001/X133d/X2302	SN_1987A_a_06_TM1	1	7	7	C43-7
2018.1.00739.S	uid://A001/X133d/X2310	3C_459_a_03_TM1	5	7	7	C43-7
2018.1.00814.S	uid://A001/X133d/X2485	HD250550_a_06_TM1	1	7	7	C43-6
2018.1.00814.S	uid://A001/X133d/X248b	GUCMA_a_06_TM1	1	6	7	C43-6
2018.1.00814.S	uid://A001/X133d/X2491	HD85567_a_06_TM1	1	7	7	C43-6
2018.1.00908.S	uid://A001/X133d/X2619	J2318-30_a_06_TM1	1	6	7	C43-6
2018.1.00908.S	uid://A001/X133d/X261d	J2054-00_a_06_TM1	1	6	6	C43-6
2018.1.00908.S	uid://A001/X133d/X2621	P323+12_a_06_TM1	1	7	7	C43-6
2018.1.00939.S	uid://A001/X133d/X26ad	NGC4418_a_05_TM1	1	7	7	C43-7
2018.1.00939.S	uid://A001/X133d/X26b9	IRAS1720_a_05_TM1	3	6	7	C43-6
2018.1.01008.S	uid://A001/X133d/X2866	MGJ0414+_a_06_TM1	1	6	7	C43-6
2018.1.01008.S	uid://A001/X133d/X2876	PSSJ2322_a_03_TM1	3	6	7	C43-6
2018.1.01008.S	uid://A001/X133d/X287a	PSSJ2322_a_04_TM1	1	7	7	C43-7
2018.1.01008.S	uid://A001/X133d/X287e	PSSJ2322_a_06_TM1	1	7	8	C43-8
2018.1.01054.S	uid://A001/X133d/X2929	2mass_J1_a_06_TM1	4	9	10	C43-9
2018.1.01103.S	uid://A001/X133d/X29ef	BRI1335_a_04_TM1	3	6	7	C43-6

2018.1.01104.S	uid://A001/X133d/X29fb	Cygnus_A_a_07_TM1	1	7	7	C43-7
2018.1.01104.S	uid://A001/X133d/X29ff	Cygnus_A_a_04_TM1	1	8	9	C43-8
2018.1.01104.S	uid://A001/X133d/X2a03	Cygnus_A_a_03_TM1	1	9	10	C43-910
2018.1.01239.S	uid://A001/X133d/X2d20	W_Hya_a_06_TM1	5	9	10	C43-10
2018.1.01135.S	uid://A001/X133d/X2dee	NGC1068_a_03_TM1	5	9	10	C43-10
2018.1.01289.S	uid://A001/X133d/X2e1c	SDSS_J20_a_03_TM1	6	6	7	C43-7
2018.1.01289.S	uid://A001/X133d/X2e20	SDSS_J01_a_03_TM1	5	6	7	C43-7
2018.1.01368.S	uid://A001/X133d/X3014	J1639+28_a_08_TM1	2	7	7	C43-6
2018.1.01374.S	uid://A001/X133d/X301f	BHB07-11_b_07_TM1	1	4	6	C43-6
2018.1.01471.S	uid://A001/X133d/X318b	3c218_b_03_TM1	1	6	6	C43-6
2018.1.01146.S	uid://A001/X133d/X31cc	HATLAS_J_a_04_TM1	2	6	7	C43-7
2018.1.01488.S	uid://A001/X133d/X31f7	NGC1377_a_03_TM1	1	7	7	C43-7
2018.1.01625.S	uid://A001/X133d/X3306	HH46_a_06_TM1	5	7	7	C43-7
2018.1.01656.S	uid://A001/X133d/X3423	IRAS_165_a_06_TM1	3	8	8	C43-8
2018.1.01190.S	uid://A001/X133d/X378b	f16_a_06_TM1	5	7	7	C43-6
2018.1.01288.S	uid://A001/X133d/X3aec	G30.82-0_a_06_TM1	3	6	7	C43-6
2018.1.01330.S	uid://A001/X133d/X3c6f	HD_14300_a_06_TM1	6	7	8	C43-8
2018.1.01458.S	uid://A001/X133d/X3ddd	Sz65_a_06_TM1	1	8	8	C43-7
2018.1.01458.S	uid://A001/X133d/X3de0	Sz71_a_06_TM1	1	7	8	C43-7
2018.1.01458.S	uid://A001/X133d/X3def	Sz123A_a_06_TM1	1	8	8	C43-7
2018.1.01458.S	uid://A001/X133d/X3df3	Sz68_a_06_TM1	1	7	8	C43-7
2018.1.01458.S	uid://A001/X133d/X3df6	Sz73_a_06_TM1	1	7	8	C43-7
2018.1.01461.S	uid://A001/X133d/X3e03	SVS13-A_a_06_TM1	1	7	7	C43-6
2018.1.01464.S	uid://A001/X133d/X3e17	B2_0827+_a_07_TM1	2	6	6	C43-6
2018.1.01598.S	uid://A001/X133d/X3f5a	PKS0023-_a_05_TM1	5	6	6	C43-6
2018.1.01669.S	uid://A001/X133d/X3fcd	PKS_0529_a_06_TM1	2	6	7	C43-6
2018.1.01669.S	uid://A001/X133d/X3fd1	PKS_0529_a_04_TM1	3	8	8	C43-8
2018.1.01178.S	uid://A001/X133d/X422c	NGC1275_a_06_TM1	3	9	9	C43-10
2018.1.00222.S	uid://A001/X133d/X83e	AzTEC-3_a_06_TM1	2	9	10	C43-10
2018.1.00222.S	uid://A001/X133d/X842	AzTEC-3_b_06_TM1	1	7	7	C43-7
2018.1.00576.S	uid://A001/X133d/Xfb8	NGC_3783_a_03_TM1	1	6	7	C43-6
2018.1.00576.S	uid://A001/X133d/Xfcd	NGC_4593_b_03_TM1	1	6	7	C43-6
2018.1.00576.S	uid://A001/X133d/Xfef	NGC_3783_a_04_TM1	1	6	7	C43-6
2018.1.01190.S	uid://A001/X1353/X8	f16_b_06_TM1	4	7	7	C43-6
2018.1.00974.S	uid://A001/X1354/Xcc	J0224-1_a_03_TM1	5	7	7	C43-6
2018.1.00974.S	uid://A001/X1354/Xd4	J0330-3_a_03_TM1	6	6	7	C43-6
2018.1.00945.S	uid://A001/X1355/Xaf	LkCa_15_a_06_TM1	2	9	9	C43-9
2018.1.01198.S	uid://A001/X1359/X2e	AS_209_a_03_TM1	4	9	10	C43-10
2018.1.01198.S	uid://A001/X1359/X31	Elias_2-_a_03_TM1	6	9	10	C43-10
2018.1.01198.S	uid://A001/X1359/X34	AS_205_a_03_TM1	2	9	10	C43-10
2018.1.01198.S	uid://A001/X1359/X3e	AS_209_b_03_TM1	1	6	6	C43-6
2018.1.01124.S	uid://A001/X13b4/X48	sgra_sta_a_06_TM1	10	9	10	C43-9
2018.1.01660.S	uid://A001/X13b4/X7a	IRAS1348_a_06_TM1	1	9	10	C43-910
2018.1.01309.S	uid://A001/X13c4/X9e	HD100546_a_06_TM1	8	9	10	C43-10
2018.1.01106.S	uid://A001/X13c4/Xd2	0480_580_a_06_TM1	4	9	9	C43-10
2018.1.00614.S	uid://A001/X13d5/X184	DS_Tau_a_03_TM1	2	8	8	C43-8
2018.1.00614.S	uid://A001/X13d5/X188	DL_Tau_a_03_TM1	3	8	8	C43-8
2018.1.01292.S	uid://A001/X13d6/Xa1	Europa_i_a_06_TM1	1	8	8	C43-8
2018.1.01292.S	uid://A001/X13d6/Xa5	Europa_3_a_06_TM1	1	8	8	C43-8
2018.1.01292.S	uid://A001/X13d6/Xb1	Ganymede_c_06_TM1	1	7	7	C43-7
2018.1.00656.S	uid://A001/X13d6/Xca	P352-15_a_07_TM1	10	7	8	C43-8

2018.1.01410.T	uid://A001/X142c/X1fa	GRB19082_a_03_TM1	1	7	7	C43-7
2018.1.01410.T	uid://A001/X142c/X1fd	GRB19082_b_03_TM1	1	6	7	C43-7
2018.1.01410.T	uid://A001/X142c/X200	GRB19082_c_03_TM1	1	6	6	C43-7
2018.1.01410.T	uid://A001/X142c/X204	GRB19082_a_07_TM1	1	7	7	C43-7
2018.1.01410.T	uid://A001/X142c/X207	GRB19082_b_07_TM1	1	6	7	C43-7
2018.1.01410.T	uid://A001/X142c/X20a	GRB19082_c_07_TM1	1	6	6	C43-7
2018.1.01652.T	uid://A001/X1457/X341	AT2019os_h_03_TM1	1	7	7	C43-7
2018.1.01652.T	uid://A001/X1457/X344	AT2019os_i_03_TM1	1	6	7	C43-7
2018.1.01652.T	uid://A001/X1462/X38	AT2019os_a_06_TM1	1	7	7	C43-7
2018.1.01652.T	uid://A001/X1462/X3b	AT2019os_b_06_TM1	1	6	7	C43-7
2019.1.01175.S	uid://A001/X1465/X16cc	hd_21997_a_08_TM1	1	2	1	C43-12
2019.1.01155.S	uid://A001/X1465/X17d7	G224_a_07_TM1	1	2	3	C43-23
2019.1.01148.S	uid://A001/X1465/X1803	Cosmic_H_a_07_TM1	2	2	1	C43-1
2019.1.01148.S	uid://A001/X1465/X1807	cB58_a_07_TM1	1	1	1	C43-2
2019.1.01142.S	uid://A001/X1465/X188d	MOSDEF_5_a_06_TM1	5	3	3	C43-23
2019.1.01136.S	uid://A001/X1465/X18ab	8080-370_a_03_TM1	1	2	1	C43-2
2019.1.01136.S	uid://A001/X1465/X18af	9194-370_a_03_TM1	1	2	1	C43-2
2019.1.01136.S	uid://A001/X1465/X18b3	9494-370_a_03_TM1	2	2	2	C43-2
2019.1.01136.S	uid://A001/X1465/X18b7	8083-127_a_03_TM1	1	2	2	C43-2
2019.1.01136.S	uid://A001/X1465/X18bb	8982-610_a_03_TM1	1	2	2	C43-2
2019.1.01136.S	uid://A001/X1465/X18bf	8655-190_a_03_TM1	1	2	2	C43-2
2019.1.01136.S	uid://A001/X1465/X18c3	7964-190_a_03_TM1	1	2	2	C43-2
2019.1.01136.S	uid://A001/X1465/X18c7	8081-370_a_03_TM1	2	2	1	C43-2
2019.1.01136.S	uid://A001/X1465/X18cb	8085-610_a_03_TM1	1	2	2	C43-2
2019.1.01136.S	uid://A001/X1465/X18cf	8086-370_a_03_TM1	1	2	2	C43-2
2019.1.01136.S	uid://A001/X1465/X18d3	8939-370_a_03_TM1	1	2	2	C43-2
2019.1.01136.S	uid://A001/X1465/X18d7	8941-370_a_03_TM1	1	2	2	C43-2
2019.1.01132.S	uid://A001/X1465/X18ff	NGC1482_a_06_TM1	1	3	3	C43-2
2019.1.01127.S	uid://A001/X1465/X193d	GDS24569_a_05_TM1	2	2	3	C43-3
2019.1.01124.S	uid://A001/X1465/X194f	ngc7710_a_03_TM1	2	3	3	C43-23
2019.1.01124.S	uid://A001/X1465/X1955	ngc4191_a_03_TM1	2	3	3	C43-23
2019.1.01117.S	uid://A001/X1465/X198d	M83_a_04_TM1	9	2	2	C43-2
2019.1.01034.S	uid://A001/X1465/X1c30	DEEP2_32_a_06_TM1	2	4	4	C43-5
2019.1.01034.S	uid://A001/X1465/X1c42	DEEP2_32_a_07_TM1	1	4	4	C43-4
2019.1.01031.S	uid://A001/X1465/X1c84	CN1_a_03_TM1	1	2	2	C43-1
2019.1.01031.S	uid://A001/X1465/X1c88	CN6_a_03_TM1	2	2	2	C43-1
2019.1.01031.S	uid://A001/X1465/X1c8c	CN13_a_03_TM1	2	2	1	C43-1
2019.1.01031.S	uid://A001/X1465/X1c90	CN73_a_03_TM1	2	2	2	C43-1
2019.1.01030.S	uid://A001/X1465/X1cae	RN114_a_07_TM1	1	2	1	C43-1
2019.1.01030.S	uid://A001/X1465/X1cb2	RN122_a_07_TM1	1	1	1	C43-1
2019.1.01030.S	uid://A001/X1465/X1cb6	RN88_a_07_TM1	1	2	1	C43-1
2019.1.01030.S	uid://A001/X1465/X1cba	RN90_a_07_TM1	1	2	1	C43-1
2019.1.01030.S	uid://A001/X1465/X1cbe	RN9_a_07_TM1	1	1	1	C43-1
2019.1.01030.S	uid://A001/X1465/X1cc2	RN73_a_07_TM1	1	2	1	C43-1
2019.1.01030.S	uid://A001/X1465/X1cc6	RN39_a_07_TM1	1	2	1	C43-1
2019.1.01030.S	uid://A001/X1465/X1cca	RN31_a_07_TM1	1	2	1	C43-1
2019.1.01030.S	uid://A001/X1465/X1cce	RN80_a_07_TM1	1	2	2	C43-1
2019.1.01027.S	uid://A001/X1465/X1cde	ELAIS-S1_a_06_TM1	3	4	4	C43-4
2019.1.01026.S	uid://A001/X1465/X1ceb	SPT0054-_a_07_TM1	1	3	4	C43-4
2019.1.01026.S	uid://A001/X1465/X1cee	SPT2307-_a_07_TM1	1	4	4	C43-4
2019.1.01026.S	uid://A001/X1465/X1cf1	SPT2152-_a_07_TM1	1	4	4	C43-4

2019.1.01026.S	uid://A001/X1465/X1cf4	SPT2129-_a_07_TM1	1	3	4	C43-4
2019.1.01026.S	uid://A001/X1465/X1cf7	SPT0611-_a_07_TM1	1	4	4	C43-4
2019.1.01026.S	uid://A001/X1465/X1cfa	SPT0509-_a_07_TM1	1	4	4	C43-4
2019.1.01026.S	uid://A001/X1465/X1cfd	SPT0402-_a_07_TM1	1	3	4	C43-4
2019.1.01026.S	uid://A001/X1465/X1d00	SPT0226-_a_07_TM1	1	3	4	C43-4
2019.1.01025.S	uid://A001/X1465/X1d12	J1007p21_a_06_TM1	1	4	4	C43-234
2019.1.01025.S	uid://A001/X1465/X1d16	J0218p00_a_06_TM1	1	4	4	C43-234
2019.1.01025.S	uid://A001/X1465/X1d1a	J0229m08_a_06_TM1	1	4	4	C43-234
2019.1.01025.S	uid://A001/X1465/X1d1e	J0246m52_a_06_TM1	1	4	4	C43-234
2019.1.01025.S	uid://A001/X1465/X1d22	J0252m05_a_06_TM1	1	4	4	C43-234
2019.1.01025.S	uid://A001/X1465/X1d26	J0319m10_a_06_TM1	1	4	4	C43-234
2019.1.01025.S	uid://A001/X1465/X1d2a	J0430m14_a_06_TM1	1	4	4	C43-234
2019.1.01025.S	uid://A001/X1465/X1d2e	J0525m24_a_06_TM1	1	4	4	C43-234
2019.1.01025.S	uid://A001/X1465/X1d32	J0923p07_a_06_TM1	1	4	4	C43-234
2019.1.01025.S	uid://A001/X1465/X1d36	J1058p29_a_06_TM1	1	4	4	C43-234
2019.1.01025.S	uid://A001/X1465/X1d3a	J1129p18_a_06_TM1	1	4	4	C43-234
2019.1.01025.S	uid://A001/X1465/X1d3e	J2002m30_a_06_TM1	1	4	4	C43-234
2019.1.01025.S	uid://A001/X1465/X1d42	J2211m63_a_06_TM1	1	4	4	C43-234
2019.1.01022.S	uid://A001/X1465/X1d63	PKS0349-_a_03_TM1	1	3	3	C43-12
2019.1.01022.S	uid://A001/X1465/X1d67	PKS0034-_a_03_TM1	1	3	3	C43-12
2019.1.01022.S	uid://A001/X1465/X1d6b	PKS0035-_a_03_TM1	1	3	3	C43-12
2019.1.01022.S	uid://A001/X1465/X1d73	PKS0043-_a_03_TM1	1	3	3	C43-12
2019.1.01022.S	uid://A001/X1465/X1d77	PKS0213-_a_03_TM1	1	3	3	C43-12
2019.1.01022.S	uid://A001/X1465/X1d7b	PKS0404+_a_03_TM1	1	3	3	C43-12
2019.1.01022.S	uid://A001/X1465/X1d7f	PKS0442-_a_03_TM1	1	3	3	C43-12
2019.1.01022.S	uid://A001/X1465/X1d83	PKS0806-_a_03_TM1	1	2	2	C43-12
2019.1.01022.S	uid://A001/X1465/X1d87	PKS0945+_a_03_TM1	1	3	3	C43-12
2019.1.01022.S	uid://A001/X1465/X1d8b	PKS1151-_a_03_TM1	1	3	3	C43-12
2019.1.01022.S	uid://A001/X1465/X1d8f	PKS1559+_a_03_TM1	1	2	3	C43-12
2019.1.01022.S	uid://A001/X1465/X1d93	PKS1648+_a_03_TM1	1	3	3	C43-12
2019.1.01022.S	uid://A001/X1465/X1d97	PKS1733-_a_03_TM1	1	2	3	C43-12
2019.1.01022.S	uid://A001/X1465/X1d9b	PKS1814-_a_03_TM1	1	3	3	C43-12
2019.1.01022.S	uid://A001/X1465/X1d9f	PKS1932-_a_03_TM1	1	3	3	C43-12
2019.1.01022.S	uid://A001/X1465/X1da3	PKS1934-_a_03_TM1	1	3	3	C43-12
2019.1.01022.S	uid://A001/X1465/X1da7	PKS1949+_a_03_TM1	1	3	3	C43-12
2019.1.01022.S	uid://A001/X1465/X1dab	PKS2135-_a_03_TM1	1	3	3	C43-12
2019.1.01022.S	uid://A001/X1465/X1daf	PKS2211-_a_03_TM1	1	3	3	C43-12
2019.1.01022.S	uid://A001/X1465/X1db3	PKS2221-_a_03_TM1	1	3	3	C43-12
2019.1.01022.S	uid://A001/X1465/X1db7	PKS2314+_a_03_TM1	1	3	3	C43-12
2019.1.01022.S	uid://A001/X1465/X1dbb	PKS2356-_a_03_TM1	1	3	3	C43-12
2019.1.01022.S	uid://A001/X1465/X1dbf	PKS0620-_a_03_TM1	1	3	3	C43-12
2019.1.01022.S	uid://A001/X1465/X1dc3	PKS0625-_a_03_TM1	1	3	3	C43-12
2019.1.01022.S	uid://A001/X1465/X1dc7	PKS0625-_b_03_TM1	1	3	3	C43-12
2019.1.01022.S	uid://A001/X1465/X1dcb	PKS1839-_a_03_TM1	1	3	3	C43-12
2019.1.01022.S	uid://A001/X1465/X1dcf	PKS1954-_a_03_TM1	1	3	3	C43-12
2019.1.01003.S	uid://A001/X1465/X1e7a	J0305-SM_a_06_TM1	1	3	3	C43-12
2019.1.01003.S	uid://A001/X1465/X1e7e	PJ231-SM_a_06_TM1	1	2	2	C43-12
2019.1.01003.S	uid://A001/X1465/X1e82	PJ308-SM_a_06_TM1	2	3	3	C43-12
2019.1.00964.S	uid://A001/X1465/X1ec3	PSJ0030-_a_06_TM1	1	3	4	C43-123
2019.1.00964.S	uid://A001/X1465/X1ec7	WG0214-2_a_06_TM1	1	3	4	C43-123
2019.1.00964.S	uid://A001/X1465/X1ecf	WISEJ025_a_06_TM1	1	4	4	C43-123

2019.1.00964.S	uid://A001/X1465/X1ed3	DESJ0405_a_06_TM1	1	4	4	C43-123
2019.1.00964.S	uid://A001/X1465/X1ed7	DESJ0408_a_06_TM1	1	4	4	C43-123
2019.1.00964.S	uid://A001/X1465/X1edb	COSMOS59_a_06_TM1	1	4	4	C43-123
2019.1.00964.S	uid://A001/X1465/X1edf	J1042+16_a_06_TM1	1	3	3	C43-123
2019.1.00964.S	uid://A001/X1465/X1ee3	HE1113-0_a_06_TM1	1	3	3	C43-123
2019.1.00964.S	uid://A001/X1465/X1ee7	GRAL1131_a_06_TM1	1	4	4	C43-123
2019.1.00964.S	uid://A001/X1465/X1eeb	2M1134-2_a_06_TM1	1	3	3	C43-123
2019.1.00964.S	uid://A001/X1465/X1eef	SDSSJ125_a_06_TM1	1	4	4	C43-123
2019.1.00964.S	uid://A001/X1465/X1ef3	2M1310-1_a_06_TM1	1	3	3	C43-123
2019.1.00964.S	uid://A001/X1465/X1ef7	J1537-30_a_06_TM1	1	3	3	C43-123
2019.1.00964.S	uid://A001/X1465/X1efb	PSJ1606-_a_06_TM1	1	3	3	C43-123
2019.1.00964.S	uid://A001/X1465/X1eff	SDSSJ164_a_06_TM1	1	4	4	C43-123
2019.1.00964.S	uid://A001/X1465/X1f03	J1817+27_a_06_TM1	1	4	4	C43-123
2019.1.00964.S	uid://A001/X1465/X1f07	WGD2038-_a_06_TM1	1	4	4	C43-123
2019.1.00959.S	uid://A001/X1465/X1f12	ERQ_J211_a_06_TM1	3	3	3	C43-23
2019.1.00959.S	uid://A001/X1465/X1f15	cQSO_J21_a_06_TM1	3	2	3	C43-23
2019.1.00951.S	uid://A001/X1465/X1f2f	1_a_06_TM1	4	2	2	C43-23
2019.1.00949.S	uid://A001/X1465/X1f3b	MJ0417-I_a_03_TM1	2	2	2	C43-1234
2019.1.00949.S	uid://A001/X1465/X1f43	MJ0417-I_c_03_TM1	2	2	1	C43-1234
2019.1.00949.S	uid://A001/X1465/X1f47	MJ0417-I_d_03_TM1	2	2	1	C43-1234
2019.1.00949.S	uid://A001/X1465/X1f4b	MJ0417-I_a_04_TM1	1	1	1	C43-123
2019.1.00949.S	uid://A001/X1465/X1f4f	MJ0417-I_b_04_TM1	1	1	1	C43-123
2019.1.00949.S	uid://A001/X1465/X1f53	MJ0417-I_c_04_TM1	1	2	2	C43-123
2019.1.00948.S	uid://A001/X1465/X1f70	SDSSJ133_a_07_TM1	1	4	4	C43-4
2019.1.00946.S	uid://A001/X1465/X1f93	J2157-36_a_07_TM1	1	3	4	C43-4
2019.1.00946.S	uid://A001/X1465/X1f9b	J0916-25_a_07_TM1	1	4	4	C43-4
2019.1.00946.S	uid://A001/X1465/X1fb3	J0131-03_a_07_TM1	1	4	4	C43-4
2019.1.00915.S	uid://A001/X1465/X1ff9	Ridge-N1_a_03_TM1	1	3	3	C43-2
2019.1.00915.S	uid://A001/X1465/X2001	Ridge-M1_a_03_TM1	1	3	3	C43-2
2019.1.00915.S	uid://A001/X1465/X2009	Ridge-S2_a_03_TM1	1	3	3	C43-2
2019.1.00915.S	uid://A001/X1465/X2011	Ridge-W1_a_03_TM1	1	3	3	C43-2
2019.1.00909.S	uid://A001/X1465/X2056	XID_276_a_03_TM1	1	3	3	C43-345
2019.1.00909.S	uid://A001/X1465/X205a	XID_276_b_03_TM1	1	2	3	C43-345
2019.1.00909.S	uid://A001/X1465/X205e	XID_276_c_03_TM1	1	3	3	C43-34
2019.1.00909.S	uid://A001/X1465/X2062	XID_276_d_03_TM1	1	3	3	C43-34
2019.1.00883.S	uid://A001/X1465/X20a9	Darth_Va_a_04_TM1	1	4	4	C43-234
2019.1.00883.S	uid://A001/X1465/X20ad	Darth_Va_b_04_TM1	1	4	4	C43-234
2019.1.00843.S	uid://A001/X1465/X2182	30_Dorad_a_06_TM1	1	2	2	C43-1
2019.1.00843.S	uid://A001/X1465/X218a	30_Dorad_b_06_TM1	1	1	1	C43-1
2019.1.00843.S	uid://A001/X1465/X2192	30_Dorad_c_06_TM1	1	1	1	C43-1
2019.1.00843.S	uid://A001/X1465/X219a	30_Dorad_d_06_TM1	1	2	2	C43-1
2019.1.00843.S	uid://A001/X1465/X21a2	30_Dorad_e_06_TM1	1	2	2	C43-1
2019.1.00840.S	uid://A001/X1465/X21b7	PSO135+1_a_07_TM1	1	1	1	C43-2
2019.1.00840.S	uid://A001/X1465/X21bb	SDSSJ013_a_07_TM1	1	2	2	C43-1
2019.1.00840.S	uid://A001/X1465/X21bf	SDSSJ222_a_03_TM1	1	4	4	C43-4
2019.1.00840.S	uid://A001/X1465/X21c7	PSO352-1_a_07_TM1	1	2	2	C43-2
2019.1.00840.S	uid://A001/X1465/X21cb	PSO055-0_a_07_TM1	1	2	1	C43-2
2019.1.00840.S	uid://A001/X1465/X21cf	SDSSJ205_a_03_TM1	1	4	4	C43-4
2019.1.00838.S	uid://A001/X1465/X21f5	ALMA_3mm_b_04_TM1	1	2	2	C43-23
2019.1.00838.S	uid://A001/X1465/X2204	ALMA_3mm_f_03_TM1	1	2	3	C43-34
2019.1.00838.S	uid://A001/X1465/X2207	ALMA_3mm_g_03_TM1	1	2	3	C43-23

2019.1.00801.S	uid://A001/X1465/X2384	r_leo_b_07_TM1	1	3	3	C43-2
2019.1.00801.S	uid://A001/X1465/X238e	R_crt_b_07_TM1	1	2	3	C43-2
2019.1.00783.S	uid://A001/X1465/X23eb	Titan_a_06_TM1	1	2	3	C43-2
2019.1.00783.S	uid://A001/X1465/X23f3	Titan_c_06_TM1	2	1	2	C43-2
2019.1.00779.S	uid://A001/X1465/X2407	SPT2052_a_07_TM1	3	3	3	C43-23
2019.1.00779.S	uid://A001/X1465/X240b	SPT2052_b_07_TM1	1	3	3	C43-23
2019.1.00779.S	uid://A001/X1465/X240f	SPT0553_a_07_TM1	3	3	3	C43-23
2019.1.00779.S	uid://A001/X1465/X2413	SPT0553_b_07_TM1	1	4	4	C43-23
2019.1.00779.S	uid://A001/X1465/X241b	SPT0553_c_07_TM1	1	3	4	C43-23
2019.1.00779.S	uid://A001/X1465/X241f	SPT2335_a_03_TM1	3	3	3	C43-345
2019.1.00779.S	uid://A001/X1465/X2423	SPT0553_a_03_TM1	3	4	4	C43-345
2019.1.00779.S	uid://A001/X1465/X2427	SPT2052_a_03_TM1	3	4	4	C43-345
2019.1.00779.S	uid://A001/X1465/X242b	SPT0348_a_03_TM1	3	3	3	C43-345
2019.1.00779.S	uid://A001/X1465/X242f	SPT0348_a_07_TM1	3	3	3	C43-23
2019.1.00779.S	uid://A001/X1465/X2433	SPT0348_b_07_TM1	1	4	4	C43-23
2019.1.00779.S	uid://A001/X1465/X2437	SPT0311_a_06_TM1	3	3	3	C43-34
2019.1.00736.S	uid://A001/X1465/X26ca	Kes75_PW_b_03_TM1	1	1	1	C43-1
2019.1.00730.S	uid://A001/X1465/X270d	J1442+02_a_06_TM1	1	3	4	C43-4
2019.1.00708.S	uid://A001/X1465/X27ad	B1-a_a_04_TM1	2	3	4	C43-3
2019.1.00702.S	uid://A001/X1465/X27df	LEGA-C_2_a_04_TM1	3	3	3	C43-123
2019.1.00702.S	uid://A001/X1465/X27e3	LEGA-C_2_b_04_TM1	3	2	3	C43-123
2019.1.00702.S	uid://A001/X1465/X27e7	LEGA-C_2_c_04_TM1	2	2	2	C43-123
2019.1.00700.S	uid://A001/X1465/X27f9	SPT0529-_a_09_TM1	1	2	2	C43-12
2019.1.00685.S	uid://A001/X1465/X284a	I08076-3_a_03_TM1	1	4	4	C43-3
2019.1.00685.S	uid://A001/X1465/X2854	I10365-5_a_03_TM1	1	3	3	C43-3
2019.1.00685.S	uid://A001/X1465/X2859	I11298-6_a_03_TM1	1	3	3	C43-3
2019.1.00685.S	uid://A001/X1465/X285e	I13471-6_a_03_TM1	1	3	3	C43-3
2019.1.00685.S	uid://A001/X1465/X2863	I12320-6_a_03_TM1	1	3	3	C43-3
2019.1.00685.S	uid://A001/X1465/X2868	I15384-5_a_03_TM1	2	3	3	C43-3
2019.1.00685.S	uid://A001/X1465/X286d	I14382-6_a_03_TM1	1	3	3	C43-3
2019.1.00685.S	uid://A001/X1465/X2872	I17136-3_a_03_TM1	1	3	3	C43-3
2019.1.00685.S	uid://A001/X1465/X287c	I16272-4_a_03_TM1	2	3	3	C43-3
2019.1.00685.S	uid://A001/X1465/X2881	I19078+0_a_03_TM1	1	3	3	C43-3
2019.1.00685.S	uid://A001/X1465/X288b	I17439-2_a_03_TM1	1	3	3	C43-3
2019.1.00685.S	uid://A001/X1465/X2890	I17545-2_a_03_TM1	1	3	3	C43-3
2019.1.00685.S	uid://A001/X1465/X2895	I18290-0_a_03_TM1	1	3	3	C43-3
2019.1.00685.S	uid://A001/X1465/X289a	I18079-1_a_03_TM1	1	3	3	C43-3
2019.1.00673.S	uid://A001/X1465/X28a3	RCS_J231_a_03_TM1	20	2	2	C43-1
2019.1.00672.S	uid://A001/X1465/X28ba	J2054-00_b_06_TM1	1	4	6	C43-6
2019.1.00663.S	uid://A001/X1465/X28d3	J113526._a_06_TM1	1	3	4	C43-4
2019.1.00663.S	uid://A001/X1465/X28e7	J214719-_a_06_TM1	1	4	4	C43-4
2019.1.00663.S	uid://A001/X1465/X28eb	J010312-_a_06_TM1	2	4	4	C43-4
2019.1.00663.S	uid://A001/X1465/X28ef	J012507-_a_07_TM1	1	4	4	C43-4
2019.1.00652.S	uid://A001/X1465/X291b	O-208681_a_03_TM1	1	3	4	C43-4
2019.1.00652.S	uid://A001/X1465/X291f	O-406444_a_03_TM1	4	3	4	C43-4
2019.1.00639.S	uid://A001/X1465/X2967	G034.77-_a_06_TM1	1	1	1	C43-1
2019.1.00634.S	uid://A001/X1465/X29a0	3C273_a_06_TM1	1	2	2	C43-1
2019.1.00558.S	uid://A001/X1465/X2bcc	Horsehea_a_07_TM1	6	2	3	C43-2
2019.1.00534.S	uid://A001/X1465/X2c8f	SMC_YSO_a_07_TM1	5	4	4	C43-4
2019.1.00534.S	uid://A001/X1465/X2c93	SMC_YSO_b_07_TM1	4	4	4	C43-4
2019.1.00533.S	uid://A001/X1465/X2c9c	G09v1.97_a_06_TM1	1	3	4	C43-34

2019.1.00533.S	uid://A001/X1465/X2ca0	G09v1.97_b_06_TM1	1	4	4	C43-345
2019.1.00486.S	uid://A001/X1465/X2e39	SPT0112-_a_03_TM1	2	2	2	C43-12
2019.1.00486.S	uid://A001/X1465/X2e3d	SPT0457-_a_03_TM1	2	2	2	C43-12
2019.1.00486.S	uid://A001/X1465/X2e41	SPT2316-_a_04_TM1	1	1	1	C43-1
2019.1.00486.S	uid://A001/X1465/X2e45	SPT2316-_b_04_TM1	1	1	1	C43-1
2019.1.00486.S	uid://A001/X1465/X2e49	SPT2354-_a_05_TM1	1	2	2	C43-1
2019.1.00486.S	uid://A001/X1465/X2e51	SPT2349-_a_04_TM1	1	1	1	C43-2
2019.1.00486.S	uid://A001/X1465/X2e55	SPT2349-_b_04_TM1	1	1	1	C43-1
2019.1.00486.S	uid://A001/X1465/X2e59	SPT2307-_a_04_TM1	1	2	2	C43-2
2019.1.00477.S	uid://A001/X1465/X2e97	D3a-1550_a_07_TM1	1	1	1	C43-1
2019.1.00477.S	uid://A001/X1465/X2e9b	SSA12-63_a_07_TM1	1	1	1	C43-1
2019.1.00477.S	uid://A001/X1465/X2ea3	ZC-40550_a_07_TM1	2	2	1	C43-1
2019.1.00477.S	uid://A001/X1465/X2ea7	ZC-41012_a_07_TM1	2	2	1	C43-1
2019.1.00466.S	uid://A001/X1465/X2f0e	PSO_J183_a_06_TM1	3	2	2	C43-1
2019.1.00454.S	uid://A001/X1465/X2f8b	Arp220_a_03_TM1	1	4	4	C43-4
2019.1.00454.S	uid://A001/X1465/X2f93	Arp220_b_06_TM1	1	2	3	C43-2
2019.1.00454.S	uid://A001/X1465/X2f97	Arp220_c_07_TM1	1	1	1	C43-1
2019.1.00447.S	uid://A001/X1465/X2faa	G14-1_a_07_TM1	2	4	4	C43-4
2019.1.00447.S	uid://A001/X1465/X2fae	G08-5_a_07_TM1	3	4	4	C43-4
2019.1.00447.S	uid://A001/X1465/X2fb2	G04-1_a_07_TM1	3	4	4	C43-3
2019.1.00411.S	uid://A001/X1465/X3057	SDSSJ004_b_03_TM1	1	4	4	C43-4
2019.1.00411.S	uid://A001/X1465/X305b	SDSSJ004_c_03_TM1	1	4	4	C43-4
2019.1.00411.S	uid://A001/X1465/X305f	SDSSJ011_a_03_TM1	1	4	4	C43-4
2019.1.00411.S	uid://A001/X1465/X3063	SDSSJ014_a_03_TM1	1	4	4	C43-4
2019.1.00411.S	uid://A001/X1465/X3067	SDSSJ020_a_03_TM1	1	4	4	C43-4
2019.1.00411.S	uid://A001/X1465/X306b	SDSSJ024_a_03_TM1	1	4	4	C43-4
2019.1.00411.S	uid://A001/X1465/X306f	SDSSJ085_a_03_TM1	1	4	4	C43-4
2019.1.00411.S	uid://A001/X1465/X3073	SDSSJ102_a_03_TM1	1	4	4	C43-4
2019.1.00411.S	uid://A001/X1465/X3077	SDSSJ104_a_03_TM1	1	4	4	C43-4
2019.1.00411.S	uid://A001/X1465/X307f	SDSSJ120_a_03_TM1	1	4	4	C43-4
2019.1.00411.S	uid://A001/X1465/X3083	SDSSJ121_a_03_TM1	1	4	4	C43-4
2019.1.00411.S	uid://A001/X1465/X3087	SDSSJ122_a_03_TM1	1	4	4	C43-4
2019.1.00411.S	uid://A001/X1465/X308b	SDSSJ125_a_03_TM1	1	3	4	C43-4
2019.1.00411.S	uid://A001/X1465/X308f	SDSSJ225_a_03_TM1	1	4	4	C43-4
2019.1.00411.S	uid://A001/X1465/X3093	SDSSJ235_a_03_TM1	1	4	4	C43-4
2019.1.00407.S	uid://A001/X1465/X30d7	GRB18102_a_03_TM1	3	2	2	C43-234
2019.1.00912.S	uid://A001/X1467/X291	Serpens_a_06_TM1	1	3	4	C43-3
2019.1.00790.S	uid://A001/X1467/X2a7	Cosmic_E_a_03_TM1	4	3	4	C43-1234
2019.1.00790.S	uid://A001/X1467/X2ab	cB58_a_03_TM1	6	2	2	C43-1234
2019.1.00790.S	uid://A001/X1467/X2af	8_00arc_a_03_TM1	1	3	3	C43-1234
2019.1.00790.S	uid://A001/X1467/X2b3	MACS0451_a_03_TM1	1	4	4	C43-1234
2019.1.01027.S	uid://A001/X1468/X1af	CDFS-18_a_06_TM1	1	4	4	C43-4
2019.1.01027.S	uid://A001/X1468/X1b3	XMM-11_a_06_TM1	2	3	4	C43-4
2019.1.00779.S	uid://A001/X1468/X1ba	SPT0311_b_06_TM1	1	4	4	C43-34
2019.1.00779.S	uid://A001/X1468/X1be	SPT0311_a_03_TM1	3	3	3	C43-345
2019.1.01158.S	uid://A001/X1469/X103	18263_An_a_07_TM1	1	4	4	C43-123456
2019.1.01158.S	uid://A001/X1469/X107	13372_19_a_07_TM1	1	4	4	C43-123456
2019.1.01158.S	uid://A001/X1469/X10b	11488_19_a_07_TM1	1	4	4	C43-123456
2019.1.01135.S	uid://A001/X1469/Xa7	2MASSJ16_a_07_TM1	6	3	3	C43-234
2019.1.01135.S	uid://A001/X1469/Xab	2MASSJ16_a_06_TM1	3	4	4	C43-234
2019.1.00720.S	uid://A001/X1469/Xc0	L483_a_07_TM1	1	3	3	C43-3

2019.1.00720.S	uid://A001/X1469/Xc4	B335_a_07_TM1	1	4	4	C43-34
2019.1.01158.S	uid://A001/X1469/Xdf	32501_20_a_07_TM1	1	4	4	C43-123456
2019.1.01158.S	uid://A001/X1469/Xe3	18054_19_a_07_TM1	1	4	4	C43-123456
2019.1.01158.S	uid://A001/X1469/Xeb	5123_198_a_07_TM1	1	4	4	C43-123456
2019.1.01158.S	uid://A001/X1469/Xef	8125_Tyn_a_07_TM1	1	4	4	C43-123456
2019.1.01158.S	uid://A001/X1469/Xf7	13694_19_a_07_TM1	1	4	4	C43-123456
2019.1.01158.S	uid://A001/X1469/Xfb	13331_19_a_07_TM1	1	4	4	C43-123456
2019.1.01158.S	uid://A001/X1469/Xff	42168_20_a_07_TM1	1	4	4	C43-123456
2019.1.00663.S	uid://A001/X146a/X87	J053816-_a_06_TM1	2	4	4	C43-4
2019.1.01166.T	uid://A001/X1473/Xc0e	TDE2_a_03_TM1	1	4	4	C43-123456
2019.1.01166.T	uid://A001/X1473/Xc11	TDE2_b_03_TM1	1	3	3	C43-123456
2019.1.01166.T	uid://A001/X1473/Xc18	TDE2_a_06_TM1	1	3	4	C43-123456
2019.1.01166.T	uid://A001/X1473/Xc1b	TDE2_b_06_TM1	1	3	3	C43-123456
2019.1.01166.T	uid://A001/X1473/Xc1e	TDE2_c_06_TM1	1	1	1	C43-123456
2019.1.00783.S	uid://A001/X1474/X185	Titan_b_06_TM1	5	2	1	C43-2
2019.1.00663.S	uid://A001/X1474/X91	J053250-_a_06_TM1	1	4	4	C43-4
2019.1.00507.S	uid://A001/X14c2/X61	CW_Leo_a_06_TM1	1	2	3	C43-34
2019.1.01016.T	uid://A001/X14d8/X3bb	GRBpol_c_03_TM1	1	2	2	C43-123456
2019.1.01016.T	uid://A001/X14d8/X3bf	GRBpol_a_04_TM1	1	2	2	C43-123456
2019.1.00678.S	uid://A001/X14d8/X3eb	CANDELS_a_03_TM1	1	3	3	C43-123456
2019.1.00678.S	uid://A001/X14d8/X3ef	CANDELS_b_03_TM1	2	3	3	C43-123456
2019.1.00678.S	uid://A001/X14d8/X3f3	CANDELS_a_04_TM1	2	3	3	C43-123456
2019.1.00678.S	uid://A001/X14d8/X3f7	CANDELS_b_04_TM1	2	3	3	C43-123456
2019.1.00900.S	uid://A001/X14d8/X404	97148_a_04_TM1	1	2	3	C43-3
2019.1.00900.S	uid://A001/X14d8/X40c	83492_a_04_TM1	1	2	3	C43-2
2019.1.01016.T	uid://A001/X14d8/X423	GRBpol_d_03_TM1	1	2	3	C43-123456
2019.1.01016.T	uid://A001/X14d8/X427	GRBpol_b_04_TM1	1	2	3	C43-123456
2019.1.01008.T	uid://A001/X14d8/X435	Unspecif_a_07_TM1	2	2	3	C43-2345
2019.1.01016.T	uid://A001/X14d8/X44e	GRBpol_e_03_TM1	1	3	3	C43-123456

Table A.2: Set 2

Project code	MOUS ID	SB name	EC	C43	C43p7	NC (OT)
2018.1.00581.S	uid://A001/X133d/X1047	Circinus_a_06_TM1	3	9	10	C43-9
2018.1.00659.L	uid://A001/X133d/X11b8	U_Del_a_06_TM1	1	9	10	C43-89
2018.1.00659.L	uid://A001/X133d/X11bd	W_Aql_a_06_TM1	1	9	10	C43-89
2018.1.00659.L	uid://A001/X133d/X11c2	V_PsA_a_06_TM1	1	9	10	C43-89
2018.1.00659.L	uid://A001/X133d/X11c7	S_Pav_a_06_TM1	1	9	10	C43-89
2018.1.00659.L	uid://A001/X133d/X11cd	U_Del_b_06_TM1	1	9	10	C43-89
2018.1.00659.L	uid://A001/X133d/X11d2	W_Aql_b_06_TM1	1	9	10	C43-89
2018.1.00659.L	uid://A001/X133d/X11d7	V_PsA_b_06_TM1	1	9	10	C43-89
2018.1.00659.L	uid://A001/X133d/X11dc	S_Pav_b_06_TM1	1	9	10	C43-89
2018.1.00659.L	uid://A001/X133d/X11e2	U_Del_c_06_TM1	1	9	9	C43-89
2018.1.00659.L	uid://A001/X133d/X11e7	W_Aql_c_06_TM1	1	9	9	C43-8
2018.1.00659.L	uid://A001/X133d/X11ec	V_PsA_c_06_TM1	1	9	9	C43-8
2018.1.00659.L	uid://A001/X133d/X11f1	S_Pav_c_06_TM1	1	9	9	C43-89
2018.1.00659.L	uid://A001/X133d/X11f7	U_Del_d_06_TM1	1	9	9	C43-89

2018.1.00659.L	uid://A001/X133d/X11fc	W_Aql_d_06_TM1	1	9	9	C43-8
2018.1.00659.L	uid://A001/X133d/X1201	V_PsA_d_06_TM1	1	9	9	C43-8
2018.1.00659.L	uid://A001/X133d/X1206	S_Pav_d_06_TM1	1	9	9	C43-8
2018.1.00659.L	uid://A001/X133d/X120c	T_Mic_a_06_TM1	1	9	9	C43-89
2018.1.00659.L	uid://A001/X133d/X1211	R_Aql_a_06_TM1	1	9	10	C43-89
2018.1.00659.L	uid://A001/X133d/X1217	T_Mic_b_06_TM1	1	9	9	C43-89
2018.1.00659.L	uid://A001/X133d/X121c	R_Aql_b_06_TM1	1	9	10	C43-89
2018.1.00659.L	uid://A001/X133d/X1222	T_Mic_c_06_TM1	1	9	9	C43-8
2018.1.00659.L	uid://A001/X133d/X1227	R_Aql_c_06_TM1	1	9	9	C43-89
2018.1.00659.L	uid://A001/X133d/X122d	T_Mic_d_06_TM1	1	9	9	C43-8
2018.1.00659.L	uid://A001/X133d/X1232	R_Aql_d_06_TM1	1	9	9	C43-8
2018.1.00659.L	uid://A001/X133d/X1238	GY_Aql_a_06_TM1	1	9	10	C43-89
2018.1.00659.L	uid://A001/X133d/X123e	GY_Aql_b_06_TM1	1	9	10	C43-89
2018.1.00659.L	uid://A001/X133d/X1244	GY_Aql_c_06_TM1	1	9	9	C43-8
2018.1.00659.L	uid://A001/X133d/X124a	GY_Aql_d_06_TM1	1	9	9	C43-8
2018.1.00659.L	uid://A001/X133d/X1255	pi1_Gru_a_06_TM1	1	9	10	C43-89
2018.1.00659.L	uid://A001/X133d/X125b	U_Her_b_06_TM1	1	9	10	C43-89
2018.1.00659.L	uid://A001/X133d/X1260	pi1_Gru_b_06_TM1	1	9	10	C43-89
2018.1.00659.L	uid://A001/X133d/X126b	pi1_Gru_c_06_TM1	1	9	9	C43-8
2018.1.00659.L	uid://A001/X133d/X1271	U_Her_d_06_TM1	1	9	9	C43-89
2018.1.00659.L	uid://A001/X133d/X1276	pi1_Gru_d_06_TM1	1	9	9	C43-8
2018.1.00659.L	uid://A001/X133d/X127c	R_Hya_a_06_TM1	1	8	9	C43-89
2018.1.00659.L	uid://A001/X133d/X1282	R_Hya_b_06_TM1	1	9	9	C43-89
2018.1.00659.L	uid://A001/X133d/X1288	R_Hya_c_06_TM1	1	8	9	C43-8
2018.1.00659.L	uid://A001/X133d/X128e	R_Hya_d_06_TM1	2	8	9	C43-8
2018.1.00659.L	uid://A001/X133d/X1299	IRC-1052_a_06_TM1	1	9	10	C43-9
2018.1.00659.L	uid://A001/X133d/X129f	IRC+1001_b_06_TM1	1	9	10	C43-9
2018.1.00659.L	uid://A001/X133d/X12a4	IRC-1052_b_06_TM1	1	9	10	C43-9
2018.1.00659.L	uid://A001/X133d/X12aa	IRC+1001_c_06_TM1	1	9	10	C43-9
2018.1.00659.L	uid://A001/X133d/X12af	IRC-1052_c_06_TM1	1	9	10	C43-9
2018.1.00659.L	uid://A001/X133d/X12b5	IRC+1001_d_06_TM1	1	9	10	C43-9
2018.1.00659.L	uid://A001/X133d/X12ba	IRC-1052_d_06_TM1	1	9	9	C43-8
2018.1.00659.L	uid://A001/X133d/X12c0	RW_Sco_a_06_TM1	1	9	9	C43-9
2018.1.00659.L	uid://A001/X133d/X12c6	RW_Sco_b_06_TM1	1	9	10	C43-9
2018.1.00659.L	uid://A001/X133d/X12cc	RW_Sco_c_06_TM1	1	9	10	C43-9
2018.1.00659.L	uid://A001/X133d/X12d2	RW_Sco_d_06_TM1	1	9	9	C43-8
2018.1.00659.L	uid://A001/X133d/X12d8	VX_Sgr_a_06_TM1	1	9	9	C43-9
2018.1.00659.L	uid://A001/X133d/X12de	VX_Sgr_b_06_TM1	1	9	10	C43-9
2018.1.00659.L	uid://A001/X133d/X12e4	VX_Sgr_c_06_TM1	1	9	9	C43-9
2018.1.00659.L	uid://A001/X133d/X12ea	VX_Sgr_d_06_TM1	1	9	9	C43-8
2018.1.00659.L	uid://A001/X133d/X12f6	SV_Aqr_b_06_TM1	1	9	10	C43-9
2018.1.00659.L	uid://A001/X133d/X12fc	SV_Aqr_c_06_TM1	1	9	10	C43-9
2018.1.00659.L	uid://A001/X133d/X1302	SV_Aqr_d_06_TM1	1	9	9	C43-8
2018.1.00659.L	uid://A001/X133d/X1308	KW_Sgr_a_06_TM1	1	9	9	C43-9
2018.1.00659.L	uid://A001/X133d/X130e	KW_Sgr_b_06_TM1	1	9	10	C43-9
2018.1.00659.L	uid://A001/X133d/X1314	KW_Sgr_c_06_TM1	1	9	9	C43-9
2018.1.00659.L	uid://A001/X133d/X131a	KW_Sgr_d_06_TM1	2	9	9	C43-8
2018.1.00659.L	uid://A001/X133d/X1320	AH_Sco_a_06_TM1	2	9	9	C43-9

2018.1.00659.L	uid://A001/X133d/X1326	AH_Sco_b_06_TM1	2	9	9	C43-9
2018.1.00659.L	uid://A001/X133d/X132c	AH_Sco_c_06_TM1	3	9	9	C43-9
2018.1.00659.L	uid://A001/X133d/X1332	AH_Sco_d_06_TM1	3	9	9	C43-8
2018.1.00689.S	uid://A001/X133d/X13ef	TYC_7851_a_06_TM1	1	9	10	C43-9
2018.1.00689.S	uid://A001/X133d/X13f5	2MASS_J1_a_06_TM1	1	9	10	C43-9
2018.1.00689.S	uid://A001/X133d/X13fb	Sz111_a_06_TM1	1	9	10	C43-9
2018.1.00689.S	uid://A001/X133d/X1401	2MASS_J1_b_06_TM1	1	9	10	C43-9
2018.1.00689.S	uid://A001/X133d/X140d	EM_star_a_06_TM1	1	9	10	C43-9
2018.1.00771.S	uid://A001/X133d/X15da	T_Tau_a_06_TM1	3	6	7	C43-6
2018.1.00771.S	uid://A001/X133d/X15df	CIDA_9_a_06_TM1	7	6	6	C43-6
2018.1.01055.L	uid://A001/X133d/X19a6	IM_Lup_a_03_TM1	3	7	7	C43-7
2018.1.01055.L	uid://A001/X133d/X19d0	IM_Lup_a_06_TM1	3	6	7	C43-7
2018.1.01055.L	uid://A001/X133d/X19d5	HD163296_a_06_TM1	3	6	7	C43-7
2018.1.01055.L	uid://A001/X133d/X19da	AS_209_a_06_TM1	3	6	7	C43-7
2018.1.01055.L	uid://A001/X133d/X19e0	MWC_480_b_06_TM1	7	7	7	C43-7
2018.1.01055.L	uid://A001/X133d/X19e5	IM_Lup_b_06_TM1	3	7	7	C43-6
2018.1.01055.L	uid://A001/X133d/X19ef	AS_209_b_06_TM1	3	7	7	C43-6
2018.1.00397.S	uid://A001/X133d/X1ad6	NGC7052_a_06_TM1	1	7	7	C43-7
2018.1.00915.S	uid://A001/X133d/X262a	CLASS_B1_a_06_TM1	2	9	10	C43-9
2018.1.00978.S	uid://A001/X133d/X279e	NGC4593_a_06_TM1	5	9	9	C43-9
2018.1.01496.S	uid://A001/X133d/X320b	IRAS_162_a_03_TM1	5	6	7	C43-6
2018.1.01526.S	uid://A001/X133d/X324f	spiderwe_b_03_TM1	1	7	7	C43-6
2018.1.01563.S	uid://A001/X133d/X32aa	Cha-MMS1_a_07_TM1	2	7	8	C43-8
2018.1.01634.S	uid://A001/X133d/X3326	IRS_63_b_07_TM1	2	6	6	C43-6
2018.1.01647.S	uid://A001/X133d/X3356	NGC_2264_a_06_TM1	3	7	7	C43-7
2018.1.01647.S	uid://A001/X133d/X335c	NGC_2264_a_04_TM1	4	8	8	C43-8
2018.1.01194.S	uid://A001/X133d/X377c	HH24_a_06_TM1	3	6	7	C43-6
2018.1.01291.S	uid://A001/X133d/X3b07	V2775_Or_a_06_TM1	1	9	10	C43-9
2018.1.01291.S	uid://A001/X133d/X3b0c	V1647_Or_a_06_TM1	1	9	9	C43-9
2018.1.01506.S	uid://A001/X133d/X3e54	NGC1068_a_03_TM1	3	6	7	C43-6
2018.1.00113.S	uid://A001/X133d/X6bd	NGC7465_a_07_TM1	1	6	6	C43-6
2018.1.01070.S	uid://A001/X134b/X15a	G12.91_a_03_TM1	1	6	7	C43-6
2018.1.01236.S	uid://A001/X1354/X16	ngc_4945_a_03_TM1	3	8	8	C43-8
2018.1.01302.S	uid://A001/X1359/X4b	LkHa330_a_06_TM1	2	8	9	C43-8
2019.1.01132.S	uid://A001/X1465/X18f7	NGC1482_b_03_TM1	2	3	4	C43-4
2019.1.01034.S	uid://A001/X1465/X1c38	DEEP2_33_a_06_TM1	1	4	6	C43-5
2019.1.00994.S	uid://A001/X1465/X1ea2	M17SW_b_06_TM1	1	3	4	C43-4
2019.1.00847.S	uid://A001/X1467/X260	04191+15_a_07_TM1	2	4	4	C43-4
2019.1.00847.S	uid://A001/X1467/X267	04489+30_a_07_TM1	1	4	4	C43-4
2019.1.01039.S	uid://A001/X1468/X1a2	M33_sarm_a_03_TM1	1	4	4	C43-4

B Software products

In this appendix we document the software tools which we have developed during this study and which will remain useful for future work. All of them are available in the JAO CVS repository.

B.1 mshistotools

The `mshistotools` module is a general toolkit to create and handle baseline length (BL) histograms. It is accessible via the JAO CVS repository directory

`AIV/science/ArrayConfiguration/beamWG/mshistotools.py`

The module provides two main classes for creating and operating on BL histograms (`Histogram1D` and `Histogram2D`) and a number of convenience functions.

```
NAME
    mshistotools

DESCRIPTION
 # Code development started as part of the ESO internal ALMA development study 2020/21
 # "New methods for ALMA beam shaping and the assessment of angular scale sensitivity"
 #
 # mshistotools.py
 #
 # A comprehensive Python module for generating observed and expected 1D and 2D BLDs
 # from given sets of MeasurementSets or Science Goal parameters, plotting them,
 # and performing operations like adding, subtracting, scaling.
 #
 # Dirk Petry (ESO)
 # Ruediger Kneissl (ESO/JAO)
 # Stefano Facchini (ESO)
 # Ignacio Toledo (JAO)
 # Maria Diaz Trigo (ESO)
 #
 # $Id: mshistotools.py,v 1.40 2021/11/15 11:57:08 dpetry Exp $

CLASSES
 builtins.object
     Histogram1D
     Histogram2D
```

```
class Histogram1D(builtins.object)
 |  1D histogramming functionality
 |
 |  Methods defined here:
 |
 |  __init__(self, values, boundaries_r)
 |      By default, initialise from an array with bin boundaries
 |
 |  check_1dhisto_couple_bins(self, histogram2)
 |      Check whether two histograms are compatible in their bins
 |
 |  compare_bins(histo1, histo2)
 |      compare the binning of the two 1D histos and return
 |      1) the binning which is valid for both (i.e. that of the larger one)
 |      2) the values of the first in new binning
 |      3) the values of the second in new binning
 |
 |      raise exception if the binning is incompatible
 |
 |  compute_metric(histo1, histo2, normalize=True, metric='chi2')
 |      compute 'chi2' with no error on number of visibilities
 |
 |  copy(self)
 |      Return a deep copy of this histogram.
 |
 |  get_average(self)
 |      Return the average number of visibility per bin
 |
 |  get_num_rad_bins(self)
 |      Return the number of radial bins in the histogram.
 |
 |  get_rad_bins(self)
 |      Return the array of radial bin boundaries.
 |
 |  get_std(self)
 |      Return the average number of visibility per bin
 |
 |  get_values(self)
 |      Return the 2d array of entries of the histogram.
 |
 |  hilobound_bins(self, lolimit=1.0)
 |      return highest and lowest bin number which contain entries > lolimit (default: 1.)
 |
 |  overplot_histo(self, histograms, colors, legend=None, title=None, xlabel=None, ylabel=None, savefig
 |      create 1d plot of multiple histograms
 |      histograms: the array of other histogram objects to overplot on the first (the object from whic
 |      colors: the array of colors for all of the histograms - the first and those from array 'histogr
 |      legend: the array of legend texts for all of the histograms - the first and those from array 'h
 |
 |  plot_histo(self, title=None, xlabel=None, ylabel=None, savefig=False, filename=None, color='blue', 
 |      create 1d plot of the histogram
 |
 |      hlines - list of additional horizontal lines to be plotted on the histogram
 |         Each line is specified by the y-axis value and a color. Optionally a linestyle ('-', '--', '
 |         can be added as third element. Otherwise '--' is used.
```

```
 |          Example: [[1.0, 'blue'], [0.6, 'red']] will plot two lines, a blue one at 1.0 and a red on
 |          Default: [] - don't plot horizontal lines
 |
 |       ylims - list containing the min and max data value to be plotted
 |          Example: [-1., 2.] - set the vertical scale to start at -1.0 and end at 2.0
 |          Default: [] - adapt to the actual minimum and maximum of the data
 |
 |   plot_histo2(self, title=None, xlabel=None, ylabel=None, savefig=False, filename=None, ax=None, co
 |       create 1d plot of the histogram
 |
 |   save(self, filename)
 |       Save the histogram in a pickle file of given name
 |
 |   ----------------------------------------------------------------------
 |   Class methods defined here:
 |
 |   add(histo1, histo2, normalize=False) from builtins.type
 |       compute the sum of two histograms
 |
 |   difference(histo1, histo2, normalize=False) from builtins.type
 |       compute the difference between two histograms
 |
 |   difference_nn(histo1, histo2, normalize=False) from builtins.type
 |       compute the difference between two histograms and set negatives zero
 |
 |   fill(values, rad_bins) from builtins.type
 |       Create 1d histogram with given radial bins and fill it from the values array
 |
 |   from_ms(vis=None, scale='linear', entry='baselines', N_rad_bins=None, N_vis_bin=1000,
rad_bins_in=None, freq='', fields=[], spws=[], intents=['OBSERVE_TARGET#ON_SOURCE'],
applyrelweights=False, applyweights=False) from builtins.type
 |       Initialise histogram from a MeasurementSet given by its name on disk
 |          with automatic or manual binning.
 |
 |
 |       Parameters
 |       ----------
 |       vis         : string
 |                     name of the MeasurementSet
 |       scale       : string
 |                     Accepted values: 'linear', 'log'. Default: 'linear'
 |                     Defines whether the automatic radial binning is linear or logaritmic
 |       entry       : string
 |                     Accepted values: 'baselines', 'ang_scales'. Default: 'baselines'
 |                     Defines the quantity to load into histogram object
 |       N_vis_bin   : integer
 |                     Default: 1000
 |                     Defines the average number of expected visibilities per bin
 |       N_rad_bins  : integer, optional
 |                     Defines the number of radial bins. If this is defined, N_vis_bin will not be
 |                     used in the setting of the bins
 |       rad_bins_in : float, array, optional
 |                     Defines the radial bins, no automatic choice will be performed
 |       freq        : float
 |                     [GHz]
```

```
 |                    Defines the reference frequency of the observation based on which
 |                    the angular scale is computed; default:
 |                    if parameter spws is given: take from spws[0],
 |                    else if parameter intents is given: take from first spw for first intent,
 |                    otherwise take from SPW 0
 |      fields      : list of integers
 |                    Field IDs for all fields to be selected. Default: use data from all fields
 |      spws        : list of integers
 |                    SPW IDs for all spws to be selected. Default: use data from all science SPWs
 |      intents     : list of strings
 |                    Intent names to select fields with the given intents.
 |                    Default: ['OBSERVE_TARGET#ON_SOURCE']
 |      applyrelweights: use the weights from MS column WEIGHT as relative weights in the histogram
 |                    (takes precedence over applyweights)
 |                    Default: False
 |
 |      applyweights: use the weights from the WEIGHT column as absolute weights in the histogram
 |                    Default: False
 |
 |      Returns
 |      -------
 |      Filled 1d histogram object
 |
 |  radial_profile_from_map(map, cellsize, rbins, mode='average') from builtins.type
 |      Create a histogram containing the radial profile of a given map
 |
 |      map - 2D numpy ndarray, dimensions: N x N where N is odd
 |
 |      cellsize - size of the cells of the map
 |
 |      rbins - list of radial bin boundaries (N + 1)
 |              or number of bins. In the latter case, the lower edge is
 |              assumed to be 0, the upper edge is taken from the dimensions of the map
 |              and the cell size.
 |
 |      mode - determines the way the histogram content is computed:
 |          "average" (default) - the content is the average over the polar angle range (360 deg)
 |          "min" - content is the minimum cell content in the annulus
 |          "max" - content is the maximum cell content in the annulus
 |
 |  ratio(histo1, histo2, normalize=False, log=False) from builtins.type
 |      compute the ratio between two histograms
 |
 |  scale(histo, factor) from builtins.type
 |      Create a histogram by scaling the input histo by a factor
 |
 |  set(values, rad_bins) from builtins.type
 |      Create 1d histogram with given values in given radial bins
 |
 |  ----------------------------------------------------------------------
 |
 |
 |
 |
```

```
class Histogram2D(builtins.object)
 |  2D histogramming functionality
 |
 |  Methods defined here:
 |
 |  __init__(self, values, boundaries_r, boundaries_theta)
 |      By default, initialise from an array with bin boundaries
 |
 |  check_2dhisto_couple_bins(self, histogram2)
 |      Check whether two histograms are compatible in their bins
 |
 |  compare_rad_bins(histo1, histo2)
 |      compare the radial binning of the two 2D histos and return
 |      1) the binning which is valid for both (i.e. that of the larger one)
 |      2) the values of the first in new binning
 |      3) the values of the second in new binning
 |
 |      raise exception if the binning is incompatible
 |
 |  compute_metric(histo1, histo2, normalize=True, metric='chi2')
 |      compute 'chi2' with no error on number of visibilities
 |
 |  copy(self)
 |      Return a deep copy of this histogram.
 |
 |  get_average(self)
 |      Return the average number of visibility per bin
 |
 |  get_azi_bins(self)
 |      Return the array of azimuthal bin boundaries.
 |
 |  get_histo1d_azimuth(self)
 |      Return the entry of 1d histogram in azimuth
 |
 |  get_histo1d_radius(self)
 |      Return the entry of 1d histogram in radius
 |
 |  get_num_azi_bins(self)
 |      Return the number of azimuthal bins in the histogram.
 |
 |  get_num_rad_bins(self)
 |      Return the number of radial bins in the histogram.
 |
 |  get_number_vis(self)
 |
 |  get_rad_bins(self)
 |      Return the array of radial bin boundaries.
 |
 |  get_std(self)
 |      Return the average number of visibility per bin
 |
 |  get_values(self)
 |      Return the 2d array of entries of the histogram.
 |
 |
```

```
|  hilobound_rad_bins(self, lolimit=1.0)
|      return highest and lowest radial bin number which contain entries > lolimit (default=1.)
|
|  plot_histo(self, cmap=None)
|      create 2d plot of the histogram
|      cmap is an optional alternative colourmap; default is plt.cm.jet
|
|  save(self, filename)
|      Save the histogram in a pickle file of given name
|
|  ----------------------------------------------------------------------
|  Class methods defined here:
|
|  add(histo1, histo2) from builtins.type
|      compute the sum of two histograms
|
|  difference(histo1, histo2) from builtins.type
|      compute the difference between two histograms
|
|  fill(values, rad_bins, a_bins, pointsym=True) from builtins.type
|      Create 2d histogram with given radial and azimuthal bins and fill it from the 2D values array.
|      phi values are expected in radians.
|      values format: values[0] is the array of r values, values[1] is the array of phi values.
|      If pointsym is True, phi values are forced in the range 0 - 180 deg and
|      duplicate entries for points are made rotated by 180 deg to achieve point symmetry.
|
|  from_ex(scale='linear', entry='baselines', N_vis_bin=500, N_rad_bins=None, N_azi_bins=20,
rad_bins_in=None, a_bins_in=None, freq=100.0, ar=None, las=None, time=0.5, interval_s=10.0,
ana_fill=False, map_size=3.0, rr=False) from builtins.type
|      Initialise histogram from a set of
|
|      Parameters
|      ----------
|      scale       : string
|                    Accepted values: 'linear', 'log'. Default: 'linear'
|                    Defines whether the automatic radial binning is linear or logaritmic
|      entry       : string
|                    Accepted values: 'baselines', 'ang_scales'. Default: 'baselines'
|                    Defines the quantity to load into histogram object
|      N_vis_bin   : integer
|                    Default: 500
|                    Defines the average number of expected visibilities per bin
|      N_rad_bins  : integer, optional
|                    Defines the number of radial bins. If this is defined, N_vis_bin will not be
used in the setting of the bins
|      N_azi_bins  : integer
|                    Default: 20
|                    Defines the number of azimuthal bins
|      rad_bins_in : float, array, optional
|                    Defines the radial bins, no automatic choice will be performed
|      a_bins_in   : float, array, optional
|                    Defines the azimuthal bins
|      freq        : float
|                    [GHz] Default: 100
|                    Defines the reference frequency of the observation
```

```
|      ar          : float
|                    [arcsec]
|                    Requested angular resolution
|      las         : float
|                    [arcsec] requested largest angular scale
|                    If las < (5. * ar), las is set to 6.5 * ar
|      time        : float
|                    [h] Default: 0.5
|                    Requested exposure time
|      interval_s  : the integration time (not used in the present implementation)
|                    [s] Default: 10.
|      ana_fill    : logical
|                    Filling histogram directly analytically
|                    Default: False (while testing)
|      map_size    : float
|                    Size of the beam map on pixels over LAS
|                    Default: 3.
|      rr          : logical
|                    Default: False
|                    For robust false is natural (r=2) and true is r=0.5
|
|      Returns
|      -------
|      Filled 2d histogram object
|
|  from_ms(vis=None, scale='linear', entry='baselines', N_vis_bin=500, N_rad_bins=None,
N_azi_bins=20, rad_bins_in=None, a_bins_in=None, freq='', fields=[], spws=[],
intents=['OBSERVE_TARGET#ON_SOURCE'], applyrelweights=False, applyweights=False) from builtins.type
|      Initialise histogram from a MeasurementSet given by its name on disk
|         with automatic or manual binning.
|
|
|      Parameters
|      ----------
|      vis         : string
|                    name of the MeasurementSet
|      scale       : string
|                    Accepted values: 'linear', 'log'. Default: 'linear'
|                    Defines whether the automatic radial binning is linear or logaritmic
|      entry       : string
|                    Accepted values: 'baselines', 'ang_scales'. Default: 'baselines'
|                    Defines the quantity to load into histogram object
|      N_vis_bin   : integer
|                    Default: 500
|                    Defines the average number of expected visibilities per bin
|      N_rad_bins  : integer, optional
|                    Defines the number of radial bins. If this is defined, N_vis_bin will not be
|                    used in the setting of the bins
|      N_azi_bins  : integer
|                    Default: 20
|                    Defines the number of azimuthal bins
|      rad_bins_in : float, array, optional
|                    Defines the radial bins, no automatic choice will be performed
|      a_bins_in   : float, array, optional
|                    Defines the azimuthal bins
```

```
 |      freq        : float
 |                    [GHz]
 |                    Defines the reference frequency of the observation based on which
 |                    the angular scale is computed; default:
 |                    if parameter spws is given: take from spws[0],
 |                    else if parameter intents is given: take from first spw for first intent,
 |                    otherwise take from SPW 0
 |      fields      : list of integers
 |                    Field IDs for all fields to be selected. Default: use data from all fields
 |      spws        : list of integers
 |                    SPW IDs for all spws to be selected. Default: use data from all science SPWs
 |      intents     : list of strings
 |                    Intent names to select fields with the given intents.
 |                    Default: ['OBSERVE_TARGET#ON_SOURCE']
 |
 |      applyrelweights: use the weights from the WEIGHT column as relative weights in the histogram
 |                    (takes precedence over applyweights)
 |                    Default: False
 |
 |      applyweights: use the weights from the WEIGHT column as absolute weights in the histogram
 |                    Default: False
 |
 |      Returns
 |      -------
 |      Filled 2d histogram object
 |
 |  psf_from_2dhisto(histo) from builtins.type
 |      Read 2D histogram and return PSF in rectangular map
 |
 |  ratio(histo1, histo2, normalize=False) from builtins.type
 |      compute the ratio between two histograms
 |
 |  scale(histo, factor) from builtins.type
 |      Create a histogram by scaling a given histogram by a given factor
 |
 |  set(values, rad_bins, a_bins) from builtins.type
 |      Create a 2d histogram with given radial and azimuthal bins and set the bin contents with values
 |      (format: values[n][m] is the contents of the nth azimuthal and mth radial bin)
 |
 |  ----------------------------------------------------------------------
 |  Data descriptors defined here:
 |
 |  __dict__
 |      dictionary for instance variables (if defined)
 |
 |  __weakref__
 |      list of weak references to the object (if defined)

FUNCTIONS
    closeall()
        Close all open plot windows.

    get_ref_freq_hz(vis, freq, spws, intents)
        Determine the reference frequency [Hz] to be used for calculating the angular scales
```

```
getinterval(vis, fields, spws, intents=['OBSERVE_TARGET#ON_SOURCE'])
    Return the INTERVAL column for the selected part of the Main table of the given MS

    vis - the MS
    fields - list of field IDs for the selection
    spws - list of SPW IDs for the selection
    intents - list of intents for the selection
           default: ['OBSERVE_TARGET#ON_SOURCE']

load(filename)
    Load the object contained in the given filename which was previously
    created with the save() method.
    Extension '.pkl' is automatically appended to the filename if it is not yet present.

save(obj, filename)
    Save the given object on disk using pickle protocol 1.
    Extension '.pkl' is automatically appended to the filename if it is not yet present.

selcriterion(vis, unflagged=True, fields=[], spws=[], intents=[])
    Create TaQL query string
        unflagged - select only unflagged data
                    default: True
        fields    - select data from the given field IDs
                    default: [] all fields
        spws      - select data from the given SPW IDs
                    default: [] all spws
        intents   - (overrides 'fields') select data for the fields of the given intents
                    default: [] all intents
specialbin(bllength_m, finerby2=False, version=1)
    Return the zero-based number of the bin containing the given BL length
    assuming the binning given by the specialbins function.

    bllength_m  - the BL length (m) for which the bin number is to be found

    finerby2 - if True, assume the finer binning as in the specialbins function
               with parameter finerby2=True
               default=False

    version - the version of the bin width definition
         default: 1

specialbins(max_m=16000, finerby2=False, version=1)
    Return numpy array of bin boundaries for special non-equidistant binning
    according to the following scheme:
    Version 1 (default):
      6 bins of 7 m width from 0 to 42,
      9 bins of 12 m width from 42 to 150,
      34 bins of 25 m  width out to 1000,
      80 bins of 50 m width out to 5000,
      from then on 100 m width out to the max BL length

    Version 2:
      Bin width follows the formula
        width(x) = 693./15300.*x+7.
      where x is the lower edge of the bin in meters.
```

```
        Lower edge of the first bin (bin zero) is ==0.

      max_m - the max BL length covered by the bins (m);
             if a fraction, it will be rounded up to the next whole metre.
             default: 16000 (m)

      finerby2 - if True, make the binning a factor 2 finer
             default: False

      version - the version of the bin width definition
           default: 1

  version()
    Return version of mshistotools as a string.
```

B.1.1 Example usage

(Under CASA 6.2.1)

Creating and handling 1D and 2D BLDs from given MSs

```
import mshistotools as msh
observation1 = msh.Histogram2D.from_ms(vis1, N_vis_bin=20, N_azi_bins=36, spws=[19],
                                        fields=[3], applyrelweights=True)
observation2 = msh.Histogram2D.from_ms(vis2, N_vis_bin=20, N_azi_bins=36, spws=[19],
                                        fields=[3], applyrelweights=True)
observation1.plot_histo()
observation2.plot_histo()
observation1.save('observation1.pkl')
observation2.save('observation2.pkl')

myradbins = observation1.get_rad_bins()

observation1_1d = msh.Histogram1D.from_ms(vis1, rad_bins_in=myradbins,
                                            spws=[19], fields=[3], applyrelweights=True)
observation2_1d = msh.Histogram1D.from_ms(vis2, rad_bins_in=myradbins,
                                            spws=[19], fields=[3], applyrelweights=True)

observation1_1d.overplot_histo([observation2_1d],colors=['green', 'blue'],
                                    legend=['Observation 1', 'Observation 2],
                                    title='BLDs of Observation 1 and 2',
                                    xlabel='BL Length (m)', ylabel='visibility hours',
                                    savefig=True, filename='obs1and2.png')

o1 = msh.load('observation1.pkl')
o2 = msh.load('observation2.pkl')
mysum = msh.Histogram2D.add(o1,o2)
mysum.plot_histo()
mydiff = msh.Histogram2D.difference(o1,o2)
mydiff.plot_histo()
myratio = msh.Histogram2D.ratio(o1,o2)
myratio.plot_histo()
```

Creating 2D and 1D BLDs from science goal parameters

```
import mshistotools as msh
import numpy as np
theradbins = np.array(range(0,int(mymaxbl/7.)+2))*7
expectation = msh.Histogram2D.from_ex(rad_bins_in=theradbins, N_azi_bins=36,
                                        freq=350.0, ar=0.1, las=12.0, time=0.5,
                                        interval_s=6.0, rr=True, ana_fill=True)
expectation.plot_histo()
```

B.2 assess_ms

`assess_ms` is a set of functions for assessing the combined baseline length distribution (BLD) of a given set of MeasurementSets (MSs). Furthermore, functions are provided for determining and applying weights to adjust the BLD of a given MS.
`assess_ms.py` is accessible via the JAO CVS repository directory

```
AIV/science/ArrayConfiguration/beamWG/assess_ms.py
```

For example usage see section 5.3.

```
NAME
    assess_ms

DESCRIPTION
    # Code development started as part of the ESO internal ALMA development study 2020/21
    # "New methods for ALMA beam shaping and the assessment of angular scale sensitivity"
    #
    # assess_ms
    #
    # Methods to assess the Baseline Length Distribution of a given list of MSs based on
    #    their science goal parameters
    # D. Petry (ESO)
    # Maria Diaz Trigo (ESO)
    #
    # $Id: assess_ms.py,v 1.42 2021/11/07 14:10:24 dpetry Exp $

FUNCTIONS
    applyweights(par_record)
        Apply the weights generated by reweight_ms to a given set of MSs

        The input parameter record is a dictionary of the format

               {'bins': list(bins),
                'weights': list(w_i),
                'vis': vis,
                'freq_ghz': freq_ghz,
                'ar_asec': ar_asec,
                'las_asec': las_asec,
                'time_s': time_s,
                'fields': fields,
                'repspwid': repspwid,
                'condition': condition,
                'binningversion': binningversion,
                'expcalcversion': expcalcversion,
                'compromise': compromise}

        as generated by reweight_ms.

    ar_asec_for_l80(l80_m, freq_ghz)
        Compute the equivalent angular resolution for a given L80
        according to ALMA THB, eq 7.4, Cycle 7 version
```

```
assess_ms(vis, freq_ghz, ar_asec_range, las_asec, time_s, ar_asec_to_test=[], targetid=None, repsp

    assess_ms
       compare the BL length histo of a given observation with
       the expectation from the PI parameters

       return True if QA2_PASS is recommended

    vis - the observed MS(s) or [] (empty list) if the observed histograms are to be taken from st
          (if a list of MSs is entered, they are combined)
          Examples:  [] - take the observed histograms from the files histo_*_absweight.pkl
                       and histo_*_relweight.pkl in the directory provided by parameter storagedir

          ['uid___A002_Xe64b7b_X2ac81.ms.split.cal','uid___A002_Xe64b7b_X2ad02.ms.split.cal']
                       - extract the observed histogram from the combination of the two given MSs
                         using targetid and repspwid for field and SPW selection.

    freq_ghz - the frequency at which the PI parameters are given (GHz)
               If set to None, the central freq of the repspwid will be used.

    ar_asec_range - the angular resolution range (arcsec)
               a list of two values: min and max of the expectation range

    las_asec - the largest angular scale (arcsec)

    time_s - the estimated necessary exposure time (s)

    ar_asec_to_test - the angular resolution(s) (arcsec)
               the list of the angular resolutions to test in the QA assessment
              default: [] = use values in parameter "ar_asec_range"

    targetid - the representative target field id or field NAME.
               Use the NAME in particular for mosaics to capture all mosaic pointings.
               (only needed if vis != [], i.e. MSs are to be read)
              default: the first science target will be used

    repspwid - the representative SPW id
               (only needed if vis != [], i.e. MSs are to be read)
              default: the SPW containing the rep. freq, i.e. freq_ghz, will be used

    condition - the condition for the calculation of the overall QA assessment
          options:
             'a' - filling fraction > pass_tresh in all bins, >=1 in the upper 10%,
                   average filling fraction > 0.9

             'b' - filling fraction >= 1 in all bins

             'c' - determine filling fraction in 10% bins, filling fraction > pass_tresh in all bi
                   >= 1 in uppermost (10th) bin, average filling fraction > 0.9

          default: 'c'

    pass_thresh - the passing threshold used in the condition given by parameter "condition".
            (This threshold is marked in the ten-bin filling fraction plots with a red line.)
          default: 0.6
```

```
        storagedir - the directory into which to store all plots and histograms
                     The plots are stored as png files. The histograms are stored via the msh.save() met
                     Stored are the histos with absolute and relative weighting.
              default: '.' (current working dir)

        binningversion - the version of the "special" binning to be used for the result histograms: 1 or
              default: 2

        expcalcversion - choose between different options to calculate the expected base line distributi
               0: ana_fill=True, rr=True
               1: ana_fill=False, rr=True
               2: ana_fill=True, rr=False
               3: ana_fill=False, rr=False
               10: use filldish.from_ex_1d for the 1D histos, rr=False
               11: use filldish.from_ex_1d for the 1D histos, rr=True
              default: 0

        weighting - apply weighting when calculating the observed BLDs
              default: True

        useL80 - if True: determine the L80 from the observation and the equivalent AR
                 and append it to the list of ARs to be evaluated for the QA2 decision
              default: True

        ffplotlim - the upper end of the filling fraction scale to plot in the ten bin plots
              default: 0. - adapt to the actual values of the filling fractions


        Example:
            assess_ms(['uid___A002_Xe27761_X5551.ms.split.cal'], ar_asec_range=[0.24,0.36], las_asec=5.,
                      time_s=112., freq_ghz=336., ar_asec_to_test=[0.24,0.31,0.36], storagedir='SPT0109-

    assess_ms_version()

    bld_l80(histo1d)
        Return the 80th percentile of the given BLD, i.e. the smallest base line length
        which is larger than 80% of the total entries of the histogram
        or None if it cannot be determined

    closeall()
        Convenience function to close all open plots.

    doqa(exphisto1d, obshisto1d, inttime_s, time_s, condition, pass_thresh, plotname, binningversion=1,
        Do the comparison expectation - observation
        return QA_PASS (True or False) and set of reasons

        ffplotlim - the upper end of the filling fraction scale to plot in the ten bin plots
          default: 0. - adapt to the actual values of the filling fractions

    reweight_ms(vis, freq_ghz, ar_asec, las_asec, time_s, targetid=None, repspwid=None, condition='c', p
        reweight_ms
           Derive weights from the BL length histo of a list of MSs and their science goal parameters

           Return dictonary containing the criteria and the two result vectors:
```

```
       1) the BL length bin definitions
       2) the reweighting factors for each bin

   (uses same input parameters as assess_ms)

vis - the observed MS(s)
      Example:
      ['uid___A002_Xe64b7b_X2ac81.ms.split.cal','uid___A002_Xe64b7b_X2ad02.ms.split.cal']
                   - extract the observed histogram from the combination of the two given MSs
                     using targetid and repspwid for field and SPW selection.

freq_ghz - the frequency at which the PI parameters are given (GHz)
           If set to None, the central freq of the repspwid will be used.

ar_asec - the angular resolution (arcsec)

las_asec - the largest angular scale (arcsec)

time_s - the estimated necessary exposure time (s)

targetid - the representative target field id or field NAME.
           Use the NAME in particular for mosaics to capture all mosaic pointings.
           (only needed if vis != [], i.e. MSs are to be read)
           if not provided, the first science target will be used

repspwid - the representative SPW id
           (only needed if vis != [], i.e. MSs are to be read)
           if not provided, the SPW containing the rep. freq, i.e. freq_ghz,
           will be used

condition - the condition for the calculation of the overall QA assessment
      options:
         'a' - filling fraction > pass_thresh in all bins, >=1 in the upper 10%,
               average filling fraction > 0.9

         'b' - filling fraction >= 1 in all bins

         'c' - determine filling fraction in 10% bins, filling fraction > pass_thresh in all b
               >= 1 in uppermost (10th) bin, average filling fraction > 0.9

      default: 'a'

pass_tresh - passing threshold for the given condition
      default: 0.85

storagedir - the directory into which to store all plots and histograms
             The plots are stored as png files. The histograms are stored via the msh.save() m
             Stored are the histos with absolute and relative weighting.
      default: '.' (current working dir)

binningversion - the version of the "special" binning to be used for the result histograms: 1
      default: 1

expcalcversion - choose between different options to calculate the expected base line distribu
       0: ana_fill=True, rr=True
```

```
           1: ana_fill=False, rr=True
           2: ana_fill=True, rr=False
           3: ana_fill=False, rr=False
          default: 0

    compromise - if True, downweight only bins with filling fraction > 1 to the level defined by
            filling fraction == 1. If False, downweight to the level of the lowest filling fraction.
          default: False

    weighting - apply weighting when calculating the observed BLDs
          default: True

    Example:
        reweight_ms(['uid___A002_Xe27761_X5551.ms.split.cal'], ar_asec=0.24, las_asec=5.,
                    time_s=112., freq_ghz=336., storagedir='SPT0109-47results')
```

B.3 filldish

The functions of the `filldish` module provide code which is analogous to the `from_ex` methods of `mshistotools` but instead of using the "analytical" method for calculating the expected BLD (section 3.2.1), it uses the "filled dish" method (section 3.2.2).
`filldish.py` is accessible via the JAO CVS repository directory

`AIV/science/ArrayConfiguration/beamWG/filldish.py`

```
NAME
    filldish

DESCRIPTION
    # Code development started as part of the ESO internal ALMA development study 2020/21
    # "New methods for ALMA beam shaping and the assessment of angular scale sensitivity"
    #
    # filldish
    #
    # Methods to generate expected Baseline Length Distributions from Science Goal parameters
    # using the FD method: fills a 2D aperture of a diameter corresponding to the angular resolution
    # with randomly placed antenna positions imposing a minimum distance between all antennas
    # corresponding to the largest angular scale. Uses mshistotools.
    #
    # D.Petry (ESO)
    #
    # $Id: filldish.py,v 1.11 2021/07/01 07:33:20 dpetry Exp $

FUNCTIONS
    checkantpos(x, y, antposs, mindist_m)
        Verify that antenna position (x,y) has a distance of at least mindist_m
        to all antenna positions in array antposs.

    filldish(nvis, maxbl_m)

    filldish2(nvis, maxbl_m, minbl_m=0.0)

    filldish3(nvis, maxbl_m, minbl_m)

    from_ex_1d(bins, freq_ghz, ar_asec, las_asec, time_s, interval_s, method=3,
               expnant=43, rr=False)
        from_ex_1d

        Generate an expected 1D BL length distribution

         bins - histo bin boundaries
             If of type int or float, bins is interpreted as the bin width for the histogram (m).
             If of type list or np.array, it is interpreted as the bin boundary array (m).

         freq_ghz    : the observing frequency
         ar_asec     : Requested angular resolution
         las_asec    : requested largest angular scale
                       If las < (5. * ar), las is set to 6.5 * ar
         time_s      : Requested exposure time
```

```
     interval_s  : the integration time (not used in the present implementation)

     method - method to generate the 'antenna positions'
               1 = random uniformly distributed (no explicit min BL length)
               2 = equidistant grid (min BL length)
               3 = random uniformly distributed (min BL length)
           default: 3

     expnant - the expected number of antennas
           default: 43

     rr - correct AR and LAS for the robust setting of 0.5 as in msh.from_ex()
           default: False

from_ex_2d(radbins, n_azbins, freq_ghz, ar_asec, las_asec, time_s, interval_s,
           method=3, expnant=43, rr=False)
    from_ex_2d

    Generate an expected 2D BL length distribution

     radbins - radial histo bin boundaries
         If of type int or float, bins is interpreted as the bin width for the histogram (m).
         If of type list or np.array, it is interpreted as the bin boundary array (m).

     n_azbins - number of (equidistant) azimuthal bins

     freq_ghz    : the observing frequency
     ar_asec     : Requested angular resolution
     las_asec    : requested largest angular scale
                   If las < (5. * ar), las is set to 6.5 * ar
     time_s      : Requested exposure time
     interval_s  : the integration time (not used in the present implementation)

     method - method to generate the 'antenna positions'
               1 = random uniformly distributed (no explicit min BL length)
               2 = equidistant grid (default)
               3 = random uniformly distributed (min BL length)
           default: 3

     expnant - the expected number of antennas
           default: 43

     rr - correct AR and LAS for the robust setting of 0.5 as in msh.from_ex()
           default: False

makefilleddishhisto(nvis, maxbl_m, bins=3, method=2, seed=12345, minbl_m=0.0)
    makefilleddishhisto - generate BL length histogram for given parameters
          assuming a fully filled array with equal density and ignoring dish diameter
          (i.e. essentially creating an ideal interferometer with image fidelity
          equal to that of an optical telescope)
       nvis - approximate number of entries in the histo
       maxbl_m - max BL length (m)
       bins - histo bin boundaries (m)
            If of type int, bins is interpreted as the bin width for the histogram.
            If of type list or np.array, it is interpreted as the bin boundary array
```

```
                (default 3)
        method - method to generate the 'antenna positions'
                    1 = random uniformly distributed (no explicit min BL length)
                    2 = equidistant grid (default)
                    3 = random uniformly distributed (min BL length)
        seed - seed for random generator (only needed for method 1)
                    (default 12345)

        Usage example:

                myhisto = makefilleddishhisto(2000000, 37, 1, 1)
                myhisto.plot_histo()

            create and plot a filled-dish BL histo for max BL length 37 m with bin width 1 m
            using the random antenna position method.

    placeants(nant, maxbl_m, minbl_m, maxiter=10000.0)
        Return array of positions of randomly placed antennas in aperture of diameter maxbl_m
        with minimum distance of minbl_m
```

B.3.1 Example usage

```
import filldish as fd
import numpy as np
theradbins = np.array(range(0,int(mymaxbl/7.)+2))*7
expectation_fd = fd.from_ex_1d(bins=theradbins, freq_ghz=115., ar_asec=0.8,
                 las_asec=16., time_s=1800., interval_s=6., method=3, expnant=43, rr=True)
expectation_fd.plot_histo()
```

B.4 thinms

The `thinms` utility provides functions to re-shape the baseline length distribution (BLD) of a given MeasurementSet by either flagging baselines ("thinning") or by down-weighting them. This can be used to study the effect of different BLD shapes and/or to bring the BLD into a known best shape for subsequent imaging.
`thinms.py` is accessible via the JAO CVS repository directory

`AIV/science/ArrayConfiguration/beamWG/thinms.py`

```
NAME
    thinms

DESCRIPTION
    # Code development started as part of the ESO internal ALMA development study 2020/21
    # "New methods for ALMA beam shaping and the assessment of angular scale sensitivity"
    #
    # thinms
    #
    # Methods to shape the Baseline Length Distribution of a given MS
    # D. Petry (ESO)
    #
    # $Id: thinms.py,v 1.1 2021/07/01 07:32:32 dpetry Exp $

FUNCTIONS
    binprob_from_fillfrac(fillfrac)
        Calculate array of bin flagging probabilities from array of filling fractions
           using binprob = 1. - 1./(fillfrac/min(fillfrac))

    binprob_mod(fillfrac, lowbins=[], lowfrac=0.333)
        Calculate array of bin flagging probabilities from array of filling fractions
        using binprob = 1. - 1./(fillfrac/min(fillfrac))
        Then modify it such that the given bin numbers in lowbins (0 to 9) are reduced
        by lowfrac (default 0.333) w.r.t. the ideal but the total number of visibilities
        stays the same.

    bl(uvw)
        Baseline length of uv(w) vector as list or array

    reweightms(vis, bindef, binprob, debug=False)
        Reweight an MS by modifying the WEIGHT column to achieve a given BLD

         vis - the MS

         bindef - the N+1 boundaries of the N BL bins

         binprob - the fractions to flag in each of the N bins

        *** Assumes there is only one field in the MS! ***

        Returns True

    thinms(vis, bindef, binprob, debug=False)
```

```
        Thin an MS by flagging to achieve a given BLD

         vis - the MS

         tenbindef - the N+1 boundaries of the N BL bins

         tenbinprob - the fractions to flag in each of the N bins

        Assumes there is only one field in the MS!

        Returns the number of flagged rows

    true_with_prob(prob)
        Return True with probability prob
```

B.4.1 Example usage

```
from thinms import *
myms = 'myobs.ms'
# bin boundaries of the "ten bin" scheme for this MS plus an eleventh outlier bin
mybindef = [14.0, 1400.0, 2786.0, 4172.0, 5558.0, 6944.0,
            8330.0, 9716.0, 11102.0, 12488.0, 13874.0, 1E9]
# filling fractions in the "ten bin" scheme as measured by assess_ms
ff = [2.5464817, 1.0470789, 0.65339828, 0.78026288, 0.89248299,
      1.32390352, 1.09104549, 1.70543259, 3.7207564,  2.62739183, 1E9]
bprob = binprob_mod(ff, lowbins=lowbins, lowfrac=lowfrac)
thinms(myms, mybindef, bprob)
```

After this treatment, the ms "myobs.ms" will have a BLD a described by the settings from which the filling fractions in array "ff" were derived.

B.5 projSelect

The script `example_case_projSelect_v1.py` contains the beginnings of a scheduling algorithm which selects the best array configuration and hour angle for the execution of a given SB. It produces a 3D plot of Filling Fraction vs. array configuration and Hour Angle. Uses mshistotools. For a description of the algorithm see section 9.2. An example plot can be seen in Fig. 9.1. `example_case_projSelect_v1.py` is accessible via the JAO CVS repository directory

```
AIV/science/ArrayConfiguration/beamWG/example_case_projSelect_v1.py
```

C Glossary

ALMA: Atacama Large Millimeter/Submillimeter Array
AR: Angular Resolution
BL: Baseline Length
BLD: Baseline Length Distribution
C43: ALMA nominal configurations with 43 antennas
C43p7: ALMA configurations based on the C43 configurations but with 7 additional antennas typically belonging to the next compact configuration
EB: Execution Block
EF: Execution Fraction
FAR: Fractional Angular Resolution
FF: Filling Fraction
GOUS: Group Obs Unit set
LAS: Largest Angular Scale
LAS2AR: Ratio of LAS to AR
L80: 80th percentile of the BL distance in meters for a given antenna array
MOUS: Member Obs Unit Set
MRS: Maximum Recoverable Scale
MS: Measurement Set
OT: Observing Tool
PSF: Point Spread Function
QA2: Level 2 Quality Assurance
RMS: Root Mean Square
SB: Scheduling Block
SG: Science Goal
THB: Technical Handbook
TM1/2: Twelve-Meter configuration 1/2
TP: Total Power

Bibliography

F. Boone. Interferometric array design: Optimizing the locations of the antenna pads. *A&A*, 377:368–376, Oct. 2001. doi: 10.1051/0004-6361:20011105.

F. Boone. Interferometric array design: Distributions of Fourier samples for imaging. *A&A*, 386:1160–1171, May 2002. doi: 10.1051/0004-6361:20020297.

F. Boone. Weighting interferometric data for direct imaging. *Experimental Astronomy*, 36:77, 2013.

D. Briggs. *High Fidelity Deconvolution of Moderately Resolved Sources.* New Mexico Institude of Mining and Technology, 1995. PhD thesis.

B. Emonts, R. Raba, G. Moellenbrock, S. Castro, C. E. Garcia-Dabo, J. Donovan Meyer, P. Ford, R. Garwood, K. Golap, J. Gonzalez, W. Kawasaki, A. McNichols, D. Mehringer, R. Miel, F. Montesino Pouzols, T. Nakazato, S. Nishie, J. Ott, D. Petry, U. Rau, C. Reynolds, D. Schiebel, N. Schweighart, J. W. Steeb, V. Suoranta, T. Tsutsumi, A. Wells, S. Bhatnagar, P. Jagannathan, J. Masters, and K. S. Wang. The CASA software for radio astronomy: status update from ADASS 2019. Proc. ADASS, page arXiv:1912.09437, Dec. 2019.

M. Holdaway and T. Helfer. Interferometric array design. *Proc. Synthesis Imaging in Radio Astronomy II, ASP Conf. Series*, 180:537, 1999.

D. Petry, M. D. Trigo, R. Kneissl, I. Toledo, and S. Facchini. New methods for alma angular-scale based observation scheduling, quality assessment, and beam shaping. *Proceedings of the SPIE, Volume 11449, id. 114491D 12 pp. (2020)*, 11449(114491D), 2020. doi: https://dx.doi.org/10.1117/12.2557596.

U. Rau, S. Bhatnagar, M. Voronkov, and T. Cornwell. Advances in calibration and imaging techniques in radio interferometry. *Proc. of the IEEE*, 97(8):1472–1481, 2009.

A. Remijan, A. Biggs, P. Cortes, B. Dent, B. Mason, N. Philips, K. Saini, F. Stoehr, B. Vila-Vilaro, and E. Villard. *ALMA Technical Handbook Cycle 7.* ALMA Doc. 7.3, ver. 1.1, 2019. https://almascience.eso.org/documents-and-tools/cycle7/alma-technical-handbook.

D. Woody. *Radio Interferometer Array Point Spread Functions I. Theory and Statistics.* ALMA Memo 389, 2001a. http://library.nrao.edu/public/memos/alma/main/memo389.pdf.

D. Woody. *Radio Interferometer Array Point Spread Functions II. Evaluation and Optimisation.* ALMA Memo 390, 2001b. http://library.nrao.edu/public/memos/alma/main/memo390.pdf.